Fundamental interactions governing the (non-)equilibrium electronic structure in low dimensions

Selene Mor

Im Fachbereich Physik der
Freien Universität Berlin
eingereichte Dissertation
zur Erlangung des Grades einer
Doktorin der Naturwissenschaften
(Dr. rer. nat.)

Freie Universität, Berlin
May 2019

This thesis work was done between 1st November 2013 and 11th February 2019 in the group of Dr. A. Julia Stähler at the Fritz Haber Institute of the Max Planck Society in Berlin.

Berlin, 11th February 2019

Erstgutachter: Prof. Dr. Martin Wolf

Zweitgutachter: Prof. Dr. Martin Weinelt

Datum der Disputation: 08.05.2019

Abstract

This thesis explores the electronic structure and ultrafast dynamics of two low-dimensional materials with focus on the role of intrinsic interactions and couplings to the environment. Charge carriers in the matter are never completely independent: they interact among each other and couple to lattice vibrations (phonons) and other excitations. Their behavior is also influenced by the environment in which the material is embedded. Moreover, confining charges to low dimensions promotes interactions and enhances the impact of the environment. All these factors lead to a variety of static and dynamic properties, and potentially to the emergence of new phases of matter. Investigating a system out of its equilibrium helps the assignment of each fundamental interaction to the related physical property. Remarkably, addressing ultrafast dynamics can also uncover novel properties which otherwise would not be accessible at equilibrium.

The first study of this thesis explores the modification of the unoccupied electronic structure of ultrathin films of SiO_2 by electron quantum confinement and investigates the electronic coupling at the interface with the Ru(0001) substrate. By means of time-resolved two-photon photoelectron spectroscopy, the formation of quantized states is resolved, whose energies are altered by the image potential of the metal.

The second and major study deals with the quasi-one-dimensional material Ta_2NiSe_5 which shows a combined electronic and structural phase transition upon heating and likely exhibits an excitonic insulator ground state. Here, the ultrafast charge carrier, exciton and lattice dynamics are disclosed by complementary time-resolved photoelectron and optical spectroscopies. The electron relaxation rate follows an anomalous dependence on the excess energy and is reduced by the transient increase of screening of the Coulomb interaction. The coherent phonon dynamics are generated by the photoinduced displacement of the charges. Optical absorption saturation restrains the number of photoexcited charges thereby hindering a photoinduced structural change. Also, the electronic band gap is transiently modulated by means of light. Nontrivially, it widens upon photoinduced strengthening of the excitonic insulator order parameter in remarkable agreement with Hartree-Fock calculations. These findings show that intrinsic interactions highly impact on the properties of Ta_2NiSe_5. Moreover, they demonstrate that it is possible to optically control the out-of-equilibrium electronic structure of a strongly interacting system on an ultrafast timescale.

These studies show that unraveling the role of fundamental interactions in low dimensions provides profound understanding and potential control of the equilibrium electronic structure and the photoinduced ultrafast dynamics of very diverse materials.

Deutsche Kurzfassung

Diese Arbeit behandelt die elektronische Struktur und die ultraschnelle Dynamik zweier niederdimensionaler Materialien, wobei das Augenmerk auf intrinsischen Wechselwirkungen und Kopplungen mit der Umgebung liegt. Ladungsträger in Materialien sind niemals vollkommen unabhängig: Sie interagieren miteinander und koppeln an Gitterschwingungen (Phononen) und andere Anregungszustände. Ihr Verhalten wird auch durch die Umgebung beeinflusst, in die das Material eingebettet ist. Darüber hinaus fördert die Verringerung der Dimensionalität die Wechselwirkungen der Ladungen untereinander und erhöht den Einfluss der Umgebung auf sie. Alle diese Faktoren führen zu einer Vielzahl statischer und dynamischer Eigenschaften und immer wieder auch zu Phasenübergängen. Die Untersuchung angeregter Zustände eines Systems hilft, eine Verbindung zwischen fundamentalen Wechselwirkungen und physikalischen Eigenschaften herzustellen. Durch die Beobachtung ultraschneller Dynamik in einem Material können zudem neuartige Eigenschaften entdeckt werden, welche im Grundzustand nicht sichtbar sind.

Im ersten Teil der Arbeit wird die unbesetzte elektronische Struktur ultradünner SiO_2-Filme untersucht, welche durch Quanteneinschluss der Elektronen und ihre elektronische Kopplung an das Ru(0001)-Substrat erzeugt wird. Unter Verwendung von zeitaufgelöster Zweiphotonen-Photoelektronenspektroskopie werden quantisierte Zustände beobachtet, deren Energien durch das metallische Bildpotential modifiziert werden.

Der zweite Teil und Schwerpunkt dieser Arbeit beschäftigt sich mit dem quasieindimensionalem Material Ta_2NiSe_5, das temperaturabhängig einen simultanen elektronischen und strukturellen Phasenübergang aufweist und wahrscheinlich im Grundzustand ein exzitonischer Isolator ist. Hier wird die ultraschnelle Ladungsträger-, Exzitonen- und Gitterdynamik komplementär mit zeitaufgelöster Photoelektronen- und optischer Spektroskopie untersucht. Die Elektronenrelaxationsrate hat eine ungewöhnliche Abhängigkeit von der Elektronenenergie und wird durch die transiente Abschirmungszunahme der Coulomb-Wechselwirkung verringert. Die Phononendynamik wird von photoangeregter Ladungsverschiebung getrieben. Eine optische Absorptionssättigung begrenzt die Zahl der angeregten Ladungsträger, wodurch ein photoinduzierter struktureller Phasenübergang verhindert wird. Durch Licht kann auch die elektronische Bandlücke temporär verändert werden. Bemerkenswerterweise vergrößert sie sich durch eine photoinduzierte Erhöhung des Ordnungsparameters des exzitonischen Isolators, was durch Hatree-Fock Rechnungen bestätigt wird. Diese Ergebnisse unterstreichen den großen Einfluss intrinsischer Wechselwirkungen auf die Eigenschaften von Ta_2NiSe_5. Darüber hinaus liefern sie den Beweis, dass die angeregte elektronische Struktur eines stark wechselwirkenden Systems auf einer ultraschnellen Zeitskala optisch kontrollierbar ist.

Diese Untersuchungen belegen die essentielle Bedeutung fundamentaler Wechselwirkungen für das Verständnis von und die Kontrolle über die elektronische Struktur und photoinduzierte Dynamik in sehr unterschiedlichen Systemen.

Contents

List of Figures

List of Tables

1 Introduction

In any physical system, the electronic and optical properties significantly rely on the intrinsic interactions among its constituents. Also, the coupling of the system to the environment can influence these properties. The study of this complexity is continuously stimulated by the desire to fundamentally understand, and potentially modify the physical properties of matter. At the same time, this study is the first step towards the utilization of a material for everyday applications like, e.g. energy storage and transfer, or computing and communication technology.

In condensed matter, important fundamental interactions are the charge-charge and the charge-lattice interactions. These govern the electronic structure and dynamics of the system, and thus, its properties in and out-of-equilibrium which are important for any application. Furthermore, by varying the electrostatic and/or chemical environment, the electronic structure can be modified based on the effective coupling of the system to its surroundings. For these reasons, one of the most intriguing scientific efforts consists in assigning each property and its out-of-equilibrium manifestation to the relevant fundamental interaction. Another important challenge is the investigation of the impact of the environment on the electronic structure. This knowledge paves the way towards the comprehension, and possibly the control of the mechanisms that regulate the electronic structure and dynamics in condensed matter.

Low-dimensional materials offer an ideal platform to study how interactions influence the electronic structure and dynamics. Confining the electron motion in space imposes constraints on the electron wave functions, resulting in new eigenstates. Consequently, the electronic structure may differ from that of the higher dimensional system. Also, the limited scattering phase space available for the electron propagation through the system [1] and the less efficient screening of the Coulomb electrostatic potential [2] favor the interactions in reduced dimensions [3]. These aspects can further modify the electronic structure. In some cases, strong interactions can even induce a transition to a completely new phase of matter [4, 5, 6]. Finally, the high surface-to-volume ratio typically makes these materials very sensitive to electrostatic potentials and the chemical environment at interfaces, offering the opportunity to reveal clear signatures of the impact of the surroundings on the electronic structure.

Many examples of modification of the electronic structure at equilibrium due to space confinement and enhanced interactions can be found in literature. In semiconducting thin films and nanostructures [7, 8, 9, 10, 11], quantized energy levels with no correspondence to the bulk electronic structure appear as a consequence of the electron confinement. In one dimension, a metal-to-insulator transition, called Peierls instability, is induced at low temperatures by the strong coupling between electrons and a periodic lattice distortion [12, 13, 14].

The variety of highly-tunable electronic and optical properties of low-dimensional, and particularly of two-dimensional (2D) materials are attracting great interest both fundamentally and technologically [15, 16, 17, 18, 19, 20]. As they often coexist in the system at equilibrium, one strategy to address them is to observe their evolution in the time domain [21, 22, 23]. This can facilitate the discernment of the fundamental interactions which may be responsible for one and/or the other property. Moreover,

because most of the potential applications intrinsically rely on the behavior of the system out of its equilibrium state, deep understanding of the dynamics of the electron and lattice subsystems on their significant timescale is demanded.

This thesis work focuses on the electronic structure and dynamics as well as their modification in two different low-dimensional systems. First, the unoccupied electronic structure of ultrathin films of silicon dioxide (SiO_2) grown on a Ru(0001) substrate is disclosed. This allows the examination of how the electronic states above the Fermi energy can be altered in low dimension and of the impact of the electrostatic and chemical environment on the electronic coupling at the interface between an ultrathin insulating film and its metallic support. The second and main topic of this thesis is the investigation of the charge carrier and lattice dynamics in the quasi-one-dimensional semiconductor Ta_2NiSe_5. This system is known to undergo an entangled electronic and structural transition characterized by a strong electron-hole interaction. The present thesis uncovers the impact of electron-hole and electron-phonon interactions on the ultrafast dynamics of Ta_2NiSe_5 and demonstrates the possibility of optically manipulate its out-of-equilibrium electronic structure on a sub-picosecond timescale.

The work tools: time-resolved spectroscopies

A powerful approach to study the electronic structure of a material is the exploitation of different spectroscopies from which complementary information on the electronic and the lattice subsystems can be obtained. In this regard, photoelectron [24] and optical spectroscopies [25] can be used to detect the momentum-resolved electronic band structure and the momentum-integrated dielectric function of the material, respectively. The desire to address also the dynamics of the system necessarily requires to extend these spectroscopies to the time domain which is relevant to the processes of interest.

Most of the scattering processes, such as charge-charge and charge-phonon scattering, occur on a sub-picosecond timescale ($< 10^{-12}$ s) [21], which defines the required time resolution of the experiments. To fulfill this requirement, the pump-probe method was first developed in the context of optical [26, 27] and photoelectron spectroscopy [28] and is nowadays extended to several other techniques like, e.g. diffraction and microscopy [29]. The basic concept of this approach is based on a pair of ultrashort pulses impinging on the sample at a controlled time delay. The first pulse ('pump') is in charge of perturbing the ground state, while the second ('probe') monitors the transient variation of specific observables of the system at variable time delays from the first pulse. In this way, the recovery dynamics of the electron and lattice subsystems back to equilibrium are temporally tracked, a process from which information on the nonequilibrium behavior of the system can be inferred [30, 31, 23]. Importantly, the application of the pump-probe technique specifically to photoelectron spectroscopy offers a unique possibility to address excited electronic states which are inaccessible via direct photoemission as they are unoccupied at equilibrium.

An important advantage of the so-called pump-probe method is the possibility to unambiguously assign the physical properties of the system to the relevant fundamental interactions. At equilibrium, this can in many cases be difficult because the observed properties appear concurrently. Optical perturbation of the ground state allows to transiently disentangle the electronic and lattice subsystems, and possibly even control their behavior in the time domain. Eventually, novel out-of-equilibrium states may be realized and probed which do not find any correspondence at equilibrium [32,

33, 34, 35, 36]. As outlined in the following, this nonequilibrium pump-probe experimental approach is utilized in both topics investigated in this thesis: the unoccupied electronic structure of SiO_2 films on Ru(0001) and the combined ultrafast electron and lattice dynamics of the quasi-one-dimensional excitonic insulator Ta_2NiSe_5.

Quantum electron confinement in ultrathin films of SiO_2 on Ru(0001)

Ultrathin films of SiO_2 grown on a Ru(0001) substrate have recently raised great interest for the realization of quasi-free-standing oxide bilayers that may be used as isolated platforms for catalytic reactions, and could serve as two-dimensional insulating material in electronic devices [37, 15]. Clearly, both applications rely on the weak electronic coupling between the oxide film and its surrounding in order to minimize the impact of the oxide on the processes of interest. In this regard, the knowledge of the unoccupied electronic structure of the oxide film and how it may be influenced by the metal support in the vicinity is crucial.

The unoccupied states of SiO_2 at the low-dimensional scale are rather unknown due to the difficulty to access them at equilibrium. Already from a fundamental point of view, since the film thickness amounts to only $\sim$2 Å [38], it is unclear how the confined electron motion perpendicular to the film may impact on the unoccupied electronic structure. Furthermore, the proximity of the metal surface raises the question about how the electrostatic image potential extending outside the metal [39] joins the inner potential of the oxide film, and whether it may modify the energetics of the latter.

To address these aspects, time-resolved two-photon photoelectron (2PPE) spectroscopy [39] is used in this thesis to resolve the unoccupied electronic states of ultrathin films of SiO_2 grown in two different thicknesses on Ru(0001). In the experiments, the unoccupied states are transiently populated by electrons photoexcited from the Ru substrate, allowing the inspection of the electronic coupling at the oxide/metal interface.

The study reveals that the unoccupied electronic structure of ultrathin SiO_2 films changes drastically compared to that of the bulk compound [40]. In particular, at a coverage lower than one bilayer, the conduction band appears quantized into weakly dispersive subbands that likely originate from electron confinement in the direction perpendicular to the oxide layer. However, quantum-well modeling suggests that the inner potential is not rectangular as expected for a completely isolated ultrathin film [3]. In fact, a spatially-varying (triangular) potential is needed to reproduce the subband energy splitting. This finding is interpreted as a modification of the well by the superposition of the image potential of Ru, eventually impacting on the energy of the CB quantum subbands.

At the coverage equivalent to two complete layers, the oxide film is only weakly bound to the substrate by means of van der Waals forces and its distance from the metal is larger [41]. For this system, the electronic structure varies significantly from that observed at the lower oxide coverage. A new occupied state appears, which attests the presence of oxygen atoms intercalated underneath the oxide film [42]. Since these oxygen ad-atoms are known to increases the distance between the film and the substrate [43], they can affect the electronic coupling between the film and the metal substrate. Also, the lowest CB quantum subband is no longer detected and the second one shifts in energy, suggestive of a different degree of spatial confinement inside the film [39].

To sum up, the investigated unoccupied electronic structure of ultrathin films of SiO_2 on Ru(0001) reflects the low dimensionality of the system through the quantization of the conduction band due to electron confinement. Importantly, the effective

well potential developing inside the film is influenced by the image potential that extends in the surrounding region outside the metal surface. In other words, it is discovered that even at the bilayer level, where SiO_2 is only weakly interacting with the substrate, the electronic structure is extremely sensitive to the electrostatic environment. Consequently, the film is never completely decoupled from its support. Clearly, this result has important implications for the emergent applications of ultrathin films of SiO_2. More generally, it provides insights on the impact of the environment on the electronic properties of a low-dimensional insulator.

The presented work was performed in collaboration with the SMART I photoelectron microscopy group at Bessy, Berlin, where the silica films were grown. The photoemission experiments were carried in the Electron Dynamiχ laboratory at the Fritz Haber Institute.

Interactions governing the nonequilibrium dynamics of the excitonic insulator Ta_2NiSe_5

The impact of electron-hole and electron-phonon interactions on the nonequilibrium properties of Ta_2NiSe_5 is the focus of the second and main topic of this thesis. The study develops in the framework of the nonequilibrium behavior of an excitonic insulator phase. This phase of matter is briefly introduced in the following to prepare the presentation of the results achieved in the present work.

In semiconductors, the naturally attractive Coulomb electrostatic interaction between a negative (electron) and a positive (hole) charge is inefficiently screened due to the low concentration of mobile carriers. Therefore, an electron and a hole pair into a bound state, termed exciton. If the Coulombic screening is further suppressed by, for instance, reducing the dimensionality of the system [44] or further lowering the density of mobile carriers, the exciton binding energy may exceed the electronic band gap of the semiconductor and exciton formation occurs spontaneously. In this case, a transition to a new phase of condensed excitons, termed excitonic insulator, is theoretically predicted. To stabilize this phase, a delicate interplay of electronic structure renormalization and lattice-ion adjustment is also expected [45, 46].

Sufficiently intense photoexcitation of a semiconductor can transiently enhance the Coulombic screening, thus weakening the excitonic coupling. This often results in a narrowing of the electronic band gap, a process referred to as 'band gap renormalization' [47, 48, 49, 50, 51, 52, 53, 32]. Concerning the photoexcitation of the excitonic insulator phase, its effects are far from trivial: on the one hand, enhancement of the Coulombic screening by means of the photoexcited carriers may reduce or even suppress the band gap, in analogy to the nonequilibrium dynamics of photoexcited semiconductors. On the other hand, an excess population of non-thermal electrons and holes is formed at the band extrema. Those may bind into coherent excitons and modulate the excitonic insulator gap. Thus, the nonequilibrium behavior of an excitonic insulator cannot simply be derived from the properties of its ground state.

The discovery of the quasi-one-dimensional, small-band-gap semiconductor Ta_2NiSe_5 encouraged the possibility to experimentally observe the excitonic insulator phase at equilibrium. Below a critical temperature $T_C = 328$ K, the system shows a transition to a more insulating phase concomitant with a structural distortion which is consistently explained by the occurrence of an excitonic insulator ground state [54, 55, 56, 57]. Nevertheless, the interplay between the electron and the lattice subsystems is still under debate [55, 56, 58]. Also, the possibility to photoinduce the electronic and structural phase transition in Ta_2NiSe_5 needs to be tested. Eventually, if Ta_2NiSe_5

effectively hosts an excitonic insulator phase below T_C, it should offer the possibility to disclose how its band gap and carrier dynamics evolve out of equilibrium.

Motivated by these open questions, the ultrafast electron and lattice dynamics of Ta_2NiSe_5 launched by an optical pulse below T_C are studied in this thesis. Specifically, the work aims at (i) explaining how the electronic and the phononic subsystems of the low temperature phase connect on the ultrafast timescale, (ii) identifying the nonequilibrium behavior of an excitonic insulator, and (iii) reconstructing the relaxation pathways that guide the electronic subsystem back to equilibrium.

In order to simultaneously probe the photoinduced electron and the lattice dynamics of Ta_2NiSe_5, time-resolved coherent optical phonon spectroscopy is employed, which is based on the pump-probe scheme explained earlier. In the context of this study, a non-collinear optical parametric amplifier is built with an optical scheme adapted from [59] in order to tune the probe photon energy to the mid-infrared (mid-IR) range. In this way, optical transitions resonant to the energy of the low-temperature electronic band gap are preferentially measured. This assumption is ultimately demonstrated by the direct comparison, shown for the first time in this work, between the time-resolved mid-IR optical response and the electron dynamics as measured by time-resolved photoelectron spectroscopy with absolute energy and momentum resolution.

This complementary optical and photoemission study reveals that coherent optical phonons couple to the electronic transitions occurring at the Γ point of the Brillouin zone, where the direct band gap opens. Also at Γ, the optical absorption of pump photons saturates above a critical fluence F_C due to half-depletion of the initial states. Remarkably, this fluence value is found to be lower than the energy threshold required for the symmetry change. Therefore, the low-temperature structural phase of Ta_2NiSe_5 remains unperturbed by the photoexcitation and the photoinduced structural phase transition is inhibited. This further implies that the dynamics of the electronic subsystem can be discussed without invoking distortions of the lattice. These results are published in Mor et al., Phys. Rev. B, 97, 115154 (2018).

The nonequilibrium behavior of the electronic band gap below T_C is then examined in order to identify the dynamical signature of the excitonic insulator phase and test the possibility to photoinduce the electronic phase transition to the high-temperature semiconducting phase. This is investigated by combining time-resolved photoelectron spectroscopy of the occupied and unoccupied band structure around the Γ point. Two main processes are identified: below F_C, the band splitting at and near Γ reduces due to transiently enhanced screening of the Coulomb interaction; above F_C, these semiconductor-like dynamics are superimposed at Γ by a competing band gap widening that persists up to $\sim$1 ps. This behavior is opposite to what is usually observed in and expected from excited semiconductors. Hartree-Fock calculations performed by D. Golež, P. Werner (University of Fribourg, Switzerland), and M. Eckstein (University of Erlangen-Nürnberg) confirm that the band gap widening arises from the out-of-equilibrium strengthening of the exciton condensate. With this study, the nonequilibrium behavior of the excitonic insulator phase in Ta_2NiSe_5 is singled out and is found to result from two combined processes: free-carrier-induced screening of the Coulomb interaction and photoenhancement of the exciton condensate density. Furthermore, control of these two processes, and thus of the electronic band gap is proven to be achievable on the ultrafast timescale upon tuning the excitation density. These results are published in Mor et al., Phys. Rev. Lett. 119, 086401 (2017).

The ultrafast relaxation dynamics of photoexcited charge carriers in the excitonic insulator phase is addressed by means of time-resolved photoelectron spectroscopy. The relaxation time of the conduction electrons is found to depend linearly with the

inverse excess energy, in clear contrast with the predictions for a Fermi liquid. This anomalous behavior likely relates to the poor screening of the Coulomb interaction. Upon increase of the excitation density, the decay dynamics slow down at any energy due to the transient enhancement of the screening by means of the photoexcited carriers. Remarkably, at Γ, the relaxation rate of photoelectrons is majorly impacted by the density of photoexcited holes at the top of the VB. Above F_C, the formation of coherent excitons appears as additional channel for the depletion of the conduction band bottom, further supporting the mechanism for the enhancement of the excitonic insulator band gap. Interestingly, there seem not to be models which can comprehensively capture the energy- and fluence-dependent charge carrier dynamics observed in Ta_2NiSe_5. The present work may hopefully trigger new theoretical studies in the framework of relaxation processes of systems with strong intrinsic interactions.

In summary, the nonequilibrium dynamics of the excitonic insulator phase of Ta_2NiSe_5 are detailed by the presented studies. (i) The electronic and the phononic subsystems are coupled at Γ at the time of the photoexcitation. The optical absorption saturation occurring at the same momentum limits the energy imparted on the phonon subsystem such that the photoinduced structural change does not take place [60]. (ii) The nonequilibrium dynamics of the excitonic insulator band gap rely on a subtle interplay of screening-induced band gap renormalization and photoenhancement of the excitonic condensate density. This allows the transient manipulation of the excitonic insulator band gap on an ultrafast timescale by tuning the excitation density of the electronic subsystem [36]. (iii) The electron relaxation dynamics exhibit a nontrivial energy dependence and are governed by the transient screening provided by the photoexcited carriers. This impressively reflects on the relaxation rate at the conduction band bottom which mainly follows the build-up of screening by means of the photoexcited holes at the VB top.

Outlook

The insights provided by this thesis unravel intriguing intricacies that govern the properties of condense matter at equilibrium as well as on the ultrafast timescale. The interplay of quantum electron confinement and electronic coupling with the environment is shown to remarkably impact the electronic structure in low dimension. The assignment of distinct dynamical processes to the relevant fundamental interaction enables the potential control of these dynamics by means of light. Furthermore, this research demonstrates that fundamental interactions can be obstacle as well as promoter of ultrafast processes: they can limit the available excitation channels, thereby helping to protect the system against a photoinduce phase transition, but also allow to address new nonequilibrium state which may not be thermally accessible.

In conclusion, this thesis work shows that in a physical system, novel properties can be revealed once the electronic structure and dynamics are disclosed and it is learned how to manipulate them. Possibly, this work will stimulate studies of other interacting systems aiming at the fundamental understanding of the intrinsic interactions and the coupling with the environment as well as their modification for potential applications.

2 Theoretical background

The electronic structure of a material in and out of equilibrium is cooperatively determined by the intrinsic interactions between different degrees of freedom of the system like, e.g. charges and phonons, and their coupling to the environment. When the dimensionality of the system is reduced, interactions typically become stronger and the impact of the environment more pronounced, likely leading to the appearance of new physical properties. Understanding these fundamental intricacies and learning how to control them on an ultrafast time scale are goals of this thesis work. These are developed by investigating two different systems, ultrathin films of SiO_2 grown on a Ru(0001) metal surface and the quasi-one-dimensional Ta_2NiSe_5.

In this section, the theoretical details of the present work are given. Section 2.1 introduces the general aspects of the low dimensionality that are connected with the change of the screened Coulomb potential of a charge in a solid. Section 2.2 presents the concept of quasiparticle introduced by Landau to describe the dynamics of a charge interacting with the available degrees of freedom of the system. In Section 2.3, the concept of electron quantum confinement and two exemplary quantum well models are discussed. In Section 2.4, the image potential is defined for the case of a bare metallic surface and in presence of adlayers. These two concepts, quantum well and image potential, are focus of the discussion on the photoemission results of SiO_2/Ru(0001). This system is presented in Section 2.5. The second topic of this thesis is the equilibrium and out-of-equilibrium behavior of a phase of matter, termed excitonic insulator, that arises from extraordinary strong Coulomb interaction between electrons and holes and combines with a lattice distortion. This phase is introduced in Section 2.6. The chosen material for this study is the low-dimensional ternary chalcogenide Ta_2NiSe_5, whose current knowledge is reviewed in Section 2.7.

2.1 Aspects of low dimensionality

The equilibrium and dynamical properties of an electron in a solid are influenced by the structural and electronic environment, as this determines the net of interactions experienced by the charge. The simplest case is presented by F. Bloch [61] for a free electron propagating in an infinite periodic arrangement of lattice ions. The wave function $\Psi_{\mathbf{k}}(\mathbf{r})$ solving the Schödinger equation reads:

$$\Psi_{\mathbf{k}}(\mathbf{r}) = \mathrm{e}^{i\mathbf{k}\cdot\mathbf{r}} u_{\mathbf{k}}(\mathbf{r}), \tag{2.1}$$

where the plane wave function of a free electron, $\mathrm{e}^{i\mathbf{k}\cdot\mathbf{r}}$, is multiplied by the $u_{\mathbf{k}}(\mathbf{r})$ function which has the periodicity of the reciprocal crystal lattice. Thus, such electron travels through the whole crystal without 'bouncing onto' the lattice ions. However, it feels their periodic potential which sets the Born-von-Kármán boundary conditions for the electron motion and thus the allowed values for the electron wave vector $\mathbf{k}$. This situation is the closest to that of an independent electron traveling inside an electric-field-free metal.

When a finite crystal is considered, the Bloch wave function is reflected back by the lattice edges, resulting in a pair of opposite standing waves, whose probability

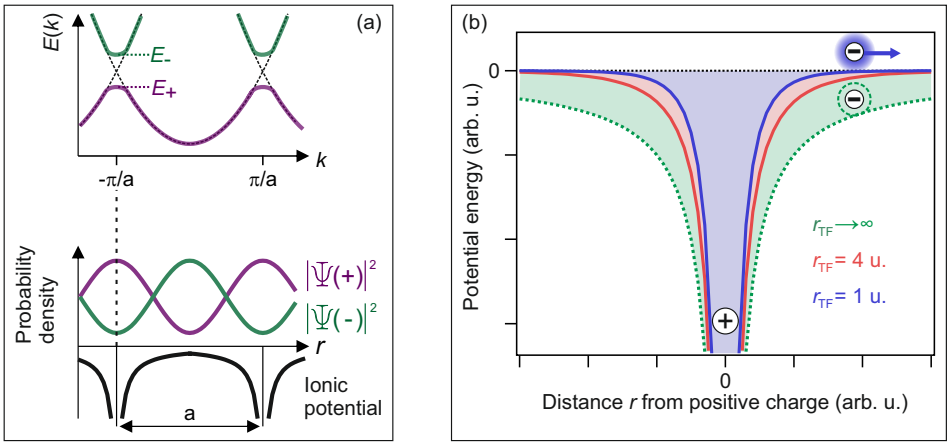

FIGURE 2.1: (a) Picture of the band gap opening at the Brillouin zone boundaries $\pm\pi/a$ in the nearly-free electron model. Modified from [2, 62]. (b) Comparison between unscreened (dashed green) and screened (red, blue) electrostatc Coulomb potential V(r).

densities, $|\Psi(+)|^2$ and $|\Psi(-)|^2$, are maximum and minimum near the ion cores, respectively, as illustrated in Fig. 2.1 (a). At the boundaries of the Brillouin Zone which correspond to the ion core sites in real space, forbidden gaps open for the allowed electronic states, as shown on top of (a). If the gap opening appears at the Fermi level E_{F}, the system turns into an insulator as the energy cost of electron transport through the crystal, i.e. of carrying an electrical current, is at least that of the size of the gap.

The described approaches refer to as free and nearly-free electron models and qualitatively capture the fundamental characteristics of a metal and an insulator, respectively. Both are based on the effective interaction of the propagating electron with the crystal environment, which is crucially determined by the ability of screening the surrounding electrostatic field by means of the other charge carriers. This fundamental concept of screening is introduced in the following.

The Coulomb electrostatic potential of a positive point charge q in vacuum decreases linearly with the inverse distance, r^{-1}, from the charge. Inside the crystal, the associated electric field is screened by the cloud of nearly-mobile electrons diplaced around the ion cores, thus the spatial extend of the Coulomb potential is exponentially damped, resulting in

$$V(r) = \frac{1}{4\pi\epsilon_0}\frac{q}{r}\mathrm{e}^{-r/r_{\mathrm{TF}}}, \tag{2.2}$$

where r_{TF} is the Thomas-Fermi screening length and shortens for higher density of electrons close to E_{F} [62]. The modified potential is shown in Fig. 2.1 (b): the shorter the decay range r_{TF} of the screened Coulomb potential (red to blue), the more mobile the propagating electron. This explains why inside a metal an electron can freely travel inside the solid over long distances without remaining trapped by the Coulomb potential, while in insulators, it is rapidly localizes around the lattice sites.

Further reducing the dimensionality of the system drastically impacts on the boundary conditions for the electron wave function and the screening of the Coulomb interaction. Consequently, new properties and behaviors of the system appear both at equilibrium and dynamically. This thesis work focuses on three aspects of the small scale:

(1) when electrons are spatially confined on a scale comparable with their mean free

path, the new boundary conditions on the electron wave function can result in the discretization of electronic levels into quantum well states (see Section 2.3);

② electrons can be bound in front of a metallic surface by the electrostatic image potential. This potential originates from the polarization of the surface and extends for several Angstrom outside the metal (see Section 2.4) [39];

③ combining low dimensionality and poor screening favors strong fundamental interactions. These interactions can on the one hand, bring the electronic and structural subsystems into instability against phase transitions, on the other hand, govern the nonequilibrium dynamics of the new phase (see Section 2.6).

The first two aspects often appear concurrently and determine the electron dynamics at surfaces and interfaces between a metal and a thin metallic [63] or organic film [64, 65]. Here, these concepts are exemplified by the energetics of ultrathin films of silicon dioxide ('silica', SiO_2) interfacing a Ru(0001) metal surface. In particular, the interplay between the quantum confined electronic states of silica and the image potential of ruthenium is investigated by means of time- and angle-resolved two-photoemission spectroscopy. The results are discussed in Chapter 4.

Intrinsic fundamental interactions are at the origin of various symmetry-broken phases of matter. In the case of Ta_2NiSe_5, studied in this thesis, the low-temperature ground state relies on the extraordinary strong interaction between an electron and its corresponding positive charge (hole), argued to result into the spontaneous formation of strongly bound pairs, called excitons, and the opening of an excitonic insulator gap in the electronic band structure around E_F [46]. The resulting electron and lattice dynamics are focus of the discussion in Chapter 5.

2.2 Dynamics of interacting electrons

As introduced in the previous section, turning on fundamental interactions in a solid by e.g., reducing the phase space of a propagating electron, results in new physical properties. Also, tuning the interaction strength by, for instance, changing the efficiency of screening the Coulomb electrostatic potential impacts on the electronic structure and dynamics. Therefore, examining the fundamental interactions experienced by the electrons inside the solid is necessary in order to predict the equilibrium and dynamical properties of the material. The description of these interactions for each electron would be impractical since the number of potentially interacting particles (electrons and atoms) amounts to the Avogadro constant (10^{23} per mole). When, however, the scattering among electrons dominates against other scattering processes involving, e.g. lattice ions (phonons) or crystal defects, the Fermi liquid theory (FLT) developed by Landau for metals [66] can successfully describe a variety of properties and dynamical behaviors of the interacting system.

In FLT, the ensemble of electrons is treated as a Fermionic gas and the initial Hamiltonian is that of a non interacting system. As the Coulomb interaction is activated, the ground state adiabatically evolves into the interacting state. This means that the new eigenvalues maintain a one-to-one correspondence to those of the non-interacting system, but also that electrons are no longer independent but become *quasiparticles* 'dressed' by the interaction. The emergent properties of such interacting particles are encoded in two physical quantities: the effective mass and the lifetime. As the Coulomb repulsion among electrons impedes their free motion, the electron mass renormalizes, i.e. quasiparticles become effectively heavier. Due to electron-electron scattering processes, the electron energy spreads around the initial

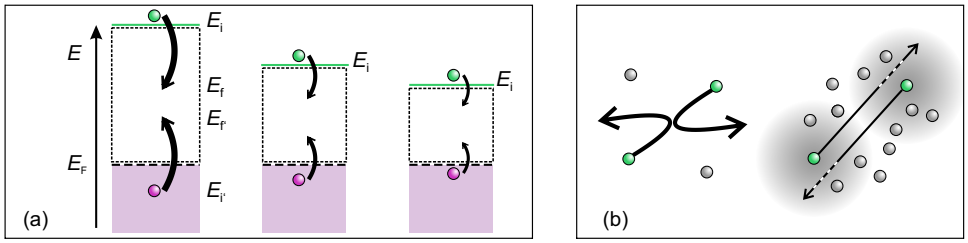

FIGURE 2.2: (a) Scattering phase space of an excitation. Thicker arrows correspond to larger scattering rate, thus shorter electron lifetime. (b) Scattering probability in absence (left) and presence (right) of Coulomb screening.

eigenvalue which is no longer a stationary state and the quasiparticle acquires a finite lifetime.

The quasiparticle concept remains valid until a nonvanishing lifetime can be assigned to the interacting electron. The electron lifetime, defined as the inverse rate of electron-electron scattering, is determined by all the possible transitions from an initial state at energy E_i into a final state of energy E_f under satisfaction of energy conservation. The situation is depicted in Fig. 2.2 (a). An electron in an initial state E_i above E_F can only scatter into a lower state E_f along with the excitation of another electron in an occupied state $E_{i'}$ into an unoccupied state $E_{f'}$. Clearly, for E_i closer to E_F, the scattering phase space reduces and correspondingly the electron lifetime increases. Conversely, at high energies the quasiparticle is more unstable against rapid scattering outside the initial state E_i and the lifetime reduces. Still, its lifetime may not vanish if the screening of the Coulomb interaction builds in sufficiently rapidly. The time for the build-up of the Coulomb screening is given by the inverse plasma frequency of the system, i.e. the oscillation period of a collective excitation, and shortens with increasing the electron density [61]. Then, two extreme cases are depicted in Fig. 2.2 (b). At low electron density, propagating quasiparticles are not efficiently screened, thus their scattering probability is large or equivalently, the screening build-up time is longer than the inverse rate of electron-electron scattering. On the contrary, at large electron density, their interaction is rapidly screened and ideally they continue to propagate along their initial direction without exchanging energy.

Formally, the scattering probability rate is described by the Fermi's Golden Rule

$$P_{i\to f} = \frac{2\pi}{\hbar}\sum_{i',f'} n_{i'}(1-n_{f'})|V_{i,i'}^{f,f'}|^2\delta(E_i - E_f + E_{i'} - E_{f'}), \tag{2.3}$$

where n_i and n_f are the Fermi-Dirac distribution (FDD) of the initial and final state populations, the δ function accounts for the energy conservation and the intermediate term $V_{i,i'}^{f,f'}$ is the interaction matrix element which contains the screened Coulomb electrostatic potential, as given by Eq. (2.2). As expected, the electron-electron scattering rate from an initial state E_i depends on two concepts: the scattering phase space, which is defined by the number of available final state n_f, and the interaction strength which is determined by the screening of the interaction with other electrons in various states $E_{i'}$. Thus, thorough these two factors, the electron lifetime explicitly depends on the excess energy of the electron with respect to E_F, and the density of electrons contributing to the screening.

An important result of the FLT is that because both the phase space and the

screening change with the dimensionality of the system, the dependence of the lifetime on the excess energy and density of electrons also varies in system of different dimensions. Effectively, the dimensionality affects the scattering phase space and interaction strength in opposite ways: when reducing the dimensionality, the phase space reduces as less final states are available for the scattering of the quasiparticle; on the contrary, the interaction strength is enhanced as the screening ability lowers. In a three-dimensional (3D) FL, the electron lifetime is found to scale inverse quadratically with the excess energy with respect to E_F and superlinearly with the electron density by a factor of $6/5$ [67]. If one dimension is scaled down, the energy dependence of the electron lifetime deviates from the 3D FLT prediction, particularly at energies close to E_F. The electron lifetime in a two dimensional (2D) FL is indeed corrected by an extra logarithmic dependence [68]:

$$\tau_{\mathrm{e\text{-}e}}^{(2\mathrm{D})} = c^{(2\mathrm{D})} \left(\frac{E - E_\mathrm{F}}{n}\right)^{-2} \ln^{-1}\left(\frac{n}{E - E_\mathrm{F}}\right), \tag{2.4}$$

where n is the electron density and $c^{(2\mathrm{D})}$ is a constant. The derivation of the constant can be found in [69]. Importantly, as a result of the logarithmic correction, the lifetime in the vicinity of E_F shortens compare to a 3D FL, an effect that can be explained by the less efficient screening of the Coulomb interaction between electrons.

Eventually, in one dimension (1D) the FLT breaks down as the propagation of an electron is hampered at any energy due to the one-directional geometry. The inevitable electron-electron interaction results in the fact that only collective excitations are supported in 1D, which can involve charge or spin ordering. Effectively, a 1D system is very susceptible to instability towards a spontaneous Peierls periodic lattice distortion [12]. One dramatic consequence of the suppressed phase space and screening in 1D is that at energies close to E_F, where the dispersion of the single band is rather linear, the inverse scattering rate is altered to [70]:

$$\tau_{\mathrm{e\text{-}e}}^{(1\mathrm{D})} \propto \frac{1}{(E - E_\mathrm{F})}. \tag{2.5}$$

Obviously, a 1D object is rather a theoretical construct. In reality, 1D-like behaviors can be observed in bulk systems formed by linear atomic chains weakly held together by van der Waals forces or in isolated wires self-assembled on a surface. Those materials are referred to as quasi-one dimensional[14, 71] and behave as predicted in 1D as long as the coupling to higher dimensions is weak. In this regard, interchain electron hopping already weakens the 1D constraint, likely leading to a dimensional crossover towards a 2D system.

Thus, the dynamics of systems whose energy redistribution occurs predominantly via electron-electron scattering can successfully predicted by the FLT and specific energy dependence of the quasiparticle lifetime are expected based on the system dimensionality. Nevertheless, in ideal FLT, the scattering with phonons is neglected, although it constitutes an important excitation decay channel in solids. Effectively, electron-phonon scattering typically accounts for the exchange of energy on the order of the thermal energy $k_\mathrm{B}T$. Therefore, upon optical excitation (on the order of few eV) it is reasonable to assume that initially, only electron-electron scattering are involved. After quasiparticles have reached energy states on the order of $E - E_\mathrm{F} \approx k_\mathrm{B}T$, scattering with phonons typically become dominant over the electron-electron scattering [72], thus contributing significantly to the quasiparticle lifetime.

In conclusion, the conditions required by the FLT behavior are typically accomplished by metals, whose high density of mobile electrons guarantees a finite lifetime

for the screened quasiparticles. However, even in metallic systems, some deviations from the FL prediction are observed due to electronic band structure and charge transport effects which are not considered by the FL model [1]. More generally, the interplay of scattering phase space and screening efficiency is crucial in determining the effective quasiparticle lifetime as they easily produce deviations from the FLT predictions. Interestingly, the lifetime of layered graphite, a narrow-band-gap semiconductor, exhibits a nontrivial inverse linear dependence on the excess energy. This non-FL behavior is assigned to imperfect screening of the Coulomb interaction due to the vanishing density of states of graphite at energy close to E_F [73]. Eventually, in systems where the poor Coulomb screening is combined with strong coupling of electrons to other degrees of freedom, the analysis of the quasiparticle dynamics will likely require to considers relaxation mechanism beyond the electron-electron scattering. In this regards, an example is provided in this thesis by the quasiparticle dynamics of the excitonic insulator Ta_2NiSe_5 (see Section 5.4).

2.3 Electron quantum confinement: Quantum well models

Electron quantum confinement is the reduction of degrees of freedom of an electron while propagating in a low-dimensional environment. Quantum-mechanically, the effect corresponds to restricting the allowed phase space of the electron wave function by imposing constraints at the space boundaries. As a result, the eigenstates solving the Schödinger equation will change, from which new macroscopic properties of the matter may emerge.

Realistic examples where electrons experience quantum confinement in any reduced dimension: An electron in a zero-dimensional (0D) nanostructure, or traveling through a one-dimensional (1D) junction between two semiconducting materials or transferring at a two-dimensional (2D) interface where it may experience strong local Coulomb potential. Microscopically, these situations are typically modeled by the Schödinger problem of a particle inside a quantum potential well.

The present work explore the impact of electron quantum confinement on the unoccupied electronic structure of ultrathin films of SiO_2 grown on the Ru(0001) metallic surface. This section presents two quantum well models that are relevant for the discussion of the experimental results.

2.3.1 Rectangular quantum well

The motion of an electron in a thin film can be separated into the propagation parallel and perpendicular to the film plane. The parallel motion should not be affected by the reduced geometry[1], thus remaining that of a (nearly-)free particle propagating inside a Bloch periodic potential. Conversely, the motion perpendicular to the film is constrained at both sides of the film which acts as a potential barrier for the electron. One of the simplest case to model this situation is the rectangular well of finite depth depicted in Fig. 2.3, left [74]. With $2z$ the direction perpendicular to the film and d the film thickness, the potential along z is zero inside the well, i.e. for $-d < z < d$, and constant outside, i.e. for $z > 0$. Thus, the Born-von-Kármán boundary conditions requires that at $z \pm d$, the amplitude and first derivative of the electron wave function join continuously those of the wave function valid in the region outside the well.

[1] This is valid until the lateral film dimensions largely exceed the film thickness, thus it can be assumed that the film extends infinitely in the plane directions.

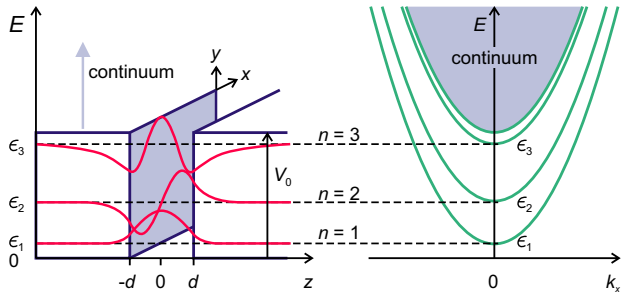

FIGURE 2.3: Model of an isolated thin film: Rectangular quantum well. The motion perpendicular to the well, i.e. along z is confined inside the well and leads to a discrete series of bound states ϵ_n. As the depth of the well is finite, there is a non-vanishing probability for the electron to escape outside the well. Within the film plane, i.e. along the x and y directions, the electron moves freely and can occupies a set of parabolic bands (green curves) with origin at the energies of the quantum states (blu lines).

Upon these constraints, the Schödinger equation for the potential along z is solved by standing waves propagating inside the well and joining continuously an exponentially-decaying function at each side of the well (red curves). The boundary conditions leads to the quantization of the allowed electron wave vectors, $k_{\mathrm{z,n}}$. The corresponding discrete eigenstates ϵ_n read

$$\epsilon_n = \frac{2\hbar^2 v_n^2}{m(2d)^2} \quad n = 1, 2, 3..., \tag{2.6}$$

and have to be found numerically. In Eq. (2.6), m is the electron mass along z and v_n a dimensionless variable which contains the corresponding wave vector $k_{\mathrm{z,n}}$. If the constant outer potential is very large ($\rightarrow \infty$) compared to the width of the well, the problem eventually resembles that of an infinite square well with $v_n = n\pi/2$ whose eigenstates are calculated analytically.

Several consequences arise from the energy quantization inside the film. First, a stacking of free-electron parabolic bands appear in the plane of the film (blue curves) with minima at the ϵ_n values. Also, the lowest level (n =1) separates from the bottom of the well: the ground states in absence of electron quantum confinement is no longer occupied. Furthermore, because the energy splitting between two levels depends inverse quadratically with the width of the well, i.e. with the degree of confinement, reducing the width of the well further separates the quantum levels which overall are shifted towards higher energies. Notably, because the quantum-mechanical solutions are non vanishing at the well boundaries but extend outside for a certain length, there is a finite probability to find an electron propagating outside the film. This aspect is relevant when considering electron transfer processes across the interface between a film and the vacuum or interface coupling between states of an heterogeneous structure, as it is the case of SiO_2/Ru(0001).

2.3.2 Triangular quantum well

The rectangular quantum well is a good approximation for a thin metallic film whose walls can be modeled by equipotential surfaces of a plane capacitor. However, when charges are distributed non-homogeneously perpendicularly to a surface, a spatially varying potential develops along that direction. For example, at the surface of an n-type semiconductor, the absorption of donors at the surface leads to a local excess

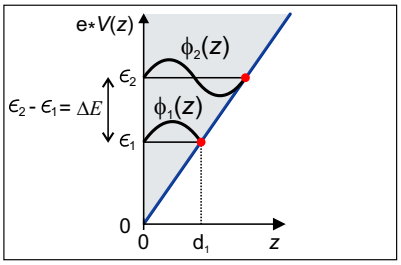

FIGURE 2.4: Illustration of a triangular potential well (solid blue) and the two lowest quantum well states. Their energies $\epsilon_{1,2}$ depend on the respective width d of the well, which in turn is defined by the slope of the potential.

electron concentration. An electrostatic potential forms in the z-direction perpendicular to the surface and can induce a downwards bending of the electronic bands at the surface [75]. If the conduction band crosses E_{F}, an accumulation layer of strongly confined electrons is formed which can be described to first approximation by a linearly-varying (triangular) potential well [76, 77]. An other example of electron confinement in a spatially-varying potential well is provided by an electron in the vacuum region in front of a metal surface being trapped by the electrostatic image potential. This concept will be discussed in the next section.

In the following, the solution for a triangular potential well is presented [78, 76]. The potential reads $V(z) = -\mathcal{E}z$ and it is sketched in Fig. 2.4). $\mathcal{E}$ is the electric field inside the well and determines the slope of the triangular potential well. The potential is zero at the bottom of the well, i.e. $z = 0$, and increases linearly as $z \to \infty$. The Schrödinger equation can be solved exactly and provides the following analytical expression of the energy spectrum ϵ_i along the z-direction:

$$\epsilon_i = \left(\frac{3}{2}\pi\hbar e\right)^{2/3} \frac{(|\mathcal{E}|)^{2/3}}{(2m_{\perp}^{*})^{1/3}} \left(i - \frac{1}{4}\right)^{2/3} \qquad i =, 1, 2, 3... \tag{2.7}$$

These energy levels are calculated with respect to the zero-energy at the quantum well bottom. It is noted that the levels becomes closed together as i increases, because the well broadens with increasing energy. Also, each level shifts towards the quantum well bottom if the potential slope reduced, i.e. the well becomes over all wider. This can be understood in terms of a weaker electron confinement and a increased delocalization of the wave function inside the well.

2.4 Electrons in front of a metal surface: the image potential

An electron in the vacuum region outside a metal surface can be trapped by an electrostatic potential extending in front of the metal. This potential is referred to as image potential (IP) and leads to a series of bound electronic states. If a layer of different material is grown on top of the metal surface, the IP has to join smoothly the inner potential of the adlayer. Depending on the alignment between the electronic states of the adlayer and the image potential states (IPSs) of the metallic substrate, the wave function of the IPSs has a certain probability to penetrate into the adlayer. This can significantly vary the energy, dispersion and lifetime of the IPSs. At the same time, the superposition of the IP on the inner potential of the adlayer can potentially

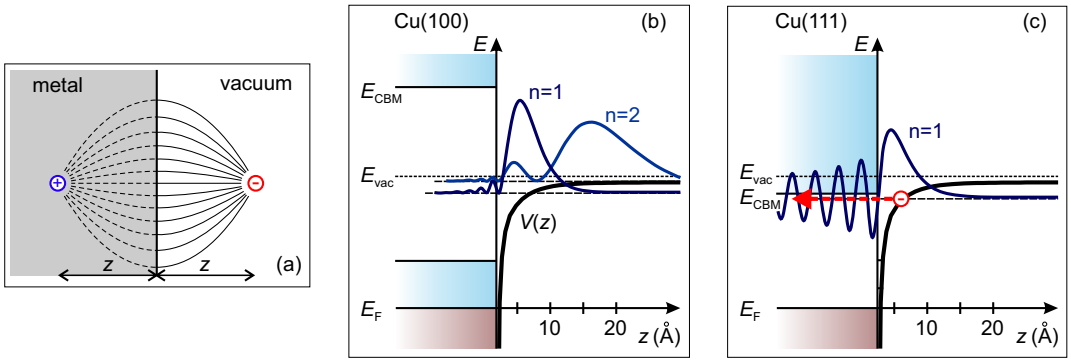

FIGURE 2.5: (a) Concept of image charge behind a metal surface. (b) - (c) The IP and the probability densities at the interface with Cu(100) and Cu(111), respectively. Modified from [79]

modify the electronic structure of the adlayer itself, which will then differ from that of a free-standing layer (i.e. in absence of the metal support). These aspects will be discussed with regard to the electronic structure of ultrathin SiO_2 films grown on the Ru(0001) surface. In this section, the concept of image potential is introduced for the case of a bare metal surface and in presence of an adlayer.

As depicted in Fig. 2.5 (a), a negative charge (-) at distance z from a metal induces an electric field (black solid lines). In the metal, the charges rearrange in order to maintain both equipotential surface and inner charge neutrality. The effect is equivalent to that of a positive charge (+), termed 'image' charge, appearing inside the metal at mirrored distance $-z$ from the surface. As a result, an attractive Coulomb force acts between the 'image' charge and the outer electron, giving rise to an electrostatic image potential (IP) extending for several Å outside the metal. In this picture, if the electron approaches the metal surface with energy lower than the vacuum barrier, it remains trapped at a certain distance from the metal surface. Effectively, the electron finds itself as inside a potential well built by the IP and the surface, and can occupy a series of bound states.

Quantum-mechanically, the picture is analogous to that of an electron orbiting around the nucleus of an hydrogen atom, where the positive charge plays the role of the nucleus and the distance $2z$ of the atomic radius. The IP is then written in the form

$$V(z) = E_{vac} - \frac{e^2}{4\pi\epsilon_0}\frac{1}{4z}, \tag{2.8}$$

where E_{vac} is the energy of an electron in vacuum at infinite distance from the metal surface and the factor 4 comes from the $2z$ separation between the two point charges. By solving the one-dimensional Schödinger equation for the potential in Eq. (2.8), the series of electron eigenstates, i.e. of image potential states (IPS), converging to E_{vac} are obtained in the form

$$E_n = E_{vac} - \frac{\mathrm{Ry}}{16}\frac{1}{(n+a)^2} \quad n = 1, 2, 3..., \tag{2.9}$$

where Ry $\approx$ 13.6 eV is the Rydberg energy, i.e. the energy of the electron ground state in a hydrogen atom, the factor 16 originates from the $2z$ distance in Eq. (2.8), and a is the quantum defect accounting for the screening of the Coulomb interaction with the image charge by means of the metal conduction electrons. Importantly, it is noted that with a a positive quantity, the second term of Eq. (2.9) cannot exceed

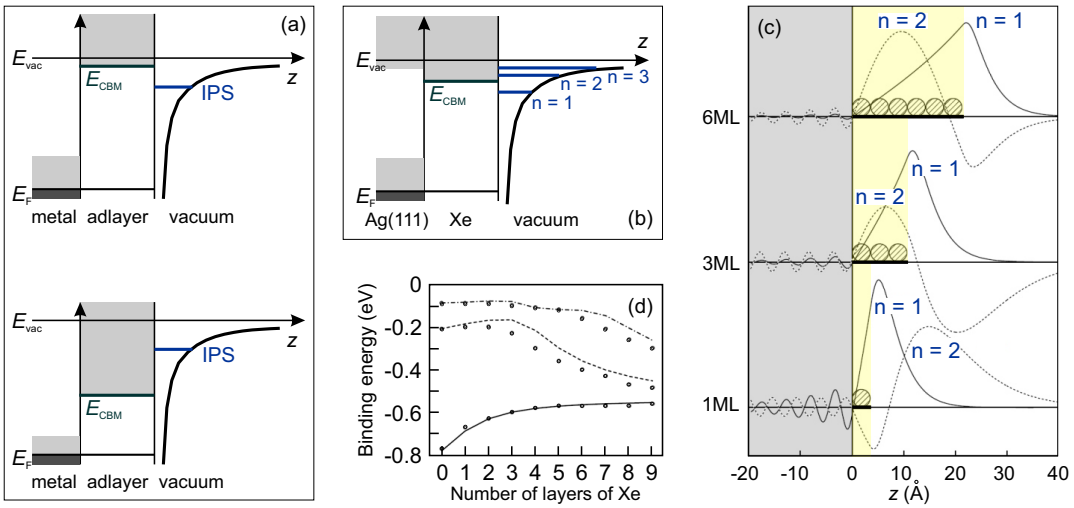

FIGURE 2.6: (a) Energy diagram for an insulating adlayer on a metal surface with the IPS lying below (top) or above (bottom) the minimum of the adlayer CB, E_{CBM}. (b) Energy diagram for the Xe/Ag(111) system. (c) Calculated wave functions of the $n = 1$ (solid lines) and $n = 2$ (dashed lines) IPSs of Xe/Ag(111) [82]. (d) Binding energies of the $n = 1$, 2, 3 IPS states as a function of number of Xe layers [83]. See main text for details.

the Rydberg energy in absolute value. This means that with E_{vac} assigned to the zero-energy, the Rydberg energy is the highest-possible binding energy for an IPS. With increasing the quantum number n, the IPS energy converges to E_{vac}, i.e. its binding energy reduces.

In Fig. 2.5 (b), the IP developing in front of the Cu(001) surface is shown together with the probability density of the $n = 1$ and $n = 2$ IPSs. The energy of both IPSs are well within the projected electronic band gap of Cu(0001) which acts as a tunneling barrier lowering for an electron in one of these states. Consistently, the probability densities of the IPSs have maximum several Åaway from the surface. As the IP is weaker towards E_{vac}, the IPS with higher quantum number is less bound. Accordingly, the probability density maximum is found at a larger distance from the metal surface. This property is eventually reflected in the lifetime of the IPSs which becomes longer for higher quantum numbers as the electrons have a lower probability to decay into the metal [80].

In Fig. 2.5 (c), a different situation is illustrated by the $n = 1$ IPS at the interface with the Cu(111) surface [79]. Its energy is almost degenerate to conduction band minimum (CBM), i.e. the top edge of the projected band gap of (Cu111). This suppresses the potential barrier and increases the probability of an electron to transfer across the vacuum/metal interface (red arrow). Accordingly, the $n = 1$ IPS wave function is found to penetrate into the bulk and the lifetime of this states significantly shortens [81].

The deposition of an adlayer on the metal surface can impact significantly on the properties of the IPSs. Two general cases can manifest which are exemplified in Fig. 2.6 (a) by an IPS in front of an *insulating* adlayer. As shown in the top, the adlayer may exhibit a gap in the energy region of the IPS. In this case, the IPS retain its character. However, the effect of the adlayer is to decouple the IPS from the metal substrate, thereby modifying its energies and lifetime. Otherwise (bottom),

the adlayer may introduce new electronic states (or even a continuum of them) in the region of the IPSs. In this case, the IPS can become degenerate with those states and turn into a resonance (IPRs) which penetrates into the adlayer and develops a quantum-well like behavior. At the same time, because the IP superimposes on the inner potential of the adlayer, it can lead to a modification of the electronic structure of the adlayer [81].

The two described cases are observed for adlayers of Xe deposited on Ag(111). The energy diagram of the system is reported in Fig. 2.6 (b) and shows how the $n = 1$, 2 and 3 IPSs of Ag(111) align with respect to the CB minimum of the rare-gas. It is noted that the lowest IPS is energetically within the Xe energy gap, thus it corresponds to the case on top of Fig. 2.6 (a). On the contrary, the $n = 2$, 3 states are within the Xe conduction band, consistent to the case shown at the bottom of (a). As a consequence of the different energy alignment at the vacuum/adlayer interface, the IPSs show different behavior as a function of Xe coverage. In Fig. 2.6 (c), the calculated wave functions for $n = 1$ and 2 are plotted as a function of the distance from the metal surface for three different coverages, one monolayer (ML), 3 ML and 6 ML. The $n = 1$ IPS finds its maximum in vacuum for any Xe coverage. Indeed, the penetration into Xe/Ag(111) is damped by the tunneling barrier of the Xe CBM. Conversely, with increasing the Xe coverage (bottom to top), the amplitude maximum of the $n = 2$ wave function is found more and more inside the Xe layer as this state couples to the degenerate Xe conduction band. Also, the wave function exhibits an oscillatory behavior reminiscent of that of a quantum-well state. The different character of the n =1 and 2 states in front of the Xe adlayer are reflected also in the evolution of their binding energy with increasing the Xe coverage. As shown in Fig. 2.6 (d), their binding energies relative to the vacuum level follow opposite trends: for the $n = 1$ IPS, it decreases with increasing the number of Xe adlayers as the IPS is increasingly decoupled from the Ag(111) surface. For the $n = 2$, 3 IPS, the binding energy increases for thicker adlayers, thus the states are mode strongly bound.

The simplest description to predict the IPS series arising in presence of an insulating adlayer is to consider the latter as a dielectric continuum. In this approach, the electronic structure of the adlayer is neglected and its role of decoupling the IPS from the metal is taken into account by the dielectric constant. Then, the new IPS eigenvalues are given, in first approximation, by

$$E_n^{\text{diel}} = E_{\text{CBM}} - \frac{0.85}{(n+a)^2}\frac{m_{\text{eff}}}{\epsilon^2} \quad n = 1, 2, 3..., \tag{2.10}$$

where ϵ is the dielectric constant of the dielectric and m_{eff} the effective mass of the quantum-confined electron [84]. However, when the IPSs interact with the electronic structure of the adlayer, this macroscopic model cannot quantitatively well predict the energies the IPSs. This is, for instance, the case of the $n = 2$ IPS of Xe/Ag(111). Then, the microscopic one-dimensional model was developed whose important difference is to take into account the high corrugation of the potential inside the adlayer originating from the screened ionic potential of the adlayer [85].

Finally, it is mentioned that a modification of the IPSs in front of inorganic and organic adlayers on a metal substrate have been also extensively studied [63, 39, 86, 65]. Again, when the projected band gap of the adlayer is found at lower energies than the IPSs, the IPS wave function can penetrate across the vacuum/adlayer interface. At the interface with the metal substrate, the presence of a projected band gap acts again as tunneling barrier and the wave function is 'reflected-back' into the adlayers, thus developing a quantuum-well character. Qualitative predictions on the thickness

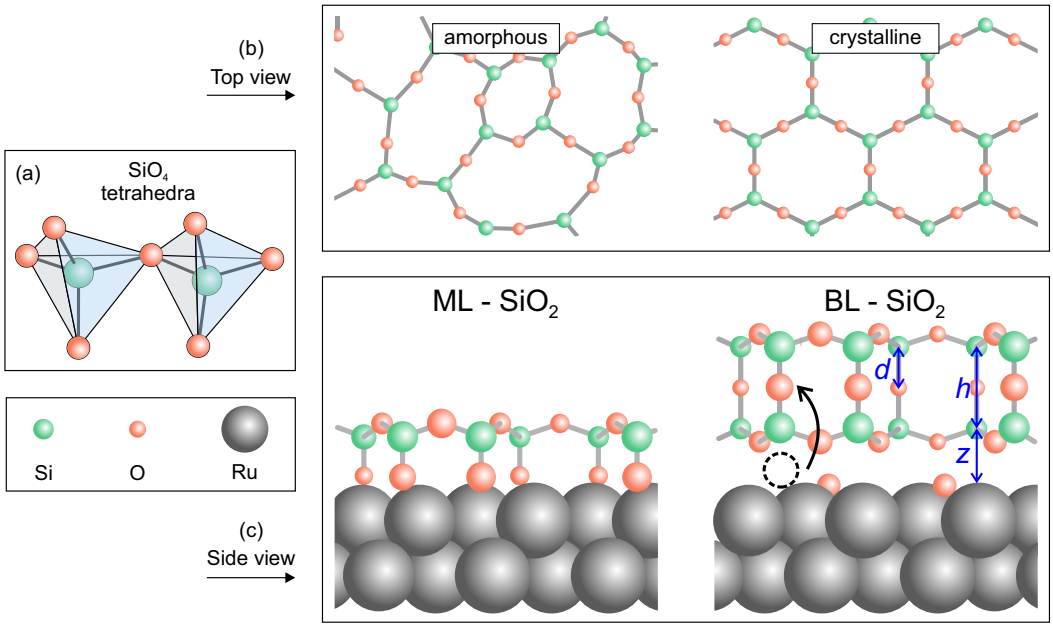

FIGURE 2.7: (a) Two basic units of the SiO_2 crystal structure. (b) Amorphous and crystalline SiO_2 atomic layers. (c) ML and 'O'-rich BL SiO_2 films on Ru(0001). Modified from [41].

dependence of the binding energies and the lifetime of such quantum-well-like IPSs can be made in analogy to the the $n = 2$, 3 IPs of Ag(111) in front of the CB continuum of the Xe coverage. Quantitatively, these dependencies can be reproduced using the one-dimensional model potential which accounts for the periodic potential of the specific adlayer.

2.5 Ultrathin films of SiO_2 on Ru(0001)

The unoccupied electronic structure of ultrathin films of SiO_2 grown on a Ru(0001) surface (in short, SiO_2/Ru(0001)) is investigated in this thesis. In this context, the study focuses on the influence of the reduce dimensionality of the oxide system and the interplay between the inner potential and the image potential of the Ru surface. To achieve this information, two-photon photoelectron spectroscopy is performed, which allows to address unoccupied electronic states with the required resolution of electron momentum and absolute energy (see Section 3.2).

In this section, the SiO_2/Ru(0001) system is introduced based on previous studies. In particular, Subsection 2.5.1 describes the structural and electronic properties of ultrathin SiO_2 films on Ru(0001) which are relevant for the present work. It emerges that new electronic properties arise when the dimensionality of the insulating system is reduced and that the interaction with the metallic substrate can be tuned by some means as, e.g. different SiO_2 coverages or oxygen intercalation at the interface. Subsection 2.5.2 describes the electronic band structure of the Ru substrate. In Subsection 2.5.3, the open questions on the electronic structure of SiO_2/Ru(0001) are presented, which will be focus of this thesis work.

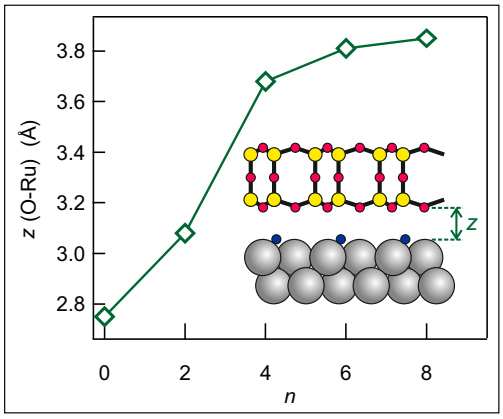

FIGURE 2.8: DFT calculation of the silica-ruthenium distance for different $(SiO_2)_8nO/Ru$ structures, with n an integer ≥ 0. Data from Table I of [43].

2.5.1 The two-dimensional silicon dioxide

Bulk silicon dioxide is a wide band gap insulator with a fundamental gap of approximately 9 eV [87, 40, 88, 89]. The basic unit of the crystal structure is the $[SiO_4]$ tetrahedron. As shown in Fig. 2.7 (a), one Si atom is surrounded by 4 oxygen atoms located at each apex of the tetrahedron [90]. The silicon atom has valence charge of 4, and it stabilizes in the unit by sharing an electron with each oxygen atom. Thus, the oxygen atoms remain with one electron available to bond with the nearest-neighbor silicon atom. Depending on how the tetrahedra arrange, SiO_2 exists both in the amorphous and crystalline form. The two phases are also referred to as 'vitreous' and 'ordered', respectively. A top view of a SiO_2 atomic layer is shown in Fig. 2.7 (b) for both structural phases. In the vitreous phase, it consists of different irregular polygons, while in the crystalline one, it exhibits a honeycomb-like network of bases of the corner-sharing $[SiO_4]$ tetrahedra.

When the lattice geometry is reduced to two dimensions, the formation of either a vitreous or a crystalline silica film is critically determined by the film growth conditions [91] as well as by the electronic coupling at the interface with the metallic substrate [41]. The ruthenium single crystal offers the optimal platform for the growth of monolayer and bilayer SiO_2 films both in the amorphous and ordered phase [42]. Indeed, ruthenium has a hexagonal closed packed (hcp) atomic structure, thus its (0001) surface shares the hexagonal symmetry of the silica film. In addition, O atoms bind more loosely on the Ru(0001) surface than on other hexagonal metallic surfaces like, e.g. Mo(112). This aspects is believed to help the growth of crystalline films with more than one layer, which indeed can not be achieved on Mo(112).

Fig. 2.7 (c) depicts sketches of silica films of different thickness grown on a Ru(0001) surface. In the silica monolayer (ML), one O atom of each tetrahedron points towards the metal surface and binds chemically with the underlying Ru atom. In the bilayer (BL) case, the O atom 'flips' by 180°, as indicated by the black arrow, and connects the two sheets of SiO_4 tetrahedra. The reorientation of the apex oxygen atoms in the BL is revealed by infrared reflection absorption spectroscopy [42] and has a chain of consequences on the properties of the system: (i) the chemical bond to the metal beneath is removed, (ii) the systems remains coupled only by weak van der Waals electrostatic interaction, and (iii) the oxide film is pushed away from the metal surface by a few Å [43]. Is is noted that during the bilayer growth, some O ad-atoms remain adsorbed on the metal surface, as shown in the picture. The presence of O/Ru is

Distance	Å	nr. interfacial O	Method	Reference
d	1.62 - 1.65	any	DFT	[43]
	1.63	any	DFT	[92]
h	5	any	STM	[93]
	4.25	any	DFT	[38]
z	2.75 to 3.85	0 to 8	DFT	[43]
	2.84 to 3.84	0 to 4	DFT	[38]

TABLE 2.1: Structural parameters of a bilayer SiO_2 film on Ru(0001).

verified by X-ray photoemission spectroscopy performed both at normal and grazing incident angle [42, 91]. The oxygen ad-atoms have double impacts on the system: (i) they affect the spatial separation between the oxide film and the metal substrate; (ii) they alter the interface electric dipole.

The effect of intercalated oxigen atoms on the distance from the substrate is supported by DFT calculations showing a lower film adhesion energy in the so called 'O'-rich system as compared to 'O'-free one [42, 43]. As a consequence, the distance between the lowest silica sheet and the metal surface is predicted to increase by several percents when increasing the O/Ru content as reported in the plot on Fig. 2.8 with data taken from [43]. Theoretical and experimental structural parameters of the bilayer SiO_2/Ru(0001) systems are summarized in Table 2.1. In particular, the film thickness h and the distance from the substrate z are used in this thesis work to define the width of the quantum potential well in which electrons inside the film are confined (see Section 2.3 and Section 4.1 for the models and the data analysis, respectively).

The second effect of the O/Ru species, namely the modification of the interface electric dipole, manifests in the change of work function when the concentration of O ad-atoms is tuned by means of annealing of the system (see Section 3.6). This is verified both experimentally by STM [41] and LEEM I-V [94] measurements, and theoretically by DFT calculation [43]. In particular, with increasing the O concentration, the work function increases up to approximately 0.8 eV relative to the work function of the 'O'-poor film [38, 95, 94] due to the favored spill out of Ru electrons by means of the O ad-atoms [41].

The electronic band gap of the BL SiO_2/Ru(0001) system is obtained via scanning tunneling microscopy (STM) conductance measurements [41] which are reported in

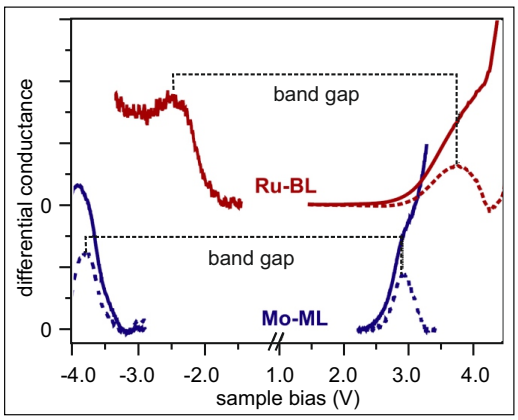

FIGURE 2.9: STM conductance spectra on both the BL SiO_2 on Ru(0001) and the ML-SiO_2 on Mo(112). Adopted from [41].

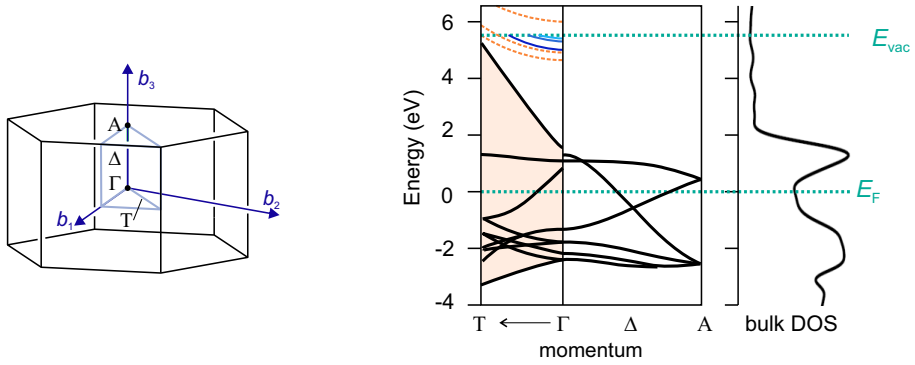

FIGURE 2.10: On the left: the Brillouin zone of Ru. On the right: The calculated electronic band structure of the bulk ruthenium (black curves) and the clean (0001) surface (orange shade and orange dashed lines) together with the bulk density of states (DOS). Blue lines are the IPSs. The measured work function of the clean Ru(0001) surface, i.e. E_F - E_{vac} ranges between 5.4 eV [96] and 5.5 eV [41]. Modified from [97]

Fig. 2.9 (solid red). The onsets of the highest occupied and lowest unoccupied energy levels are identified by the maxima of the background-substracted data (dashed red). Their energy separation results of 6.5 eV. For comparison, the STM conductance spectrum of the ML-SiO_2 film grown on Mo(112) is shown (blue) and provides a band splitting of 6.7 eV. Both the films exhibit therefore a smaller electronic band gap than the value reported for the bulk compound. This aspect is quite remarkable, as the electronic band gap usually increases when the dimensionality of the system decreases. The latter behavior is referred to as 'size effect' and manifests when the electron spatial confinement becomes comparable to the wavelength of the electron wave function. However, this concept may not straightforwardly apply to the SiO_2/Ru(0001) system due to the presence of the IP of Ru80001) possibly impacting on the effective potential inside the film. This hypothesis is motivates and is one of the focus of the present thesis work. Furthermore, metal substrate induces a tensile stress on the lowest silica sheet which is theoretically predicted to reduce the electronic band gap of the oxide with respect of a completely free-standing silica bilayer [92].

2.5.2 Electronic band structure of the ruthenium substrate

In the following, the electronic band structure of the bare ruthenium is detailed. Fig. 2.10 shows the unit cell of ruthenium. Selected the high-symmetry k points are labeled. Two significant lines departing from the Γ point of the Brilloiun Zone are identified: the $\Gamma-$T and the $\Gamma-\Delta-$A line, which run parallel and perpendicular to the (0001) surface, respectively. The plane of the (0001) surface, on top of which the silica film are grown, is defined by the b_1 and b_2 unit vectors.

The calculated electronic band structure of bulk ruthenium along those two high-symmetry directions are shown on the right, superimposed by the calculated surface electronic bands of the (0001) plane (orange shades) [97]. Along the $\Gamma-$T line, the bulk and surface band structures overly on top of each other in the energy range between approximately -3 eV and +5 eV relative to E_F. This is the energy interval of interest for the two-photon photoelectron spectroscopy study performed in this thesis work. Above approximately 4.5 eV, other high energy unoccupied surface bands are reported as orange dashed lines. Finally, the $n = 1, 2, 3$ IPS of the pure Ru(0001)

surface are depicted by blue solid lines. Those states are identified by means of time-resolved 2PPE spectroscopy [98]. Their binding energy with respect to the vacuum level lye at -0.661 ± 0.020 eV, -0.187 ± 0.015 eV and -0.087 ± 0.010 eV (blue lines). Their lifetime ranges from 11 ± 2 fs to 174 ± 10 fs, thus increasing with increasing the quantum number (see Section 2.4).

On the right to the band structure, the momentum-integrated electronic density of states is displayed [97]. Above E_F, the unoccupied density of states extends continuously up to 2 eV, peaking around 1 eV, which corresponds to the position of a weakly dispersive empty d band at the Γ point. Above 2 eV, the density of states is drastically suppressed up to the vacuum energy level of the clean (0001) surface because a projected electronic band gap opens at the Γ point.

2.5.3 Summary and open questions

Based on the previous works, an energy diagram of the BL SiO_2/Ru(0001) system is proposed in Fig. 2.11. The Ru electronic band structure is sketched as a function of electron momentum (bottom left axis) and the white region indicates a gap in the unoccupied electronic states with minimum at Γ approximately 2 eV above E_F. At high energy, the IPSs of the clean Ru(0001) are drawn. Concerning the energetics of the oxide film, only the onset of the upper valence band and the lowest conduction band are known from STM measurements. Those are marked by two gray-dashed bars. The SiO_2 electronic structure will depend on the potential developing inside the film and at the interfaces. A possible potential for a thin film of SiO_2 in the vicinity (i.e. few Å) of the Ru surface is depicted by the blue solid lines as a function of the distance from the metal surface (bottom right axis). It consists of the inner periodic potential joining the IP of Ru at both interfaces. The dashed line is the IP of the clean Ru(0001) surface, i.e. in absence of SiO_2.

The present work aims to resolve the *unoccupied* electronic structure of ultrathin films of SiO_2/Ru(0001) which plays an important role on the electronic coupling and dynamics occurring at the oxide/metal interface. In particular, three fundamental questions are addressed here:

- Does the electronic structure of the oxide film reflect the reduce dimensionality of the system? As discussed in Section 2.3, the energetics of ultrathin films is often characterized by discrete energy levels that arise from electron quantum confinement perpendicularly to the film. The effect is typically modeled by a series of quantum states inside a potential well whose width varies with the film thickness. Thus, if conduction electrons are confined in the oxide film, distinct electronic states are expected to appear above the energy of the conductivity onset. Also, their energies should vary for different film thicknesses.

- Does the IP of the metal substrate influence the unoccupied electronic states developing inside the oxide film? When the IPSs align to the conduction band of an adlayer, their wave function may penetrate into the adlayer, possibly developing a quantum-well character (cf. Section 2.4). This possibility should be checked for the IPS in front of an ultrathin film of SiO_2/Ru(0001). Moreover, even in absence of IP resonance with the SiO_2 conduction band, the image potential extends for a large distance outside the metal surface and likely superimposes the inner potential of the oxide (see sketch in Fig. 2.11). This superposition may modify the potential inside the film and thus the energetics of the latter.

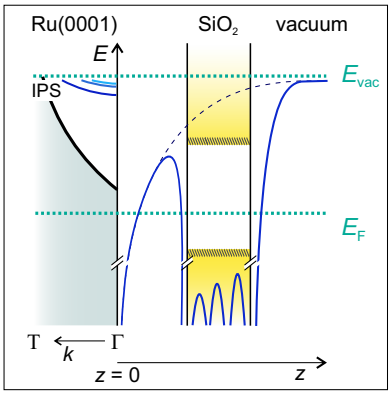

FIGURE 2.11: (a) Possible energy diagram of BL SiO_2/Ru(0001) system.

- How strong is the electronic coupling at the metal/oxide interface? The coupling between two electronic states of the oxide and the metal, respectively, is determined by the spatial overlap of the involved wave functions. Given the electronic structure described in Fig. 2.11, this may occurs at momenta different from Γ and energies above the bottom of the projected band gap of Ru. At Γ, the wave function of an unoccupied electronic state of the oxide may extend outside the film and penetrate into the Ru bulk, resulting in a nonvanishing probability to observe charge injection across the interface. Therefore, the interface coupling is expected to depend on structural properties such as the distance of the film from the substrate. Its strength will be reflected in the time scale on which a population of SiO_2 conduction electrons decays into the Ru bulk.

To investigate these aspects, two SiO_2/Ru(0001) systems with different oxide coverage are measured by means of time-resolved two-photon photoelectron spectroscopy: a BL SiO_2 which only physisorbs on Ru(0001) and a 1.4 ML that couples, on average, more strongly due to the terraces of single ML chemically bound to Ru. The different interaction strength together with the change of film thickness will succeed in explaining the different electronic structures of the two films. Also, the experiments are performed such that the SiO_2 unoccupied states can be populated only by electrons injected across the metal/oxide interface from occupied states of Ru. This procedure will allow to resolve these states and infer on the interface electronic coupling from their spectral intensity and their lifetime.

2.6 The excitonic insulator phase

Fundamental interactions among charges and between charges and other degrees of freedom of the system, such as phonon or spins, manifest on specific energy and timescales and depending on their strength, they can determine the ground state and the nonequilibrium behavior of the material. Different phases of matter are typically identified based on their dominating coupling mechanism. Remarkable examples are the Mott insulating phase [45], that originates from the suppression of the interorbital electron hopping due to strong on-site Coulomb electrostatic repulsion, the Peierls insulating phase [12], where the electronic band gap gap opens as a consequence of strong electron-phonon coupling in systems affected by a lattice instability, and the conventional superconducting state, which is based on phonon-mediated pairing of electrons at low-temperatures.

This thesis work investigates the ground state and nonequilibrium physics of an excitonic insulator system. As described in more detail later in this section, this insulating phase of matter is predicted by theory to form in small electronic band gap materials upon spontaneous binding of phase-locked electron-hole pairs (coherent excitons) due to the poorly-screened attractive Coulomb interaction between a negative and a positive charge. Additionally, a structural distortion is expected to help the excitonic insulator ground state to stabilize. Thus, it can be shown that the physics of the excitonic insulator phase shares similarities with both conventional superconductivity [99] and Peierls lattice instability [12] which are briefly reviewed in the following.

Conventional superconductors are described by the Baarden-Cooper-Schrieffer (BCS) theory: the electron-phonon interaction helps overscreening the repulsive Coulomb interaction between electrons, thus assisting the pairing of two electrons with opposite momentum and energy close to E_{F} into a bound state, called Cooper pair. At sufficiently low temperatures, such bosonic pairs condense into a phase-locked phase and can travel without scattering through the crystal, thus being responsible for the superconductivity. In analogy to a BCS superconductor, an excitonic insulator arise from the pairing of two charges into a bound state and the phase coherence of the pairs to obtain a macroscopic condensate. However, while the Cooper pairing requires the mediation of the lattice, the exciton formation relies on the naturally attractive Coulomb interaction between an electron and a hole.

Peierls' theorem states that one-dimensional systems are unstable against the deformation of their crystal structure. This causes a localization of charge carriers because of the strong interaction between electrons and lattice vibrational modes (phonons). As the structural distortion occurs, the electronic distribution accommodates such that the elastic energy cost is compensated by the electronic energy gain by opening a gap around E_{F}. Similarly to a Peierls phase transition, the opening of the electronic band of an excitonic insulator is concurrent with some lattice ion adjustment. However, while in a Peierls system the band gap opening is a consequence of the structural distortion gap which renormalizes the Brillouin zone, in an excitonic insulator the gap already opens due to the spontaneous hybridization of strongly coupled valence and conduction bands and the lattice deformation should simply favor such hybridization.

The excitonic insulator phase essentially relies on the strong electron-hole Coulomb interaction. To describe the origin of this phase, two complementary theoretical pictures were proposed by N. F. Mott [45] and R. S. Knox [100], respectively. Their principles are schematically illustrated in Fig. 2.12 (a) and (b). Mott considers a semi-metal with a small fraction of free electron and holes at a finite temperature (left in (a)). Due to the low density of mobile carriers, the screening of the attractive Coulomb interaction is inefficient and an electron and a hole can bind into a pair (exciton). If the Coulombic screening is further reduced, e.g. by a lower concentration of free carriers or a reduction of the system dimensionality (right in (a)), the exciton formation can eventually occur spontaneously, provided the thermal energy fluctuations being smaller than the electron-hole binding energy.

In the Knox' picture, the initial, normal phase is a small-band gap semiconductor. There, the minimum energy cost to form an exciton is defined by the optical gap $E_{\mathrm{g}}-E_b^{\mathrm{EXC}}$, where E_{g} is the electronic band gap, and E_b^{EXC} is the exciton binging energy. As shown in Fig. 2.12 (b, left), E_{g} defines the energy splitting between the valence band maximum and the conduction band minimum in absence of excitonic coupling. E_b^{EXC} reduces the excitation gap by accounting for the renormalization

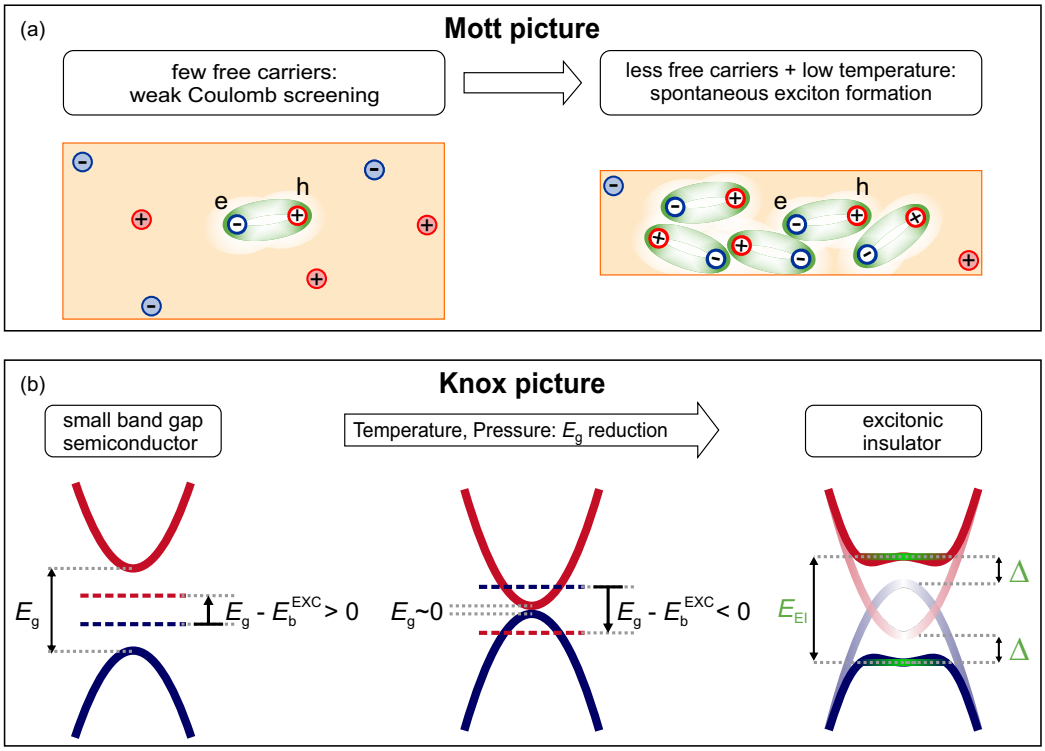

FIGURE 2.12: Theory predictions of the spontaneous exciton formation [101]. (a) Mott picture: in semimetals, the weakly screened Coulomb interaction favors the attraction of an electron and a hole into a bound state (exciton). At low sufficiently temperature, the exciton formation can become a spontaneous spocess. (b) Knox picture: in a small-band-gap semiconductor, when the exciton binding energy exceeds the size of the band gap, the exciton formation becomes energetically favorable and leads to a further opening of the electronic band gap.

energy of a conduction electron and a valence hole when they are bound into a pair[2]. Then, E_b^{EXC} is determined by the effective masses of the electron and the hole as

$$E_b^{\mathrm{EXC}} = 13.6\frac{\mu}{m_0\epsilon^2} \quad (\mathrm{eV}), \tag{2.11}$$

where μ is the reduced effective mass of the electron and hole bands, m_0 is the Bohr electron mass and ϵ the dielectric constant. Now, if the E_g can be arbitrarily decreased by tuning some external parameters, it may become smaller than E_b^{EXC} (center in (b)). In this circumstance, the energy required to form an exciton becomes negative or, in other words, the formation of exciton in the ground state becomes energetically favorable. As a result, the system evolves into a new, more insulating ground state (right in (b)).

Both descriptions rely on the strong coupling between the valence band and the conduction band which enables the electron-hole pairing already at equilibrium. The mechanism is further favored by a reduced energy splitting of the bands, as it is the case of semimetals exhibiting a finite, indirect overlap or semiconductors with a small direct band gap. In case of an indirect band gap, to avoid electronic band crossing

[2]In a single-particle picture, E_b^{EXC} is typically referred to as the energy relative to the CB minimum of a conduction electron bound to a valence hole. In Fig. 2.12 (b, left), this energy is distributed between the two fundamental entities, i.e. the electron and the hole (dashed lines), to facilitate the depiction of the mechanism by which the excitonic insulator phase is formed (See main text).

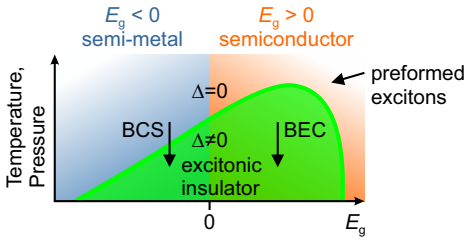

FIGURE 2.13: Electronic phase diagram of an excitonic insulator.

during the transition to the excitonic insulator phase both a charge-density-wave and a periodic lattice distortion are expected to occur concomitantly [46, 102]. For this reason, in semimetals it may be difficult to distinguish this phase transition from a Peierls instability [103, 104, 105]. On the contrary, in direct semiconductors, it is sufficient that the valence and conduction states have different symmetry to allow their levels to cross without the implication of the charge-density-wave. However, lattice ions still have to accommodate to the electrostatic potential of the new phase, with possible change of the crystal symmetry [101].

Finally, in analogy to conventional BCS superconductors, a macroscopic excitonic insulator phase is realized only when the excitons condense into a phase-coherent state. Then, as depicted on the right of Fig. 2.12 (b), the new ground state stabilizes by opening a many-body gap 2Δ in the single particle excitation spectrum, which superimposes on the band gap of the semiconducting normal phase. The Hamiltoninan describing such new phase is presented in the next subsection.

2.6.1 BCS modeling of the excitonic insulator phase

The electronic phase diagram of an excitonic insulator is shown in Fig. 2.13. Depending on the normal phase from which the excitonic instability is approached two theoretical frameworks are used to describe the excitonic insulator phase. On the one hand, the BCS theory captures the phase transition to the excitonic insulator phase when the system in the normal phase is a semi-metal. In this case, the presence of a rather large number of mobile carriers prevents the formation of excitons above the critical point for the phase transition. Once the transition occurs, it results in a macroscopic fraction of loosely bound excitons. On the other hand, the Bose-Einstein condensation (BEC) describes the phase transition starting from a small-band-gap semiconducting phase. Here, the low carrier concentration allows for a population of preformed excitons which gain coherence at the critical point and lead to a coherent state of tightly bound excitons.

Modeling the excitonic insulator phase is intrinsically a many-body problem. In mean-field approximation, the description can be reduced to the problem to a single particle feeling the averaged Coulomb interaction potential of the other particles [61]. With this approach, an exciton is treated as a weakly interacting 'quasiparticle', where a bare electron behaves as a nearly-free entity but with a different effective mass as it is 'dressed' by the contribution of the interaction with the hole. Due to the analogy with the BCS mean-field model, such theoretical treatment for the excitonic insulator phase is also referred to as BCS modeling independently on the nature of the normal phase. However, a fundamental difference has to be considered and relates to the interaction potential. In the case of Cooper pairing, the effect of overscreening of the Coulomb interaction by means of phonons is necessary to allow two electrons to

attract to each other in the momentum space: the pairing mechanism is mediated by an *ad hoc* deformation of the lattice. In the case of spontaneous exciton formation, the bare Coulomb potential is naturally attractive between the electron and the hole, which allows for a simpler formalism of the interacting term of the Hamiltonian.

In the case of a direct-band-gap semiconductor, like the Ta_2NiSe_5 compound investigated in this thesis, a two-band model is able to capture the phase transition to the excitonic insulator phase. The mean-field Hamiltonian for the excitonic insulator phase is composed of a one-electron part H_0 and a Coulomb interaction part H_{int}. In second-quantized notation, it reads

$$H = H_0 + H_{int}, \tag{2.12}$$

where

$$H_0 = \sum_{\mathbf{k}} \left(\epsilon_{c\mathbf{k}} a^\dagger_{c,\mathbf{k}} a_{c,\mathbf{k}} + \epsilon_{v\mathbf{k}} a^\dagger_{v,\mathbf{k}} a_{v,\mathbf{k}} \right), \tag{2.13}$$

and

$$H_{int} = \sum_{\mathbf{q}} \left(\rho_{v,\mathbf{q}} V_{\mathbf{q}} \rho^\dagger_{c,\mathbf{q}} \right) \tag{2.14}$$

Here $a^\dagger_{c,\mathbf{k}}$ and $a_{v,\mathbf{k}}$ are the operators creating an electron in the conduction band (c) and a hole in the valence band (v), both with wave vector $\mathbf{k}$. The band dispersions are chosen parabolic, i.e. $\epsilon_{c\mathbf{k}} = \epsilon^0_c + \hbar^2 k^2/2m_{\mathrm{c}}$ and $\epsilon_{v\mathbf{k}} = \epsilon^0_v + \hbar^2 k^2/2m_{\mathrm{v}}$ (with $\epsilon^0_v, m_{\mathrm{v}} < 0$). The interaction part contains the Coulomb interaction potential $V_{\mathbf{q}} = 4\pi e^2/\epsilon(\mathbf{q}) q^2$ and the density operators $\rho_{j,\mathbf{k}} = \sum_k a^\dagger_{j,\mathbf{k}+\mathbf{q}} a_{j,\mathbf{k}}$, with $j = c, v$.

To obtain the renormalized excitation spectrum, the equations of motion for the time-ordered Green's functions describing the conduction and valence band, respectively, have to be solved with the mean-field Hamiltonian given by Eq. (2.12). The Green's function for the conduction band reads

$$\begin{aligned} G_{c,\mathrm{p},\omega} &= \frac{\omega - \epsilon_{v\mathbf{p}}}{(\omega - \epsilon_{c\mathbf{p}})(\omega - \epsilon_{v\mathbf{p}}) - |\Delta_{\mathbf{p}}|^2} = \\ &= \frac{1}{\omega - \epsilon_{c\mathbf{p}} - \frac{|\Delta_{\mathbf{p}}|^2}{\omega - \epsilon_{v\mathbf{p}}}}, \end{aligned} \tag{2.15}$$

where $|\Delta_{\mathbf{p}}|^2$ is the order parameter of the excitonic insulator phase. The order parameter contains the coherence factors, $u^2_{\mathbf{p}}$ and $v^2_{\mathbf{p}}$, which relate to the probability of finding an electron either unpaired or bound to a hole (in analogy with the probability to form a Cooper pair in the BCS superconducting state). To conserve the total number of particles, the coherence factor satisfy $u^2_{\mathbf{p}} u^2_{\mathbf{p}} + v^2_{\mathbf{p}} u^2_{\mathbf{p}} = 1$.

By knowning the Green's functions, the renormalized band dispersion in the condensate phase is obtained from the the poles of the respective Green' function as

$$\Omega_{\pm,\mathrm{p}} = \frac{1}{2}(\epsilon_{v\mathbf{p}} + \epsilon_{c\mathbf{p}}) \pm \sqrt{(\epsilon_{v\mathbf{p}} - \epsilon_{c\mathbf{p}})^2 + 4|\Delta_{\mathbf{p}}|^2}. \tag{2.16}$$

Clearly, as far as $|\Delta_{\mathbf{p}}| \neq 0$, the renormalized spectrum exhibits a gap which adds up to the band splitting of the normal, semiconducting phase. For $|\Delta_{\mathbf{p}}| = 0$, the normal phase for the direct semiconductor is retrieved.

Finally, the third term in the denominator of Eq. (2.15), $\frac{|\Delta_{\mathbf{p}}|^2}{\omega - \epsilon_{v\mathbf{p}}}$, directly connects to the complex one-electron self-energy function $\Sigma_{j,\mathrm{p},\omega}$ which is experimentally addressed by photoemission spectroscopy (cf. Section 3.2). More precisely, the coherence factors, $u^2_{\mathbf{p}}$ and $v^2_{\mathbf{p}}$, are the spectral weights of the two split dispersions $\Omega_{\pm,\mathrm{p}}$ and the

complex self-energy function, $\Sigma_{j,\mathrm{p},\omega}$, weights the measured photoelectron intensity of each band.

2.6.2 First experimental evidences of an excitonic insulator phase

Following the theoretical predictions, several experiments aimed at proving the existence of the excitonic insulator phase, which after several decades is now finding an almost general consensus. The experimental challenge was not only to find a material suitable to host an excitonic insulator ground state but also to identify an unabiguous signature of such phase of matter. Based on the precedents arguments, an ideal candidate for the realization and the detection of an excitonic insulator ground state had to offer (1) a small band gap to reduce the cost of forming excitons and favor the formation of a large number of pairs; (2) a low concentration of mobile carrier to reduce the Coulombic screening, thereby increasing the binding energy and the lifetime of the exciton.

In this regard, gasses of ultracold atoms and semiconducting nanostructures appeared as good candidates by virtue of the inefficient Coulombic screening of the charges. On these systems, attempts were done to form a consendate of excitons upon manipulation of the valence and conduction orbital overlap with pressure and photoiexcitation of a large number of excitons in a confined volume [106, 107, 108]. In the late 60s, the resistivity of various divalent metals (Calcium, Strontium, Ytterbium) and the group V semi-metals (Bismuth, Antimony, Arsenite) was measured as a function of pressure and temperature with the hope to observe the collapse of the semiconductor electronic band gap and the appearance of a more insulating, excitonic phase [46, 109]. However, due to the absence of clear anomalies, their behaviors could not be unambigously distinguished from that of conventional insulators.

About ten years later, the resistivity of the layered semi-metal $TiSe_2$ was measured as a function of temperature upon application of an external pressure. An anomalous increase was measured around 150 K, which could be suppressed with increasing pressure. These observations suggested to correlate the occurrence of a variation of the band overlap with an electronic phase transition [110, 111, 112]. At the same critical temperature, a periodic lattice distortion concomitant with the doubling the Brillouin zone was reported [113]. The crucial consequence of this behavior of $TiSe_2$ is that the (negative) indirect electronic band gap becomes direct and the valence and the conduction band can hybridize. The band hybridization was then widely investigated by means of photoemission spectroscopy which identified a peculiar flattering of the top of the hybridized VB as the fingerprint of an excitonic condensate [114, 102]. However, because the electronic phase transition was concomitant with a periodic lattice distortion and the appearance of a charge-density-wave, disentangling between the role of electron-phonon and electron-hole interaction has been a standing debate [115]. Nowadays, both couplings are rather consensually believed to contribute to the formation and stabilization of an excitonic ground state in $TiSe_2$ [105]. Eventually, in 2017, an electronic collective mode (plasmon) was resolved in the low-temperature phase of $TiSe_2$ by momentum-resolved electron energy loss spectroscopy and was argued to prove the presence of an exciton condensate at equilibrium [116].

In the 80s, the layered ternary calcogenides Ta_2NiS_5 and Ta_2NiSe_5 were successfully synthesized. Both materials are semiconductors with a small direct band gap at room temperature of 0.13 and 0.36 eV, respectively, thus favoring the possibility of band hybridization. Upon cooling, their band gap continuously was found to widen, indicative of a transition to a more insulating ground state [117, 54]. Additionally, Ta_2NiSe_5 uniquely exhibited an anomaly in the resistivity at 328 K, suggestive of the

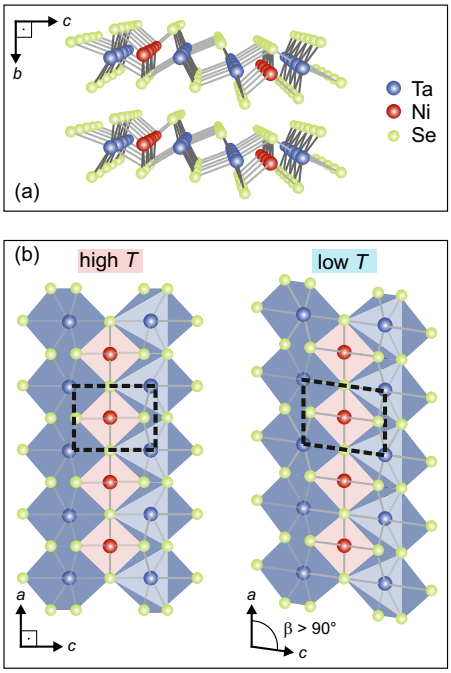

FIGURE 2.14: (a) Crystal structure of Ta_2NiSe_5. (b) Top-view of the a-c plane in the high-temperature orthorhombic phase (left) and in the low-temperature monoclinic phase, i.e. below $T_C = 328$ K (right). Modified from [56].

occurence of an excitonic instability [54, 56, 57]. This material, being the main player of this thesis work, is presented in greater detail in the next section.

2.7 The quasi-one-dimensional Ta_2NiSe_5: an excitonic insulator

The physics of an excitonic insulator is addressed in this thesis by investigating the ground state and the nonequilibrium properties of the ternary chalcogenide Ta_2NiSe_5. From previous equilibrium studies it emerges that the system undergoes an coupled electronic and structural phase transition at 328 K which is consistent with the realization of an excitonic insulator ground state at low temperatures. This section gives an overview on the experimental and theoretical background on the material.

2.7.1 Concurrent structural and electronic anomalies in Ta_2NiSe_5

The crystal structure of Ta_2NiSe_5 is shown in Fig. 2.14 (a). It consists of three-atom thick layers stacked along the b axis and weakly bound via Van der Waals electrostatic interaction. Within the a-c plane, nickel (Ni) single chains alternate with tantalum (Ta) double chains along the a axis, as depicted in Fig. 2.14 (b). As a result, along the c axis the sequence of Ta-Ni-Ta atoms forms the basis for a quasi-1D crystal structure. Selenium (Se) chalcogen atoms coordinate tetrahedrally around the Ni atoms and octahedrally around the Tantalum (Ta) atoms.

At high temperatures, the crystal exhibits an orthorhombic symmetry, as shown on the right of Fig. 2.14 (b). Below a critical temperature $T_C = 328$ K, both transmission electron microscopy and X-ray diffraction identify a slight, continuous increase of the β angle up to 90.53(1)°, indicative of a shearing atomic motion along the a axis [117,

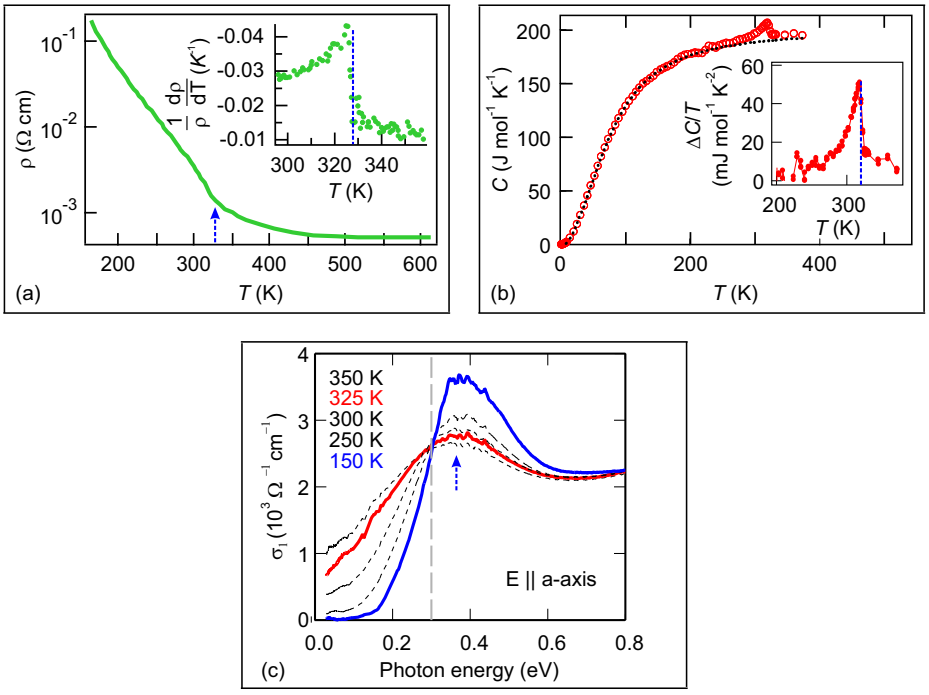

FIGURE 2.15: (a) Electrical resistivity measurement along the a axis. Inset: the logarithmic derivative of the resistivity near the phase transition at $T_C = 328$ K. The blue dashed lines indicate the transition point. The data are digitized from [54]. (b) Temperature dependence of the heat capacity showing an anomaly at T_C. Modified from [57]. (c) Optical conductivity with electric polarization along the a axis. Below T_C, an excitonic resonance appears in the excitation gap above 0.3 eV. Modified from [57].

54]. As a result, the in-plane symmetry evolves from orthorombic to monoclinic upon cooling below T_C, as illustrated on the right of Fig. 2.14 (b).

The equilibrium electronic properties of Ta_2NiSe_5 are investigated as a function of temperature via measurements of the electrical resistivity [54, 56, 57], the heat capacity [57], and the optical conductivity [118, 57, 58]. At the common temperature T_C, all these studies report an anomalous change in the respective observable, as outlined in the following.

Transport measurements are displayed in Fig. 2.15 (a) and show that the resistivity increases with decreasing temperature from 500 K to T_C, as expected for a conventional semiconductor. However, at T_C, a continuous but significant change of its temperature dependence occurs, as revealed by the derivative of the resistivity shown in inset. As a consequence of this anomaly, the resistivity increases by approximately one order of magnitude near T_C and the system becomes more insulating.

Fig. 2.15 (b) shows that the heat capacity decreases upon cooling as predicted by the Debye model (black dashed line)[119]. Additionally, around T_C, an anomalous peak appears, which is reminiscent of the discontinuity in the specific heat function of BCS superconductors at the transition point [120]. This feature is assigned to a change of the electronic entropy of the system and the appearance of a new ground state.

The complex optical conductivity is retrieved by reflectivity and ellipsometry measurements and its immaginary part, reported in Fig. 2.15 (c), reveals a continuous opening of the excitation gap upon cooling below T_C. The effect manifests by (i) a spectral weight transfer above 0.3 eV and (ii) the appearance of an absorption peak

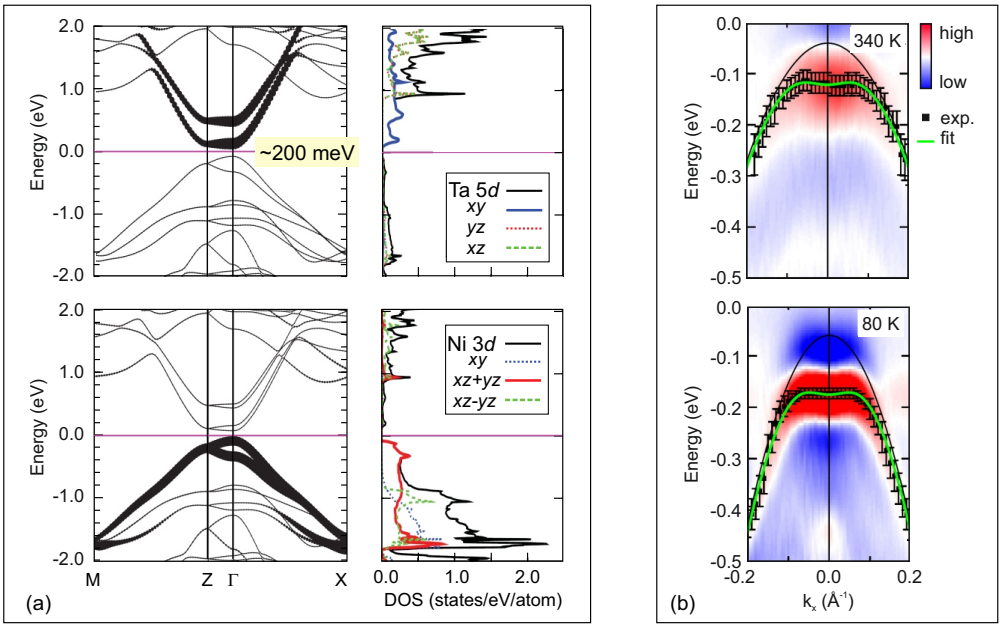

FIGURE 2.16: (a) DFT band structure calculation (left) and partial density of states (right) of the high temperature semiconducting phase of Ta_2NiSe_5. Reported from [55]. (b) Second derivative plots of the ARPES spectra above and below T_C. The black solid line is the tight-binding model without excitonic coupling, which clearly does not capture the VB-top flat dispersion. This is accounted for by the green line where the excitonic interaction is included in the model function. Modified from [56].

in the energy window of the conduction band edge. The intensity of this resonance increases with decreasing temperature, supporting its excitonic character.

In conclusion, at a common critical temperature T_C, several electronic properties exhibit an remarkable anomaly. This is concomitant to a second-order phase transition to a more insulating state with strong excitonic properties. Remarkably, the electronic phase transition occurs at the same T_C as the lattice symmetry change, supporting an interplay of the electronic and lattice subsystem in stabilizing the system at low temperatures.

2.7.2 The temperature-dependent electronic band structure: measurement and modeling

Based on previous theoretical and experimental studies, it is now shown that the electronic band structure of Ta_2NiSe_5 in the high-temperature (HT) normal phase fulfills the requirements for a second-order transition to the excitonic insulator ground state. Also, the connection between the temperature-induced modifications of the electronic band structure and of the lattice symmetry are highlighted.

The HT electronic band structure calculated by density-functional-theory (DFT) is reported in Fig. 2.16 (a) [56]. At the Γ point of the Brilloiun zone, a small, direct electronic band gap opens by approximately 200 meV. Along the Γ-X direction, the dispersion of the upper valance band and the lowest conduction band evolves like a one-dimensional cosine function, consistent with the predictions of a 1D two-band semiconductor model [121, 55]. This momentum direction corresponds in real-space to the a crystallographic axis of the Ta and Ni atomic chains.

The projected density of states reveals that the conduction and valence bands are mainly formed by Ta $5d_{xy}$ and Ni $3d_{xz+yz}$ orbitals, respectively. These orbitals are arranged in parallel chains along the a axis. This finding indicates that charge-transfer type of exciton is formed across the atomic chains upon hopping of an electron from a Ni site to its nearest-neighbor Ta site. Consequently, the excitonic properties of Ta_2NiSe_5 are expected to be influenced by the interchain distance. In this regards, a recent study suggested that the spatial separation between the electron and the hole can possibly delay their recombination across the direct band gap, thereby increasing the exciton lifetime [58].

The evolution of the occupied electronic band structure along the Γ-X direction is investigated by several ARPES studies upon cooling below T_C [122, 123, 56]. Fig. 2.16 (b) reports two second-derivative spectra of the top-most VB above (top) and below (bottom) T_C, respectively [56]. At both temperatures, the band is dispersive at $k \neq 0$ vectors, while it flattens around the Γ point. However, below T_C, both the dispersion of the band and the flattening of the VB top are much more pronounced. Additionally, the VB top is significantly shifted towards a higher binding energy with respect to E_F and its spectral width narrows. Remarkably, these behaviors of the VB top appear consistent with the blueshift of the excitonic resonance observed by optical conductivity (cf. Fig. 2.15 (c)).

Before describing the modeling of these ARPES spectra, an interesting observation is done on the change of VB dispersion at $k \neq 0$. The latter was analyzed in a precedent ARPES work by fitting a nearly-free-electron parabolic dispersion to both the LT and HT spectra (not shown, [123]). Interestingly, a lower electron effective mass was found below T_C, equivalent to a larger bandwidth of the VB. The authors connected this finding to the structural phase transition as follows: At low temperatures, the lattice distortion shortens the distance between two neighboring Ta and Ni atoms (compare between the high- and low-temperature crystal symmetries in Fig. 2.14 (b)), thereby possibly increasing the overlap of the respective outer-most orbitals. This observation indicates that the change of VB dispersion with varying temperature appears connected to the concomitant structural instability.

The model of the data of Fig. 2.16 (b) is now described. In order to reproduce the VB dispersion in the full k-range, a tight-binding model with coupled valence and conduction bands is fit to the spectra. The result is shown by the green curves in Fig. 2.16 (b) and compared with the analogous fit model without excitonic coupling (black curve). Clearly, turning on the interchain hybridization leads to a very good agreement with the data. Particularly, it allows to reproduce the flattening of the VB top also in the spectrum below T_C where the discrepancy from a parabolic dispersion is the largest. The results of these models indicates the followings: Above T_C, the system exhibits mostly a semiconductor band structure, though with a deviation at the VB top which reveals excitonic fluctuation even above the critical point of the phase transition. This observation is consistent with the pre-formation of incoherent excitons in a BEC picture (cf. Fig. 2.13). Below T_C, the VB structure maintains the semiconducting character at large momenta but it drastically deviates from it at the top of the VB, indicative of a strong excitonic interaction. This finding, in combination with the increased binding energy and narrowed bandwidth at the VB top, consistently supports the formation of a coherent state of excitons at the top of the VB at Γ.

These findings inspired lot of theoretical effort aiming at a decription of the LT electronic phase of Ta_2NiSe_5. In this framework, the extended Falicov-Kimball model (EFKM) [124, 125] was developed. This is based on the Hubbard Hamiltonian [126] in order to include the correlation effects of the electron-hole Coulomb interaction in the

single-particle spectrum. The EFKM Hamiltonian consists of three terms: an on-site energy split term which accounts for the semiconducting normal phase; a nearest-neighbor electron hopping term t; an inter-orbital Coulombic term U. The U term expresses the electrostatic repulsion between electrons on different orbitals and thus can be considered as the inter-orbital attraction between a holes and an electron. In this sense, U is responsible for the formation of an excitonic band gap that adds on top of the semiconductor band gap. As a result, the electronic band gap consists of two contributions, the one of the underlying semiconductor and that of the excitonic insulator.

In conclusion, theoretical and experimental studies show that the occupied electronic band structure of Ta_2NiSe_5 features at low temperature the dispersion of an insulator with strong excitonic coupling at the band extrema. Notably, the flattening of the VB top strongly resembles the excitonic signature of the layered compound $1T$-$TiSe_2$ ([114, 104] and cf. Subsection 2.6.2). This feature is already visible above T_C, suggesting the formation of incoherent excitons before the phase transition takes place. The thermally-induced changes of the VB dispersion and the structural phase appear mutually connected. The mechanism behind this interplay is depicted in Fig. 2.17: In the high-temperature phase, the system is a semiconductor with orthorhombic lattice symmetry. An exciton can form across the atomic chains upon electron hopping from a Ni site to the nearest-neighbor Ta site. Below T_C, the lattice distortion shortens the interatomic distance between a Ni and a Ta site, favoring the orbital overlap and the formation of more strongly bound excitons. In a mutual way, the hybridization of the VB and CB can exert a new electrostatic force on the ionic potential which favors the structural change.

2.7.3 Summary and open questions

In systems with a small electronic band gap and a weak screening of the Coulomb interaction, a macroscopic phase, termed excitonic insulator, is predicted to occur at low temperatures if the binding energy of the electron-hole pairs is found to exceed the size of the electronic band gap. Previous theoretical and experimental studies at equilibrium observe that the transition to this phase relies on a delicate interplay of interband coupling between the VB and the CB, which favors exciton coherence, and lattice adjustment, in order to minimize the total energy.

The quasi-dimensional Ta_2NiSe_5 exhibits an entangled electronic and structural phase transition at $T_C = 328$ K. Above T_C, the system is a direct semiconductor with an orthorhombic crystal symmetry. Close to T_C, hybridization of the VB and CB orbitals is likely connected to an instability against spontaneous exciton formation. This behavior at LT goes along with (1) a flattening of the VB top and (2) change of the in-plane crystal symmetry. Theoretical works indicate that these features are consistent with the realization of an excitonic insulator phase.

So far, the change of the electronic band gap has been inferred from optical absorption measurements and, indirectly, from the temperature-dependent shifting of the VB in photoemission spectroscopy. However, it has never been directly measured with absolute energy resolution by combining the temperature-dependent behavior of both the valence *and* conduction band. This is one of the goals achieved in this thesis work. Complementary, the thermally-induced structural phase transition is also addressed following the evolution of the Raman spectrum across T_C.

Moreover, all the equilibrium studies highlight the mutual role of the electron-hole Coulomb interaction and the electron-phonon coupling on the formation and the stabilization of an excitonic insulator phase. However, as their effects manifests

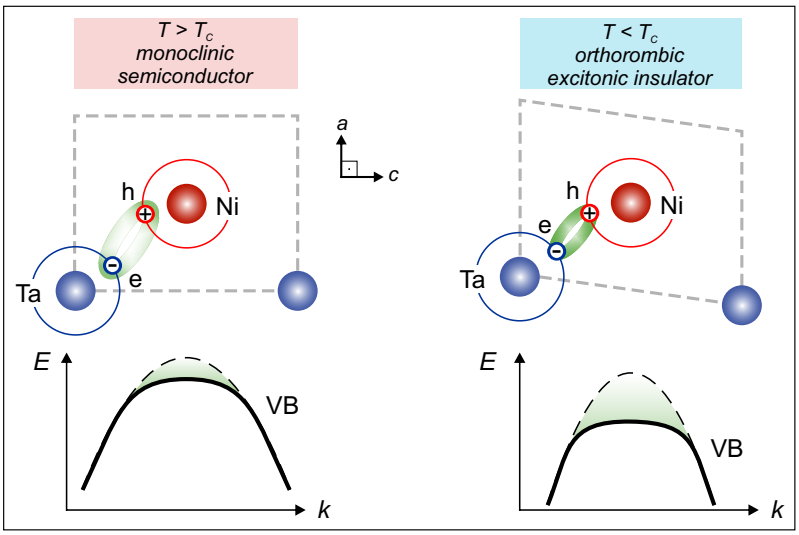

FIGURE 2.17: Schematic of the high- (left) and low- (right) temperature phases of Ta_2NiSe_5: above T_C, incoherent excitons pre-form across the atomic chains (top) and the VB top weakly flattens due to the excitonic fluctuations (bottom). Below T_C, excitons gain coherence concomitantly with the reduction of the Ta-Ni distance. The VB top further deviates from the band dispersion of a noninteracting semiconductor and stabilizes at a higher binding energy.

concurrently at equilibrium, it is not straightforward to separately investigate the electronic and the structural properties of the LT phase of Ta_2NiSe_5. Furthermore, it is currently unknown how these fundamental interactions govern the out-of-equilibrium behavior of Ta_2NiSe_5 and specifically the ultrafast dynamics of its electronic and structural phase. Eventually, it is until now not explored the possibility to gain control on these dynamics on an ultrafast timescale.

These challenges motivate the present thesis work and the choice to investigate Ta_2NiSe_5 by means of nonequilibrium spectroscopic tools. In particular, time-resolved coherent phonon optical spectroscopy is employed in order to verify if the structural phase transition can be induced when the system is excited by an ultrashort pulse with photon energy exceeding the electronic band gap. In this way, insights are gained on the dynamical coupling between the electron and lattice subsystems on a sub-picosecond timescale. The photoinduced nonequilibrium behavior of the occupied and unoccupied electronic structure is investigated below T_C by means of time-resolved photoelectron spectroscopy. This work sheds light on the role of transient screening of the Coulomb interaction and strong excitonic coupling of the VB and CB on the dynamics of the electronic band gap. These results are corroborated by Hartree-Fock theoretical calculations obtained from a close collaboration with D.Golež, M. Eckstein and Ph. Werner. Eventually, the relaxation pathways of the photoexcited carriers are reconstructed by time-resolved photoemission spectroscopy of the unoccupied electronic structure in order to unveil how the excited electronic subsystem couples with other excitations to recover its equilibrium.

Though all these studies, the fundamental interactions governing the nonequilibrium behavior of an excitonic insulator are detailed in the energy, momentum and time domains. Furthermore, the possibility to optically modulate the excitonic insulator band gap of Ta_2NiSe_5 on an ultrafast timescale will be demonstrated.

3 Experimental details

This chapter is devoted to the description of the experimental tools used in this thesis work. Section 3.1 introduces the pump-probe method which sets the base of sub-picosecond time-resolved spectroscopies. Sections 3.2 and 3.3 present the principles of photoelectron and coherent optical phonon spectroscopy, respectively. Sections 3.4 and 3.5 describe the relevant experimental setups. In particular, the mid-infrared (mid-IR) non-collinear optical parametric amplifier (NOPA) built during the course of this thesis is presented in more detail in Subsection 3.4.1. Finally, Section 3.6 describes the preparation of the investigated samples prior to the photoemission experiments.

3.1 A non-equilibrium approach to look at strongly interacting systems: the pump-probe method

A powerful approach to understand the fundamental interactions characterizing the ground state of a system is to perturb the latter and follow the resulting real time dynamics of some observables. In fact, while at equilibrium interactions on different energy scales appear simultaneously, dynamically they can be discriminated as they manifest on distinct characteristic timescales [22, 23]. However, the dynamics of the electrons and the ion cores typically occur on timescales between few femtoseconds (fs) and several picoseconds (ps), which beat the bandwidth-limited temporal resolution of the electronic instrumentation. To overcome this limitation, the pump-probe technique has been developed in the context of ultrafast spectroscopies.

Pump-probe spectroscopies are based on the stroboscopic effect, i.e. on the capability to capture a series of distinct 'snapshots' of a continuous evolution. The concept is sketched in Fig. 3.1 (a): the matter is excited from its equilibrium state with an ultrashort pulsed electromagnetic field (pump); the intensity variation ($\Delta I(t)$) of some observables of the system is the recorded by means of a non-perturbing pulse (probe) at variable time delays until the signal of the equilibrium state is restored.

Experimentally, the pump-probe method necessitates (1) a temporal resolution higher than the duration of the system evolution and (2) a detection sensitivity capable to discern small dynamical variations. The first requirement is achieved by using pulses whose duration is on the order of the observed dynamics and by controlling the time delay between the two pulses on a scale shorter than the duration of the investigated processes. Effectively, temporal resolution of approximately 10% of the pulse duration can be achieved in this way [127]. The second requisite is accounted by an appropriate acquisition technique adopted to the spectroscopy performed[1], and sufficiently high statistics per snapshot. Eventually, the pump-probe method benefits from the possibility to tune the wavelength of each pulse independently. The tunability of the pump photon energy enables for selective excitation of the system along specific pathways. By varying the probe wavelength, it is possible to access the dynamics of the system on different energy scales.

[1] See for instance the lock-in amplifier detection utilized in the time-resolved optical spectroscopy of this thesis work, (cf. Section 3.3.2)

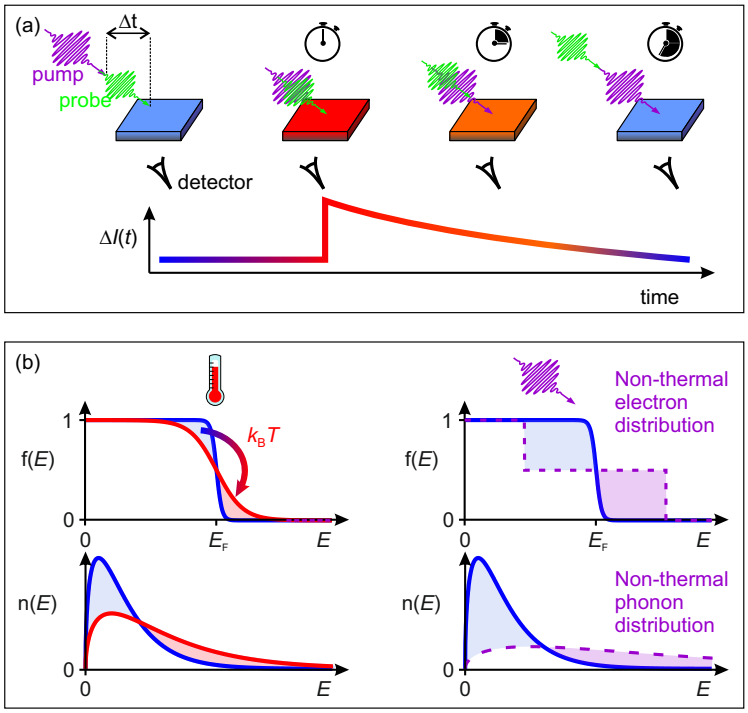

FIGURE 3.1: (a) Principle of the pump-probe method for ultrafast spectroscopies. (b) Comparison of the effects of a thermal and an impulsive optical excitation on the electronic and phononic subsystems. See text for details.

There is a substantial difference between the perturbation induced on the ground state by the pump pulse and a quasi-static stimulus like e.g. a temperature change. The effect is schematically shown in Fig. 3.1 on the Fermi-Dirac distribution of the electrons, $f(E)$, and the Max-Boltzmann distribution of the phonons, $n(E)$, of the perturbed system: upon thermal excitation, electrons and phonons redistribute continuously at higher energies keeping the two subsystems in a quasi-thermodynamical equilibrium with a well defined, but higher temperature. Upon ultrashort impulsive excitation, a sudden injection of electrons into high-energy states destroys the thermodynamic equilibrium with the lattice. Additionally, the Fermi-Dirac functional does not hold for such excited electron distribution, thus an electronic temperature is initially not defined.

If the potential landscape of the system is not altered by the pump excitation, the relaxation dynamics are governed by the same interactions that act in the system at equilibrium. Particularly, after an early recovery on a few-femtosecond timescale [2], the electronic distribution resembles that of a Fermi-Dirac population with an increased effective temperature. Thus, understanding the evolution of the electronic system during its thermalization provides information on the lifetime of its states and the fundamental coupling between different states and/or to other degrees of freedoms like, e.g. phonons.

If intense pump pulses are used, a dramatic change in the potential landscape may be induced, and consequently, the relaxation dynamics can follow completely new pathways. This concept applies particularly to materials whose phase diagram at equilibrium hosts different thermal phases. Then, two scenarios can be expected:

[2] This timescale depends on the efficiency of electron-electron scattering via interband and intraband transitions [21].

either the phase transition to the higher temperature phase is photoinduced or the system evolves to a new metastable phase which is thermally inaccessible. In such highly out-of-equilibrium states, the elementary interactions manifesting concurrently in the ground state are transiently decoupled and can be experimentally distinguished on both the ultrafast timescales and the specific energy domains.

In this work, the pump-probe approach is applied to photoemission spectroscopy in order to study (1) the ultrafast dynamics of unoccupied electronic states of ultrathin SiO_2 films at the interface with the Ru(0001) substrate, and (2) the photoinduced electronic band structure dynamics of Ta_2NiSe_5. Furthermore, the electron and lattice dynamics of Ta_2NiSe_5 are simultaneously investigated by means of time-resolved coherent phonon spectroscopy recording the pump-induced variation of mid-infrared reflectivity. The theoretical principles and the experimental realization of these techniques are presented in the following sections.

3.2 Probing charge carriers at surfaces and interfaces: photoelectron spectroscopy

Angle-resolved photoemission spectroscopy (ARPES) is a powerful tool to investigate electronic properties of a system as it directly addresses the electronic band structure of the material [24, 128]. The technique is based on the quantum photoelectric effect [129, 130] and measures the kinetic energy, E_{kin}, and the parallel momentum, $k_{\parallel}$, of electrons which are photoemitted from the sample surface upon photon absorption. This information relates to the energy distribution of the electrons inside the material by means of the relationships of energy and momentum conservation:

$$(E - E_{\mathrm{F}}) = h\nu - \Phi - E_{kin}, \tag{3.1}$$

$$k_{\parallel} = \sqrt{2mE_{kin}}\sin\theta, \tag{3.2}$$

where $(E - E_{\mathrm{F}})$ is the electron energy with respect to the Fermi level E_{F} prior to photoemission, $h\nu$ the photon energy, Φ the work function of the material, m the electron mass and θ the polar emission angle of the electron. Φ is defined by the energy difference between E_{F} and the vacuum level E_{vac}, and is typically on the order of few eV [131]. By tuning the photon energy $h\nu$, different electronic states are experimentally addressed which satisfy Eq. (3.1). When low-energy photons, in the range of visible-near UV, are used, only direct electronic transitions are accessible due to the negligible momentum carried by the photon. Moreover, because the highest photon energy used in this thesis work is 6.20 eV, the accessible momenta of the Brillouin Zone are restricted to those around the Γ point (i.e., $k = 0$), as prescribed by Eq. (3.2).

The geometry of an electron photoemission process is depicted in Fig. 3.2 (a). It shows that the electron momentum is indeed conserved in the direction parallel to the surface along which the translational symmetry of the crystal is preserved. On the contrary, the perpendicular component is not conserved because the electron has to overcome the vacuum barrier defined by the work function, Φ. The zoomed-out picture on the right shows that the photoelectron escape depth, z_{el}, is much shorter than the optical absorption length, z_{opt}. This quantity, z_{el}, is defined by the mean free path of the electron during its travel towards the surface. A set of z_{el} values is reported in Fig. 3.2 (b) as a function of the kinetic energy imparted by the absorbed photon [132]. It is noted that the optical absorption length at the photon energies used in the present work (red box) is on the order of several tens of nm, while the

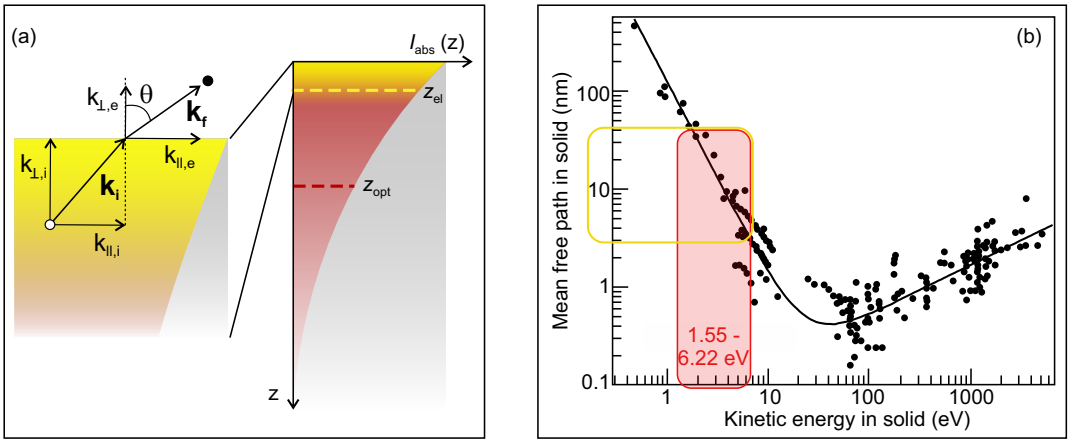

FIGURE 3.2: (a) Schematic of a photoemission process. The red shadow is the illuminated portion of the sample bulk and the dashed line the optical penetration depth. The yellow shadow is the portion of sample probed by photoemission and the dashed line the electron escape depth. (b) Universal curve of the electron inelastic mean free path, z_{el}. The red box indicates the photon energy range used in this thesis work, the yellow box the relative z_{el}. Data digitized from [132].

corresponding z_{el} values range only from few nm up to approximately 50 nm. Thus, ARPES spectroscopy using light in the visible-near UV range is an extremely surface sensitive technique.

Theoretical modeling of a photoemission event - The photoemission process is rather complex, thus it is usually treated by theory under approximation of 'frozen' orbitals and independent particles. The first assumption considers the electronic states as unaltered during the sudden ionization of the system. The independent-particle approximation implies a collision-free propagation of the electrons towards and outside the surface such that the memory of their initial state is preserved.

Under those assumptions, a photoemission event is described by the phenomenological 'three-step' model [133, 134] illustrated in Fig. 3.3 (a): (1) for each photon absorbed, an electron in the bulk is excited; (2) the electron travels towards the surface and (3) escapes into vacuum. Ideally, the collected spectrum is a projection of the electronic states from which electrons are photoexcited (blue shade). However, the picture depicts a more realistic situation where a fraction of 'secondary' electrons is slowed by inelastic scattering processes (orange arrow) like, e.g. electron-electron and electron-phonon collisions. As results, secondary electrons escape the surface with minimal kinetic energy and collect in the low-energy portion of the spectrum (orange shade). Importantly, their contribution to the spectrum becomes more significant when low photon energy is used, as it is the case of the two-photon photoelectron spectroscopy described in Subsection 3.2.1.

For completeness, it is mentioned that the quantum treatment of the photoemission process is obtained by the 'one-step' model which is depicted in Fig. 3.3 (b). Here, photoemission is considered as a single coherent process between an initial Bloch eigenstate of the unperturbed system and a final free-electron-like state with an amplitude that decays exponentially into the solid. The two states must satisfy the energy and momentum conservation laws and their wave functions have to obey the boundary conditions imposed by the surface [135].

In the three-step model discussed above, the transition probability for an optical

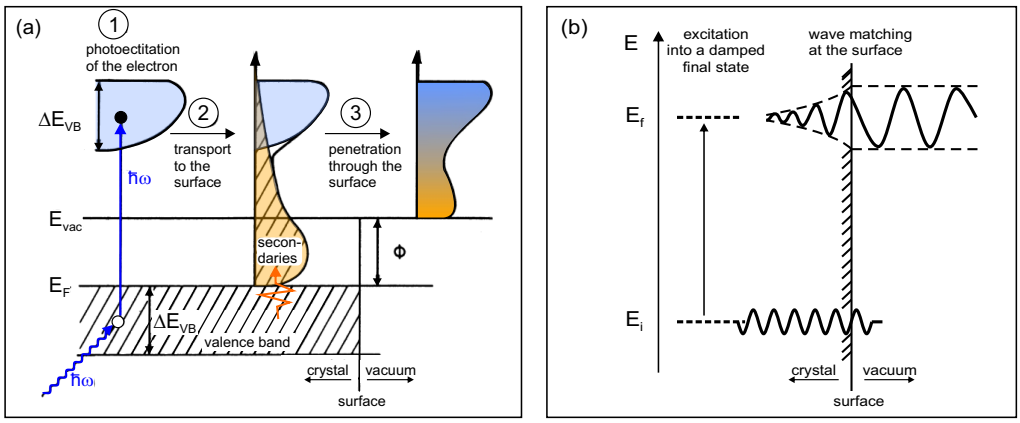

FIGURE 3.3: (a) The phenomenological three-step model and (b) the quantum-mechanical one-step model of a photoemission event, modified from [24] (see text for details).

excitation between an initial state Ψ_i and a final state Ψ_f is described by the Fermi's golden rule. Accordingly, the associated photoemission intensity, $I(E, \mathbf{k})$ is given by the product of three terms [136]:

$$I(E, \mathbf{k}) = I_0(E, \mathbf{k}, \mathbf{A}) \cdot A(E, \mathbf{k}) \cdot f(E). \tag{3.3}$$

The first term is proportional to the dipole matrix element $|M_{\mathbf{k}_{i,f}}|^2 = \langle \Psi_i | \, \mathbf{A} \cdot \mathbf{p} \, | \Psi_f \rangle$, where $\mathbf{A}$ is the vector potential of the radiation field and $\mathbf{p} = \hbar\mathbf{k}$ the electron momentum[3]. Additionally, it is weighted by a factor $\delta(\mathbf{k}_i - \mathbf{k}_f + G, E_f + E_i - h\nu)$ accounting for the energy and momentum conservation. The second term $A(\mathbf{k}_i, E)$ is the single-particle spectral function and contains information on the excitation spectrum of the system.

In case of a strongly interacting electron system, many-body effects affect the photoemission spectral line as well as the dispersion of the relative electronic bands [24, 134]. For these systems, the spectral function is expressed in terms of the complex self-energy function Σ that describes the electron propagation. In particular, the real and imaginary part of the self-energy function provide the energy renormalization and the state lifetime of the interacting electron, respectively. Thus, beyond the single particle picture discussed so far, ARPES is also sensitive to many-body couplings between the electrons and other degrees of freedom of the system like, e.g. phonons [137, 138, 139], spin [140] or nearest-neighbor charges [104, 56, 141].

3.2.1 Two-Photon photoelectron spectroscopy

Two-photon photoelectron spectroscopy (2PPE) is the most suitable technique to study the unoccupied electronic states of a material [39]. The technique is based on the pump-probe approach and employes a pair of ultrashort laser pulses with sub-ps time duration and photon energies lower or comparable to the work function. The pump pulse excites a transient population of electrons from occupied initial states into intermediate states above E_F, and the probe pulse promotes this transient electron

[3]The three-step model treats this term in dipole approximation (i.e., $\nabla \cdot \mathbf{A} = 0$ over the bulk atomic distances, which is true for ultraviolet radiation used in ARPES measurements), thereby it excludes indirect transitions that might become appreciable at the surface where the electromagnetic field exhibits a strong spatial dependence. Such contributions are taken into account by the 'one-step' model.

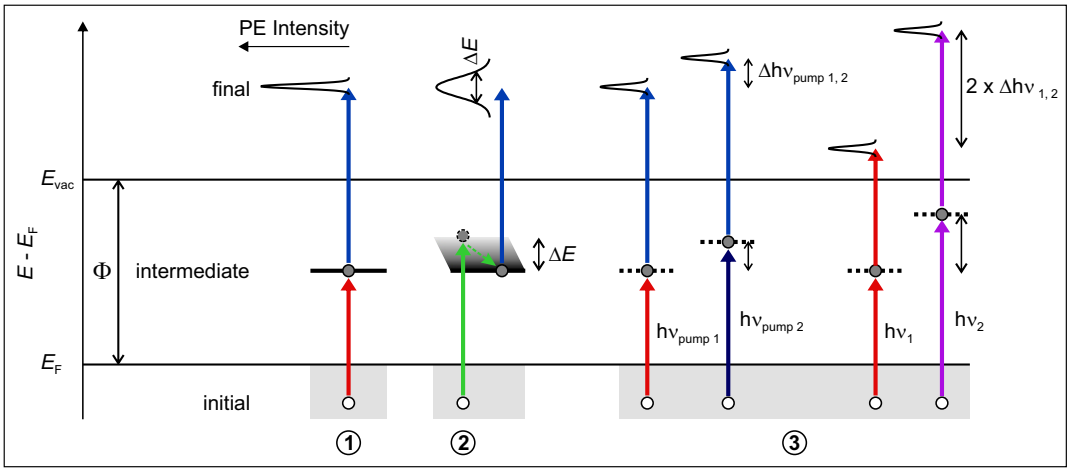

FIGURE 3.4: Two-photon photoemission via ① resonant, ② non-resonant and ③ virtual transitions to an unoccupied intermediate state. Arrows of different colors correspond to pulses with different photon energy. Black solid and dashed horizontal lines are real and virtual intermediate states, respectively. See main text for details.

population into final states above the vacuum level. In this way, a 2PPE process involves both the occupied and unoccupied band structure around the Γ point of the Brilloiun zone and the energy and momentum of the relevant electronic states can be addressed.

Different pathways allow an electron to be photoemitted via the absorption of two photons. As depicted in Fig. 3.4, these pathways are classified into three mechanisms on the basis of the type of intermediate state involved. Mechanism ① consists of a resonant excitation into a 'real' intermediate state. Its transition probability is the largest and results in a sharp, intense spectral line. Mechanism ② involves a non-resonant electron excitation occurring when the pump photon energy does not match the energy difference between the initial and the intermediate state. Here, the excited electron rapidly loses its energy via inelastic scattering processes and reaches the nearest 'real' intermediate state from which it is photoemitted by absorbing one probe photon. Its spectral feature results in a much weaker peak, which is broadened because of the lost of phase and momentum in the scattering processes. Finally, mechanism ③ occurs when any 'real' intermediate states can be addressed neither resonantly nor non-resonantly, and the electron is photoemitted via a 'virtual' intermediate state (dotted lines) which is solely populated within the pump pulse duration. Particularly, this excitation mechanism can occur also by absorption of two photons within the same pulse. Its transition probability it generally low but becomes significant when intense, ultrashort pulses are used, as it is the case of 2PPE experiments.

Notably, distinct photoemission pathways can lead to energetically-overlapping spectral lines. In order to reveal the nature of the intermediate state, being either 'real' or 'virtual', the pump photon energy can be varied. If the electron is photoemitted from a 'real' intermediate state, the peak does not shift in energy (case ① or ②). If, otherwise, the intermediate state is 'virtual', the peak shifts by the difference in photon energy between the two pump pulses used (i.e. compare two leftmost schemes of mechanism ③). Eventually, when single-pulse 2PPE spectra are recorded and the photon energy is varied, if photoemission from an initial states occurs via a 'virtual' intermediate state, the peak shifts by twice the photon energy difference (compare two rightmost schemes of mechanism ③).

Energy scales in 2PPE An exemplary 2PPE spectrum is shown as green curve in the energy diagrams of Fig. 3.5. The energy scale in (a) refers to the kinetic energy of the photoelectrons with respect to the vacuum level E_{vac}. The low- and high-kinetic energy cutoffs of the 2PPE spectrum correspond to the secondary electron and the Fermi-Dirac distribution (FDD) edges, respectively. The first is given by photoemission of inelastically scattered electrons which leave the sample with the minimal kinetic energy, $E_{\text{kin, sec}}$, to overcome the work function (cf. Fig. 3.3). The FDD edge defines the highest possible kinetic energy, $E_{\text{kin, F}}$, provided to the electrons which leave the surface upon photoemission via a 'virtual' state[4]. The scheme in (a) also shows that the work function Φ is obtained by the difference between the total photon energy, $h\nu_1 + h\nu_2$, and the spectrum width, $E_{\text{kin, F}} - E_{\text{kin, sec}}$.

Between the low- and high-energy cutoffs, spectral peaks appear as a result of photoemission processes via one of the mechanisms displayed above. The 2PPE spectrum can be then displayed with respect to different energy scale relative to E_{F} in order to assign each peak to the relative state and retrieve the absolute energy of the latter. These energy scale are thus defined in the following:

- Final state energy ($E_{\text{fin}} - E_{\text{F}}$): In (b), the spectrum is plotted as function of the energy of the final states relative to E_{F}. In this scale, the energy of the secondary electron cutoff coincides with the work function value, while that of the FDD edge to the sum of the photon energies. This representation is useful when the origin of the peaks is not yet known and the spectrum may result form the coexistence of spectral lines of occupied and unoccupied electronic states as well as of final state resonances. Importantly, if a peak results from photoemission into a final state resonance, its energy position does not change when varying the photon energy.

- Intermediate state energy ($E_{\text{interm}} - E_{\text{F}}$): From the final state energy scale, the energy of the intermediate states relative to E_{F} is calculated by subtracting the photon energy of the probe pulse. As shown in (c) and (d), both pulses can potentially act as probe, while the other pulse is responsible to promote electrons into distinct unoccupied states above E_{F}.

- Initial state energy ($E_{\text{initial}} - E_{\text{F}}$): Upon subtraction of the total photon energy, $h\nu_1 + h\nu_2$, from the final state energy, the energy of the initial states is obtained. This provide a measurement of the binding energy of the occupied electronic states below E_{F}.

3.2.2 Photoelectron spectroscopy in the ultrafast time domain

The dynamics of the electronic band structure of a material are directly addressed with sub-picosecond time resolution by applying the pump-probe method to the photoelectron spectroscopy. Because 2PPE spectroscopy is based on the absorption of two photons in order to excite (pump) and photoemit (probe) an electron, respectively, the extension to the time domain is straightforwardly obtained by tuning the time delay, Δt, between the pulses of two separated beams and recording the photoemission intensity of the transiently populated intermediate electronic states (light blue circles) [39, 21]. Fig. 3.6 (a) displays a time-resolved 2PPE process. At zero time

[4] In semiconductors, the density of states at the Fermi level vanishes, thus the FDD edge is experimentally measured on a metallic surface in electrical contact with the semiconducting sample (see Fig. 3.19).

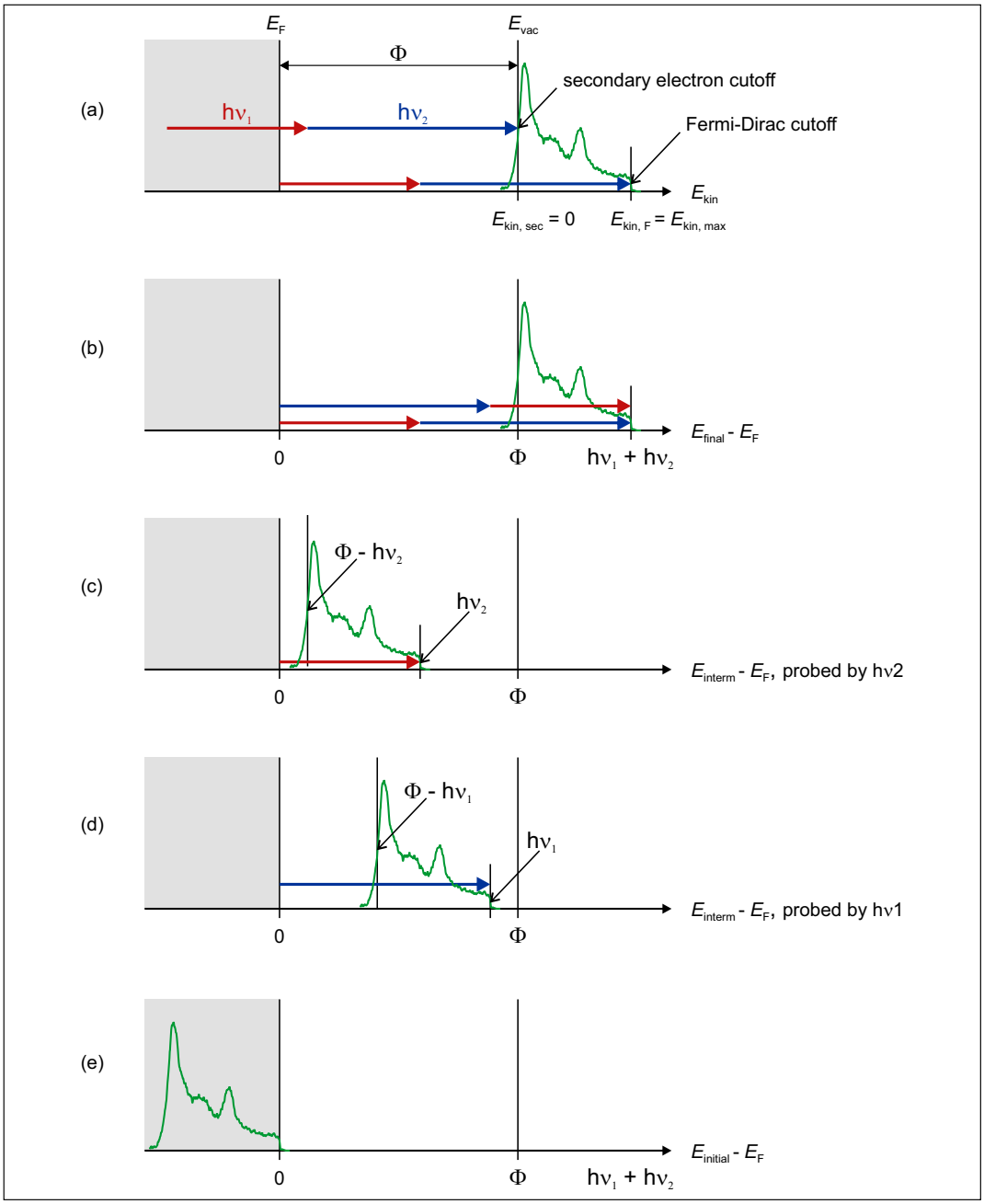

FIGURE 3.5: Representation of the different energy scales of a two-color 2PPE spectrum: (a) kinetic energy with respect to E_{vac}. (b) final state energy relative to E_{F}; (c) and (d) intermediate state energy relative to E_{F} as probed by $h\nu_1$ and $h\nu_2$ photons, respectively; (d) initial state energy relative to E_{F}.

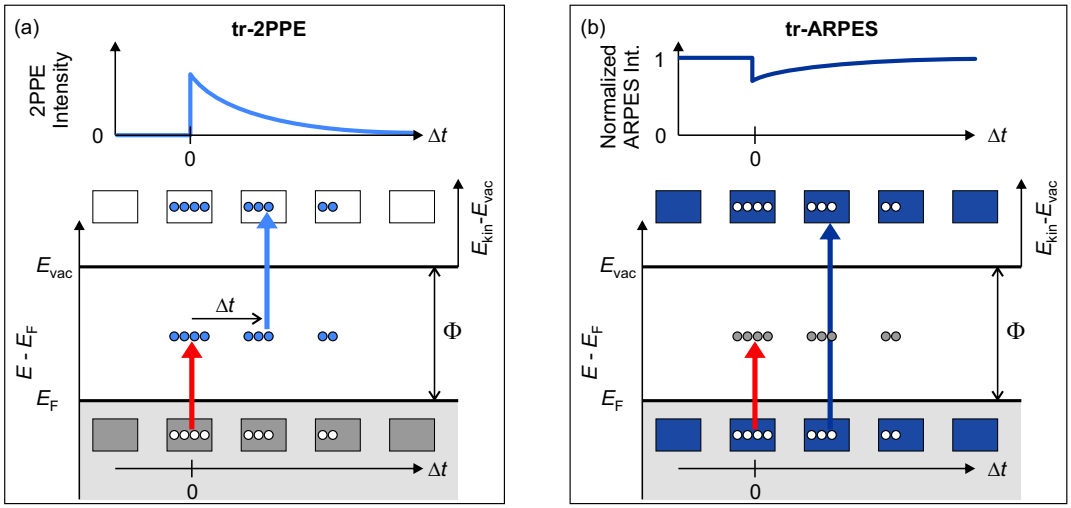

FIGURE 3.6: Pump-probe method applied to 2PPE (a) and ARPES (b) probing unoccupied and occupied electronic states, respectively. See main text for detailed descriptions.

delay, $\Delta t = 0$, the pump pulse (red arrow) excites electrons (light blue circles) into previously unoccupied states above E_F, leaving a population of holes (empty circles) below E_F. At variable time delays following the perturbation, $\Delta t > 0$, the probe pulse (light blue arrow) excites electrons from the transiently populated intermediates states into the vacuum, the photoemission yield at each time delay (light blue curve on top graph) depending on the population decay rate of these states. If the delay between the two pulses is reversed, the role of the two photons is exchanged and the photoemission intensity is recorded from different intermediate states. Thus, in a tr-2PPE data plot both positive and negative time delays can carry information on the dynamics of the unoccupied electronic structure of the investigated system.

In a tr-ARPES experiment, shown in (b), the UV probe pulse (blue arrow) has a photon energy grater than Φ, thus it directly photoemits electrons from states below E_F (blue box). At zero time delay, $\Delta t = 0$, the pump pulse (red arrow) with photon energy lower than the work function, Φ, perturbs the electronic ground state, by exciting electrons above E_F, producing a population of holes in the occupied bands. At variable time delays following the perturbation, the photoemission intensity of the UV probe pulse is recorded and its yield depends on the rate of re-population of the occupied electronic states. As sketched in the top-plot (blue curve), the time-resolved ARPES intensity is typically normalized to that recorded prior to the perturbation of the ground state in order to quantify the depopulation of the occupied electronic states at each time delay. It is noted that the relative variation of PE intensity is typically very small due to the large density of occupied states around E_F. For instance in metals, only few % of the electrons at E_F are typically excited despite the rather large pump fluence values used, which are on the order of tens of μJ cm^{-2} to few μJ cm^{-2} [69]. However, in systems with low density of states at E_F, as it is the case of Ta_2NiSe_5, the relative depopulation may become significant and result in a more dramatic reduction of photoemission intensity after the pump photoexcitation. As discussed in the present thesis work on Ta_2NiSe_5, this exceptional condition allows to accurately follow the hole population dynamics in the occupied bands.

Although the transient variation of electron occupancy below E_F is usually small, the reduction of electron density in the occupied states can drastically modify the

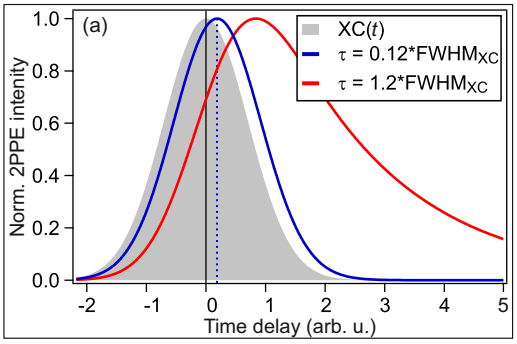

FIGURE 3.7: Simulation of the time-resolved 2PPE intensity.

screening of the Coulomb interaction in the system. This change can induce significant modification of the electronic band structure such as energy shifts and dispersion changes whose detection is one of the key advantages of tr-ARPES. In semiconducting and insulating materials, pump-induced changes of the Coulombic screening may result in the renormalization of the electronic band gap [49, 51, 32]. Finally, upon pump-induced change of the screening of the Coulomb potential, ion cores may respond via the excitation of collective modes in the time domain such as coherent phonons [142, 143]. If a phonon couples to an electronic state probed by tr-ARPES, both the intensity and the position of the relevant spectral lines may exhibit a modulation at the frequency of the phonon in energy-resolved photoemission spectrum.

In summary, tr-ARPES and tr-2PPE spectroscopy combine the absolute energy and momentum selectivity of the standard photoelectron spectroscopy with the ultrashort time resolution of a pump-probe measurement. As a result, the transient distribution of electrons and holes following the optical perturbation of equilibrium ground state are potentially measured as a function of energy, momentum and time. In this way, information on the relaxation dynamics of the charge carriers and the photoexcited band structure are addressed.

Modeling the time-resolved photoemission intensity The quantum mechanical treatment to describe the time-resolved photoemission yield requires the solution of a set of optical Bloch equations accounting for all the involved electronic states (initial, intermediate and final) [144]. In this formalism, both the decay and the dephasing of the excitation enter as distinct parameters, despite them not being experimentally easily disentangled. However, when non-resonant excitation into unoccupied electronic states is induced, the coherence of the excitation is lost and the problem can be reduced to the solution of rate equations where only decay processes are relevant. In this framework, the photoemission intensity is more simply described by

$$I_{\mathrm{PE}}(t) = \mathscr{G} * R(t), \tag{3.4}$$

where $\mathscr{G}$ is the Gaussian cross-correlation of the pump and probe pulses and $R(t)$ is the response function of the system describing the evolution of the electron (hole) population in the intermediate (initial) state. Thus, the $R(t)$ function contains the bare lifetime τ of the probed electronic state [39, 145, 1]. Formally, $R(t)$ is obtained by solving the coupled rate equations for all the states involved in the population decay. For a simple decay process involving only two states, the solution is given by a single exponential function. For more complex dynamics, other components enter in

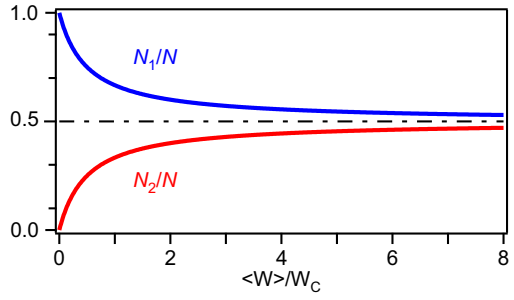

FIGURE 3.8: Steady-state population as a function of the radiative energy density in a two-level system due to spontaneous emission saturation. After [144].

the response function $R(t)$. Some examples of rate equations involving multiple decay steps are reported in [146, 147].

A simulated time-resolved photoemission intensity is shown in Fig. 3.7 by the red curve. Here, $R(t)$ is defined by a step function, accounting for an instantaneous response at the excitation time, multiplied by a single exponential decay, modeling the evolution of the system at later time delays. The gray shaded Gaussian is the cross-correlation of the two laser pulses. Then, the simulated data consists of two dynamics: (1) an intensity increase around zero time delay, and (2) a decrease at later time delays. The first is due to the photoexcitation of electrons (holes) into the intermediate (initial) state, while the second reflects the transient occupancy of the state by the electrons (holes). Thus, the time constant of this intensity decay provides a measurement of the state lifetime τ.

Finally, the blue curve shows the transient photoemission intensity resulting from photoexcitation into a state whose lifetime is shorter than the pump-probe cross-correlation: notably, a shift of the intensity maximum with respect zero-time delay and a slight asymmetry of the transient signal can still be resolved. Experimentally, this means that, provided sufficiently high statistics of the experimental data, dynamics faster than the nominal temporal resolution given by the pump-probe cross-correlation can be measured. Effectively, if the zero-time delay is independently evaluated on an almost zero-lifetime state of a reference sample or in situ at high-energy states, sub-resolution lifetime down to only few fs can be retrieved [127, 145, 148]. This assumption is used in Chapter 4, when evaluating the intermediate state lifetimes in ultrathin silica films on a metal surface.

Electron population in a two-level system As explained in the previous section, time-resolved photoelectron spectroscopy measures a transient electronic population which is promoted upon pump photon absorption from the ground state to an excited state. The electron redistribution in this 'two-level' system depends on the number of absorbed photons and can be modeled as a function of the transferred energy density by means of two coupled Einstein rate equations for a pair of nondegenerate states. The coupled rate equations for the ground state population N_1 and the excited state population N_2 read:

$$\mathrm{d}N_1/\mathrm{d}t = -\mathrm{d}N_2/\mathrm{d}t = N_2 A - N_1 B_{12}\langle W\rangle + N_2 B_{21}\langle W\rangle, \tag{3.5}$$

where A, $B_{12}\langle W\rangle$ and $B_{21}\langle W\rangle$ are the probabilities of spontaneous emission rate from the excited state, stimulated absorption rate into the excited rate and stimulated emission rate from the excited rate, respectively. $\langle W\rangle$ is the mean energy density at

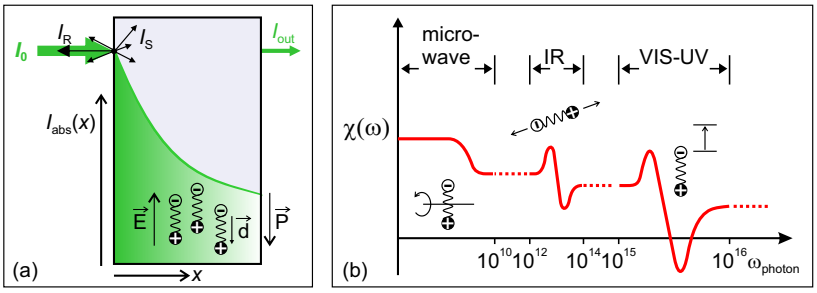

FIGURE 3.9: (a) Light propagation in an absorbing medium involving reflection, scattering and absorption processes. $\vec{P}$, $\vec{E}$ and $\vec{d}$ are the macroscopic polarization, the electric field and the field-induced microscopic electric dipole, respectively. (b) Sketch of the optical susceptibility χ providing the excitation spectrum of the medium.

the frequency of the pump photon.

By using the boundary condition $N_1 + N_2 = N = constant$, it can be shown [144] that there is a steady-state solution of Eq. (3.5) that evolves as a function of the radiative energy density as displayed in Fig. 3.8: the two populations evolve linearly with the energy density up to a critical value $\langle W \rangle_s$, above which they approach the constant value $N/2$. Thus, when N_2 becomes close to N_1, the absorption of one photon is balanced by the emission of another photon. As a consequence, $N_2 > N_1$ is not allowed in a two-level system, preventing population inversion to occur. This situation describes the condition for absorption saturation of pump photons which will be important for in the discussion of the photoexcited population dynamics in Ta_2NiSe_5 presented in Chapter 5.

3.3 Probing simultaneously electrons and lattice: optical spectroscopy

Optical spectroscopy is a photon-in photon-out technique. It is directly sensitive to the optical susceptibility function of the system which describes the way an electromagnetic field interacts with the matter. As depicted in Fig. 3.9 (a), when light propagates through a dense medium, its initial intensity, I_0, is attenuated by several processes such as reflection at the surface (I_R), diffusion by scattering centers inside the medium (I_S) and absorption by the material itself ($I_{abs}(x)$). Optical spectroscopy analyzes the intensity of the light emerging from the sample to potentially gain insight on the electronic and structural properties of the investigated material. In the present thesis work on Ta_2NiSe_5, two types of optical spectroscopy are employed: (1) Raman spectroscopy, which collects the frequency-resolved inelastically scattered light, I_S, thereby probing the lattice subsystem via its incoherent phonon spectrum (see Section 3.3.1) and (2) coherent optical phonon spectroscopy performed by measuring the time-resolved variation of the reflected light intensity, I_R, by which simultaneous information on the carrier and lattice dynamics are obtained with sub-picosecond time resolution (see Section 3.3.2).

The light-matter interaction manifests macroscopically in a net polarization **P** of the electron cloud, as sketched at the bottom of Fig. 3.9 (a). As long as the optical field **E** is much weaker than the crystal field, **P** and **E** relate linearly[5] via the optical

[5]Here an isotropic medium is assumed. In case of an anisotropic medium, the relation turns into a tensor and holds separately for each nonequivalent direction.

susceptibility function, χ:

$$\mathbf{P} \propto \chi \mathbf{E}. \tag{3.6}$$

The optical susceptibility function is an intrinsic property of the material and contains information on its electronic, vibrational and rotational resonance modes, as summarized in the sketch of Fig. 3.9 (b). It can be shown that χ connects to the intensity of the interacting optical field via the complex refractive index, $\tilde{n}$, and in turn to the adsorbed light intensity via the Lambert-Beer exponential law for an absorbing medium [149]. Thus, optical spectroscopy allows to directly probe the optical susceptibility function and, through that, the excitation spectrum of both the electron and lattice subsystems of the material.

In the following, the electron-mediated inelastic scattering of a photon with the lattice is detailed, because this fundamental interaction is at the base of both optical spectroscopies used in this work. The process is referred to, as Raman effect [150, 151]: A photon interacts with the electron cloud by promoting an electron into a virtual excited state and inducing a polarization, $\mathbf{P}$. The excited electron relaxes by exchanging energy with lattice excitations and a photon is inelastically scattered at the difference frequency of the incoming photon and the involved phonon. Macroscopically, a lattice displacement $\mathbf{Q}$ is induced [6] [152] which connects to the induced polarization via the susceptibility function χ.

To show that, the lattice displacement $\mathbf{Q}$ is expressed in terms of the associated wave vector $\mathbf{q}$ and frequency Ω of the phonon:

$$\mathbf{Q}(\mathbf{r}, t) = \mathbf{Q}_0 \cos(\mathbf{q} \cdot \mathbf{r} - \Omega \cdot t). \tag{3.7}$$

For a monochromatic incident radiation, the electric field is given by:

$$\mathbf{E}(\mathbf{r}, t) = \mathbf{E}_0 \cos(\mathbf{k} \cdot \mathbf{r} - \omega_0 \cdot t). \tag{3.8}$$

Thus, the induced polarization is obtained by expanding χ in a Taylor series with respect to $\mathbf{Q}$:

$$\mathbf{P}(\mathbf{r}, t, \mathbf{Q}) = (\mathbf{P}(\mathbf{r}, t))_{Q_0} + \left(\frac{\partial \chi}{\partial Q}\right)_{Q_0} \mathbf{Q}(\mathbf{r}, t)\mathbf{E}(\mathbf{r}, t) + ..., \tag{3.9}$$

and inserting Eq. (3.7) and Eq. (3.8), which results in the following expression [7]:

$$\mathbf{P}(\mathbf{r}, t, \mathbf{Q}) = (\mathbf{P}(\mathbf{r}, t))_{Q_0} + \frac{1}{2}\left(\frac{\partial \chi}{\partial Q}\right)_{Q_0} \mathbf{Q}_0\mathbf{E}_0[\cos((\mathbf{k}-\mathbf{q})\cdot\mathbf{r}-(\omega_0-\Omega)t)+\cos((\mathbf{k}+\mathbf{q})\cdot\mathbf{r})+(\omega_0-\Omega)t))]. \tag{3.10}$$

The polarization consists now of three terms with different frequencies and wave vectors. The first one accounts for the Rayleigh elastic scattering of light without energy exchange with the lattice, while the second and the third terms describe the Raman inelastic scattering processes of a photon exchanging energy with the lattice. In particular, the $((\mathbf{k} - \mathbf{q}) \cdot \mathbf{r} - (\omega_0 - \Omega)t)$ term, known as Stokes process, refers to the emission of a phonon with wave vector $\mathbf{q}$ and frequency Ω and the corresponding loss in momentum and energy by the scattered photon. The $((\mathbf{k} + \mathbf{q}) \cdot \mathbf{r} - (\omega_0 + \Omega)t)$ term is referred to as anti-Stoke process and it corresponds to the stimulated process where

[6] The lattice displacement $\mathbf{Q}$ can be seen as the macroscopic equivalent of the effect produced on the atoms by the local dipole moment $\boldsymbol{\mu}$ due to the field-induced electron displacement $\mathbf{d}$ (see Fig. 3.9 (a)).

[7] The trigonometry identity $\cos(\mathrm{A})\cos(\mathrm{B}) = 1/2[\cos(\mathrm{A} - \mathrm{B}) + \cos(\mathrm{A} + \mathrm{B})]$ is used here.

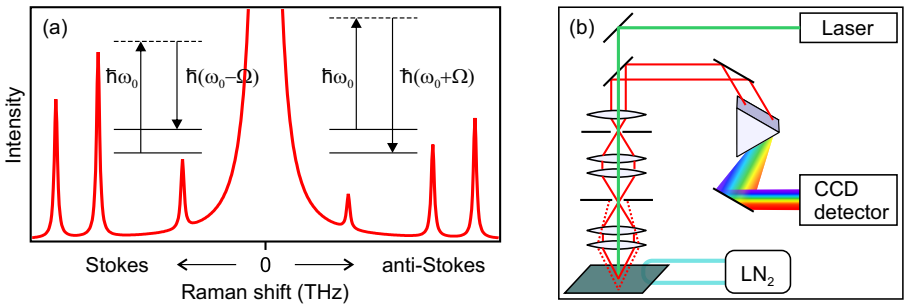

FIGURE 3.10: (a) A typical Raman spectrum showing the Rayleigh, Stokes and anti-Stokes lines. (b) Schematic of the employed confocal Raman spectroscopy setup.

a phonon is annihilated and its energy $\hbar\Omega$ and momentum $\hbar\mathbf{k}$ are transferred to the scattered photon.

Thus, by resolving the frequencies of the incoherent scattered light, the phonon spectrum of the scattering medium is retrieved.

3.3.1 Raman spectroscopy

This optical spectroscopy directly applies the principle of inelastic Raman scattering by illuminating the material with continuous-wave (CW) visible light and collecting the frequency-resolved scattered light intensity. An idealized Raman spectrum is shown in Fig. 3.10 (a). It consists of a plot of intensity of scattered light as a function of the Raman shift, i.e. of the frequency difference between the scattered and the incident photons. Several spectral lines distribute symmetrically with respect to the Rayleigh component ($\omega = 0$), as expected from Eq. (3.10). Negative Raman shifts correspond to Stoke processes, while positive to anti-Stoke ones. The number of lines relates to the number of vibrational and rotational modes supported by the system with a given symmetry. Generally, if the lattice symmetry is lowered by, e.g. a structural distortion, the degeneracy of some vibrational levels is removed and consequently new Raman peaks are expected to appear in the spectrum.

Each Raman line is described by its intensity, width and frequency. The peak intensity depends on the scattering probability of the light with the relevant phonon mode[8]. The linewidth is related to the phonon lifetime via the energy-time uncertainty principle. However, more information is contained in the width of a Raman line, like, e.g. the impurity concentration. Therefore, determining the lifetime of the phonon from its Raman spectral line is not always straightforward. Finally, the frequency carries information on the energy exchanged between the photon and the lattice. Raman shifts below few tens of THz (i.e., few 100s of meV) identify scattering processes with high-energy optical phonons. Those will be investigated here in the two structural phases of Ta_2NiSe_5.

The Raman spectroscopy experiments are performed in the laboratory of Dr. A. Trunschke at the Inorganic Chemistry Department of the Fritz Haber Institut, Berlin. The experimental setup is based on a commercial TriVista Raman Microscope System TR557 (S&I GmbH) equipped with a 750 mm-focal length monochromator (Princeton Instruments) and a liquid nitrogen cooled charge-coupled device (CCD) system

[8] As the initial phonon occupation for a Stoke process is usually greater than that for an anti-Stoke one, a Stoke peaks has usually higher intensity than its symmetrical anti-Stoke line.

(PyLoN:2kBUV). A diode-pumped solid-state laser illuminates the sample with approximately 50 mW continuous wave (CW) polarized light radiation at a wavelength of 532 nm. The detection scheme is shown in Fig. 3.10 (b) and is based on a confocal geometry. It is equipped by an additional aperture in front of the first pair of lenses facing the sample. This prevents the light scattered outside the beam focus from being collected on the detector, thereby improving the experimental spatial resolution. In order to vary the temperature of the Ta_2NiSe_5 sample, a liquid nitrogen cryostat combined with a heating stage is employed. Because of the experimental geometry and the reduced dimension of the sample, direct temperature measurements on the sample is not possible during the measurements. Instead, the thermocouple is connected to the sample holder and the temperature discrepancy is independently evaluated and results of approximately 15 K.

3.3.2 Time-resolved coherent optical phonon spectroscopy

Sub-picosecond time-resolved optical spectroscopy is based on the all optical pump-probe scheme (see Section 3.1) and investigates the photoinduced transient variation of the susceptibility function as a function of time. As explained in the following, this allows to simultaneously retrieve information on both the electronic and lattice dynamics. There are manifold types of time-resolved optical spectroscopy methods which essentially diversify for the wavelength range of the pump and probe beams and the detected optical property (reflectivity, transmittivity, photoluminescence, frequency conversion, just to mention some of the most common). In this work, near-infrared pump and mid-infrared probe photons are employed and the probe reflectivity signal is recorded. The signal detection exploits a lock-in amplifier which allows to resolve very small variations of the intensity signal (the signal-to-noise ratio can be up to 10^6). Particularly, intensity modulation due to excitation of coherent optical phonons is detected. Because of this capability, the employed optical spectroscopy technique is also referred to as time-resolved coherent optical phonon spectroscopy.

As mentioned above, in the configuration applied in this work the transient change of probe reflectivity, $\Delta R(t)$, with respect to the reflected intensity at equilibrium, R_0, is recorded. The $\Delta R(t)$ signal originates from a transient modulation of the refractive index $\tilde{n}$ through the optical susceptibility χ. This can be written in the form [153]:

$$\Delta R(t) = \frac{\partial R}{\partial n}\Delta n(t) \approx \frac{\partial R}{\partial \chi}\frac{\partial \chi}{\partial N_{\mathrm{el}}(t)}N_{\mathrm{el}}(t) + \frac{\partial R}{\partial \chi}\frac{\partial \chi}{\partial Q}Q(t), \tag{3.11}$$

where $N_{\mathrm{el}}(t)$ is transiently excited electron density and Q the the time-dependent amplitude of the lattice displacement defined in Eq. (3.7). The two terms iof Eq. (3.11) show that the change in time of the probe reflectivity is due to (1) a polarization of the electron cloud and (2) the activation of optical phonon modes. Both effects are initiated by the absorption of pump photons and their evolution in time depends on the processes involved in the relaxation of the system back to equilibrium. In the following, the two contributions to $\Delta R(t)$ are separately discussed.

The incoherent optical response - The first contribution it is related to the pump-induced modulation of the electron density and it is referred to as the incoherent optical response for reasons that will be clear later. This signal is generally assigned to the pump-induced change of absorption conditions for the probe photons at each pump-probe time delay [154, 155]. The simplest case exemplifying this concept is given by a degenerate (i.e. monochromatic) pump-probe measurement of an absorbing medium

for which photon transmission at that wavelength can be neglected: at the excitation time, pump photons partially depopulate some initially occupied levels. Thus, the optical transition from those levels is partially bleached for the probe photons and some of them are not absorbed. As a result, the initial reflectivity at the probe wavelength is expected to increase. This process is referred to as ground state bleaching. At times following the photoexcitation, the system releases the excess energy via different relaxation pathways. These can include inter- and intraband scattering of excited electrons and, on a longer timescale (i.e. typically after few hundreds of femtoseconds), inelastic Raman scattering involving the emission of incoherent phonons [156, 157]. In this way, the equilibrium absorption conditions for the probe pulse are restored and the incoherent reflectivity evolves back to the intensity at the equilibrium state.

Therefore, the transient incoherent optical response is indirectly connected to the carrier relaxation dynamics through the pump-induced changes imparted on the optical susceptibility at the frequency of the probe photon. However, the incoherent optical response is fundamentally different than a photoemission signal. Photoemission spectroscopy directly measures an actual electron population in the electronic bands with absolute energy and momentum resolution (cf. Eq. (3.1) and Eq. (3.2)). Optical spectroscopy measures a polarization between states that are separated in energy by the energy of the probe photon. This implies two intrinsic differences: (1) The optical signal is also sensitive to coherences between states even in absence of a real electron occupation of those states. (2) The optical signal integrates all the accessible transitions over the Brilluoin zone, thus it lacks of information on the electron momentum. Therefore, the interpretation of the incoherent optical response in terms of the involved electronic transitions typically relies on modeling, such as the Drude-Lorenz model [149], which demands to measure the optical response over a wide range of frequency.

Exceptionally, this work will, for the first time, show that the time-resolved incoherent optical response of Ta_2NiSe_5 measured at the (single) photon energy resonant to the electronic band gap can be directly correlated to the specific charge carrier dynamics at the top of the valence band at Γ without the need of sophisticated models. This is achieved by comparing complementary tr-ARPES of the occupied states around E_F whose transient occupancy variation with respect to the equilibrium can be accurately detected thanks to the low-density of states of Ta_2NiSe_5(cf. Subsection 3.2.2).

The coherent optical response - The second contribution to the reflectivity change contains the modulation of χ due to the coherent excitation of optical phonon modes. This is based on Raman scattering processes occurring at the photoexcitation time. As detailed later, the generation may occur both resonantly and nonresonantly. Importantly, both mechanisms relay on the fact that when the pump laser pulse is sufficiently shorter than the period of a fundamental lattice vibration, phonons are excited in a coherent manner, i.e. with defined phase relationship [153]. Under this condition, a macroscopic modulation of the probe reflectivity intensity is produced.

The coherence of the phonon excitation relies on the broad bandwidth of the ultrashort pump pulse capable of hosting several combinations of two photons whose energy difference matches the vibrational mode energies, $\omega_1 - \omega_2 = \Omega_Q$ [158]. This is the fundamental difference from a Raman process induced by CW light, where the atomic vibrations lack of phase relationship. As explained in the following, this coherence property has important implications on the possibility to investigate the phonon dynamics as a function of the time following the excitation.

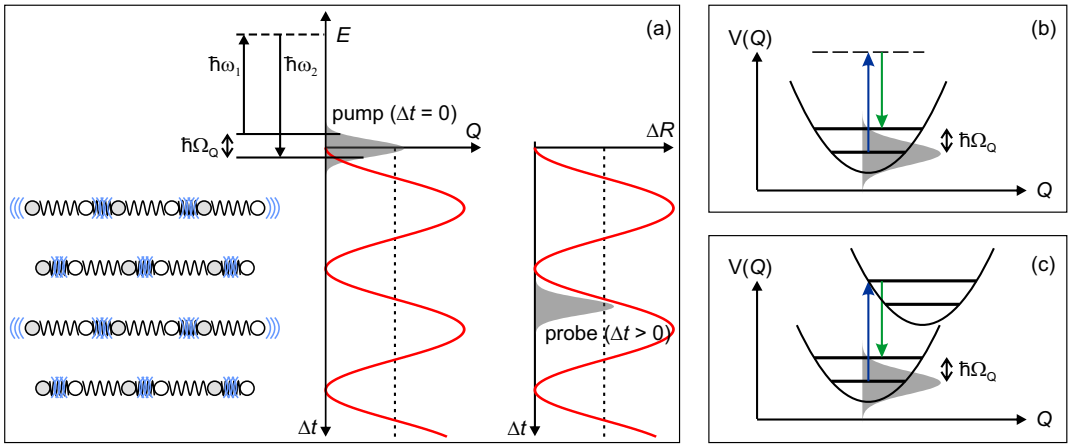

FIGURE 3.11: (a) Coherent phonon generation and detection. The pump pulse induces a coherent ionic motion Q via stimulated Raman scattering. This motion is monitored stroboscopically through the modulation of the probe ΔR as a function of pump-probe time delay, Δt. Adapted from [153]. Generation mechanisms of coherent phonons: (b) nonresonant impulsive stimulated Raman scattering and (c) resonant displacive excitation of coherent phonon. See main text for details.

As depicted in Fig. 3.11 (a), phase-locked nuclear vibrations are induced by the ultrashort pump pulse resulting in a macroscopic oscillation of the Q amplitude at the frequency of the activated phonon. This oscillation periodically modulates the real part of refractive index, n, and thus the optical susceptibility χ. Therefore, the probe pulse, with much shorter duration than the period of the phonon mode, can experience a periodically varying refractive index while interacting with the sample and the effect appears in an oscillatory modulation of its reflected intensity, ΔR, as a function of pump-probe delay. In the present example, the maximum of the Q vector amplitude and of the reflectivity variation, ΔR, remains constant over time because damping processes are neglected. However, in a realistic case, processes such as phonon dephasing and inelastic scattering with e.g. impurities of the lattice contribute to the amplitude decay of the coherent optical response of the system.

Finally, the generation of coherent optical phonons can be achieved both resonantly and non-resonantly [159, 160]. A non-resonant excitation, shown in Fig. 3.11 (b), does not require absorption in the material, but only a virtual transition by which photons exchange energy with the lattice by an amount $\hbar\Omega$ covered by the pulse bandwidth, as explained before. The mechanism is referred to as impulsive stimulated Raman scattering. The optical signature is a sine oscillation as a function of time, in agreement with the solution for an impulsively excited harmonic oscillator. Under resonant conditions, shown in Fig. 3.11 (c), the pump absorption induces electronic transitions in the material and the equilibrium atomic coordinate Q shifts due to the change of the electronic distribution (i.e. the polarization of the electron cloud). Thus, this mechanism is called displacive excitation of coherent phonons and manifests in time with a cosine oscillation of the optical signal. Thus, by phase analysis of the phonon component of the optical response, the relevant generation mechanisms can be revealed.

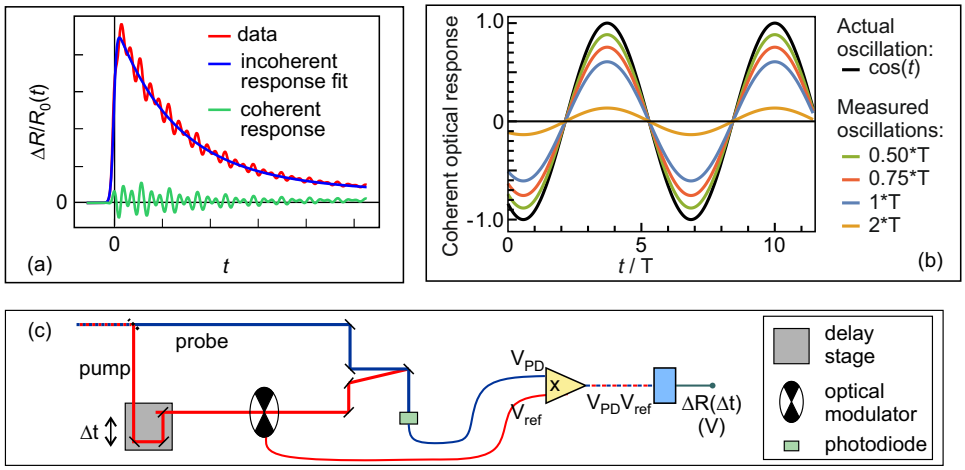

FIGURE 3.12: (a) Model of a $\Delta R(t)$ data (red), fit curve of the incoherent part (blue) and the coherent component (green). (b) Simulated amplitude of the coherent optical response sampled by a Gaussian pulse of different widths. (c) Optical pump-probe setup with lock-in detection.

Description of the experimental data and setup

Based on the previous discussion, a $\Delta R(t)$ data would look as the model shown in red in Fig. 3.12 (a). It consists of a superposition of an non-oscillatory part and a periodic component that correspond to the incoherent and coherent optical response, respectively. This model curve resembles the data recorded in this work and it is used in the following to present the adopted procedure for the data analysis.

In order to evaluate the incoherent optical response, an empirical function in the form of

$$y(t) = \mathscr{G} * (A \cdot \exp(-t/\tau_1) + B \cdot \exp(-t/\tau_2)) \tag{3.12}$$

is fit to the data. $\mathscr{G}$ is the Gaussian intensity profile of the cross-correlation between the pump and probe pulse and it determines the slope of the pulse duration-limited rise of the $\Delta R(t)$ intensity at the excitation time (i.e. at time zero). The double exponential function allows for the determination of the amplitudes, A and B, and time constants, τ_1 and τ_2 of the incoherent relaxation dynamics. Those parameters quantify the intensity and the timescale of the scattering processes involved in the relaxation dynamics.

The oscillatory component of the phononic response is singled out from the total transient optical response upon subtraction of the fit curve obtained by Eq. (3.12). The obtained signal is analyzed in two ways. First, it is fast-Fourier transformed (FFT) to retrieve the frequencies of the N coherent optical phonons to be compared to the inelastic Raman shifts at comparable temperatures. In a second step, the coherent optical response is modeled via a sum of N damped harmonic oscillators convoluted with the $\mathscr{G}$ function:

$$y(t) = \mathscr{G} * \left(\sum_{i=1}^{N} A_i \cdot \exp(-t/\tau_i) \cdot \cos(\omega_i \cdot t + \phi_i) \right), \tag{3.13}$$

where A_i is the initial oscillation amplitude, τ_i the decay time, and ϕ_i the initial phase of the ω_i-phonon. The phonon frequencies previously obtained upon fast-Fourier transformation are used in this model as initial parameters for the fitting procedure.

Eq. (3.13) indicates that the possibility to resolve a coherent oscillation relies not only in the respective amplitude parameter A, but also on the temporal resolution of the experiment, as parametrized by the Gaussian function $\mathscr{G}$. This aspect is exemplified in Fig. 3.12 (b): a single-frequency oscillation is simulated here various times by a sinusoidal function convoluted with a Gaussian intensity profile. The amplitude of the sinusoidal function is kept the same and the Gaussian width is varied. Clearly, cross-correlations broader than the phonon period drastically suppress the oscillation amplitude. Thus, when the temporal resolution approaches or is even longer than the period of the phonon oscillation, the relative optical modulation cannot be resolved and the oscillatory component in $\Delta R(t)$ is smeared out. Therefore, on the one hand short pulses are demanding in the experiment. On the other hand, this effect should be taken into account when comparing the relative amplitude of distinct phonon modes as obsained by means of time-resolved coherent optical phonon spectroscopy and time-integrated Raman spectroscopy.

The experimental setup adopted in this work employes a lock-in amplifier detection [161] because the total pump-induced change of optical reflectivity, $\Delta R(t)$, is typically very small. The experiment scheme is shown in Fig. 3.12 (c). The pump beam intensity is periodically modulated by a motorized optical chopper that switches on and off the beam at a fixed reference frequency f_{ref} (here, $f_{\mathrm{ref}} = 470$ Hz is used). As a consequence, the probed signal at each pump-probe time delay contains also a modulation at the reference frequency. The signal V_{PD} is collected by a photodiode and multiplied in the lock-in amplifier by the reference signal V_{ref} provided by the chopper. Eventually, the pump-probe correlated signal ΔR is singled out from the noncorrelated background intensity by applying a low pass filter to the amplifier output signal. This procedure is repeated for each pump-probe time delay, which is set by adjusting the path length of the pump beam by means of a motorized translational stage with micrometer precision.

Finally, in this work, the temperature dependence of the transient optical response is measured in order to investigate the electron and phonon dynamics of the two phases of Ta_2NiSe_5. Thus, the measurements are performed inside a commercial cryostat (Oxford Instrument) allowing to control the temperature of the sample and to cool it with liquid Nitrogen down to 80 K at a base pressure of $\approx 10^{-6}$ mbar.

3.4 The laser systems for ultrafast spectroscopy

In this section, the two femtosecond laser systems used in this work are introduced and the respective features relevant to the employed spectroscopic techniques are highlighted. The major part of the measurements are performed with a Coherent laser system which is presented in more detail in the next subsection. In particular, the optical setup connected to the Coherent laser output is described. This is devoted to the generation of a wide range of harmonics of the laser fundamental output by means of frequency mixing processes in non-linear crystals. In Subsection 3.4.1, particular focus is given on the mid-infrared optical parametric amplifier (OPA) built in the context of this thesis. Further details about the whole capability of the Coherent laser system can be found in [162, 163], the operation principles of the attached commercial visible OPA is given in [77], and finally the generation, characterization and compression of an ultrashort white-light broadband continuum is reported in [162, 163]. In 2018, a set of photoemission experiment on the BL SiO_2/Ru(0001) compound is carried with the newly installed Light Conversion laser source. This is presented in Subsection 3.4.2.

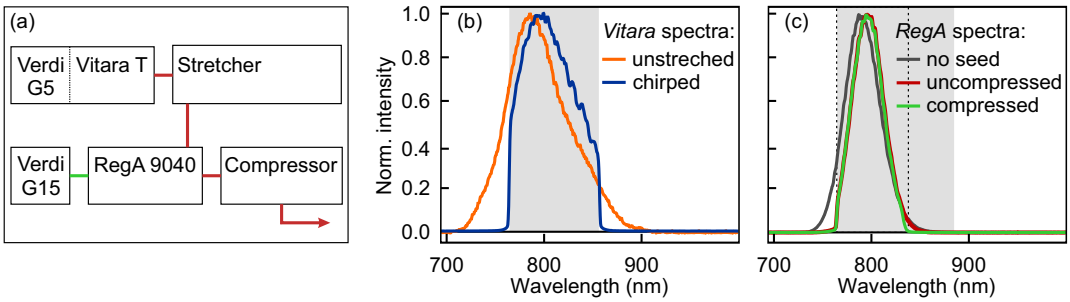

FIGURE 3.13: (a) The Coherent laser system and the optical setup. (b) Oscillator laser spectra before (orange) and after (blue) traveling through the grating stretcher. (c) *RegA* laser spectra: not amplified (gray), amplified (red), amplified and temporally compressed (green).

As general remarks, subpicosecond time resolution and high statistics are demanded in an ultrafast spectroscopy experiment (cf. Section 3.1). Those requisites are achieved by both employed laser systems which can provide short laser pulses ($<$ 40 fs) and high photon flux. Time-resolved photoemission and optical spectroscopies also benefit from the use of laser systems with a high pulse repetition rate, allowing for a higher event probability. Both systems can operate in the range of repetition rate between tens and hundreds kHz. The repetition rate is then optimized for the investigated material in order to avoid build-up of excitation due to long-lived states that to not relax within the time separation between two consecutive pulses. Moreover, the pulse wavelength tunability is desired in order to selectively excite and probe specific transition in the studied system. This is accounted for by the frequency mixing processes mentioned above and detailed later for each laser systems. Further specific requirements for a photoemission experiment, which both laser systems provide, are (1) a high pulse energy to increase the transition probability, (2) sufficiently high photon energy to overcome the work function of the material, which in case e.g. of, metals, is around 4-5 eV, (3) a narrow pulse bandwidth to achieve selective electronic transitions and a better energy resolution of the acquired spectra.

3.4.1 The Coherent laser system

A schematic of the Coherent laser system components and the relative laser spectra is shown in Fig. 3.13. As depicted in (a), the laser system consists of a Coherent *Vitara-T* oscillator and a Coherent *RegA 9040* regenerative amplifier. In both optical cavities, the gain medium is a Sapphire crystal doped with Titatium (Ti:Sa). Its absorption spectrum ranges between 400 and 600 nm, there both *Vitara-T* and Coherent *RegA 9040* are pumped by 532 nm (CW) semiconductor laser heads with powers of 5 W (*Verdi G5*) and 12 W (*Verdi G12*), respectively. The bandwidth of the Ti:Sa emission spectrum ranges from 680 to 1100 nm, with maximum at 790 nm. Such broad spectrum makes the Ti:Sa gain medium suited to the generation and the amplification of near-infrared ultrashort-pulses, as predicted by the 'time-bandwidth product' relation [164].

Passive Kerr-lens modelocking, based on the field strength-dependence of the refractive index of the gain medium [165], allows for the generation of approximately 580 mW-broadband pulses in the oscillator at a repetition rate of 80 MHz. The relevant spectrum is shown in Fig. 3.13 (b) by the orange trace: it is centered at the wavelength of 800 nm (i.e. 1.55 eV photon energy), but can be tuned between 790 nm

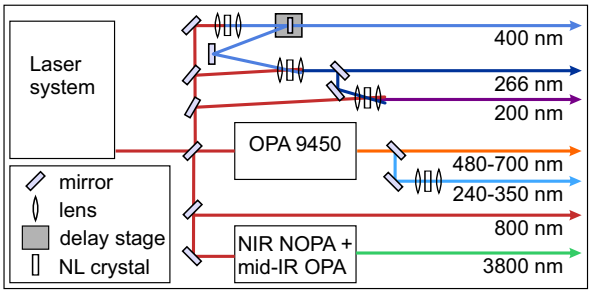

FIGURE 3.14: The optical setup connected to the Coherent *RegA 9040* laser system.

and 820 nm. Its bandwidth of 125 nm (i.e. 58 THz) results in extremely short pulses (<20 fs) after the beam has traveled through an internal prism compressor (the working principle of the compressor can be found in [166]). However, the output pulse energy of ∼7.3 nJ is not sufficient for driving nonlinear optical processes. In fact, those pulses serve as 'seed' for the regenerative amplifier where they are amplified and reach an output field strength on the order of 1 MW cm^{-2} for a 100 μm-radius focused beam. Then, to avoid crystal damages due to the high peak intensity of the focused beam, the 'seed' pulses are temporally spread ('chirped') in a broadband grating stretcher before entering the amplifier cavity. This cause a partial bandwidth loss due to the finite size of the grating media, as visible on the right-hand side of the blue spectrum of Fig. 3.13 (b) and highlighted by the gray-shaded area.

The coupling of the seed pulses into the *RegA* amplifier cavity is controlled by a Tellerium Dioxide (TeO_2) acousto-optic modulator named 'cavity damper'. Once one pulse is injected, it propagates back and forth through the cavity for an adjustable number of round trips until the amplification process reaches a saturation. At this point, the pulse is ejected while containing the most of the energy stored in the Ti:Sa crystal. The cavity damper works in combination with a second opto-acoustic element present in the cavity, called Q-switch. The Q-switch is in charge of preventing (allowing) lasing during the injection (ejection) of a seed pulse. In this way, the Ti:Sa crystal is efficiently prepared for the amplification of the next injected pulse. The pulse injection/ejection frequency determines the pulse repetition rate, which in case of the *RegA* amplifier can be tuned from 40 to 300 kHz. Finally, the RegA output is sent to a grating compressor where amplified laser pulses of up to 6.7 μJ per pulse (at a repetition rate of 300 kHz) at a central wavelength of 800 nm and a with pulse duration of 40 fs are finally obtained. A summary of the RegA spectra prior (gray) and after (red) amplification is reported in Fig. 3.13 (c). It can be noted that the spectrum of the amplified output reflects the bandwidth 'cut' of the seed pulses. An additional bandwidth reduction results after the beam propagation through the grating compressor (green), as marked by the vertical dashed lines.

The optical setup connected to the Coherent laser system is schematized in Fig. 3.14. The compressed *RegA* beam can be split in various way by a set of beam splitters and then steered towards different nonlinear optical setups. From top to bottom, the second, third and forth harmonics of the fundamental output are generated in β-barium borate (BBO) non-linear crystals. Particularly, the third and the forth harmonic generations have been designed in a non-collinear sum-frequency mixing geometry to facilitate separating the frequency-mixed output from the two incoming beams [162]. To extend the photon energy range to the full visible spectrum, 50% of the *RegA* output can be sent to a commercial *Coherent 9450* OPA capable of generating signal

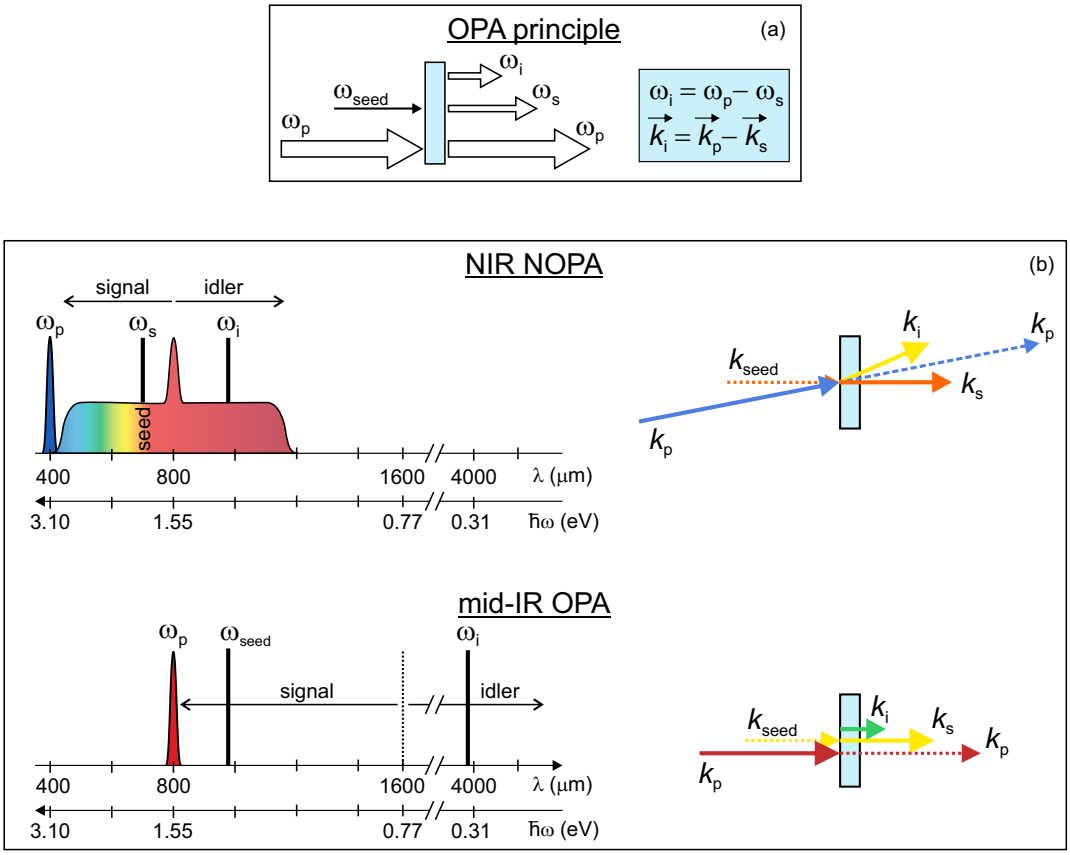

FIGURE 3.15: (a) Principle of the optical parametric amplification. The arrow length is scaled with the photon energy of each pulse satisfying the energy conservation law and the thickness indicates qualitatively the relative intensity between pump, seed, signal and idler beams. (b) Schemes of the wavelength region and the wavevector geometry of the near-infrared noncollinear (top) and mid-infrared collinear (bottom) stages used in this thesis work.

pulses from 480 to 700 nm. The OPA output frequency can be further up-converted by means of an external BBO nonlinear crystal optimized for second harmonic (SH) generation. Furthermore, part of the *RegA* fundamental can be used without further frequency conversion and 10% of it can be employed to generate a white-light continuum (not shown in Fig. 3.13) used for time-resolved broadband optical spectroscopy [167] and time-resolved broadband electronic sum-frequency-generation spectroscopy [168]. Finally, 50% of the *RegA* output can be split off and sent to the two-stage OPA operating in the NIR to mid-IR regime. As the latter frequency-mixing component is set up within the framework of this thesis, it will be presented in details in the following subsection.

Generation and characterization of mid-IR pulses

The transient reflectivity measurements performed on Ta_2NiSe_5 required the probe beam wavelength to be tuned to resonance with the electronic band gap which is approximately 0.3 eV in the low-temperature phase of this material. Accordingly, the photon energy spectrum was extended to the mid-IR range by means of a tunable two-stage OPA, with an optical scheme adapted from [59]. In the following, the principle of the optical parametric amplification and its application to the two-stage OPA are

described . Then, the set up of the two-stage OPA and the characterization of its output pulses are presented.

As depicted in Fig. 3.15 (a), in a parametric amplification process an intense 'pump' beam with photon frequency ω_p interacts in a nonlinear crystal with a weak beam with photon energy ω_{seed} (lower than ω_p). As results, the 'seed' is amplified into an intense 'signal' beam with frequency $\omega_s = \omega_{\text{seed}}$ and a third 'idler' beam with frequency ω_i is produced to ensure the conservation of photon energy and momentum.

Fig. 3.15 (b) shows how the OPA principle is applied to each stage of the set up used in this thesis. On the left-hand side, the wavelength region of each amplification step is displayed, while on the right-hand side the relevant wavevector geometry is schematically represented. In the near-infrared non-collinear optical parametric amplifier (NIR NOPA, top), the second harmonic of the Ti:Sa laser output (ω_p, blue) pumps the nonlinear crystal which is seeded by the white-light side of a broadband continuum in order to provide a large wavelength tunability. The phase matching condition determines which seed wavelength (k_s, orange arrow) is amplified and thus the frequency of the NIR idler photons (k_i, yellow arrow). Those NIR photons are then used to seed a collinear mid-IR OPA (bottom) pumped by the fundamental (ω_p, red) of the Ti:Sa laser system. As a results, mid-IR pulses (k_i, green arrow) are obtained as 'idler' in the amplification process.

The geometry of the setup is depicted in Fig. 3.16 (a): it is rather compact and consists of two parallel arms that guide the propagation of the pump beams (bottom arm) and the amplification processes (top arm), respectively. Half of the *RegA* amplifier output intensity at 800 nm (1.55 eV), corresponding to 4 μJ pulse energy[9], is steered towards the 'pump' arm and 10% of it is split off by a beam splitter (BS) and back-folded into the second arm. The transmitted part is focused on a 0.4 μm-thick BBO nonlinear crystal to generate SH pulses at 400 nm (3.1 eV) with a conversion efficiency of approximately 30%. Due to the narrow acceptance bandwidth of the BBO crystal and the broad pulse bandwidth (35 nm) of the fundamental beam, the use of thin crystal is necessary to convert the full spectrum and thereby maximize the conversion efficiency. A 0°-high reflective 400 nm / high transmissive 800 nm dielectric mirror (DM1) separates the SH from the fundamental beam. This DM1 is mounted on a delay stage to adjust for the temporal overlap between the 400 nm pump beam and the white-light continuum seed in the NOPA. The SH pump beam is focused by a spherical mirror (SM1, f = 150 mm) into the BBO crystal. The 800 nm transmitted beam travels through a $\lambda/2$-waveplate (WP) which rotates the beam polarization by 90° to account for the phase-matching condition in the collinear OPA. Finally, a spherical mirror (SM2, f = 350 mm) focuses the 800 nm pump beam into the mid-IR collinear amplifier.

In order to generate the broadband white-light continuum, the 10%-split off 800 nm beam is focused (f = 50 mm) into a 4 mm-thick Yttrium aluminum garnet (YAG) non-linear crystal. The bandwidth and the intensity of the white-light spectrum are optimized by adjusting a variable neutral density (ND) filter and an aperture (A) placed in front of the focusing lens. A YAG crystal is chosen in order to extend the continuum spectrum further to the IR range, as these photons serve as seed for the NIR non-collinear amplification which is obtained in a 2 mm-thick BBO crystal (Typ I, 30° cut). The non-collinear phase matching condition allows for broadband and efficient frequency conversion. In this work, the NOPA is tuned to provide idler pulses at the wavelength of 990 nm (1.25 eV) and with a power of approximately

[9]This pulse energy corresponds to 160 mW at 40 kHz, the repetition rate being chosen to account for the complete signal recovery between two consecutive pulses in the experiments on Ta_2NiSe_5.

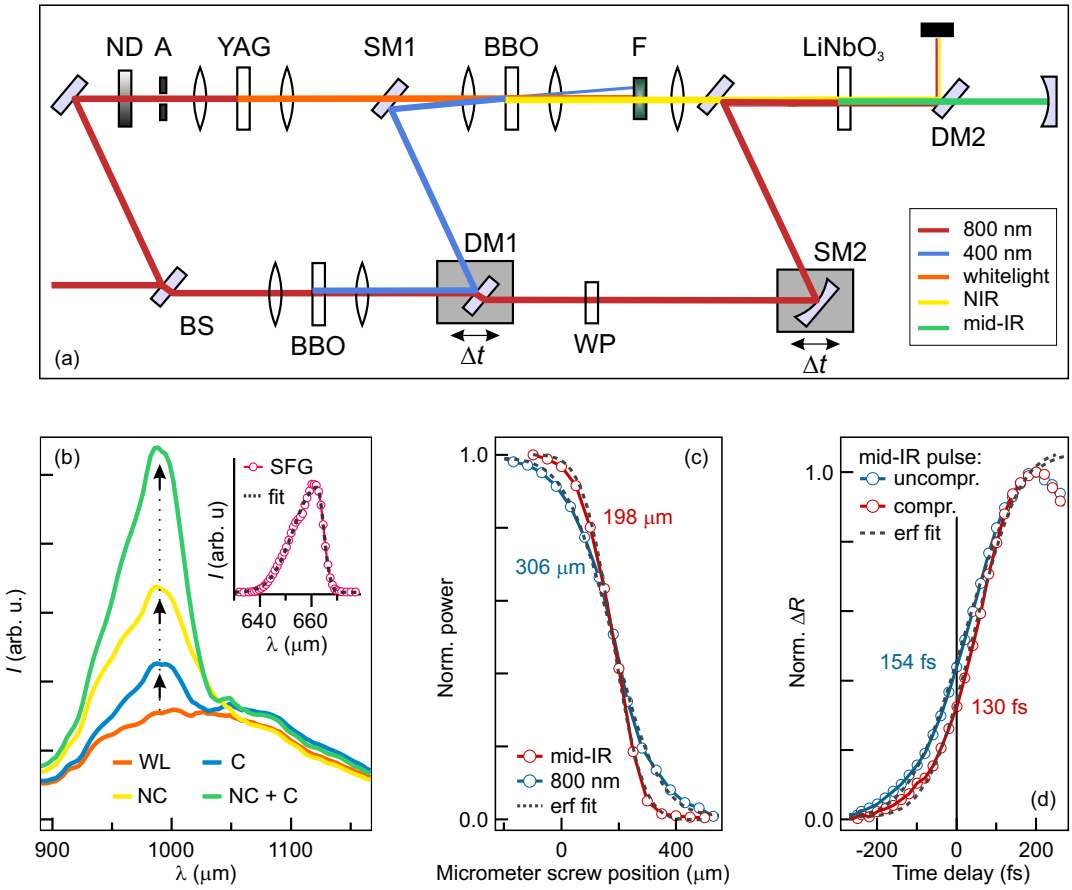

FIGURE 3.16: (a) Schematic of the two-stage optical parametric amplifier built in this thesis work. (b) Spectra acquired after the last dichroic mirror (DM2): the white-light continuum (orange), the two separate non-collinear (NC, yellow) and collinear (C, blue) amplifications at 990 nm (after blocking the 800 nm or the 400 nm beam, respectively), and the total NIR amplification (green). (c) Measurement of the mid-IR (red) and 800 nm (blue) beam spot radii. (d) Comparison between uncompressed (blue) and compressed (red) mid-IR pulses.

3.5 mW. After amplification, the continuum seed and the SH pump are filtered out both geometrically, thanks to the non collinearity of the amplification process, and optically by means of a selective filter (F). The NIR idler and the 800 nm pump beams are then focused collinearly behind a 1 mm $LiNbO_3$ nonlinear crystal (Type I, 47° cut). This collinear configuration has the main advantage of increasing the interaction length between the two beams inside the crystal: the slight self-focusing caused by the intensity dependence of the refractive index counteracts the natural beam divergence. In this way, the beam profiles remain constant during the propagation through the crystal [169]. Additionally, this geometry minimizes the spatial chirp of the mid-IR idler pulse. In the end, approximately 1 mW of mid-IR photons is generated. The mid-IR beam is then separated from the 800 nm pump by means of a Calcium fluoride (CaF_2) dichroic mirror (DM2), collimated by a spherical mirror (SM, $f = 750$ mm) and finally steered towards the sample position [10]. The pump-probe measurement are performed inside a cryostat equipped by a CaF_2 window that ensures higher a transmission (T) in the mid-IR range, on the order of 95%, than Sapphire (T ≈ 85%)

[10]The mirror alignment after the mid-IR beam collimation is done with a CW HeNe laser beam steered along the mid-IR beam path.

or Quartz (T $\approx$ 40%) windows [170]. Eventually, the mid-IR $\Delta R(t)$ intensity is detected by a Mercury Cadmium Telluride (MCT) amplified photodetector and sent to the lock-in amplifier.

Fig. 3.16 (b) reports the spectra of each amplification step involved in the two-stage NOPA. The spectral component at 990 nm (1.25 eV) of the continuum seed (orange) is amplified in both non-linear crystals, as shown by the respective spectra (yellow and blue), and the combination of those results in an intensity increase of the NIR pulses by a factor of approximately 3 (green). Consequently, emission of mid-IR idler photons in the second amplification is expected at the photon energy corresponding to the difference between the pump (1.55 eV) and the seed (1.25 eV) photons. Because the output wavelength lies outside the detection range of the available NIRQuest spectrometer, its measurement is retrieved by frequency up-conversion of the mid-IR spectrum by means of 800 nm gate pulses inside a BBO crystal. The resulting sum-frequency-generation spectrum is reported in the inset of Fig. 3.16 (b) and shows a peak intensity at 662 nm (1.87 eV). Consequently, the mid-IR photons have to have wavelength of 3.8 μm (0.33 eV), consistent with the expected value within the bandwidth of the pulses entering the mid-IR NOPA.

The measurement of the mid-IR beam spot size is performed with the optical 'knife-edge' technique: the beam power is recorded while a knife is translated through the beam 'waist' using a micrometer translational stage. With the beam propagating along the z-direction and the knife edge being translated along the x-direction, the power meter measures the integral of the Gaussian beam intensity between, ideally, -∞ and the position X of the knife for each stage step, i.e.

$$P(X) = P_{\mathrm{TOT}} - \sqrt{\frac{\pi}{2}} I_0 w_y \int_{-\infty}^{X} \mathrm{e}^{-2(x-x_0)^2/w_x^2}\, \mathrm{d}x, \tag{3.14}$$

where P_{TOT} is the total beam power, I_0 is the peak intensity, x_0 the knife edge position at the peak intensity along the x-direction and $w_{x,y}$ the width of the Gaussian intensity distribution along the x and y axis, respectively. Fig. 3.16(c) shows the data normalized to the maximum (red markers). Using the integral definition of the error function, P(X) can be modeled by the following expression:

$$P(x) = A/2 * (1 + \mathrm{erf}[2\sqrt{\ln(2)}(x - x_0)/\mathrm{FWHM}]) + y_0, \tag{3.15}$$

where A is related the total beam power and y_0 is an offset-parameter that accounts for the experimental zero-background of the power meter. Clearly, this function fits well to the data (black dashed line in Fig. 3.16 (c)) and provides an estimation of the beam spot size, defined here as the full width at half maximum (FWHM) of the Gaussian intensity distribution [11]. Importantly, this procedure allows to adjust the spot size of the pump beam (blue markers in Fig. 3.16 (c)) during the pump-probe experiment in order to achieve a homogeneous excitation density over the probed sample region.

The pulse duration of the mid-IR pulses is estimated directly on the correlated signal $\Delta R(t)$ around time zero, as measured on Ta_2NiSe_5 via pump-probe measurements. Indeed, under the assumption of instantaneous (or equivalently, of time-resolution-limited) response of the material at the wavelength of the pump and the probe pulses, the slope of the initial intensity rise is defined by to the cross-correlation of the two

[11] Here a circular beam spot is assumed. A more precise measurement would require to repeat the same procedure while translating the knife along the y-axis.

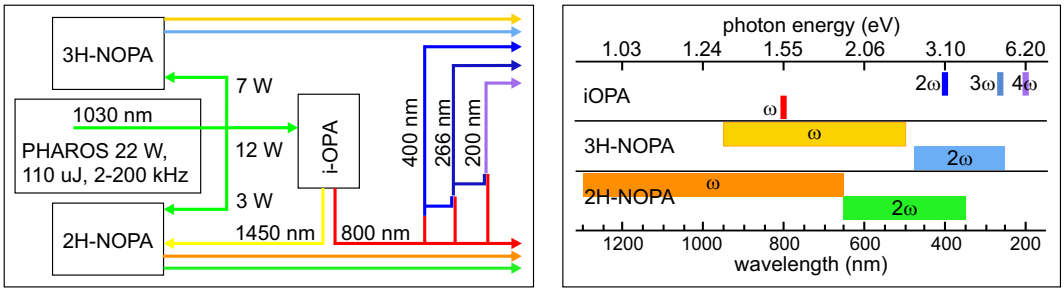

FIGURE 3.17: (a) The optical setup based on the Light Conversion laser source. (b) Wavelength range for each OPA.

pulses and can be modeled by:

$$\Delta R(t) = A/2 * (1 + erf[2\sqrt{ln(2)}(x)/FWHM]), \tag{3.16}$$

where $A/2$ accounts for the initial signal amplitude and FWHM is the Gaussian pulse width. Being the pulse duration of the pump pulse at 800 nm equal to 40 fs[12], the temporal duration of the mid-IR probe pulse is given by:

$$FWHM_{mid-IR} = \sqrt{FWHM^2_{cross-corr} - FWHM^2_{800\ nm}}. \tag{3.17}$$

Fig. 3.16 (d) shows the initial $\Delta R(t)$ of Ta_2NiSe_5 for both uncompressed (blue) and compressed (red) probe pulses. To compress the mid-IR pulses, optical media with group velocity dispersion (GVD) of opposite signs are used [171]. In particular, the positive dispersion introduced by the CaF_2 entrance window of the cryostat is efficiently compensated by a 5 mm-thick Si wafer which is inserted into the mid-IR beam path. Consistently, a steeper slope of $\Delta R(t)$ around time zero is obtained in this case, and a FWHM of 130 fs is calculated by (3.17) for the mid-IR pulse. This value is verified also on a reference VO_2 sample which is known to have instantaneous response at the wavelengths of interest.

3.4.2 The Light Conversion laser system

The photoemission measurements performed in March 2018 on the BL SiO_2/Ru(0001) sample are performed with the newly installed Light Conversion laser source which is briefly described here. The system consists of a compact laser head (*Pharos*) connected to an internal OPA (iOPA) and two software-controlled NOPAs. In this way, the wavelength tunability of the laser output spans continuously from near-infrared to UV light, making this laser system particularly suitable for two-photon photoemission experiments. For a brief overview, the scheme of the laser system modules is sketched in Fig. 3.17 (a), while in (b) the wavelength region of each OPA is reported.

The *Pharos* laser head includes the oscillator, the stretcher, the chirped pulse amplifier, and the compressor. The gain media are ytterbium dopes potassium gadolinium tungstate (Yu:KGW) crystals, thus the *Pharos* output is centered at 1030 nm (1.20 eV). After amplification and pulse compression, the 22 W, 35 fs, 110 μJ/pulse

[12]This value has been obtained by an autocorrelation measurement based on frequency-resolved optical grating (FROG) technique and performed inside the commercial Swamp Optics Grenouille autocorrelator device in combination with its Femtosoft Technologies QuickFrog software package.

fundamental output is divided into three beams. From top to bottom, the first beam (7 W) is used in one of the NOPAs (3H-NOPA) both as pump after up-conversion to its third harmonic, and to generate the continuum seed. The second (12 W) is steered into the iOPA, and the third one (3 W) is frequency-doubled inside the other NOPA (2H-OPA) and it is used as pump beam.

The iOPA is aligned to produce a 0.9 W signal centered at 800 nm (1.55 eV). This output allows for efficient the generation of the second, third and forth harmonics in external BBO nonlinear crystals. A collinear geometry is used for all these frequency mixing processes in order to increase the overlap volume inside the crystal between the two incoming beams. The residual fundamental beams are then geometrically separated from the frequency-mixed output during the propagation through the first prism of the pulse compressor. The idler of the iOPA at 1450 nm (0.85 eV) is send to the 2H-NOPA for the continuum seed generation.

All the signal of the three OPAs are compressed and the optimal pulse duration is approximately 35 fs (measured at 800 nm). In order to widen the wavelength range, both NOPAs can operate to produce the second harmonic of the signal. This output is compressed externally with fused-silica-prism compressors. Finally, the laser system ordinarily operates at 200 kHz. Though, its repetition rate can be tuned down to 2 kHz by means of an electro-optical pulse picker which conserve the pulse energy.

3.5 The ultrahigh vacuum system and the electron analyzer

As presented in Section 3.2, photoemission spectroscopy is a surface-sensitive technique. Therefore, control on the sample surface conditions is demanded and can be achieve in a ultrahigh vacuum (UHV) environment. In addition, UHV conditions minimize the probability of scattering of photoemitted electrons during their travel towards the analyzer, a process that would alter the information on the energy and momentum of the photoelectrons.

The UHV equipment - The employed UHV system is schematically depicted in Fig. 3.18 (a) and detailed descriptions can be found in [77, 162]. It consists of two main parts, the preparation and the spectrometer chambers, which are connected by a manual gate valve. A sample transfer line is kept in UHV and interfaces with the preparation chamber via a second manual gate valve. Inside the chamber, the sample is hold by a manipulator kept inside a cryostat, and can be transferred in between the two chambers without breaking the vacuum. The spectrometer chamber is equipped with two apertures: a MgF_2 window through which the laser beams enter the chamber and impinge onto the sample, and a flange where the hemispherical analyzer (*PHOIBOS 100*, Specs GmbH) is attached.

To reach the required UHV conditions, the preparation chamber is pumped by a turbo molecular pump (*HiPace 700*, Pfeiffer Vacuum AG) connected to a back pumping system consisting of a small turbo molecular pump and a membrane pump. In this way, a base pressure in the low 10^{-10} mbar range is achieved. The spectrometer chamber is pumped by the same turbo molecular pump sitting in the preparation chamber, while the gate valve in between the two volumes is open. Additionally, an ion pump operates in the spectrometer chamber in order to improve its base pressure down to approximately 5×10^{-11} mbar, and maintain this volume pumped while the gate valve is closed.

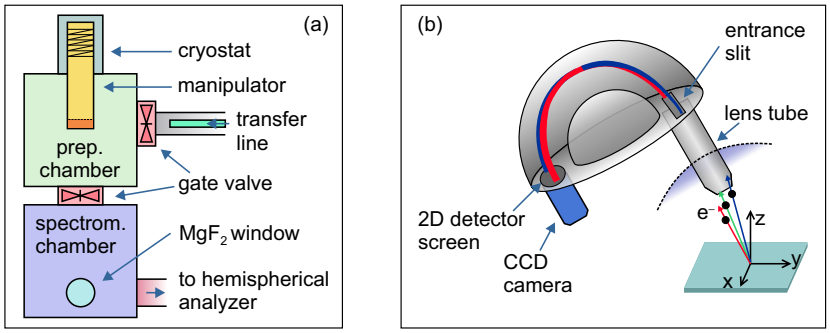

FIGURE 3.18: (a) Scheme of the UHV system. (b) Main components of an hemispherical analyzer.

The sample manipulator consists of two segments: a motorized element (yellow) with four degrees of freedom (three translational directions and the azimuthal angle around the vertical axis) and a removable part (orange) hosting the sample holder. This detachable part holds the sample and is supplied by a thermocouple measuring the temperature directly on the crystal. Furthermore, it provides the electrical contacts necessary for the sample heating or, alternatively, the application of a bias voltage during the acquisition of the photoemission spectra. The manipulator is attached to the cryostat operating with either liquid nitrogen, capable of cooling the sample down up to 90 K, or with liquid helium, in order to reach a minimum sample temperature of 40 K.

The preparation chamber is implemented with several tools for *in situ*-preparation and characterization of the sample surface:

- An electron gun electrically contacted with the sample allows for the cleaning of the surface via sputtering with accelerated argon (Ar^+) ions. The Ar^+ ion beam is produced by impact of Ar_2 with the electrons thermoemitted from the filament of the gun under precise control of the ion kinetic energy, the Ar_2 background pressure and the sample temperature.

- Annealing of the sample, potentially also in controlled pressure background, e.g. of oxygen gas, helps impurity desorption and can be used to induce a surface reorganization. A wide temperature range from room temperature up to 1600 K is covered thanks to the use of three different heating systems:

  1. With an internal cryostat heater, temperatures up to 450 K can be achieved. The highest temperature is set by damage threshold of the diode sensor, which is installed inside the fixed part of the manipulator. The main advantage of this current-free heating method is the compatibility with photoemission measurements, for which the application of an electrical bias voltage to the sample is required (see Section 3.2);
  2. During the surface preparation, resistive heating can be employed. In this case, the current flows through two tantalum (Ta) wires holding the sample. Thanks to the high resistivity of Ta, temperatures up to approximately 1000 K can be reached.;
  3. Hard materials as, e.g. ruthenium (Ru) need to be annealed at much higher temperatures during their surface cleaning. Electron bombardment heating can heat the sample up to 1550 K, the limitation being the melting point

of the NiCr/Ni thermocouple (type K). This technique is based on the thermoemission of electrons from a tungsten filament and the acceleration of the electron beam towards the non-polished crystal surface by means of a positive high voltage that is applied directly to the filament, while the sample is electrically grounded. A crucial technical issue is to keep the thermocouple wires, which are spot welded onto the Ru sample edge, further away from the heating source with respect to the distance of the grounded sample. This prevents arc-overs between the filament and the thermocouple with consequent breakage of the wires.

- Exfoliation of the samples is obtained via cleaving with a stainless steel screw driver. This methos is used on the layered Ta_2NiSe_5 crystals.

- Molecular films can be deposited on the prepared substrate under controlled temperature and pressure either via molecular gas dosing through a valve (both a leak valve and a pinhol doser are available) or by means of evaporation of solid molecules in a Knudsen cell [147, 77].

- A quadrupole mass spectrometer is used to perform thermal desorption spectroscopy. This technique is used to quantify the film coverage after deposition as well as to characterize the morphological phase of the molecular film. The quadrupole mass spectrometer is also employed to conduct rest gas analysis in order to investigate the chemical composition of the chamber environment and check for the presence of contaminants in the dosed gas.

- A commercial low-energy electron diffraction (LEED) spectrometer (*ErLEED 1000-A*, SPECS GmbH) is used to characterized the structural symmetry of the prepared surface. This can give indirect information on the presence of impurities or the occurrence of surface reconstruction.

The hemispherical electron analyzer - The calibration and operating principles of the spectrometer are extensively described in [172, 162]. Fig. 3.18 (b) shows its main components: the lens tube collects the photoemitted electrons within an emission angle range that is defined by the angle of the sample with respect to the entrance of the tube[13] and the width of the entrance slit; the hemispherical capacitor deflects the trajectories of the collected electrons along the direction perpendicular to the entrance slit according to their initial kinetic energy. Once deflected towards the exit slit, electrons are multiplied by a micro-channel plate detector before impinging onto a two-dimensional phosphor screen. Finally, a CCD camera is placed behind the screen and records the spatial distribution of the photoelectrons with respect to their spread in the emission angle and the kinetic energy.

With the settings applied in this set up, the nominal analyzer energy resolution $\sigma_{analyzer}$ is on the order of 50 meV. However, the actual experimental energy resolution is always evaluated from the width of the low-energy spectrum cutoff. Indeed, this edge is not affected by the spectral content, while it accounts for any detrimental contribution to the spectral broadening like, e.g. inhomogeneities of surface work function, σ_{inhomo}, and the finite bandwidth of the photon pulses σ_{XC}. The latter is on the order of few tens of meV for the photon energies used in this work

[13]The dashed line delimits the portion of lens tube which enters the chamber. During the spectra acquisition, the sample is placed at a working distance of 4 mm from the tip of the lens tube entrance. This distance allows to collect most of the photoelectrons, as they escape from the sample with relatively low kinetic energy due to the limited photon energy employed in a 2PPE experiment.

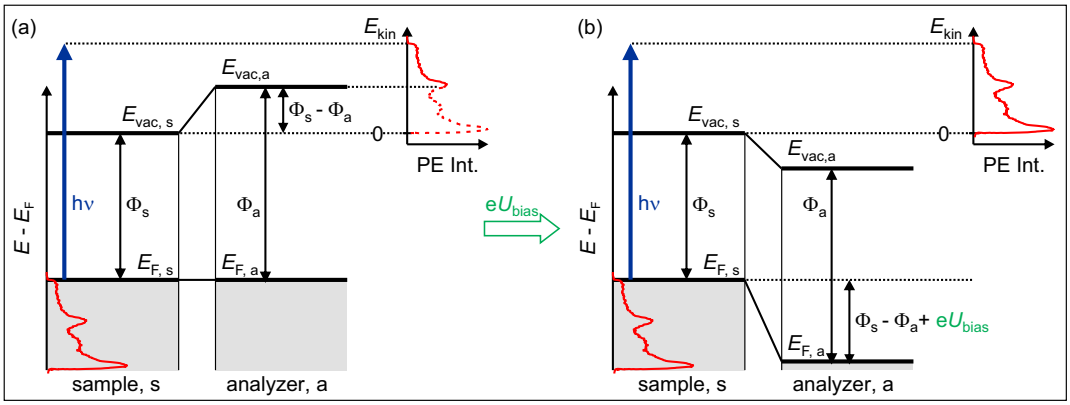

FIGURE 3.19: (a) Energy potential diagram of a photoemission measurement.

and it is directly known by measuring the laser spectrum with a fiber spectrometer. Then, the low energy spectrum cutoff is modeled by a step-like function, accounting for the ideal low-energy cutoff, convolved with a Gaussian function of width $\sigma_{cutoff} = \sqrt{\sigma^2_{analyzer} + \sigma^2_{inhomo} + \sigma^2_{XC}}$. This parameter gives the experimental upper limit for the energy resolution of a static photoemission spectrum.

Scheme of a photoemission experiment - During a photoemission experiment, the sample and the analyzer are in electrical contact, thus their Fermi levels align. This is shown by the energy diagram depicted in Fig. 3.19 (a). Because the work function of the sample and of the analyzer are generally not the same, their vacuum levels result shifted against each other by the difference between the two work functions, $\Phi_s - \Phi_a$. As visible in (a), if the analyzer work function exceeds that of the sample and rather the low-photon energies are employed, the impact on the recorded photoemission spectrum is remarkable: only a fraction of photoelectrons is emitted from the sample surface with sufficient kinetic energies to overcome the work function difference between the sample and the analyzer (solid red part of th espectrum). Consequently, part of the photoemission spectrum (dashed red) is not detected by the latter. To pass this barrier, a negative bias voltage eU_{bias} is applied to the sample. As displayed in (b), the voltage value is chosen such that the vacuum level of the analyzer shifts below that of the sample and all the photoemitted electrons are accelerated towards the detector and collected on the screen.

3.6 Sample preparation for photoemission spectroscopy

This section describes the procedures for the preparation and characterization of the investigated systems performed prior to the photoemission experiments.

3.6.1 The preparation of ultrathin SiO_2 film on Ru(0001) substrate

The study of ultrathin SiO_2 films grown on the Ru(0001) surface is developed in collaboration with T. Schmidt's group of the SMART I beam line at Bessy II, Adlershof. In particular, the film is grown in the UHV microscope chamber at Bessy II and measured by means of photoemission spectroscopy in the UHV chamber of the Electron Dynamiχ laboratory at the Fritz Haber Institute, Berlin (for the latter, see the description in the previous section).

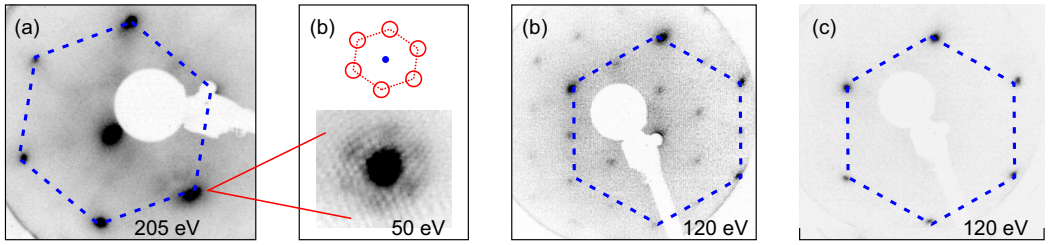

FIGURE 3.20: (a) LEED pattern of a contaminated Ru(0001) surface. (b) Moiré pattern of Cu ad-atoms on a Ru(0001) surface (c) (2×2)- 3O reconstruction on Ru(0001) (d) LEED of a clean Ru(0001) surface.

To transfer the sample under clean conditions, a portable UHV chamber equipped by a battery-driven ion getter pump is used. In this way, after a preliminary cleaning of the Ru substrate[14], the crystal is transferred at a background pressure of $\approx 10^{-7}$ mbar to the SMART I beam line station, where the silica film is grown and morphologically characterized in 10^{-10} mbar UHV ambient. Subsequently, the SiO_2/Ru(0001) sample is transferred out of the UHV microscope chamber and carried under vacuum condition back to the chamber equipped for the photoemission experiments.

The main contamination of a Ru single crystal is the intercalation of oxygen and carbon atoms [173]. Various cycles of sputtering and annealing are required to remove those contaminants from the first layers underneath the surface. The recipe for the cleaning of the Ru(0001) surface is adapted from previously developed procedures whose description can be found in [98, 146, 91]. In the present work, the metal surface is sputtered at room temperature for 30 minutes with Ar^+ ions accelerated by a potential difference of 1.5 keV (corresponding to an emission current of ≈ 5 μA). Then, 1×10^{-6} mbar of oxygen gas is leaked into the chamber and the sample is heated up to 1170 K for 5 minutes. At this temperature, carbon atoms diffuse from the bulk to the surface, oxidize with the surrounding oxygen to form CO molecules and desorb from the Ru sample. Afterwards, the oxygen valve is closed and the sample temperature is increased in UHV up to 1450 K for 5 minutes and finally above 1520 K for approximately one minute. These higher-temperature annealing steps allow for the cleaning of the surface from residual oxygen ad-atoms. With increasing the number of preparation cycles, the time duration of the last annealing step is gradually reduced down to few seconds while its temperature is increased up to 1540 K. In this way, the the oxygen ad-atoms can be efficiently removed before new contamination can diffuse from the bulk to the atomic layers of interests for the photoemission measurements. In all those steps, electron bombardment heating from the backside of the sample is applied. The values of the filament current, the high voltage and the emission current are approximately 2.7 A, +800 up to +1000 V[15], and 15 mA.

The preparation of the metal substrate is routinely monitored by comparing the LEED pattern to references taken from the literature [98, 146, 91]. Fig. 3.20 (a) shows the LEED pattern at kinetic energy of 250 eV and at room temperature after only few cleaning cycles: one identifies six bright spots at the vertex of a hexagon centered around the (0,0) elastic LEED spot, in agreement with the hexagonal symmetry of

[14]The experiment is repeated two times. The preparation of the Ru surface was carried out in the UHV preparation chamber of Dr. Kramer's group in August 2016 and in that of the Electron Dynamiχ group in March 2018.

[15]The maximum high voltage required to reach the highest temperature strongly depends on the filament-sample distance that is of $\approx$2 mm in this work.

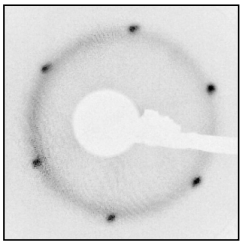

FIGURE 3.21: LEED of the amorphous silica film on Ru(0001) at 131 eV.

the Ru(0001) surface. The diffuse intensity distribution indicates that the surface is not optimally clean. Indeed, as displayed in Fig. 3.20 (b), the zoomed-in diffraction pattern at 50 eV reveals a hexagonal superstructure (also named Moiré pattern, [174]) around each first-order spot which likely indicates long-range carbon contamination occupying Ru vacancies. In contrast, Fig. 3.20 (d) reports the LEED pattern of a clean surface: the first-order Ru spots are much sharper than in (a) and no additional spots are present. Few hours after a complete surface preparation, the LEED pattern looks like that in Fig. 3.20 (c): weak diffraction spots indicate a (2×2) surface reconstruction. Similar pattern is also obtained if the annealing steps in UHV are skipped or the last one above 1540 K is too long. This indicates that the (2×2) reconstruction is connected to the presence of oxygen ad-atoms.

Further checks of the cleanliness of the Ru surface are performed via measurement of the sample work function and thermal desorption spectroscopy (TDS) of D_2O layers deposited on the Ru(0001) surface. In agreement with the literature [98, 146], a work function of 5.42 eV and a negligible TDS peak above 180 K (e.g. above the desorption temperature of the D_2O bilayer from the Ru(0001) substrate) are observed for the clean Ru(0001) surface. However, prior to the film growth in the PEEM chamber, a series of sputtering and annealing cycles are performed in-situ and the surface is fully characterized by low-energy electron probe both in diffraction and microscopy mode.

The SiO_2 film is prepared as described in [91]. The procedure follows directly an annealing process of the Ru(0001) surface and involves the following steps:

1. the preparation of the (2×2) - 3O surface reconstruction by leaking 1×10^{-6} mbar oxygen in the UHV chamber while the crystal cools down between 1170 K and 470 K. This reconstruction serves as guide pattern for the deposition of silicon;

2. the evaporation of silicon in 2×10^{-7} mbar of oxygen and its deposition on the metal surface at room temperature. The SiO_2 coverage is followed indirectly by monitoring the intensity change of the (0,0) spot during the film growth [91];

3. the surface oxidation by heating up the sample up to 1045 K in 5×10^{-6} mbar oxygen;

4. the sample cooling in oxygen background up to 470 K and in UHV down to room temperature. Depending on the cooling rate, either crystalline or amorphous film are obtained [42, 175]. In this work, vitreous silica films are studied, whose fingerprint in the LEED pattern is a diffuse ring superimposed on the first-order Ru diffraction spots [91], as shown in Fig. 3.21. Importantly, this preparation leaves a non-negligible concentration of oxygen atoms between the metal surface and the oxide film.

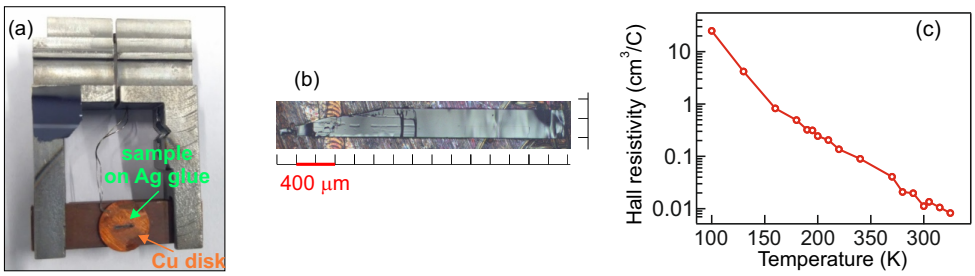

FIGURE 3.22: (a) The Ta_2NiSe_5 crystal on a Cu disk. (b) Microscope image of the cleaved surface. (c) Temperature dependent Hall resistivity [36].

5. the surface re-oxidization after the transfer of the system to the photoemission UHV chamber. This is achieved by means of one annealing cycle at 920 K and with 2×10^{-6} mbar of oxygen.

In this thesis, two silica films are studied. One has a SiO_2 coverage equivalent to 1.4 ML and a work function of 5.42 eV, as measured on the photoemission spectrum right after the re-oxidation of the surface. The second film is a complete bilayer with a work function of 6.20 eV. This significant increase of the work function with respect to the 1.4 ML system is most likely due to the presence of a high concentration of oxygen ad-atoms chemisorbed on the Ru(0001) surface underneath the silica film [41, 43]. Indeed, work function increases up to 6.26 eV are reported by previous studies for the case of a BL deposited on an oxygen-saturated Ru(0001) surface [95, 38]. In fact, preliminary measurements performed in the course of this thesis work on another SiO_2 bilayer reported an intermediate work function value of 5.80 eV, suggestive of a lower amount of O ad-atoms. However, this film unfortunately revealed rather unstable surface conditions during the photoemission experiments, thus the relative tr-2PPE data are not discussed in this thesis work. Significantly, these observations further highlights the high sensitivity of the film to its chemical environment.

3.6.2 The preparation of the Ta_2NiSe_5 crystal

Ta_2NiSe_5 single crystals grow with a typical size of $0.04 \times 1 \times 10$ mm^3 by means of chemical vapor transport [117, 36]. The samples are provided by Prof. N. Katayama, Prof. M. Nohara and Prof. H. Takagi (Japan). In order to perform photoemission experiments, clean surfaces are obtained via mechanical cleaving in the direction perpendicular to the atomic planes. To achieve this, the sample is glued with a UHV-compatible, conducting silver epoxy glue (Epo-Tek E4110) onto a copper disk, as shown in Fig. 3.22 (a). The same glue is used to glue an aluminum post perpendicularly to the sample surface. The silver epoxy glue is cured at $T = 150$ K for approximately 30 min. The so-prepared sample is inserted into the sample holder and transferred to the preparation chamber where it is cleaved by pressing onto the Al post with a stainless steel screwdriver. The cleaving is done with the sample at 100 K and at $\approx 1 \times 10^{-9}$ mbar background pressure resulting in a surface with $\approx 0.4\ mm^2$-large smooth areas, as visible in the microscope image reported in Fig. 3.22 (b). Due to the very low thickness of the crystal, the same sample can be cleaved only once. Successful cleaving results in the photoemission spectra in electronic bands with well defined dispersion and a work function of 5.40 eV. Because of the rapid degradation of the surface even in UHV conditions, continuous measurements can be performed for approximately three days.

sample:	SiO_2/Ru(0001)	Ta_2NiSe_5		
experiment:	tr-2PPE	tr-ARPES	tr-2PPE	$\Delta R(t)$
$\Delta E_{\mathrm{static}}$:	50 meV	86 meV	30 meV	
$\Delta \tau_{\mathrm{UL}}$:	66 fs	110 fs	130 fs	130 fs

TABLE 3.1: Experimental parameters of this thesis work.

Concerning the doping level of the measured crystals, it is noted that the optical band gap of Ta_2NiSe_5 is approximately 0.3 eV at 110 K [118, 56]. In this thesis work, the static ARPES data at the same temperature shows that the upper VB lies at E - E_{F} = -0.11 eV, which is smaller than half the band gap value. This suggest a slight p-doping of the sample which is further verified on another sample of the same growth batch by means of Hall resistivity measurements performed by Prof. Katayama and co-workers. The result is shown in Fig. 3.22 (c): the Hall resistivity coefficient is positive on the whole temperature range, thus confirming that the sample is hole-doped.

3.6.3 Experimental parameters of this thesis work

In Table 3.1, a summary of the experimental parameters is given here as brief reference for the reader. In the photoemission experiments, the energy position of E_{F} is always determined on the Au sample holder, which is in electrical contact with the sample. The energy resolution, $\Delta E_{\mathrm{static}}$, of the static spectra is evaluated from the low-energy secondary electron cut-off of the Au spectrum. However, in the time-resolved photoemission data, relative spectral shift on the order of 15% of the energy resolution can be resolved due to the high statistics of the data. This is discussed in detail in Chapter 5 with regard to the observed transient shifts of the occupied electronic bands of Ta_2NiSe_5.

Concerning the temporal resolution $\Delta\tau$ of the photoemission experiments, the upper limit $\Delta\tau_{\mathrm{UL}}$ is conservatively estimated from the width of the cross-correlation intensity of a pulse duration-limited unoccupied electronic state. In the optical experiments on Ta_2NiSe_5, the time resolution is extracted from the time constant of the abrupt reflectivity variation at the excitation time both in-situ and on a reference VO_2 sample.

4 Unoccupied electronic states of ultrathin SiO_2 films on Ru(0001)

Ultrathin films of SiO_2 grown on a Ru(0001) substrate are attracting great attention due to the possibility to change their electronic properties, and specifically their interaction with the substrate, by varying the number of oxide layers and the amount of chemisorbed oxygen at the oxide/metal interface [41, 43, 38]. Previous studies show that a SiO_2 monolayer (ML) is chemically bound to the Ru(0001) surface, while a complete bilayer (BL) becomes quasi-free standing and its distance from the support increases. At intermediate coverages, terraces of strongly bound MLs and weakly-coupled BLs coexist on the Ru(0001) surface. X-ray photoelectron spectroscopy combined with DFT calculations show that for BL coverages, accumulation of oxygen on the metal surface underneath the film is favored and that the interface energy level alignment can be reversibly tuned by changing the amount of these oxygen adatoms [43, 38].

As outlined in Section 2.5, all these aspects should modify the electronic coupling at the oxide/metal interface and impact on the unoccupied electronic band structure of the oxide film which however, has not been investigated so far. In this regard, it is unknown whether the image potential of Ru may influence the energetics of the oxide (cf. Section 2.4). Clearly, in order to identify the effects of the environment on the electronic properties of the oxide system, the unoccupied electronic structure of the SiO_2 should be first understood. In particular, at these ultrathin coverages (i.e. less than 2 Å), quantum electron confinement may be already relevant for describing possible modifications of the electronic structure, e.g. with respect to the three-dimensional compound (cf. Section 2.3).

The present chapter presents the unoccupied electronic structure of ultrathin films of SiO_2/Ru(0001) with two different thickness, a 1.4 ML and a complete BL. These electronic structures are discussed with regard to the reduced dimensionality of the oxide films and the presence of the image potential extending in the region outside the metal surface. The impact of intercalated oxygen on the BL SiO_2/Ru(0001) electronic structure is also addressed. To achieve this information, time-resolved two-photon photoemission (tr-2PPE) spectroscopy is employed to gain access to both the energetics and the dynamics of the electronic states.

The unoccupied band structure of the 1.4 ML is found to exhibit two unoccupied states which have no correspondence with the bulk electronic band structure. Modeling of their energy separation supports the formation of quantum well states, likely originating from the quantum electron confinement perpendicularly to the film. However, the quantum well potential is not the rectangular one of a completely isolated film (cf. Subsection 2.3.1). In fact, a triangular well better accounts for the experimental results, supporting an influence of the spatially-varying image potential of Ru on the electronic structure of the oxide (cf. Subsection 2.3.2). In the BL film, those states do not appear as clear resonance on the spectra. Since in the experiment those states are populated by electrons excited from the Ru substrate, this observation suggests a weaker electronic coupling at the metal/oxide interface. A new

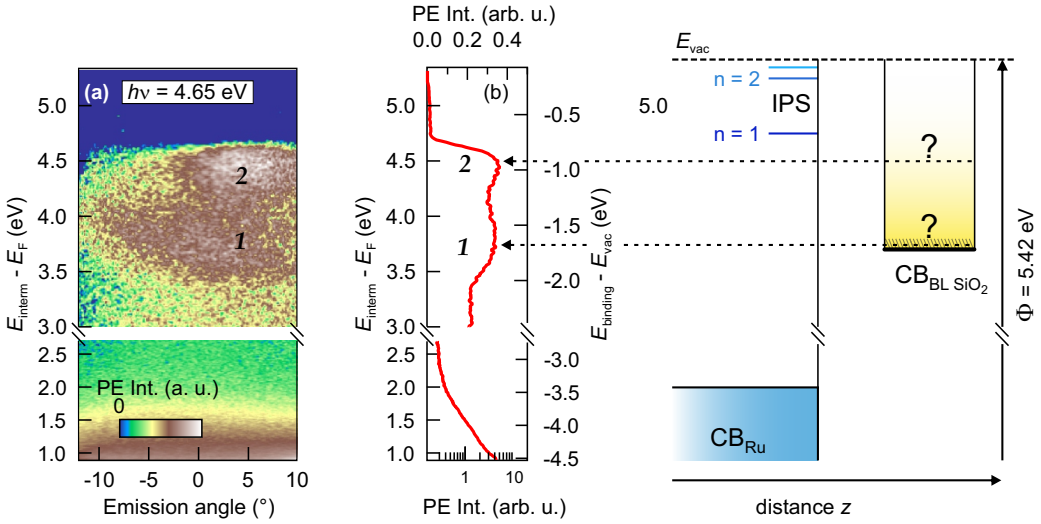

FIGURE 4.1: (a) Angle-resolved 2PPE spectrum of 1.4 ML SiO_2/Ru(0001) with 4.65 eV photon energy and (b) corresponding angle-integrated spectrum. On the right, the expected energy level diagram at zero-emission angle.

occupied electronic state is rather observed, likely signature of the intercalation of oxygen ad-atoms underneath the oxide film.

It should be noted that these results represent a preliminary study of the electronic properties of the system. Unresolved aspects and criticalities will be therefore also carefully addressed. At the same time, the presented tr-2PPE data is used to introduce the capabilities of the time-resolved photoemission spectroscopy in preparation for the second and main study of this thesis which concerns the electronic structure and dynamics of Ta_2NiSe_5, as presented in Chapter 5.

4.1 Electronic state quantization in 1.4 ML SiO_2/Ru(0001)

First, the unoccupied electronic states of 1.4 ML of SiO_2 grown on a Ru(0001) surface are characterized by single-color 2PPE spectroscopy with $h\nu = 4.65$ eV photon energy. In Fig. 4.1 (a), the photoemission (PE) spectrum is plotted as a function of intermediate state energy (left axis, cf. Fig. 3.5 in Section 3.2.1) with respect to the Fermi level, E_F, and emission angle (bottom axis) with respect to the direction normal to the film. At low energies, a broad spectral intensity extends up to approximately 2 eV. At higher energies, two electronic states, labeled by 1 and 2, are resolved in the spectrum. After integration over the shown interval of emission angles, the spectrum is plotted in Fig. 4.1 (b) as a function of both intermediate state energy (left) with respect to E_F and binding energy (right, cf. Fig. 3.5 in Section 3.2.1) with respect to the vacuum level, E_{vac}. It should be noted that different intensity scales (bottom and top) are used for better visibility in the low and high energy part of the spectrum, respectively.

Few qualitative observations on the three spectral features can already be made. To do this, the PE spectrum is compared with the in-scale energy level diagram at zero-emission angle, i.e. at the Γ point of the Brillouin zone, which is reported on the right-hand side. This diagram is based on the references from literature discussed in Section 2.5. The work function value, Φ, is that of the measured film (cf. Subsection 3.6.1). The diagram depicts the Ru conduction band (light-blu shade) extending

around Γ up to approximately 2 eV above E_F. At higher energies, a projected band gap opens up to E_{vac} in the bulk unoccupied electronic band structure of Ru. The position of the image potential states (IPSs) of the bare Ru(0001) surface is marked by blue lines. For instance, the $n = 1$ image potential state has a binding energy of -0.661 ± 0.020 eV with respect to E_{vac} [98]. The top of the electronic band gap of the 1.4 ML SiO_2 coverage is not available in literature. Here, the energy of the conductivity onset of a SiO_2 bilayer on Ru(0001) is tentatively assumed, whose maximum is measured by STM to be 3.8 eV above E_F (black solid line in the energy level diagram, cf. also Fig. 2.9 adopted from [41]).

It is observed that the low-energy 2PPE intensity extends in the energy region corresponding to the Ru conduction band, CB_{Ru}, at Γ, and the expected electronic band gap of the oxide film. The states 1 and 2 appear well within the projected band gap of Ru. Also, they peak at much larger binding energy with respect to E_{vac} than the IPSs of the clean Ru(0001) surface. Possibly, both states locate above the electronic band gap of the oxide film. In summary, these comparisons suggest (i) that the low-energy PE intensity originates from photoelectrons populating the Ru CB. (ii) The states 1 and 2 cannot be assigned to neither bulk Ru unoccupied electronic states nor IPSs of the bare metal surface. It is rather suggested that these two electronic states relate to the presence of the oxide film on top of the metal.

Concerning the nature of the states 1 and 2, two complementary pictures may be possible.

1. The states 1 and 2 could be unoccupied electronic states of the ultrathin oxide film. Notably, these states do not find any correspondence with the unoccupied electronic band structure of bulk (three-dimensional) SiO_2 which has a very large gap (∼ 9 eV [89]) at the relevant energies. Importantly, their energy may be affected by the image potential of Ru extending several Å outside the surface [39, 65].

2. These states could be IPSs of Ru, with energies modified by the presence of the dielectric film in the vicinity of the metal surface. Modification of IPSs by metallic [63], insulating [176] and organic [64] ad-layers have indeed been extensively reported in literature. More recently, modified IPS have been observed also on oxide thin films, namely NiO, grown on Ag(0001) [177].

To inspect these two cases, the unoccupied electronic band structure of 1.4 ML SiO_2/Ru(0001) is investigated by means of time- and angle-resolved 2PPE spectroscopy and a quantitative spectral analysis is performed.

The first tr-2PPE data is obtained by means of a pair of pulses with different color and with the pump-probe scheme displayed in Fig. 4.2 (d). Both beams are polarized in the plane of incidence ('p'-polarization), thus their electric field, $\vec{E}_p$, decomposes at the sample surface into an in-plane, $\vec{E}_{/\!/}$, and a perpendicular, $\vec{E}_\perp$, component. At positive time delays, $\Delta t > 0$, the pulse with 4.65 eV photon energy arrives first and acts as pump by exciting electrons into previously unoccupied electronic states above E_F. The pulse with 3.10 eV photon energy probes the transient electron population of these unoccupied electronic states by recording PE spectra at various time delays. At negative delays, the pulse ordering is reversed, i.e. the 4.65 eV pulse acts as probe emitting photoelectrons excited above E_F by the 3.1 eV pump pulse. A pump-probe cross-correlation of 70 fs is measured ex-situ on a pulse-duration-limited surface state of Cu(111) (not shown). It is pointed out that with the chosen pulse colors, the direct population of SiO_2 unoccupied states by electrons from the SiO_2 valence band is avoided as their energies are lower than the energy of the oxide band gap (6.5 eV [41]).

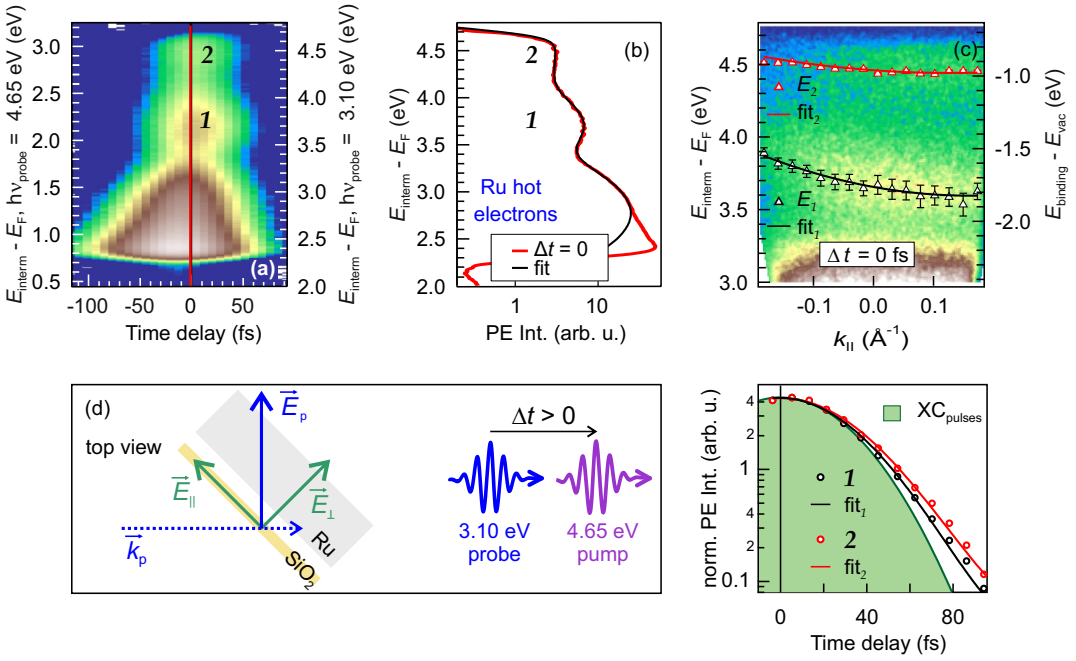

FIGURE 4.2: (a) Tr-2PPE spectrum of 1.4 ML SiO_2 on Ru(0001) with p-polarized 4.65 eV pump and 3.10 eV probe photons (at positive time delays). (b) Spectrum at zero time delay. The black line is the fit. (c) Momentum-resolved spectrum at zero time delay. Markers indicate the best fit position of the states 1 and 2 at various wave vectors. The solid lines are the nearly-free-electron models to the state dispersions. (d) Scheme of the experiment. (e) Tr- PE intensity (markers) of the states 1 and 2 and relative fits (curves). The green shaded peak is the Gaussian cross-correlation of the pump and probe pulses.

Thus, these unoccupied states can be populated only via charge injection from the Ru occupied states through the interface.

With this experimental scheme, the tr-2PPE spectrum displayed in Fig. 4.2 (a) is recorded. The PE intensity is plotted as a function of intermediate state energy (left and right axis) and pump-probe time delay (bottom). The energy axis on the left (right) corresponds to electronic states probed by 4.65 eV (3.10 eV) photons at negative (positive) time delays. The PE intensity at each time delay is integrated in emission angle. Also, it is subtracted by the background intensity at time delays far from the pump-probe temporal overlap where the PE spectrum consists only of the single-color 2PPE contribution of each pulse[1].

The resulting pump-probe correlated intensity is maximum around the temporal overlap, i.e. at zero time delay, and decreases in both directions. At zero-time delay, different spectral features are probed above E_F which can potentially be produced by both pulses. The low-energy part of the spectrum consists of a broad intensity distribution which superimposes on the pump-probe correlated signal of the secondary electrons (cf. Fig. 3.3 in Section 3.2). This energy region as probed by 4.65 eV photons (left axis) corresponds to the position of the Ru CB around Γ (cf. energy level diagram in Fig. 4.1), while as probed by 3.10 eV (right axis) lies well within the Ru projected band gap as well as the expected SiO_2 electronic band gap. Therefore, this spectral intensity is assigned to the excitation of electrons in the Ru CB whose dynamics evolve in the spectrum at negative time delays. At higher energies, two spectral features appear above the upper edge of the Ru CB. Their positions are

[1]This delays exceed the time interval reported in Fig. 4.2 (a).

comparable to the intermediate state energies of the unoccupied electronic states 1 and 2, respectively, observed in the single-color 2PPE spectrum with 4.65 eV photons of Fig. 4.1. Therefore, they most likely correspond to these two states and thus are produced upon excitation of electrons by 4.65 eV photons. This is corroborated by noting that the single-color 2PPE spectrum recorded with 3.10 eV (not shown) does not exhibit any PE intensity at the corresponding intermediate state energies, i.e. between approximately 2 and 3 eV above E_F, consistently with the presence of the projected electronic band gap of Ru at Γ in this energy region.

Therefore, in order to characterize the states 1 and 2, the following analysis concentrates on the electron population excited by 4.65 eV photons, thus on the positive time delay part of the tr-2PPE data. Accordingly, the intermediate state energy axis used from now on is the one calculated for 3.10 eV probe photons (right in Fig. 4.2 (a)). It is recalled that 4.65 eV pump photons have not enough energy to enable excitation across the band gap of SiO_2. This implies that the states 1 and 2 are populated via the excitation of electrons from the Ru occupied states.

The characterization of the states 1 and 2 requires the knowledge of their energy, dispersion and lifetime. This information can provide insights on the origin, the degree of localization and the interface electronic coupling of these states, respectively. Spectral analysis is then performed by fitting various spectra in the energy region above which the electron population in the Ru CB can be resolved from the secondary electron distribution. One exemplary spectrum is extracted at zero-time delay from the time-resolved data set in (a) and reported in Fig. 4.2 (b) (red curve). The relevant fit (black curve) consists of a sum of three Gaussian functions multiplied by the Fermi-Dirac distribution (FDD) cutoff and describes very well all spectral features.

In order to obtain the energy and the dispersion of the states 1 and 2, this analysis is repeated on spectra extracted at various emission angles and at time-zero. In this way, the best-fit energy position of each peak is retrieved at various momenta, as reported in Fig. 4.2 (c) by the red and black markers on top of the energy- and momentum-resolved PE intensity plot. The error bar is the static energy resolution evaluated from the slope of the secondary-electron cutoff (cf. Subsection 3.6.3). The two states exhibit different dispersion. To rationalize this, both data sets are fit by the nearly-free-electron model (black and red solid lines) with the effective electron mass, m^*, and the energy minimum as fit parameters. The fit results are reported in Table 4.1 and discuss later. First, the procedure to obtain the state lifetimes is described.

The lifetime of the two states is evaluated on the temporal evolution of their transient electron occupancy. The latter is obtained for each state from the integrated intensity of the relative Gaussian peak at various time delays. The transients are plotted as a function of pump-probe delay in Fig. 4.2 (e) (green and red circles). Both curves show a weak, but experimentally significant intensity at positive delay times that exceeds the temporal cross-correlation of the two pulses (green shaded area). In order to quantify the state lifetimes, an empirical fit function given by an exponential decay convolved with the Gaussian temporal response is successfully fitted to both transients (solid lines). Here, the pulse width parameter is fixed at the pump-probe cross-correlation value. Due to the lack of an independent measurement of the temporal overlap between the pump and probe pulses, time-zero is determined in situ from the cross-correlation at the highest accessible energies and its hold in the fit procedure. This leads to an uncertainty on the best-fit lifetime values which is quantified in the present analysis by evaluating the range of values for which the fit converges solidly.

State	E_{interm} - E_{F} (eV)	E_{bind} - E_{vac} (eV)	m^*/m_0	τ (fs)
1	3.70 ± 0.05	-1.72 ± 0.05	1.6	6 to 12
2	4.51 ± 0.05	-0.91 ± 0.05	3.3	8 to 14

TABLE 4.1: Analysis results of the 1 and 2 unoccupied electronic states of 1.4 ML silica on Ru(0001) probed by tr-2PPE with 'p'-pol probe photons.

The results of the data analysis are now summarized in Table 4.1. The energy of each state is given with respect to both E_{F} and E_{vac}. The state dispersion is expressed in terms of the ratio between the effective electron mass and the free-electron mass, m^*/m_0. For the lifetime, τ, its lower and the upper limit yielding to fit convergence are reported.

The state 1 lies 3.70 eV above E_{F} and has a binding energy of -1.72 ± 0.05 eV with respect to the vacuum level. Its dispersion evolves away from Γ with an effective mass 1.6 times higher than that of a free electron. The decay time is well below the FWHM of the pump-probe cross-correlation, between 6 and 12 fs. The state 2 separates by approximately 0.8 eV from the state 1 and by -0.91 ± 0.05 eV from the vacuum level. It shows an effective mass more than three times higher that of a free electron and its lifetime is estimated between 8 and 14 fs.

This analysis shows that both states exhibit a rather large binding energy with respect to the vacuum level. Also, the state 1 is quasi-resonant to the maximum energy of the conductivity onset reported for BL SiO_2/Ru(0001) and the state 2 lies well above this reference value. The large effective masses indicate that the two states do not have a free-electron-like character, but they are rather localized in the momentum direction parallel to the film surface. The extremely short lifetime of both states suggests the presence of efficient decay channels for the transient electron population.

Before discussing the origin of the states 1 and 2, information on their symmetry is retrieved by recording the tr-2PPE spectrum with the probe electric field entirely polarized in the plane of the sample surface ('s'-polarized light) and comparing it with the spectrum measured with 'p'-polarized probe photons. rotating the probe beam polarization changes the matrix elements, and thus the electronic states, that contribute to the photoemission intensity (cf. Section 3.2). For instance, the detection of IPSs requires an electric field component perpendicular to the surface, i.e. 'p'-polarized probe light has to be chosen. With 's'-polarized light, the matrix element for an IPS vanishes, thus the IPS detection is typically forbidden [178, 179, 180].

In the next data set, the 's'-polarized probe beam with 3.10 eV photon energy is employed. The experimental geometry is depicted in Fig. 4.3 (b) and shows that the probe beam is polarized in the sample surface and has no polarization component perpendicular to it. The pump beam at 4.65 eV is kept 'p'-polarized. The relevant tr-2PPE spectrum is shown in (a) and consists of two main features. At low energies, electron distribution in the Ru CB can be recognized. In the high-energy part of the spectrum, a spectral feature 3 is detected. To obtain its energy and dispersion, spectra are evaluated at various emission angles and at time-zero by fitting with a double-Gaussian function that accounts for the two main spectral features. The lifetime of state 3 is obtained by single-exponential-decay fitting of the transient integrated intensity of the relevant Gauss peak. The best-fit parameters relative to the state 3 are summarized in the table of Fig. 4.3. The state lies 4.17 ± 0.05 eV above E_{F}, corresponding to a binding energy of E_{binding} - E_{vac} = -1.25 ± 0.05 eV. It exhibits a

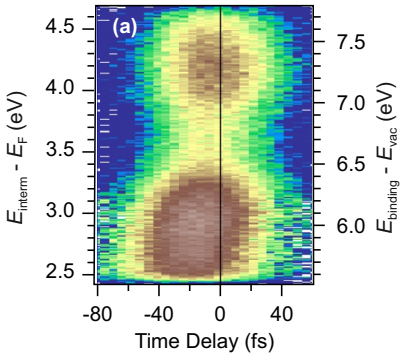

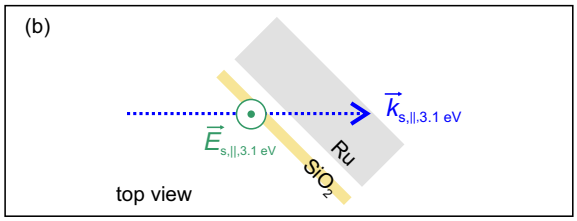

State	E_{interm} - E_F (eV)	$E_{binding}$ - E_{vac} (eV)	m^*/m_0	τ (fs)
3	4.17 ± 0.05	-1.25 ± 0.05	2.84	6 to 14

FIGURE 4.3: (a) Tr-2PPE of 1.4 ML SiO_2 on Ru(0001) with p-polarized 4.65 eV pump and s-polarized 3.10 eV probe photons. (b) Scheme of the experiment. Bottom right, fit parameters of the 3 unoccupied state.

high effective mass, and almost pulse-duration limited lifetime[2]. Comparison of the fit results of this state with those of the states 1 and 2 allows to conclude that a new, distinct feature is probed with 's'- polarized light, while the states 1 and 2 are no longer detected.

To sum up, the unoccupied electronic band structure of the 1.4 ML SiO_2/Ru(0001) system exhibits three electronic states with (i) high binding energies with respect to the vacuum level, (ii) large effective masses, (iii) extremely short lifetimes and (iv) different polarization dependence. In particular, the state 3 is efficiently detected by the 's'-polarized 3.10 eV probe beam, while its matrix element either vanishes or is very small when p-polarized probe beam is used. This observation reveals that this state cannot be an IPS. This statement is corroborated by both the high binding energy with respect to the vacuum level, which largely exceeds the upper limit for an IPS of -0.85 eV (cf. Section 2.4), and the large effective mass, whereas an IPS is expected to exhibit a free-electron-like dispersion in the surface plane. Possibly, the state 3 is an unoccupied state of the oxide and is localized within the film plane.

The discussion now focuses on the origin of the states 1 and 2 which are probed by 'p'-polarized light. As pointed out earlier, both states exhibits too high binding energies relative to E_{vac} to be assigned to bare IPSs of the Ru(0001) surface. Thus, two hypothesis were formulated: 1. they could be discrete unoccupied states of the thin oxide film; 2. these states may be modified IPS of Ru degenerate with the SiO_2 CB.

- **QW states of the ultrathin SiO_2 film** - The SiO_2 film thickness amounts to less than 2 Å. At this length scale, quantization of the electronic states may be expected due to electron confinement in the direction perpendicular to the film. As illustrated in Fig. 4.4 (a), for an isolated film, this situation is modeled by a rectangular QW with energy barrier on both sides defined by the vacuum level (cf. Section 2.3). This leads to a splitting of the CB and the formation of QW states inside the oxide film. This model is tested for the investigated system by calculating the energy splitting between the first two QW states for a rectangular QW with realistic thickness. However, the calculation largely overestimates the measured separation between the 1 and 2 states. This failure reveals that the two states cannot be described as pure quantized states of an isolated film.

[2]As before, the lower and upper limit of the lifetime are reported in the table.

- **IPS coupled to SiO_2 CB** - As sketched in Fig. 4.4 (b), the states 1 and 2 may be considered as IPS of the metal surface with energies modified by the coupling with the SiO_2 CB (cf. Section 2.4). Because the position of the IPSs of the clean Ru(0001) is well above the SiO_2 CB minimum[3], their binding energy in front of the silica adlayer may increase due to the attractive interaction exerted by the adlayer potential [176]. However, to retain the IPS character, the binding energy of these should not exceed the Rydberg energy of -0.85 eV below the vacuum level set by Eq. (2.9) and the dispersion parallel to the surface should remain rather close to that of a free electron. Also, the resonance with the SiO_2 CB should significantly shorten the IPS lifetime as it provides an efficient decay channel for an electron in the IPS. Eventually, in order to be measured by photoemission, an IPS requires photons with a polarization component perpendicular to the metal/vacuum interface.

  In agreement with the prediction for an IPS coupled to the SiO_2 CB, both states 1 and 2 are solely probed by 'p'-polarized photons and have much shorter lifetimes than the bare IPSs of clean Ru(0001) [98]. Also, their binding energy consistently increases with respect to the position of the IPS in absence of the SiO_2 adlayer. However, both binding energies are significantly larger than -0.85 eV, unambiguous test to exclude pure image states. Moreover, the parallel effective masses are higher than that of a free electron, particularly for the state 2. This reveals a significant localization of the two states in the direction parallel to the sample surface, in contradiction with the characteristic behavior of an IPS. Therefore, the states 1 and 2 cannot be described simply by a modification of the IPSs of Ru.

- **CB quantum subbands in a triangular potential** - The above discussions demonstrate that neither QWSs of an isolated thin film nor modified IPRs of the metal surface reflect the nature of the unoccupied states 1 and 2. In the following, the two cases are merged. In particular, a new QW potential is considered which may develop when the ultrathin oxide film is not isolated but 'surrounded' by the spatially-varying IP of the metal. To justify this picture, it is noted that both the distance of the film from the surface (< 2 Å) and the its thickness (~ 3 Å) are very small compared to the large region where the IP typically extends outside a metal (> 10 Å). Consequently, on both sides of the film the IP is non-zero and joins continuously the inner potential of the oxide[4]. The situation is sketched in Fig. 4.4 (c): The blue curves depict the IP in the vacuum regions, modified at both sides of the film. The white curves are the periodic potentials inside the respective crystals. Notably, the oxide inner potential is also altered after joining the outer potential at both interfaces. The intuitive picture is that the inner potential along the direction perpendicular to the film results from the superposition of the IP on the QW [85].

  As a consequence of the superimposed IP, the rectangular QW model no longer applies for the SiO_2 film and the energies of the quantum states will be determined by the new QW. To verify if this picture describes the states 1 and 2 of the 1.4 ML SiO_2/Ru(0001) system, the complex spatially-varying potential extending from the metal surface into the oxide film is approximated to a triangular potential. The model is depicted in (c), right (cf. Subsection 2.3.2). In this case, the new eigenvalues ϵ_i of each CB quantum subbands are determined

[3] It is noted that the work function does not change after deposition of the SiO_2 film.
[4] Such potential would be described explicitly by the 1D model potential [85]

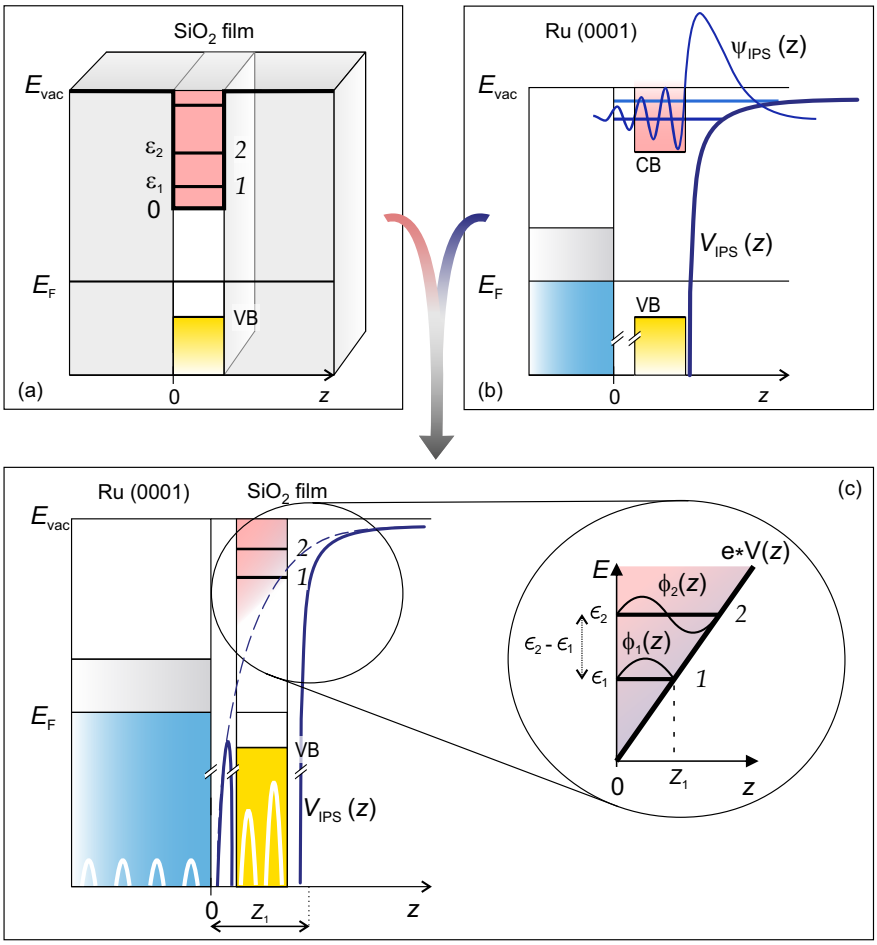

FIGURE 4.4: (a) CB quantization of an isolated thin film. (b) IP resonance of the Ru(0001) metal surface modified by oxide film. (c) QW potential joining the IP: the rectangular QW potential modifies into a triangular one. See main text for details.

by the width, Z_i, of the well for the particular wave function ϕ_i. Intuitively, the minimum width for the subband 1, i.e. the deepest QW state in the triangular well, is defined by the distance Z_1 indicated on the right bottom of Fig. 4.4 (c) and consisting of the sum of the film thickness and the distance between the film and the metal surface. For less-bound states, the experienced width of the well is larger. As reported in Subsection 2.3.2, the solution of the Schrödinger equation for a triangular potential yields to the eigenvalue series expressed by Eq. (2.7).

To apply the QW model, the approach is to use the experimental value of the energy splitting $\epsilon_2 - \epsilon_1$ to estimate the width Z_1 of the triangular QW for the lowest QW state ϵ_1. This calculated QW width is then compared to the expected value given by the sum of the film thickness and the distance between the film and the metal (see Z_1 in Fig. 4.4 (c), bottom left). Using the parameters reported in Table 2.1, the expected value for Z_1 is 0.81-0.88 nm. It is noted that because the parameters hold for an 'O-rich' bilayer of SiO_2 on Ru(0001), this reference can be taken as upper limit for the 1.4 ML system which consists of a mixture of single and double layer domains. In the following, the procedure to estimate Z_1 from the experimental results is described.

The parameter Z_1 relates to the energy ϵ_1 with respect to the QW bottom through the space-charge electric field $\mathcal{E}$ of an electron inside the well [76]. The relationship reads:

$$\epsilon_1 = e\mathcal{E}Z_1, \tag{4.1}$$

where e is the elementary charge. Therefore, in order to obtain Z_1, $\mathcal{E}$ is evaluated explicitly and ϵ_1 expressed as a function of Z_1.

To evaluate $\mathcal{E}$, the energy splitting $\epsilon_2 - \epsilon_1$ is written using Eq. (2.7):

$$\epsilon_2 - \epsilon_1 = \left(\frac{3}{2}\pi\hbar e\right)^{2/3} \frac{(|\mathcal{E}|)^{2/3}}{(2m_\perp^*)^{1/3}} \left[\left(\frac{7}{4}\right)^{2/3} - \left(\frac{3}{4}\right)^{2/3}\right] \tag{4.2}$$

where $m_\perp^*$ its the effective mass in the direction along the well (i.e. perpendicular to the film) and $\mathcal{E}$ the space-charge electric field of interest. The $m_\perp^*$ parameter is unknown for SiO_2, therefore a typical value of $0.1 \cdot m_0$ is assumed [76]. The measured $\epsilon_2 - \epsilon_1$ is 0.81 eV and provides an estimate of $\mathcal{E}$ of 5 x 10^8 V/m.

Now, using the uncertainty principle,

$$Z_1 p_1 \sim \hbar, \tag{4.3}$$

ϵ_1 is expressed in terms of Z_1:

$$\epsilon_1 = \frac{p_1^2}{2m_\perp^*} \sim \frac{\hbar^2}{Z_1^2} \cdot \frac{1}{2m_\perp^*}, \tag{4.4}$$

where p_1 is the momentum of an electron in the state 1 and $\hbar$ the Planck constant.

Eventually, Eq. (4.4) is inserted in Eq. (4.1) and Z_1 is calculated for the $\mathcal{E}$ value estimated before. The QW width Z_1 results of 0.9 nm. Notably, despite the simplicity of the model, the QW width Z_1 is reproduced reasonably well.

Thus, the proposed model suggests that quantization of the SiO_2 CB occurs as a consequence of the spatial electron confinement inside the oxide. However, the

eigenstates of the QW are not those of a rectangular well but result from a potential which is spatially varying in the direction perpendicular to the film. This evidence is interpreted as a modification of the inner potential after joining the IP of the metal at both sides of the film. This modification indicates that the oxide film is not completely isolated but couples with the electrostatic environment. The latter, defined by the IP of the metal, influences the electronic structure of the film, and specifically the energy of the CB quantum subbands 1 and 2.

With regard to the electronic coupling between these SiO_2 states and the Ru electronic structure, further indications can be found in (i) the excitation mechanism of electrons into the oxide film and (ii) the decay time of the electron population into the Ru bulk. (i) As mentioned earlier, in these experiments, the unoccupied electronic states of SiO_2 can be populated only by excitation of valence electrons of Ru across the metal/oxide interface. At $k \neq 0$, the excitation requires spatial overlap of the relevant wave functions at energies higher than the top of the SiO_2 electronic band gap. Around Γ, electron injection relies on the penetration of the SiO_2 wave functions inside the Ru bulk. The efficient detection of the two states 1 and 2 around Γ reveals a nonvanishing interface electronic coupling. Since their spectral intensity is maximum already around the time of pump-probe overlap, the excitation of electrons most likely involves vertical transitions directly into the wave functions of the CB quantum subbands, which thus are found to extend outside the film into the metal. (ii) The measured lifetime of electrons in both quantum subbands is extremely short, on the order of 10 fs (cf. Table 4.1). This observation is indicative of efficient scattering of the electrons back to the Ru bulk, further supporting the electron coupling at the oxide/metal interface.

In summary, new unoccupied electronic states are discovered on the 1.4 ML SiO_2/Ru(0001) system at energies where the three-dimensional SiO_2 would exhibit a large gap. Their large binding energy with respect to the vacuum level and the high effective masses parallel to the film indicate that these states are not pure IPSs of the metal support. Also, their energy splitting is not reproduced by the calculation for a rectangular QW with realistic width. Thus, these are not even pure quantum states of an isolated SiO_2 film. Finally, a simple model calculation based on a triangular QW supports that these **states originate from the quantization of the SiO_2 CB inside a well potential modified by the superposition of the IP of Ru.** The resulting QW states exhibit very short lifetime indicative of efficient electron coupling between the oxide and the metal. Altogether, the unoccupied electronic structure of 1.4 ML SiO_2 results from the electron quantum confinement inside the oxide film, influenced by the IP of the metal surface.

To corroborate these findings, further investigations are suggested here. From a theoretical point of view, the model calculation should be verified for a more accurate estimate of the space-charge field by knowing the exact perpendicular effective mass. Also, it would be helpful to compare these predictions with calculations by the 1D potential model for an IPS in front of an adlayer in order to into account for the real periodic potential of the oxide [85]. Experimentally, because the energy of the QW states are expected to vary with the width of the well, it would be interesting to compare the electronic structure of SiO_2/Ru(0001) systems where the coverage of SiO_2 and/or the distance between the oxide and the metal surface[5] are systematically

[5]As described in Section 2.5, the latter can be achieved by tuning the amount of oxygen physisorbed at the Ru surface underneath the bilayer terraces of the oxide.

varied. In this regard, first insights are provided by the electronic structure of the 'O-rich' BL system on Ru(0001) that is presented in the following section.

4.2 Energy level alignment at the BL SiO_2/Ru(0001)interface

BLs of SiO_2 are only physisorbed on the Ru(0001) substrate via van der Waals forces. This has two important consequences on the structural and electronic properties of the system. (1) The distance between the film and the metal support increases with respect to the case of a chemically bound ML, thus varying the electronic coupling at the oxide/metal interface [41, 43, 38]. (2) The adsorption of oxygen on the metal surface underneath the BL film is favored. As a result, the distance of the film from the substrate further increases due to the repulsive interaction between the interfacial O ad-atoms and the O atoms of the silica film [42, 43, 38]. Moreover, depending on the amount of interfacial oxygen, the work function is reported to increase by up to 0.8 eV with respect to the 'O-poor' BL with no interfacial O content [95] and the charge transfer between the film and the metal is calculated to be significantly suppressed with increasing the interface oxygen concentration [38].

These properties rise the question about the unoccupied electronic structure of a BL SiO_2 film on Ru(0001) and how it may differ from that of a SiO_2 film of lower coverage. How does the electronic states align at the interface with the metal? What is the influence of the image potential on the energetics of the film when the distance from the metal surface is increased? In analogy with the findings for the 1.4 ML coverage, is the quantization of the SiO_2 CB observed? To address these questions, the electronic band structure of an amorphous, 'O-rich' BL SiO_2 on Ru(0001) is measured in this thesis by means of 2PPE spectroscopy and compared to that of the 1.4 ML. It is pointed out that the presence of oxygen on the metal surface underneath the oxide film mainly derives from two factors. (i) During the film oxidation following the deposition, some O content chemisorb on the metal surface (cf. Subsection 3.6.1). This content is not desorbed prior to the photoemission experiments. (ii) Additionally, further O ad-atoms are offered to the metal during the daily 'refreshing' of the sample surface which is performed in O_2 background pressure (cf. Subsection 3.6.1). Thus, it is reasonable to assume a significant accumulation of O ad-atoms at the metal/oxide interface of the investigated system.

First, the metal surface supporting the BL SiO_2 film is characterized in order to identify possible spectroscopic signatures of the presence of interfacial oxygen. To achieve this, both single-color 2PPE spectra and LEED patterns are recorded after different steps of surface annealing during which the clean Ru(0001) surface is gradually recovered. Since the LEED pattern of the interfacial oxygen ad-atoms is well known from the literature [91], these LEED measurements serve as reference to check the persistence of oxygen on the metal surface, thus supporting or excluding the assignment of electronic states observed in the 2PPE spectra to the interfacial oxygen content.

The LEED patterns following each annealing step are shown in Fig. 4.5 (a) to (c). They are all recorded at the same energy of 130 eV. As reported in (a), after heating the sample for 1 minute to 1240 K, the pattern consists of six bright spots (marked by the red circles) at the vertex of an hexagon, superimposed by a diffuse ring of weak intensity. Additionally, less intense spots (marked by the yellow circles) distribute in a (2×2) symmetry, i.e. at half-distance between two consecutive bright spots and between each bright spot and the central diffraction spot[6]. In a second step, the

[6]The central diffraction spot is not visible in the snapshot because covered by the electron gun.

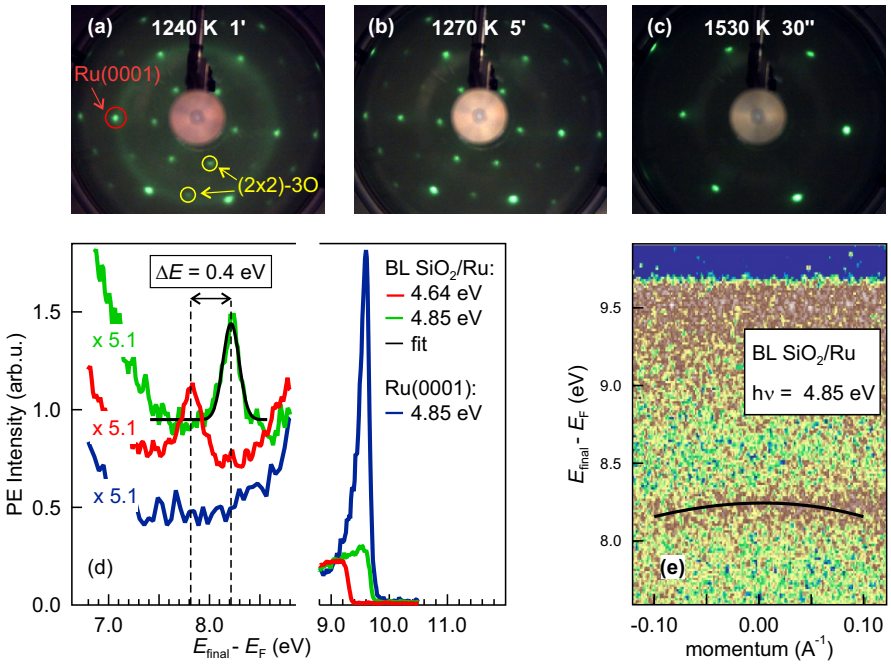

FIGURE 4.5: LEED patterns of (a) the SiO_2/Ru(0001) surface after 1 minute annealing at 1240 K, (b) the Ru(0001)-(2 × 2)-3O surface after 5 minutes at 1270 K and (c) the clean Ru(0001) after 30 minutes at 1530 K. (d) Single-color 2PPE spectra of the Ru(0001)-(2 × 2)-3O surface with 4.64 eV (red) and 4.85 eV (green) photon energy and of the clean Ru(0001) surface (blue) with 4.85 eV photon energy. (e) Momentum-resolved 2PPE spectrum of Ru(0001)-(2 × 2)-3O. The black curve is guide to the eye.

sample is annealed for 5 minutes at 1270 K, i.e. above the 'dewetting' temperature of the oxide film. This produces the LEED pattern in (b): the diffraction ring is no longer present, while all the spots are still clearly visible. Particularly, the (2 × 2)-3O spots appear sharper and more intense than in (a). Eventually, the sample is 'flashed' for 30 seconds at 1530 K, i.e. at sufficiently high temperature for the complete removal of the chemisorbed oxygen from the Ru(0001) surface (cf. Subsection 3.6.1). As displayed in (c), only the hexagonal pattern is observed.

The hexagonal pattern observed in all three LEED patterns originates from electron diffraction by atoms of the Ru(0001) planes (cf. Subsection 3.6.1). The ring is the diffraction signature of the amorphous silica film [91]. Its weak and diffuse intensity after the first annealing step (a) is consistent with the partial removal of the oxide coverage upon heating. The (2 × 2) spots resemble the LEED pattern of the Ru(0001)-(2 × 2)-3O surface reconstruction which is induced prior to the film growth upon deposition of an oxygen ad-layer (cf. Subsection 3.6.1). Therefore it is argued that the (2 × 2) pattern relates to the presence of oxygen at the metal/oxide interface. This assignment is supported by two observations: the (2 × 2) pattern is better resolved after complete removal of the overlying SiO_2 film (b). Even more significantly, it disappears upon surface annealing above the desorption temperature of the chemisorbed O atoms (c). In conclusion, prior to heating of the sample to the highest temperature, the presence of oxygen species on the metal surface underneath the oxide film is experimentally verified for the investigated system.

The single-color 2PPE spectra recorded after the two annealing steps at the higher temperatures are reported in Fig. 4.5 (d) as a function of final state energy (cf. Fig. 3.5

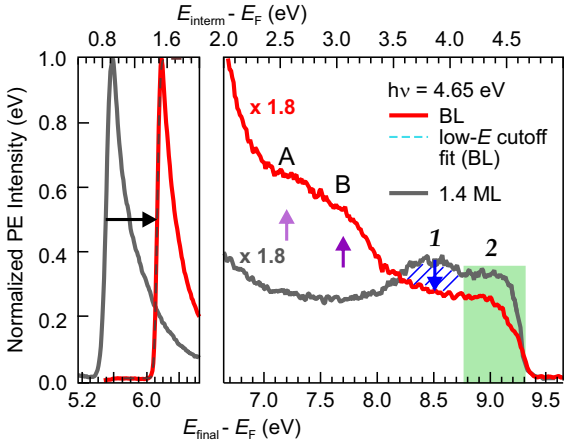

FIGURE 4.6: Spectra of the BL (red) and the 1.4 ML (gray) SiO_2 on Ru(0001). Main features are highlighted by arrows and colors (see main text for details).

in Section 3.2.1) with respect to E_F. In particular, after annealing at 1240 K, the electronic structure is probed both with 4.64 eV (red) and 4.85 eV (green) photon energy. By varying the beam color, it is indeed possible to assign spectral features to either initial, intermediate or final states of the electronic structure (cf. Section 3.2.1). The two spectra are characterized by a pronounced peak appearing on top of the secondary electron intensity distribution. Gauss fitting of this peak (black solid curve) returns an energy position of E_{final} - E_F = 7.82 ± 0.04 eV and 8.21 ± 0.04 eV when measured with 4.65 eV and 4.85 eV photons, respectively. Thus, within the experimental accuracy, the difference of peak energy position between the two spectra is equal to twice the difference of photon energy between the two beams. This reveals that the relative state is an initial state. This finding is also supported by the slightly negative dispersion of this state, as shown in the momentum-resolved 2PPE spectrum recorded with 4.85 eV photon energy of Fig. 4.5 (e). The black curve is a guide to eye. The energy of this occupied state is then calculated to be -1.48 ± 0.04 eV below E_F (cf. Fig. 3.5 in Section 3.2.1). After 'flashing' of the surface at 1530 K, i.e. complete removal of residual oxygen, the peak of this occupied state is no longer present in the spectrum (blue) as measured by 4.85 eV photons. Instead, a strong feature dominates the spectrum at the highest final state energies accessible with the photon energy emploied. Its intensity peaks at E_{final} - E_F = 9.67 ± 0.04 eV, which corresponds to a binding energy of -0.65 ± 0.04 eV with respect to E_{vac}.

The comparison of these 2PPE spectra, combined with the information obtained by the relative LEED patterns, discloses that **the occupied state at E - E_F = -1.48 ± 0.04 eV arises from the presence of oxygen ad-atoms on the metal substrate**, because its spectral features disappears above the desorption temperature of the interfacial oxygen. In the following, this 'oxygen-related' state will be referred to as O(Ru) surface state. The state at E - E_{vac} = -0.65 ± 0.04 eV is measured only on the bare Ru(0001) surface and has a binding energy with respect to E_{vac} which is in very good agreement with the value reported for the n = 1 IPS [98] of the clean Ru(0001) surface within the experimental accuracy. Thus, the peak is assigned to this unoccupied surface state of the metal substrate.

After spectral characterization of the substrate, the BL SiO_2 electronic structure is presented in the following. In Fig. 4.6, a 2PPE spectrum of BL SiO_2/Ru(0001) (red) is displayed as a function of both final (bottom) and intermediate (top) state

energy with respect to E_F. For comparison, the 1.4 ML SiO_2/Ru(0001) is also shown (gray). Both spectra are measured with the same photon energy of 4.65 eV. On the final state energy axis, the work function of the two samples is read directly from the position of the low-energy secondary electron cutoff. Clearly, the one of the BL sample is shifted to a higher energy with respect to that of the 1.4 ML, as indicated by the black arrow. Fitting the low-energy cutoff of the BL spectrum with an error function (black dashed) results in a work function value of 6.22 eV. This is 0.80 eV higher than that of the 1.4 ML as well as of the clean Ru(0001) [41]. At final state energies above approximately 7 eV, some spectral intensity is gained with respect to the 1.4 ML spectrum in the energy region indicated by the purple arrows. This spectral contribution seems composed by two features, labeled A and B. At the energies corresponding to the CB quantum subband 1 of the 1.4 ML (blue arrow), the BL does not exhibit any peak. Finally, at the energies of the 1.4 ML CB quantum subband 2 (green shaded area), a spectral feature may be resolved, though cut by the FDD cutoff.

The work function of the BL is significantly higher than other values reported in the literature. For instance, previous STM and LEEM I-V measurements sensitive to *relative* changes of the work function do not observe any work function variations between an 'O-rich' BL SiO_2/Ru(0001) and the clean Ru(0001) surface, for which values between 5.4 and 5.5 eV are reported [41, 94]. However, increment of the amount of oxygen chemisorbed on the metal surface is known to increase the BL SiO_2/Ru(0001) work function [43]. For an 'O-rich' BL SiO_2/Ru(0001) which has reached the (2 × 2)-3O saturation coverage on the metal surface, a work function of 6.26 eV is reported [95, 38]. Notably, this value is very close to that of the BL system investigated in this thesis, supportive of the realization of an almost saturated (2 × 2)-3O coverage underneath the measured BL. This hypothesis is corroborated by the previously discussed 2PPE and LEED combined studies. The lower work function of the 1.4 ML is then consistently justified by a lower concentration of adsorbed oxygen on the metal surface which indeed can only take place underneath the BL terraces.

The discussion of the further spectral signatures of the BL SiO_2/Ru(0001) sample requires a more detailed analysis which is reported in Fig. 4.7. In a first step, the PE intensity of the secondary electron distribution is fit by an exponentially decaying function multiplied by an error function that accounts for the low-energy spectrum cut-off and convolved by the Gaussian instrumental function. This fit curve (dashed orange) is subtracted from the data and the residual spectrum (red markers) is fit by a sum of three Gaussian functions (color shades) multiplied by a FDD function centered at E_{final} - $E_F = 2h\nu = 9.30$ eV. The fit (blue) can reproduce the spectrum very well and provide the best-fit position of each Gaussian peak. Their final state energies are $E_A - E_F = 7.15$, $E_B - E_F = 7.75$ and $E_C - E_F = 8.79$ (each ± 0.04 eV).

Peak B: O(Ru) occupied state If the peak B would be an unoccupied electronic states below E_{vac}, it would have an energy of 3.10 eV above E_F. Clearly, this position is below the onset of the conductivity of the BL, thus the peak B cannot belong to the BL SiO_2. At the same time, it cannot be an unoccupied state of the bulk Ru, as the energy is well within the projected band gap at Γ. Notably, the energy of the peak B in the final state axis is comparable to that of the O(Ru) occupied surface state measured on the (2×2)-3O Ru surface. Its width of 0.5 ± 0.04 eV is approximately 5 times larger. These results are confirmed also on BL SiO_2/Ru(0001) spectra measured with another photon energy (not shown). Since no other state is expected at that energy in the electronic structure, **the peak B most likely corresponds to that O(Ru) occupied state.** The broadening of the peak width possibly results

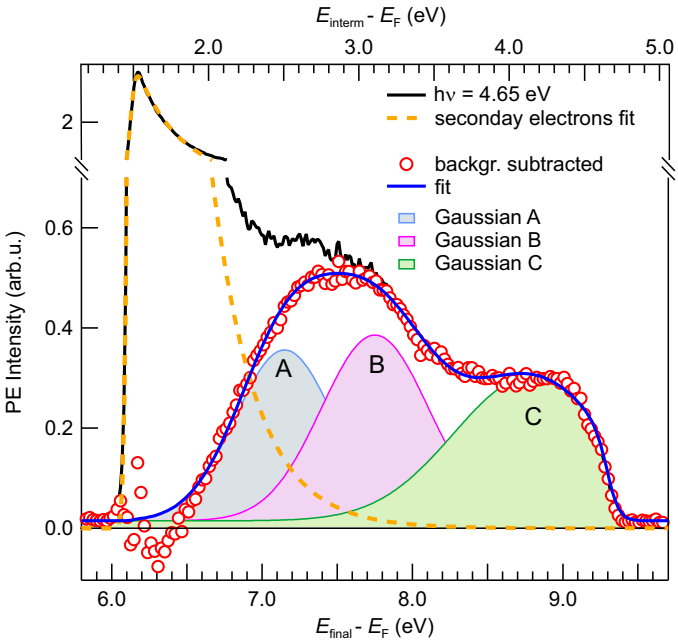

FIGURE 4.7: Spectrum (black) of BL SiO_2/Ru(0001) with 4.65 eV photons. The dashed orange line is the fit of the secondary-electron background intensity. The blue line is the fit of the background-subtracted spectrum consisting of three Gaussian function (color shades) multiplied by the FDD function.

from an increased coupling to the continuum of bulk Ru occupied states around Γ [63, 181, 65, 177]. Indeed, one plausible explanation of such coupling enhancement with respect to the bare (2 × 2)-3O Ru surface is the compression exerted by the overlying SiO_2 film [41] due to the Coulomb repulsion between the O(Ru) atoms and those of the lowest SiO_4 tetrahedra (cf. Fig. 2.7).

Peak A: final state pinned to E_F The assignment of the peak A is difficult and disfavored by the weak spectral intensity. Its position on the intermediate state energy axis is $E_{\text{interm}} - E_F = 2.50 \pm 0.04$ eV. When referring to the energy level diagram proposed in Fig. 4.1, right (cf. also Subsection 2.5.3), it is noted that this energy is within both the Ru projected band gap and the BL SiO_2 electronic band gap. Thus, the peak A cannot be an intermediate state of the BL SiO_2/Ru(0001) system. Furthermore, the peak finds no correspondence in other 2PPE spectra of, e.g. either the (2×2)-3O Ru surface or the 1.4 ML sample.

In the following, a set of 2PPE spectra of the BL system is discussed which suggests that the peak A could be a final state. Importantly, these measurements follow a set of experiments where water (D_2O) coverage was deposited on the SiO_2 surface[7]. Before recording the spectra, the water coverage was desorbed and the sample further treated via annealing at 900 K in order to recover the pristine SiO_2 surface. However, irreversible modifications of the 2PPE spectrum are observed, though the spectral feature A is preserved. The data are reported in Fig. 4.8 as a function of final state energy and are recorded with two different photon energies, 4.84 eV (black) and 4.65 eV (red), respectively. For comparison, the 2PPE spectrum of the 'fresh' BL SiO_2/Ru(0001) system measured with 4.84 eV prior to the experiment with water dosing is discussed (dashed gray), together with the relative Gaussian fit of the peak

[7]This experiment is not reported in this thesis work.

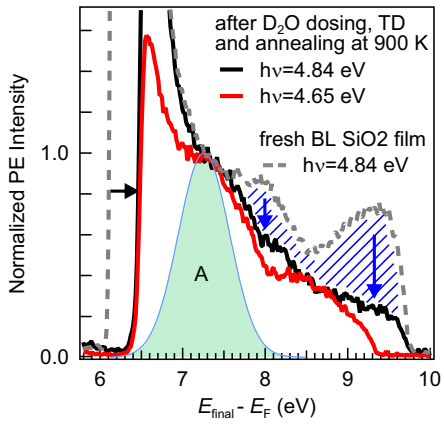

FIGURE 4.8: Photoemission spectra of BL SiO_2/Ru(0001) (dashed gray, black, an red). The Gaussian peak (light blue shade) is the fit to the state A. See main text for details.

A (light blue shade, cf. analysis in Fig. 4.7 for 4.65 eV photons). All the spectra are normalized to the intensity at the energy of the Gaussian peak A.

First, it is observed that the low-energy spectrum cutoff is shifted by several hundreds meV to a higher energy with respect to that of the 'fresh' BL spectrum (black arrow), thus the work function is higher than the initial value. Furthermore, the spectral intensity at the energy of the CB quantum subband 2 is reduced and this and the peak B are less resolved (cf. black-solid and gray-dashed spectra measured with the same photon energy of 4.84 eV. The intensity reduction is indicated by the blue arrows). Conversely, the spectral feature A appears unaltered on both the measured spectra. Particularly, its position does not vary despite the work function change, nor depends on the photon energy. The modification of the work function indicates that the surface electric dipole of the BL system is modified. This is possibly due to the interaction of the oxide with the water, irreversibly altering the film morphology. The fact that the peak A does not shift neither with the change of work function nor with varying the photon energy suggests that **the feature corresponds to a final state of the BL SiO_2/Ru(0001) which is pinned to E_F**.

Peak C: CB quantum subband 2 of SiO_2 The state C is measured at $E_{\text{final}} - E_F = 8.79 \pm 0.04$ eV by 4.65 eV photons. However, as observed earlier, its spectral profile appears cut on the high-energy side, as if the photon energy used was too limited to completely resolve the peak. Thus, as displayed in Fig. 4.9, a set of 2PPE spectra is recorded and the photon energy is gradually increased until the feature appears separated from the FDD cutoff. This is achieved by means of 5.32 eV photons (blue), which thus yield the most accurate measurement of the state energy. The fit results are summarized in the table. With increasing the photon energy, the best-fit peak position moves to a higher energy. Quantitatively, this energy shift is only partially due to the increase of photon energy, while majorly to the fact that the peak maximum is gradually better captured by more energetic photons. Based on the result given by 5.32 eV photons, the peak has an intermediate state energy of 4.79 ± 0.04 eV above E_F. In addition, nearly-free-electron modeling of the state dispersion returns an effective mass of 2.8 times that of a free electron (not shown).

Notably, both the intermediate state energy and the electron effective mass have reasonably close values to those of the CB quantum subband 2 of the 1.4 ML for which an energy of 4.51 ± 0.05 eV above E_F and an effective mass of $3.3^* m_0$ were measured.

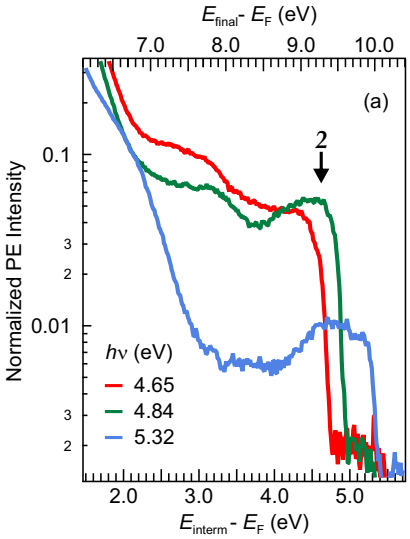

hν (eV)	E_{final} - E_F (eV)	E_{interm} - E_F (eV
4.65	8.79 ± 0.04	4.14 ± 0.04
4.84	9.30 ± 0.04	4.46 ± 0.04
5.32	10.11 ± 0.04	4.79 ± 0.04

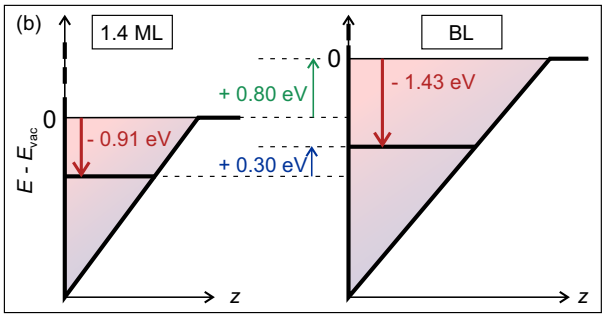

FIGURE 4.9: (a) 2PPE spectra of BL SiO_2/Ru(0001) measured with 4.65 eV (red), 4.84 eV (green) and 5.32 eV (light blue). In the table, the analysis results for the 2 unoccupied electronic state. (b) Schematic of the triangular QW for the 1.4 ML and the BL and the relative shift of the CB quantum subband 2 due to the combined change of the QW width and the work function. See main text for details.

It seems therefore plausible to assign the peak C to this unoccupied electronic state of the oxide film. This assignment implies that the energy of the subband relative to E_F increases by approximately 0.30 eV in the BL with respect to the thinner film. This is shown in Fig. 4.9 (b) (blue arrow) depicting the triangular QWs and relative QW state 2 for both the 1.4 ML and the BL. Notably, because the work function also increases by 0.80 eV (green arrow), the binding energy of the state with respect to E_{vac} is effectively higher in the BL than in the 1.4 ML (compare the two red arrows).

This increase of the binding energy with increasing film thickness can be intuitively explained by considering the QWS nature of the state. Upon widening of a quantum potential well, the delocalization of an electron in the well increases and the electron eigenstate lowers (i.e. it shifts towards the QW bottom, cf. Section 2.3). Various examples can be found in literature. For instance, the energy of quantum well states forming in thin films of hexafluorobenyene (C_6F_6) weakly coupled to Cu(111) lowers with increasing the film thickness due to increased electron delocalization inside the molecular film [64, 65]. The binding energy of IPSs which developed into a quantum-well like states inside a metal adlayer increases with increasing the metal coverage while the quantum-well like state further delocalizes inside the adlayer. For the BL film grown on Ru(0001), the width of the triangular QW at each energy is expected to increase with respect to the 1.4 ML because of three factors: 1. the thicker SiO_2 coverage; 2. the larger distance of the film from the metal due to the weak van-der Waals interaction; 3. the further increased distance from the metal due to the decoupling induced by the interfacial oxygen atoms. Consequently, it is reasonable to expect an increased binding energy of the quantum subband for the BL film.

Finally, a schematic of the energy level diagram of the BL SiO_2/Ru(0001) system is reported in Fig. 4.10. The blue line depicts the total potential given by the inner periodic potential of the two materials superimposed by the IP of Ru. The vertical arrows show the vertical transition potentially induced from bulk occupied states of Ru by the pump pulse. Below E_F, an occupied electronic states at -1.48 eV is

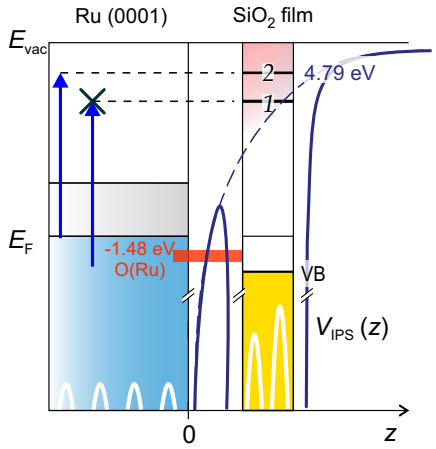

FIGURE 4.10: Energy level diagram of the BL SiO_2/Ru(0001) interface.

resolved, which attests the presence of chemisorbed oxygen underneath the film. This oxygen concentration is believed to majorly cause the increase of work function of the measured BL system with respect to the thinner film. Above E_F, the CB quantum subband 2 of the oxide film appears 4.79 eV above E_F. Its binding energy with respect to the vacuum level is higher than in the 1.4 ML, a property explained by the increased delocalization of the state inside the film. Its spectral intensity is rather weak, indicative of weaker interface electron coupling between this state and the Ru electronic structure. This observation is consistent with the increased decoupling by the interfacial oxygen underneath the BL [43]. Based on the latter argument, it is proposed that the lower CB quantum subband is not observed in the BL as result of a complete decoupling of this state from the electronic band structure of the metal substrate.

4.3 Summary and Conclusions

The presented work investigates the origin of the unoccupied electronic structure of ultrathin films of SiO_2 grown on the Ru(0001) surface. The goal is to identify signatures of the reduced dimensionality of the films and the impact of the electrostatic environment surrounding the oxide on the electronic states that are relevant for dynamical processes as e.g., electron transfer at the interface with the metallic support. Thus, time-resolved two-photon photoemission spectroscopy is applied to two different systems, namely a 1.4 ML and an 'O'-rich BL of amorphous silica, which differ by film thickness and coupling strength to the Ru surface.

The discovered electronic structure of the 1.4 ML film is characterized by two discrete electronic states above E_F which are highly bound with respect to the vacuum level and have extremely short lifetimes. Their properties do not corresponds to neither QW states of an isolated thin film nor pure IPSs of Ru potentially degenerate to the conduction band of the oxide adlayer. Instead, simple model calculations show that these states are reproduced by a quantum potential well which spatially-varies through the film. This result is interpreted as a modification of the QW of the film by means of the superimposed IP. Therefore, the states are assigned to quantum subbands of the SiO_2 CB with energies modified by the IP superimposing the inner potential of the thin film. These results reveal that the electronic structure of the 1.4 ML originates from the interplay of two factors: electron quantum confinement

inside the oxide film and electronic coupling to the outer electrostatic environment produced by the metal surface.

The energetics of the BL is found to be strongly affected by the presence of oxygen atoms chemisorbed on the Ru surface: the work function significantly increases and the unoccupied electronic states of SiO_2 are less coupled to the electronic structure of Ru. In particular, electron injection across the metal/oxide interface into the lower CB quantum subband seems to be fully suppressed. The higher quantum subband is still observed, however at a higher binding energy with respect to the vacuum level, likely connected to an increased localization of this state inside the oxide film. Clearly, the electronic structure of the 'O'-rich BL SiO_2/Ru(0001) differs quite remarkably from that of the thinner film, suggesting that the electronic properties of these low-dimensional systems are very sensitive to changes of their structural parameters and their coupling to the substrate.

5 Ultrafast dynamics in the quasi-1D excitonic insulator Ta_2NiSe_5

Theory predicts that the excitonic insulator phase can stabilize in materials with a small electronic band gap when the Coulomb interaction between conduction-band electrons and valence-band holes is very poorly screened due to the low carrier concentration [46]. This condition may lead to the pairing of electrons and holes into excitons with large binding energy exceeding the magnitude of the electronic band gap. Consequently, spontaneous formation and condensation of excitons is predicted to occur during the transition to the excitonic insulator phase (cf. Section 2.6). While such spontaneous excitonic coupling involves strong orbital hybridization between the valence and conduction band, the lattice potential concurrently adjusts in order to find a new energy minimum for the system. Thus, the excitonic insulator phase manifests entangled to a structural change. Experimental proof of the existance of an excitonic insulator at equilibrium has been a research challenge for a few decades due to the difficulty to unambiguously discern between features of the excitonic coupled phase and those of the underlying noninteracting band structure [46, 101, 182].

Thus, in this work a different approach is followed, which involves the investigation of the *nonequilibrium*[1] properties and dynamics of Ta_2NiSe_5, a quasi-one-dimensional (quasi-1D), small-electronic-band-gap material that recently stood out among other excitonic insulator candidates due to its combined electronic and structural phase transition at low temperatures (LT) consistent with a strong excitonic coupling [54, 122, 55]. The photoinduced structural dynamics are studied by means of coherent optical phonon spectroscopy and connected to the photoinduced hole dynamics of the upper VB at Γ obtained by tr-ARPES. This study identifies the dominant mechanism for both the coherent excitation of the lattice and the decay of one phonon specific of the LT phase, thus overcoming the intrinsic momentum-integration of the optical probe. The ultrafast dynamics of the electronic band gap is traced by means of time-resolved ARPES and 2PPE spectroscopy. By that, disentanglement of the nonequilibrium behavior of the semiconductor band structure and the overlaid excitonic insulator state is ultimately achieved. Particularly, two near-infrared excitation density regimes are discovered, where the electronic band gap either renormalizes due to transiently enhanced Coulomb screening, or atypically widens, due to strengthening of the excitonic insulator order parameter. Eventually, by means of time-resolved 2PPE spectroscopy the electron relaxation dynamics are resolved as a function of excess energy and excitation density. A combined energy and fluence dependence of the electron relaxation time reveals that the excitation does not behave as predicted by the Fermi liquid theory (FLT) and discloses a key role of the Coulomb screening and, likely, the strong excitonic coupling in governing the decay of the photoelectron population.

The results on the photoinduced structural dynamics are published in Mor *et al.*, *Phys. Rev. B*, 97, 115154 (2018). The study of the ultrafast electronic band gap dynamics is published in Mor *et al.*, *Phys. Rev. Lett.* 119, 086401 (2017).

[1] See Section 3.1.

5.1 Thermally-induced structural and electronic phase transitions

As outlined above, the focus of this thesis is on the nonequilibrium dynamics of the LT electronic and structural phases of Ta_2NiSe_5. This will be afforded by monitoring the behavior of specific observables of the two subsystems upon an ultrashort photoexcitation. It is therefore necessary to first identify the order parameters for each subsystem and understand their evolution during the thermally-induced phase transition. To achieve this, temperature-dependent Raman and photoemission (PE) spectroscopy are employed in order to identify signatures of the low-temperature phase of Ta_2NiSe_5 at equilibrium. In particular, temperature-dependent Raman spectroscopy singles out a Raman-active mode at 4.0 THz, which is specific of the monoclinic crystal symmetry of Ta_2NiSe_5 below the critical temperature $T_C = 328$ K, thus providing a marker for the structural phase change. The intensity of this mode is found to drop continuously upon heating of the sample, in agreement with the second-order character of the phase transition.

The evolution of both the occupied and unoccupied electronic band structure of Ta_2NiSe_5 is followed by photoemission measurements upon heating the sample towards T_C. The photon energies used give access to the portion of Brillouin zone close to the Γ point, where the direct electronic band gap opens. In particular, two valence bands are mapped via direct photoemission, consistent with previous ARPES studies. Furthermore, for the first time, the energy position of the two lowest conduction bands is measured by means of 2PPE spectroscopy. Thanks to these two complementary approaches, the band gap narrowing upon heating above T_C is ultimately verified.

Thus, in this section, fingerprints of the combined structural and electronic phase transition in Ta_2NiSe_5 are identified, namely the disappearance of a Raman mode above T_C and the modulation of the electronic band gap at Γ. Their concurrent evolution with temperature supports an interplay of the lattice and the electrons in Ta_2NiSe_5 during the thermally-induced phase transition. This finding is consistent with previous experiments [122, 58, 183, 184] and theoretical modelings [55, 183] highlighting the mutual role of the two subsystems in stabilizing the ground state of each phase at the respective temperature.

5.1.1 The Raman mode at 4.0 THz: a marker of the LT monoclinic phase

As discussed in Section 2.7, the structural distortion occurring in Ta_2NiSe_5 upon temperature variation goes along with a change in the lattice symmetry. As a result, the number of nondegenerate vibrational modes should vary between the two phases. In addition, because Ta_2NiSe_5 has a quasi-one-dimensional structure in the plane of the layers (cf. Fig. 2.14), the phonon spectrum should exhibit a certain anisotropy between the a and c in-plane axes. As shown in the following, all this information is achieved by Raman spectroscopy combining temperature and light polarization dependence.

Fig. 5.1 (a) reports the Raman spectra recorded at temperatures varying from 98 K up to 423 K. For this data set, the CW light beam is polarized along the c axis of the Ta_2NiSe_5 crystal structure, i.e. perpendicular to the Ta-Ni-Ta atomic chains. Many spectral lines up to approximately 9 THz are observed, in agreement with DFT calculations [185]. Most of the peaks persist at all temperatures of the explored range. The dashed lines mark two low-frequency modes that exhibit the highest intensity both in the LT and HT phase. Additionally, the Raman mode highlighted by the red arrow

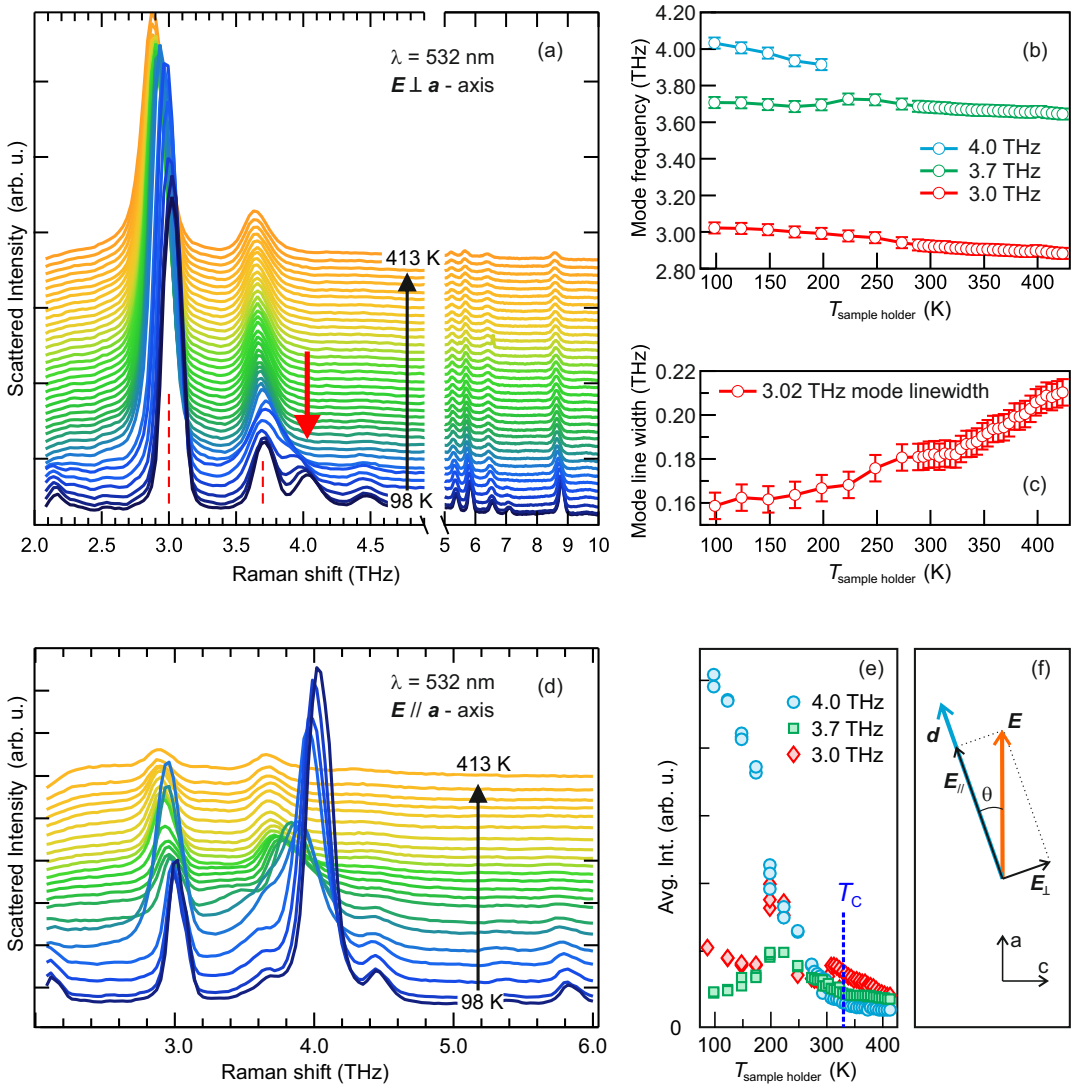

FIGURE 5.1: Temperature- and polarization- dependent Raman spectra of Ta_2NiSe_5. (a) Spectra recorded with the electric field polarized perpendicular to the a axis. (b) Mode frequency and (c) linewidth of the peaks in (a) as a function of temperature. (d) Spectra recorded with the electric field polarized parallel to the a axis. (e) Temperature evolution of the peak averaged intensities. Modified from [60]. (f) Expected real space representation of the 4.0 THz mode.

is found to be solely present at the lowest temperatures and to rapidly disappear upon heating. Therefore, while the symmetry of the crystal structure increases from monoclinic to orthorhombic with increasing the sample temperature, the number of active Raman modes is found to reduce [186].

To extract quantitative information on the three main Raman active modes mentioned above, the low-frequency part of each spectrum is analyzed by a sum of three Gaussian functions. The mode frequency is plotted as a function of temperature in Fig. 5.1 (b). At the lowest temperature, the three Raman modes lie at 3.02 ± 0.03 THz, 3.71 ± 0.03 THz and 4.03 ± 0.03 THz, respectively. In the following, those frequencies will be referred to as 3.0, 3.7 and 4.0 THz. All modes exhibit a weak but continuous softening with increasing temperature, accompanied by a line broadening. The effect is clearer for the case of the 3.0 THz mode, because it appears well isolated in the Raman spectrum. Its spectral line shifts by up to 5% towards lower frequency at the highest measured temperature. Concurrently, the line broadens by approximately 30%, as shown in Fig. 5.1 (c). The frequency shift of the 3.7 and 4.0 THz modes is robustly quantified up to 200 K, whereas above this temperature the two lines merge due to the overall spectrum broadening and the 4.0 THz intensity weakens rapidly. Both the shifting and the broadening effects of the three Raman lines are very small and can be attributed to thermal effects such as the expansion of the sample volume, the change of the phonon levels occupancy and, eventually, the anharmonic interaction between different phonons [187]. On the contrary, the strong temperature-dependence of the intensity of the 4.0 THz mode is likely to be connected to the underlying change of lattice symmetry upon heating, and thus, it is further investigated.

In the following, the temperature-dependent Raman spectra recorded with electric field polarization along the a axis is presented. This axis corresponds to the in-plane crystallographic direction of the Ta and Ni atomic chains (cf. Fig. 2.14) along which shear distortion is exerted during structural phase transition. The results are shown in Fig. 5.1 (d). Qualitatively, they exhibit the same Raman modes probed with polarization parallel to the c axis at the respective temperatures. Particularly, they confirm the disappearance of the 4.0 THz line upon heating towards T_C. However, the intensity of the 4.0 THz mode is strongly enhanced when the electric field is polarized parallel to the Ta and Ni atomic chains. Fig. 5.1 (e) shows the averaged intensity of the three main peaks as a function of temperature: while the intensity of the 3.0 and 3.7 THz mode remain rather constant[2], the 4.0 THz mode drops continuously as the temperature increases towards T_C. Interestingly, its intensity vanishes already well below T_C, namely around 275 K, further supporting that this mode is very sensitive to the continuous phase transition.

There exists only few works on the Raman active modes of bulk [188] and ultrathin [185] Ta_2NiSe_5 which, however, do not discuss the low-temperature (LT) Raman mode at 4.0 THz. Therefore, a real space representation of the relevant atomic oscillation remains unknown. However, an argument is proposed here based on the observed polarization dependence of the 4.0 THz mode intensity. Indeed, the induced dipole moment associated to a Raman scattering process is given by $\mu = \frac{\partial \alpha}{\partial d}\, d\, E\, \cos(\theta)$, where α is the polarizability, d the electron displacement, E the electric field polarized at an angle θ with respect to the displacement vector, as sketched in Fig. 5.1 (f). Therefore, its intensity is maximum when the electric field polarization and the displacement vector are aligned, and vanishes when they are orthogonal to each other. Because the 4.0 THz mode intensity is strongly enhanced when coupled with light

[2]The intensity change between 200 and 225 K is not been observed in every data set, thus most likely originates from accidental sample drifts.

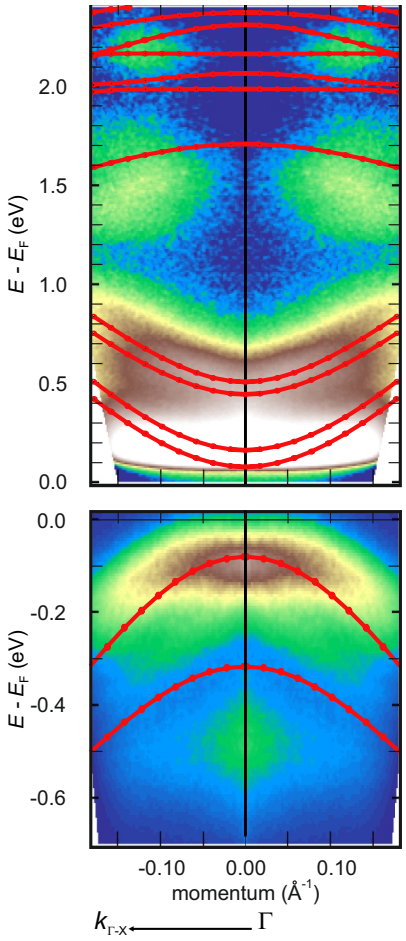

FIGURE 5.2: Photoemission of the occupied (bottom) and unoccupied (top) electronic band structure of Ta_2NiSe_5 in the LT phase measured by ARPES ($h\nu$ = 6.22 eV) and 2PPE ($2 \times h\nu$ = 5.28 eV), respectively, superimposed by DFT calculation (red dot-line curves) from [55]. Spectra and calculation are symmetrized with respect to the zero emission angle.

polarized along the a axis, it can be argued that the induced electric dipole likely contains a component at 4.0 THz that preferentially oscillates along the direction of the Ta and Ni atomic chains. This anisotropy provides another evidence of the quasi-one-dimensionality of the lattice of Ta_2NiSe_5 in the plane of the atomic layers.

In conclusion, the thermally-induced structural phase transition of Ta_2NiSe_5 can be tracked by following the disappearance of the Raman mode at 4.0 THz, unambiguous marker of the LT monoclinic phase. This phonon mode possibly involves a preferential atomic motion in the direction of the shear lattice distortion. The continuous decrease in the peak intensity upon heating towards T_C is a manifestation of the second-order character of the structural change.

5.1.2 Shifting of the occupied *and* unoccupied electronic bands: signatures of the electronic phase transition

The upper VB of Ta_2NiSe_5, with its maximum at the Γ point of the Brillouin zone, is observed by previous ARPES works to shift in energy upon temperature changes. This behavior was interpreted as a modulation of the direct band gap under the assumption that the lowest CB either does not change energy or it undergoes an opposite shifting

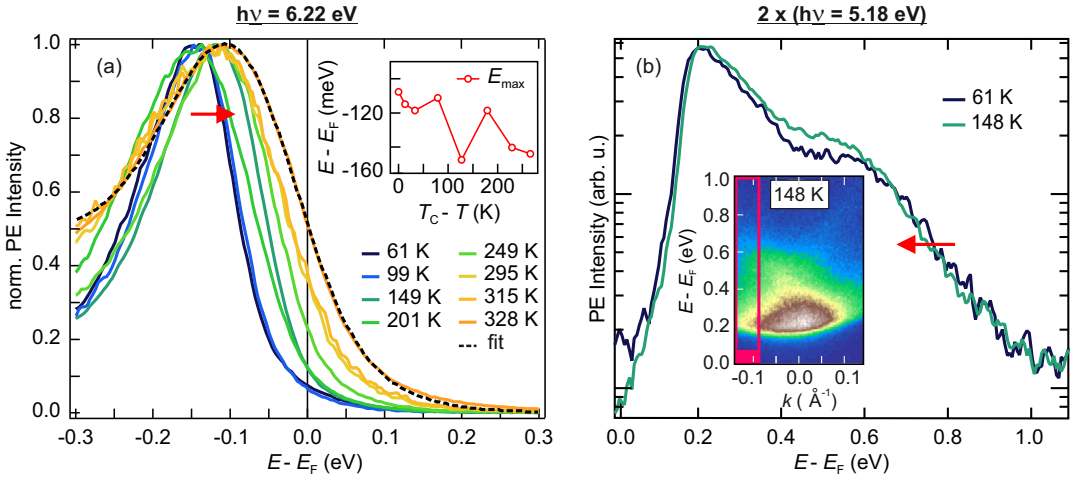

FIGURE 5.3: (a) Temperature dependence of the upper valence band at Γ. Inset: Energy position of the VB at the maximum PE intensity. (b) Temperature dependence of the lowest CB at $k \neq 0$. Inset: Momentum-resolved 2PPE spectrum at 148 K. The red bar indicates the momentum region of integration of the relative spectrum (green curve).

behavior. In this work, both the occupied and unoccupied electronic bands near the Γ point are experimentally addressed on the same crystal sample and their evolution with temperature is resolved.

Fig. 5.2 displays the photoemission spectra along the $\Gamma - X$ momentum direction as recorded at 110 K, i.e. in the LT phase, with light polarized along the Ta and Ni chains. For direct comparison, the DFT calculations of the electronic band structure from [55] is plotted on top of the experimental data. Both band structures are symmetrized with respect to the Γ point. The bottom graph shows the direct photoemission spectrum recorded with 6.22 eV: two VBs are probed with maxima at $E - E_F \approx$ -0.5 and -0.1 eV, respectively, consistent with previous angle-resolved photoelectron spectroscopy results [122]. Those VBs are known to be mostly formed by 4*p* Se-3*d* Ni orbitals [55]. The top of upper VB at Γ shows the pronounced flattening assigned by previous experimental and theoretical works to the realization of the excitonic insulator ground state (cf. Section 2.7).

The top graph reveals the unoccupied electronic band structure of Ta_2NiSe_5 probed by 2PPE with 5.28 eV photons. The agreement with the theoretical prediction is very good. The spectrum shows two low-energy dispersive CBs with minima at the Γ point detaching from the secondary electron distribution[3]. Also, a less dispersive band is confirmed approximately 1.5 eV above E_F, and some photoemission intensity appears above 2 eV, consistent with DFT calculated flat bands. The DFT calculation assign the measured CBs to 5*d* orbitals of the Ta atoms [55]. This implies that an electronic transition from states in the vicinity of E_F involves the transfer of an electron across the Ni and Ta chains, which likely involves the coupling to phonons. This coupling is an important topic of the present work and is discussed later in Section 5.2.2) and Appendix C.

In the following, the temperature dependence of the upper VB and the low-energy dispersive CBs is presented. Fig. 5.3 (a) shows a set of ARPES spectra of the upper VB at Γ at temperatures below and above T_C. Upon heating, a clear shifting of the

[3]To spectrally separate the primary and secondary electron spectral contributions a higher photon energy would be needed. However, the limitation arises here from the work function of the sample (5.42 eV).

peak towards E_F[4] is observed, consistent with previous works [122, 123, 56]. This shift is accompanied by a continuous broadening of the peak. To gain quantitative information on the heating-induced band shift, the VB energy position is evaluated upon modeling of the spectra with a fit function composed of the sum of two Gaussian functions multiplied by the Fermi-Dirac distribution (FDD) function. The two Gaussian functions account for the asymmetric shape of the valence band spectrum and allow to reproduce the spectra very well, as exemplified by the dashed line. The energy position of the intensity maximum of the modeled VB is plotted in inset as a function of temperature. Clearly, it reveals **a continuous shift of the VB towards E_F which amounts up to a few tens of meV upon heating towards T_C.**

In order to unambiguously assign the shifting behavior of the valence band to a modulation of the direct electronic band gap, the thermally induced dynamics of the conduction band is monitored by means of 2PPE spectroscopy with 5.18 eV photons. Based on previous temperature-dependent conductivity measurements [57] and the observed VB shift, the CB is expected to shift only slightly towards E_F upon heating. The energy distribution curves at two different temperatures are shown in Fig. 5.3 (b). They are extracted at $k \neq 0$ from the momentum-resolved spectra, as indicated in inset by the red bar, in order to avoid major contributions of the secondary electrons. The PE intensity of the two spectra is not normalized and allow to directly observe a shift of the conduction band edge towards E_F (red arrow). In addition, a slight upshift of the low-energy cutoff is visible, which possibly originate from small differences in the emission angle or the work function of the cleaved surface[5]. In either cases, the behavior is opposite to that of the CB edge, thus rigid shifts of the spectra can be excluded. Therefore, the shift of the CB edge is assigned to a change of the CB energy relative to E_F. Specifically, the CB shift towards E_F upon increase of the temperature towards T_C. **The CB shift is thus opposite to that observed in the VB a downshift, ultimately proving that the electronic band gap shrinks at temperatures closer to T_C.**

[4] E_F is estimated independently from a reference spectrum of Gold.

[5] The thermal expansion of the sample holder upon heating caused the sample to move such that it was not possible to return exactly on the same sample position between measurements at different temperatures.

5.2 Inhibition of the photoinduced structural phase transition

The concurrent changes of the electronic band structure and the lattice symmetry with varying the temperature suggest that the two subsystems are coupled at equilibrium. On the one hand, the lattice distortion likely modify the orbital overlap, likely affecting the coupling between the $4p$ Se - $3d$ Ni VB and the $5d$ Ta CB. On the other hand, electron-hole pairing across the Ta and Ni atomic chains can influence the Ta-Ni bonds, possibly altering the lattice potential energy minimum.

This section investigates how the two subsystems behave out of equilibrium and if it is possible to disentangle the relevant dynamics. The tool chosen is coherent optical phonon spectroscopy which monitors the transient change of the mid-IR reflectivity of Ta_2NiSe_5 induced by an ultrashort near-infrared pump pulse. The wavelength of the probe photons is tuned in a two-stage NOPA built in the contest of this study (see Section 3.4.1) in order to be resonant to the electronic band gap of the system in the LT phase. Below T_C, the ground state of Ta_2NiSe_5 is increasingly perturbed by tuning the excitation density of pump photons. However, by comparing the coherent phonon response at all excitation fluences with the Raman spectrum of the HT phase, no sign of a non-thermally photoinduced structural phase transition is found. In fact, a saturation of the mid-IR optical response is observed before the system is excited strongly enough to undergo the structural change to the orthorhombic symmetry.

A comparison of these results with time-resolved ARPES data allows correlating the mid-IR incoherent optical response to the hole dynamics at Γ and in the vicinity of E_F. Possibly, such direct correlation between the two techniques was never performed before. This important result provides the explanation for the inhibited photoinduced structural phase transition in Ta_2NiSe_5 in terms of saturation of the near-infrared pump photon absorption at the Γ point.

This section is organized as follows: Subsection 5.2.1 introduces the time-resolved mid-IR optical spectroscopy experiment performed in this work and shows the possibility to follow the structural phase transition as a function of temperature. In Subsection 5.2.2, the time-resolved ARPES results are discussed, which show the effect of the absorption of near-infrared pump pulses on the low density of states of the topmost VB at Γ. In Subsection 5.2.3, the correlation between the time-resolved mid-IR incoherent optical response and the transient occupancy of the upper VB at Γ is demonstrated. Subsection 5.2.4 discusses the photoinduced phonon dynamics of the LT phase probed by the mid-IR coherent optical response and the origin of the inhibited photoinduced structural change is explained. The robustness of the blocking mechanism is discussed in Subsection 5.2.5.

5.2.1 Coherent optical phonons marking the thermally-induced structural change

The scheme of the optical spectroscopy experiment is depicted in the inset of Fig. 5.4 (a). Ultrashort pump pulses at 1.55 eV induce electronic transitions at various momenta. The electronic band structure presented in the previous section allows to identify two resonances at 1.55 eV with the upper VB as initial state: (A) into flat unoccupied d bands at Γ and (B) into the lowest conduction band at larger k vectors. Both excitation channels mostly involve electron transfer from Ni $3d$ to Ta $5d$ orbitals [55]. Mid-infrared probe photons at 330 meV, being resonant to the excitonic-insulator band gap, primarily monitor the photoinduced changes of interband transitions from the topmost VB at Γ into the lowest-CB bottom [58].

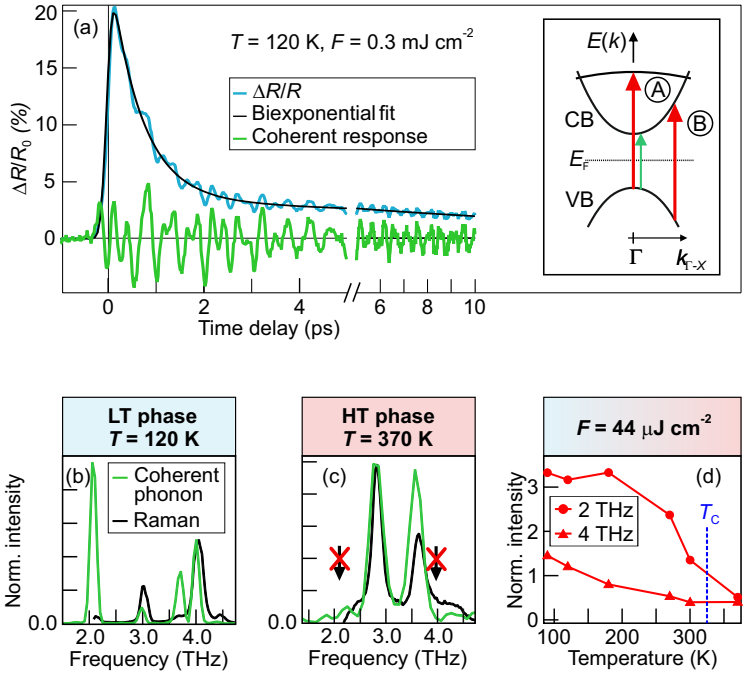

FIGURE 5.4: (a) Mid-IR $\Delta R(t)/R_0$ in the LT phase at T = 120 K (blue curve) and residual coherent optical response (green curve) after subtraction of the incoherent part (black curve). Inset: Scheme of the electronic band structure of Ta_2NiSe_5 and of the pump (red arrow) -probe (green arrow) optical experiment. (b) and (c) Fourier transforms of the coherent optical responses (green curves) and Raman spectra (black curves) of the LT and HT phases. Adapted from [60]. (d) Temperature dependence of the peak area of the 2 THz and 4 THz phonon mode normalized over the 3 THz mode peak area.

All the measurements are done at the repetition rate of 40 kHz to allow the system to fully relax to equilibrium prior to the next pulse excitation, thus ensuring the study of the dynamics of the LT phase. In fact, preliminary transient reflectivity measurements with 1.55 eV pump and visible probe photons exhibit a long-lived correlated intensity when measuring at the higher repetition rate of 200 kHz. Consequently, the photoinduced dynamics of a pre-excited state was probed rather than that of the LT ground state. A more detail description of this data set can be found in Appendix A.

Furthermore, based on the Raman spectroscopy results, the light polarization is chosen parallel to the a axis, i.e. to the Ta and Ni atomic chains, in order to maximize the probability of exciting and probing the coherent phonons of interest. This was also tested on the preliminary data recorded with visible probe photons by varying the polarization of both the pump and probe beams (See Appendix A).

Finally, when measuring in the LT phase, the pump incident fluence values are kept on the order of few hundreds of μJ cm^{-2} which corresponds to an absorbed energy density, E_{abs}[6], of a few tens of J cm^{-3}. This amount ensures that the temperature increase, ΔT [7], caused by the pump photon absorption is never exceeding the transition critical temperature of the LT structural phase and consequently the probed dynamics can be safely assigned to that of the LT monoclinic phase. Therefore, any

[6] E_{abs} is estimated as $\frac{(1-R-T)\cdot F}{d}$, where the optical constants, R and T, and the optical penetration depth, d, at 1.55 eV are calculated from the complex dielectric constant at 80 K [118]. The calculation of d leads to 37 nm both at 80 K and at 295 K.

[7] ΔT is given by $\frac{E_{\text{abs}}}{C_s \cdot m}$ and the specific heat is taken from [58]

change in the phononic response can be attributed to the optical perturbation of the lattice potential rather than to local heating.

The possibility to probe the structural phase transition of Ta_2NiSe_5 using coherent optical phonon spectroscopy with mid-IR optical probe is first verified by measuring the time-resolved mid-IR reflectivity at various sample temperatures both below and above T_C. Fig. 5.4 (a) shows the transient relative change of reflectivity, $\Delta R(t)/R_0$, in the LT phase at 120 K for an excitation density of 0.30 mJ cm^2 (blue curve). The signal intensity is normalized over the mid-IR reflectivity value, R_0, measured independently at equilibrium. The reflectivity variation consists of an incoherent optical response superimposed by an oscillatory part. At the photoexcitation time, the incoherent optical response increases abruptly by approximately 20% and decays on a picosecond timescale. The decay dynamics are well reproduced by a biexponential function convolved with the cross-correlation of the pump and probe pulses, as expressed by Eq. (3.12). The resulting fit is shown as black curve on top of the raw data and will be discussed later in the chapter.

The bare oscillatory optical response is obtained after subtraction of the biexponential fit curve from the raw data and is displayed in Fig. 5.4 (a) (green curve). The signal exhibits fast periodic oscillations superimposed by a slow amplitude modulation. The first are due to the excitation of coherent optical phonons (see Fig. 3.11), the latter results from beating of multiple adjacent oscillating modes. The frequencies of these modes are the retrieved by means of time-integrated fast Fourier transform of the full coherent optical response. In Fig. 5.4 (b), the resulting time-integrated coherent phonon spectrum (green curve) is compared to the inelastic Raman one (black curve) at a sample temperature below T_C. The agreement between the two spectra is very good: **as in Raman spectroscopy, the three phonon modes at 3.0, 3.7 and 4.0 THz are observed. In addition, a coherent phonon mode at 2.1 THz can be resolved**, whose frequency was not accessible in the Raman spectroscopy experiment. The FFT analysis is repeated also on consecutive 2-ps-wide time intervals through the whole time delay window (not shown, see Appendix A for details on this analysis method[8]). This set of FFT spectra (i) do not reveal any frequency shift with increasing the time delay within the experimental resolution, whereas (ii) the relative intensities of the modes changes over time. These findings, respectively, indicate that at the measured temperature and the employed pump fluence, **(i) the phonon relaxation dynamics do not involve softening of the modes and (ii) that the four modes have different lifetimes.**

The coherent phonon spectrum of the HT structural phase at 370 K is shown in Fig. 5.4 (c), together with the Raman shifts at a comparable temperature. Once again, the two techniques return nearly coinciding spectra. In particular, the 2.1 and 4.0 THz phonon modes disappear, as they are not supported by the HT orthorhombic crystal symmetry. Fig. 5.4 (d) shows the temperature dependence of the peak area of the 2.1 and 4.0 THz phonon mode after normalization over the peak area of the 3.0 THz mode[9]. The mode at 3.0 THz is taken as reference because it is present in both structural phases. The excitation density is of 0.44 mJ cm^{-2} for all the data points. Both intensities are maximum and greater than 1 at low temperatures, indicating that the two modes at 2.1 and 4.0 THz dominate the phonon spectrum in the

[8]The same FFT procedure is adopted in Appendix A for the optical data of Ta_2NiSe_5 recorded with visible light probe

[9]The absolute intensity of the coherent phonon spectra cannot directly be compared between measurements at different temperatures due to experimental constraints. For instance, upon temperature changes, different sample spots are probed. Because the sample is cleaved, each spot may have slightly different orientation and thus reflection intensity.

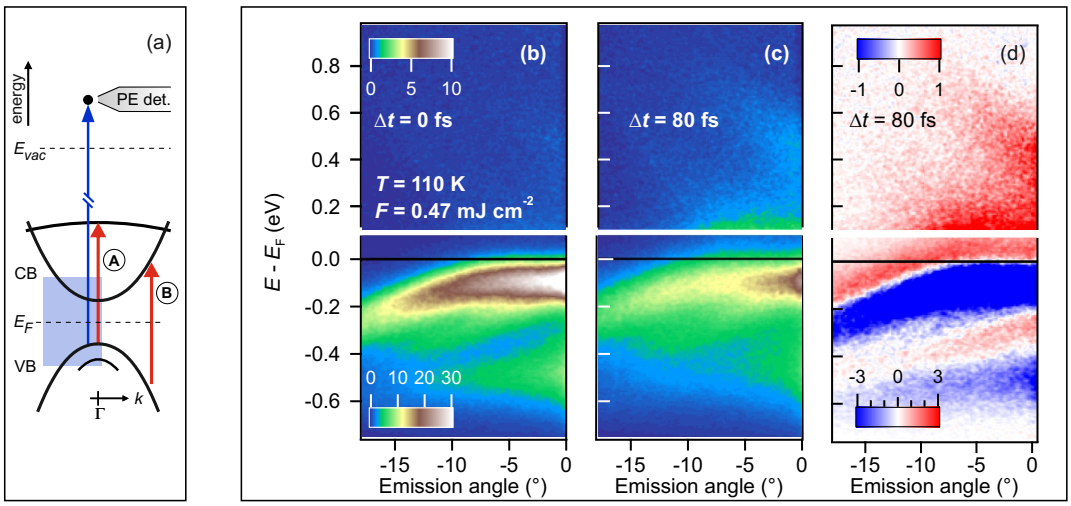

FIGURE 5.5: (a) Schematic band structure of Ta_2NiSe_5 in the LT phase. Blue shade is the energy and momentum region probed by the UV photons. (b)-(c) ARPES spectra of the Ta_2NiSe_5 band structure around Γ at 110 K: at equilibrium, at 80 fs after photoexcitation (c). (d) Differential ARPES spectrum at 80 fs.

monoclinic phase. Upon temperature increase, both amplitudes decrease continuously and eventually vanish above the critical point for the phase transition. Actually, the intensity of the mode at 4.0 THz is already negligible few tens of degree below T_C, in agreement with the temperature dependence of the Raman shift at the same frequency. These results verify that **the mid-IR optical coherent response of Ta_2NiSe_5 allows to follow the heating-induced change of the lattice symmetry with varying the sample temperature. Particularly, the temperature-dependent intensity of the LT phonon modes at 2.1 and 4.0 THz can be assigned as order parameter of the second-order structural phase transition.**

5.2.2 Threshold of near-infrared pump photon absorption at Γ

The near-infrared photon energy used to perturb Ta_2NiSe_5 largely exceeds its optical band gap at Γ, thus electrons are excited into various unoccupied electronic states, leaving a population of holes below E_F. The photoinduced carrier dynamics impact on the transient optical response of Ta_2NiSe_5, and particularly on its incoherent part (cf. Section 3.3.2). To identify the effect on the mid-IR reflectivity at the wavelength of the optical band gap, the perturbation of the electronic subsystem at Γ induced by the near-infrared pump photons is first addressed by means of complementary tr-ARPES and tr-2PPE spectroscopy. These look directly at the initial and final states of the photoexcitation at Γ, respectively. Later, it will be shown that these carrier dynamics launched at Γ directly correlate to the photoinduced variation of the mid-IR incoherent optical response. This finding exceptionally provides momentum specificity to the information carried by the momentum-integrated optical probe. Moreover, it reveals the nature of the mid-IR incoherent optical response of Ta_2NiSe_5.

The scheme of the tr-ARPES experiment is illustrated in Fig. 5.5 (a). As in the coherent optical spectroscopy measurements, near-infrared pump photons at 1.55 eV are employed to optically excite two electronic transitions from the upper VB: (A) to the flat unoccupied d band at Γ, and (B) to the lowest CB, but at larger momenta.

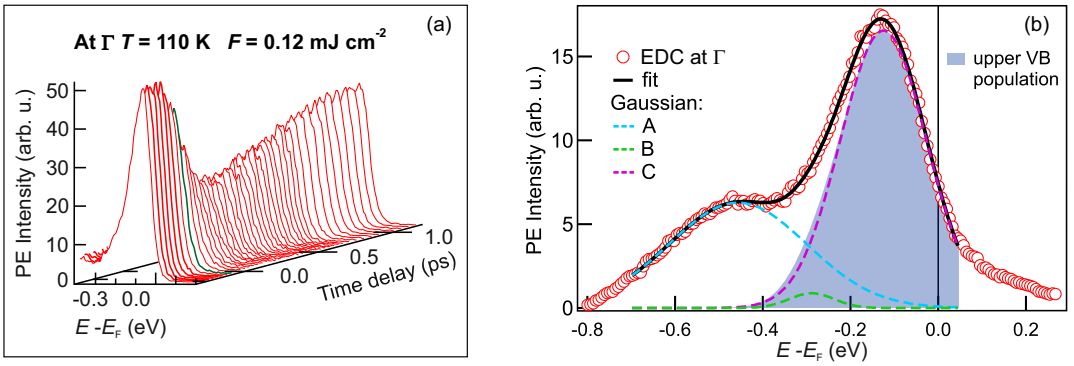

FIGURE 5.6: (a) EDCs at Γ for various time delays. (b) EDC (red markers) analysis: the black curve is the fit, dashed curves are the three Gaussian terms, the blue shade is the upper VB electron occupancy. See text for details.

The out-of-equilibrium occupied and unoccupied electronic band structure in the momentum interval near the Γ point (blue-shaded region) is monitored by time-resolved ARPES using $h\nu = 6.20$ eV probe photons. Notably, the part of the band structure involved in the transitions (B) cannot be directly monitored by photoemission because it lies outside the momentum interval accessible to the probe pulses.

The equilibrium electronic band structure of Ta_2NiSe_5 at 110 K is reported in Fig. 5.5 (b) as a function of energy (left axis) with respect to E_F and emission angle (bottom axis) relative to the surface normal. It exhibits the two VBs with maxima at $E - E_F \approx$ -0.5 and -0.1 eV, respectively, as presented in Fig. 5.2. The photoexcited electronic band structure at the early time delay of 80 fs is displayed in Fig. 5.5 (c). It shows that the PE intensity of both VBs is strongly suppressed, and concurrently, some spectral weight is transferred from much lower occupied electronic bands (not probed) into the low-energy CBs around Γ. As the latter intensity is much weaker, two color scales are used for the occupied and unoccupied electronic band regions, as indicated by the respective legends. The effects of the near-infrared pump pulse on the band occupancy around Γ is even more evident in the differential spectrum on Fig. 5.5 (d) obtained by subtracting the PE intensity at equilibrium from the photoexcited spectrum at 80 fs. The differential spectrum exhibits, below E_F, a depopulation (blue) with respect to the equilibrium occupancy which is remarkably strong for the upper VB. Above E_F, a positive (red) PE intensity reveals a population of photoexcited electrons in the two dispersive CBs (cf. Fig. 5.2).

The transient changes of occupancy of the upper VB at Γ, which is induced by the transition (A), is focus of the following analysis. The effect is first qualitatively shown in Fig. 5.6 (a) by a set of energy distribution curves (EDC) extracted at various time delays. The data is recorded at 110 K, upon a near-infrared photoexcitation of 0.12 mJ cm^{-2}. The spectral intensity decreases at the excitation time (green spectrum) and recovers almost completely to that of the equilibrium spectrum within 1 ps. The abrupt intensity suppression is expected for occupied electronic states which are partially depleted by the excitation of electrons above E_F. The intensity recovery is due to the re-population of the VB during the electron relaxation. In order to evaluate both the abrupt depopulation of the upper VB at Γ and the timescale of its re-population, the transient electron occupancy is extracted from the data as described in the following. Each EDC between $E - E_F =$ -0.70 and +0.05 eV is modeled by a sum of three Gaussian functions multiplied by the FDD and convolved

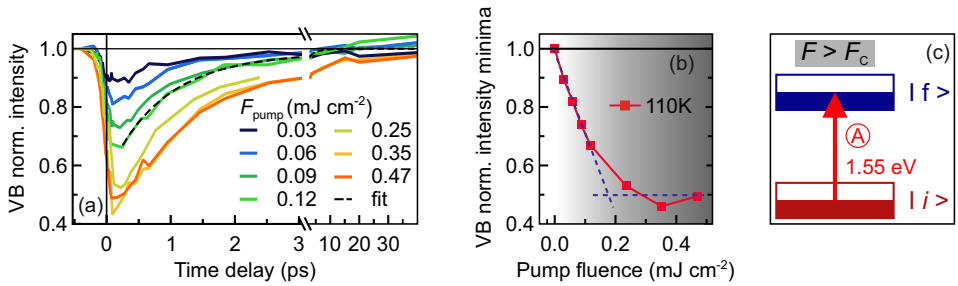

FIGURE 5.7: (a) Transient electron population of the upper VB at Γ at various fluences. The black line is the single exponential fit.(b) Minima from (a) as a function of pump fluence: Above $F_C = 0.2$ mJ cm^{-2}, the VB depopulation saturates at 50%. Dashed lines are linear fits. From [36]. (c) Two-level system with half-depleted the initial state $|i\rangle$ displaying the condition for pump photon absorption saturation at Γ in Ta_2NiSe_5.

by the instrumental response, as exemplified by the black solid curve in Fig. 5.6 (b)[10]. Then, the electron occupancy of the top-most VB at each time delay is obtained from the integral intensity of the relevant spectral peak (blue shade in Fig. 5.6 (b)) which is described by:

$$\left(\left(\sum_i \mathrm{A}_i \cdot e^{\frac{-(E-E_i)^2}{w_i^2}}\right) \cdot \frac{1}{e^{\frac{E-E_\mathrm{F}}{\mathrm{k_B}T}}+1}\right) * e^{\frac{-E^2}{(\Delta E)^2}}. \tag{5.1}$$

where i = B, C, i.e. the sum runs over the two Gaussian accounting for the asymmetric line shape of the upper VB. In Eq. (5.1), the parameters of the two Gaussian functions, B and C, the FFD and the Gaussian instrumental function are taken from the best-fit results of the complete spectrum.

The transient electron population of the upper VB at Γ is displayed in Fig. 5.7 (a) for different incident pump fluences. Each signal is normalized to its value at the earliest negative delay, i.e. to the electron occupancy at equilibrium. **With increasing the excitation density, the VB is further depopulated**. Moreover, if the transients are normalized to the intensity minimum at the lowest pump fluence (not shown), it is noted that **the recovery of the equilibrium electron occupancy slows down with increasing the excitation density.** Both fluence-dependent behaviors are quantified in the following.

Fluence-dependent VB depopulation The average intensity around the minimum of each curve in Fig. 5.7 (a) provides an estimate of the abrupt depopulation of the upper VB at Γ at the respective excitation density. This quantity is shown in Fig. 5.7 (b) as a function of pump fluence. Already at the lowest excitation densities, the electron occupancy decreases by few tens of percents. The depopulation scales linearly with the pump fluence up to a critical value $F_C = 0.2$ mJ cm^{-2}. Above this critical excitation density, the depopulation of the upper VB at Γ saturates at ≈ 50% of the equilibrium occupancy and does not further evolve. This massive depopulation reveals that **at Γ, the low density of states of Ta_2NiSe_5 in the vicinity of E_F allows for a dramatic suppression of the VB occupancy upon resonant excitations with 1.55 eV pump photons.** Furthermore, during the excitation, i.e. within the pump pulse duration, these optical transitions occur as in **a two-level**

[10]More details on the spectral analysis can be found in Appendix B.

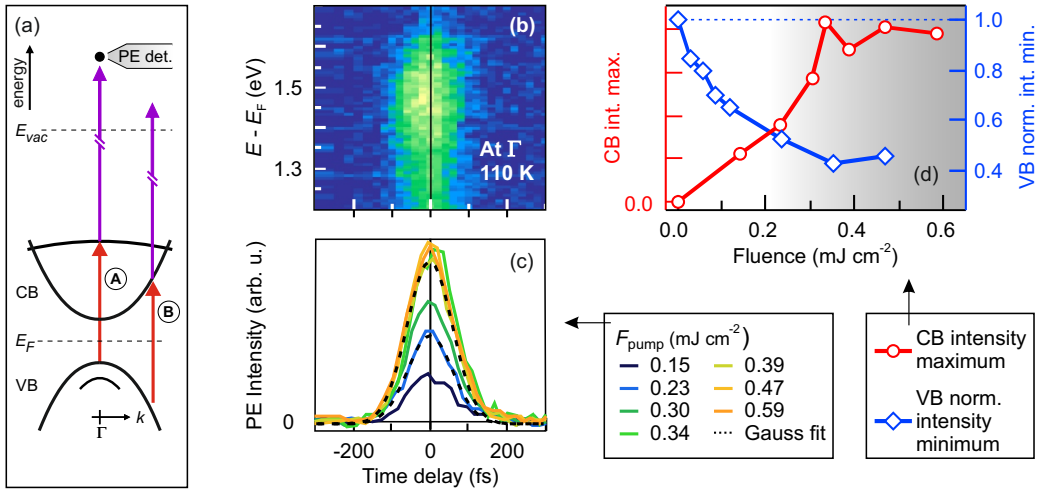

FIGURE 5.8: (a) Scheme of the time-resolved 2PPE experiment. (b) Transient 2PPE intensity at Γ as a function of intermediate energy, $E-E_F$and (c) energy-integrated cross-correlation at various pump fluences. The dashed curve are the Gaussian fits. (d) CB population (red) and corresponding VB as a function of pump fluence. See text for details

system: once the initial state is depleted by half of the equilibrium population, the optical absorption reaches a saturation threshold and the number of excited electrons remains constant even for larger pump photon fluences (see Fig. 5.7 (c) and cf. Fig. 3.8).

In order to test this hypothesis, the population of the corresponding final state of the transition (A) is investigated as a function of excitation density. When considering the unoccupied electronic band structure at Γ, it is noted that a flat d band is energetically resonant with the transition (A) (cf. Fig. 5.2). Its transient PE intensity is then measured by means of time-resolved 2PPE spectroscopy. The scheme of the experiment is shown in Fig. 5.8 (a): after excitation at 1.55 eV, probe pulses with 5.28 eV photon energy monitor the transient electron population of both the flat d band at Γ and the dispersive CB at $k \neq 0$. The energy- and time-resolved PE intensity of the flat d band at Γ is displayed in Fig. 5.8 (b) and reveals a short-lived population excited between approximately 1.3 and 1.6 eV above E_F.

After integration between 1.3 and 1.6 eV above E_F, the transient PE intensity is displayed in Fig. 5.8 (c) for various pump fluences. All transients can be simply fit by a Gaussian function[11] (dashed black), indicating that the occupancy of this electronic band is pulse-duration limited at all excitation densities (cf. Subsection 3.2.2). For this reason, the integral of the cross-correlation intensity can be interpreted as the total occupancy of the electronic band during the pulse excitation. The latter is plotted in Fig. 5.8 (d) as a function of excitation density and is compared with the occupancy minimum of the corresponding initial state, i.e. the upper VB at Γ previously evaluated by time-resolved ARPES. At modest excitation densities, as long as the initial state is depopulated proportionally to the increasing pump fluence, the CB population builds up linearly. For pump fluences higher than F_C, i.e. as the VB is half-depleted within the pulse duration, the increase of CB population reduces. Thus, **the occurrence of optical absorption saturation at the upper VB at Γ is**

[11]The Gaussian accounts for the cross-correlation between the pump and probe pulses and its full width at half maximum provides the upper limit $\Delta\tau_{UL}$ of the temporal resolution (cf. Subsection 3.6.3)

corroborated by a reduced occupation of the resonant CB. The absence of a complete intensity saturation in the final state possibly originates from intraband scattering of electrons that are excited into the flat d band in the proximity of Γ but outside the chosen momentum interval of integration.

Fluence-dependent recovery time of the VB population Upon photoexcitation, various unoccupied electronic bands are populated at different momenta by the near-infrared pump photons. Consequently, the carrier relaxation should involve several scattering processes that will take place on distinc characteristic time scales. These processes include intra- and interband scattering of free electrons and holes with, e.g. charge carriers and phonons, and on a longer timescale, electron-hole recombination and phonon-phonon scattering allowing the system to fully equilibrate. As described in Section 2.2, the rate of all these processes depends on both the number of excited free carriers, transiently modifying the screening of the Coulomb interaction, and the available scattering phase-space. As a result, the relaxation time should vary with the excitation density.

Based on these observations, the re-population of the upper VB at Γ is expected to be described by a multiexponential fit function accounting for the various scattering processes. Moreover, the time constants relevant to each decay process should exhibit a dependence on the pump fluence. All the transients reported in Fig. 5.7 (a) are indeed well fitted by a biexponential function at time delays following the maximum intensity drop, as indicated by the black dashed curve. In the range of employed pump fluences, the fast decay time ranges between 540 and 1160 (± 110 fs). The slow decay component is on the order of 20 ps.

The fit results confirm that the recovery of the equilibrium VB electron occupancy involves distinct scattering processes taking place on different timescale. Furthermore, the dynamics become slower with increasing the excitation density. This can be explained by a transient increase of the Coulombic screening and a reduction of the scattering phase space. Notably, the role of screening and scattering phase space will be focus of the discussion about the relaxation dynamics of the photoexcited electrons in the CB. This topic is presented in details in Section 5.4.

In conclusion, upon near-infrared photoexcitation, the upper VB at the Γ point, whose density of states at equilibrium is rather low, is massively depopulated. A saturation threshold for the absorption of the pump photons at Γ is even reached for fluences exceeding $F_C = 0.2$ mJ cm^{-2}. The top of the upper VB corresponds to the main initial state of the mid-IR optical transitions probed in the optical spectroscopy experiments. Consequently, the present findings have important implications on the transient incoherent optical response which is subject of the following discussion.

5.2.3 The mid-IR incoherent optical response probes the hole dynamics at Γ

The mid-IR incoherent optical response is now analyzed and compared with the previously discussed hole dynamics at the top of the upper VB top at Γ. The incoherent component of an optical signal is usually interpreted as fingerprint of the pump induced carrier dynamics. Actually, as discussed in Section 3.3.2, the time-resolved incoherent optical response signal measures the transient change of the susceptibility function at the frequency of the probe photon, where the changes are mostly due to pump-induced intraband and interband optical transitions. Thus, the previous assumption is rigorously applicable if the dynamics of the probed resonances can be correlated to that of the carrier population measured by photoemission with absolute

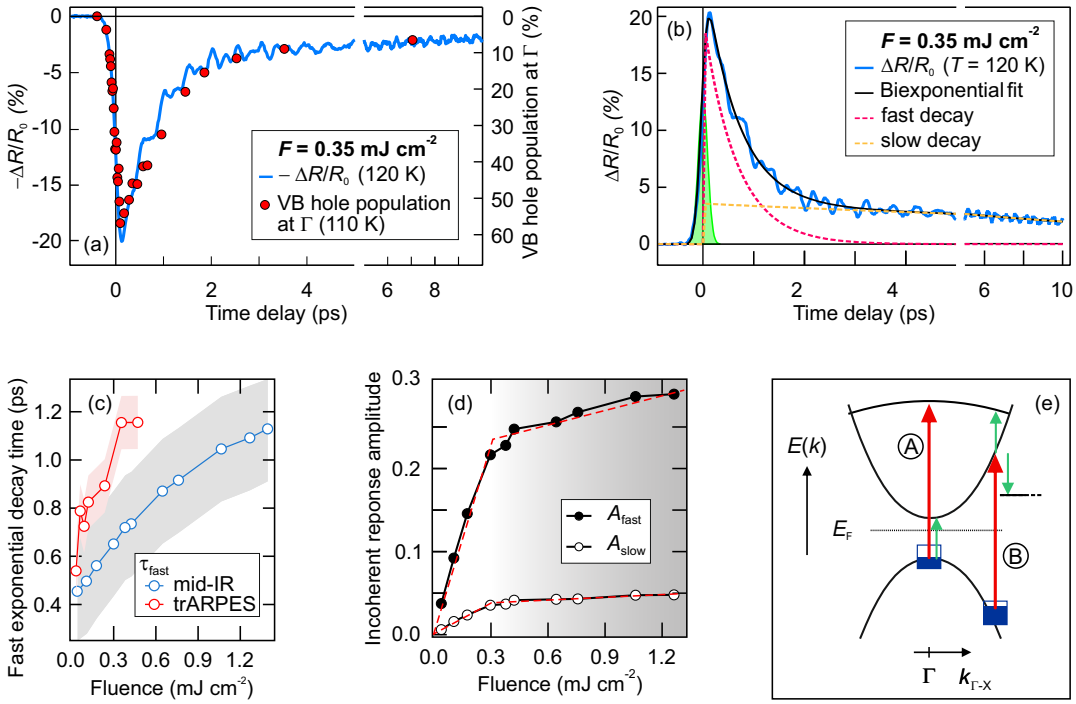

FIGURE 5.9: (a) Time-resolved mid-IR reflectivity change (blue curve) and transient VB hole population at Γ upon comparable photoexcitation of the LT phase. (b) Fitting of the mid-IR incoherent optical response with a biexponential function (solid black). The purple and orange dashed curves are the two exponential components for the fast and slow decay dynamics, respectively. The green Gaussian is the cross-correlation of the pump and probe pulses. (c) Fluence dependence of the fast decay time constant of the incoherent optical response (blue circles) and the VB hole population (red circles). Shades are the error bars. (d) Initial amplitudes of the fast and slow decay dynamics of the incoherent optical response as a function of pump fluence and broken line fits (dashed curves). Modified from [60]. (e) Scheme of the two optical excitations at Γ and at $k \neq 0$ and related mid-IR probe resonances. See main text for details.

energy and momentum resolution. This effort is achieved in this thesis work and is presented in the following.

Fig. 5.9 (a) shows the time-resolved mid-IR optical response (blue curve) at 120 K upon photoexcitation with 0.35 mJ cm^{-2} near-infrared pump photons. Remarkably, the signal agrees very well with the temporal evolution of the hole population of the upper VB at Γ (red circles) recorded upon the same 1.55 eV photoexcitation density and at a comparable temperature. This finding indicates that **the incoherent optical response at the wavelength resonant to the electronic band gap directly correlates with the hole dynamics occurring at the upper VB in the vicinity of E_F.**

The incoherent optical signal is accordingly described by a biexponential function (see Eq. (3.12)) whose fit curve (black solid) is displayed in Fig. 5.9 (b) on top of the raw data (blue). The two components of the fit are exemplified in the graph by the purple and orange dashed curves. The green Gaussian curve is the cross-correlation of the pump and probe pulses[12]. The fit can reproduce the incoherent optical response very well and allows one to identify a fast and a slow timescale for

[12]The experimental temporal resolution is estimated by the time-resolution limited increase in the incoherent response at time zero on Ta_2NiSe_5 and on a VO_2 reference sample.

the signal recovery on the order of 1 and 15 ps, respectively, thus comparable with the decay time constants of the upper VB hole population at comparable pump fluence.

As a function of the excitation density, both decay time constants of the incoherent optical response are found to increase, consistent with the results for the hole relaxation in the upper VB. The fluence dependence of the fast decay time is shown in Fig. 5.9 (c) (blue markers). The slow decay dynamics behave qualitatively the same. The fast decay time increases continuously with increasing pump fluence, although with a slightly reduced slope at the higher fluence values. The parameter is compared with the fast decay time constant of the hole population decay (red markers) and a good agreement is observed at all fluence values within a factor less than 2, further confirming the correspondence between the dynamics of the two observables.

The amplitudes of the two decay components account for the mid-IR reflectivity variation at the photoexcitation time. Their fluence dependence is reported in Fig. 5.9 (d): Both amplitudes increase with increasing the excitation density. Remarkably, their fluence dependence exhibits a slope change and two linear regimes are identified: (1) at low fluence values, the amplitudes rapidly increase for higher excitation density; (2) above a common fluence value, the slope of both curves is drastically reduced, though without completely flattening. A broken line fit (dashed red line) reveal that **the excitation-density dependence of the incoherent response strongly decreases above the critical fluence $F_C = 0.30 \pm 0.08$ mJ cm^{-2}. Notably, this value is comparable with the saturation threshold for the pump photon absorption at Γ revealed by time-resolved ARPES. This aspect further corroborates the correspondence between the hole dynamics at the top of the upper VB and the transient change of mid-IR incoherent optical response.** The discrepancy between the two values of the critical fluence can be justified by noting that both values refer to the incident, not the absorbed fluence. Optical and photoelectron spectroscopy are being bulk and surface sensitive, respectively. Consistently, the value obtained via optical probe is higher than that found with tr-ARPES, as result of the larger probed volume.

The fact that both amplitudes slightly continue to increase above F_C indicates that other mid-IR resonances marginally contribute to the incoherent optical response and that these resonances are not affected by the pump photon absorption saturation at Γ. Therefore, these resonances are most likely initiated from excited states that are transiently populated at $k \neq 0$, i.e. by means of transitions (B). This is exemplified in Fig. 5.9 (d). Consequently, it is inferred that transitions (B), which were not probed by the UV photons in the time-resolved ARPES experiment, do not reach saturation above F_C. In conclusion, the analysis of the mid-IR incoherent optical amplitude as a function of excitation density reveals that **limited energy can be imparted on the system via transition (A) due to the rapidly achieved saturation of pump photon absorption. On the other hand, the channel (B) at $k \neq 0$ remains open for further excitation above F_C.**

Thus, this compelmentary photoemission and optical spectroscopy study allows to definitely assign the main contribution of the mid-IR incoherent optical response to the photoinduced hole dynamics occurring at the Γ point of the Brillouin zone, where the electronic band gap opens. Additionally, it reveals that the charge carrier population photoexcited via transitions (B) at momenta $k \neq 0$ continues to build up with increasing the pump fluence. Consequently, as depicted schematically in Fig. 5.9 (e), two excitation regimes below and above F_C are identified: Below F_C, both transitions, (A) and (B), increasingly contribute to excite free carriers with increasing the fluence of the pump pulse. Above F_C, while at vectors $k \neq 0$ the situation is unchanged, the

contribution of the transition (A) remains constant due to the absorption saturation of pump photons. Clearly, depending on how the optical coherent phonons are activated in the system, i.e. how they couple with the photoinduced electronic transitions, the discussed carrier dynamics will impact on the photoinduced lattice dynamics, and eventually, on the possibility to optically induce the structural change.

5.2.4 Blocked photoinduced structural phase transition

The photoinduced dynamics of the lattice in the LT monoclinic phase is now investigated. In particular, the evolution of the mid-IR coherent response is analyzed as a function of the excitation density and connected to the concurrent carrier dynamics monitored by the incoherent optical signal.

The FFT spectrum in Fig. 5.4 (b) indicated that the coherent optical response of the LT phase is the superposition of four optical phonon modes. Accordingly, the signal at 120 K is well reproduced by a sum of four damped cosine oscillations (see Eq. (3.13)), as exemplified in Fig. 5.10 (a) by the black dashed curve. The initial amplitude, the frequency, the phase and the lifetime of each phonon term are taken as free parameters and the fit is applied to the data points starting from approximately $\Delta t = 0.5$ ps after photoexcitation, i.e. where the modulation of the signal is not altered by the subtraction of the intense incoherent background.

The best-fit parameters of each phonon oscillation allows to reconstruct the nonequilibrium structural phase on Ta_2NiSe_5 and their fluence dependence to infer on the photoinduced lattice dynamics as a function of excitation density. The initial phase of all modes is approximately an integer multiple of π independently on the excitation density (not shown). Consequently, the phonon oscillations are of cosine type, with their maximum amplitude close to time zero. This indicates that the atomic motion is predominantly activated via non-resonant displacive excitation of coherent phonons [153].

Fig. 5.10 (b) reports the frequency of each mode as a function of pump fluence. All modes retain the same frequency over the whole excitation density range, except for a slight redshift of the 4.0 THz phonon mode which softens by about 0.2 THz at the highest pump fluence values. This shifting behavior is on the order of that observed in the temperature dependent Raman measurements (see Fig. 5.1). Analogously, the effect is likely due to thermal expansion of the sample and anharmonic coupling between phonons rather than a photoinduced macroscopic symmetry change. Indeed, the latter is usually combined with a complete phonon softening down to zero frequency (See, for instance, the case of charge-density-wave materials undergoing a structural phase transition [189, 190, 115]).

In the following, the initial amplitude and the lifetime of the phonon modes are analyzed as a function of pump fluence. In particular, the phonon amplitude can be interpreted, in most cases, as a marker of the structural phase of Ta_2NiSe_5 at the time of the photoexcitation. As a consequence, if the photoinduced structural phase transition occurs abruptly, the amplitudes of the LT phonons at 2.1 and 4.0 THz -as spectators of the LT crystal symmetry- will decrease with increasing the excitation density and eventually vanish if the energy threshold for the lattice change is reached upon photoexcitation. Otherwise, the phonon amplitude will remain finite at any pump fluence. In this case, the persistence of the LT crystal phase after photoexcitation is quantified by the lifetime of the 2.1 and 4.0 THz LT phonon modes that is taken as lower boundary [191]. The phonon amplitudes are shown in Fig. 5.10 (c) as a function of excitation density: they all rise linearly with the excitation density, indicative of an increase of the phonon occupancy at the respective frequencies. However, once

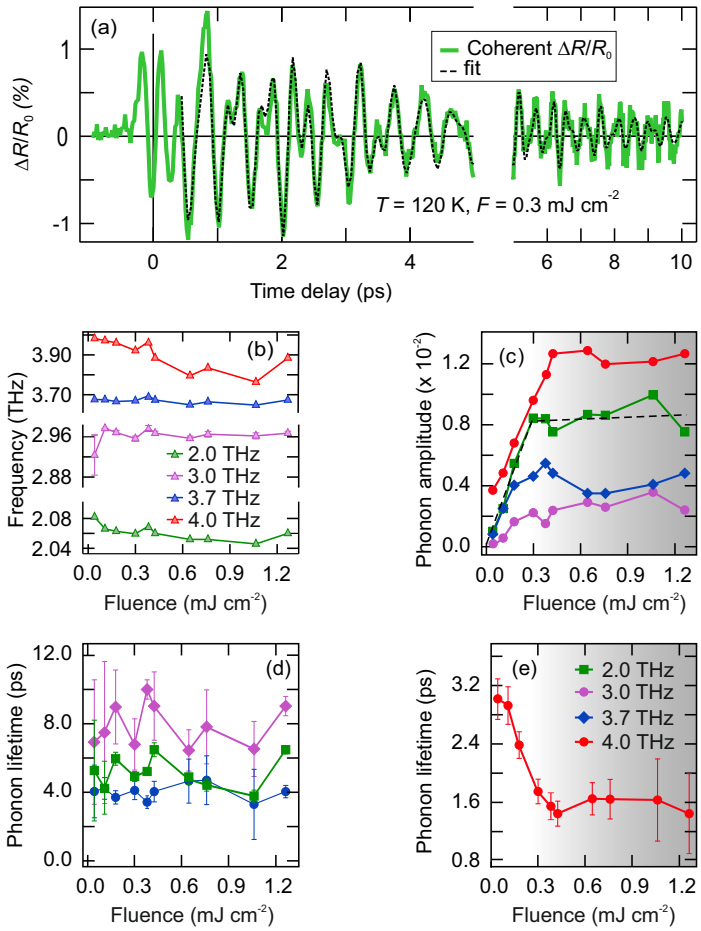

FIGURE 5.10: (a) Bare mid-IR coherent optical response in the LT phase as a function of time delay (green curves) and relative fit curve (dashed black curve). Fluence dependence of the fit parameters modeling the coherent optical response at 120 K: (b) frequencies, (c) amplitudes, and (d)-(e) lifetimes of phonon modes. Modified from [60].

the saturation threshold of pump photon at Γ is reached at $F_C = 0.30 \pm 0.08$ mJ cm^{-2}, all amplitudes settle at a constant value. In particular, none of the LT phonon modes exhibits any amplitude decrease regardless the fluence of the incident pump photons. These findings provide two evidences: on the one hand, **the excitation of all coherent phonons occurs via the transition (A), i.e. through the coupling with charge carriers excited from the upper VB at the Γ point.** On the other hand, **the transition to the HT structural phase does not occur within the pulse duration**.

The lifetime of the phonon modes specific of the LT phase is now examined in order to verify if the transition is driven nonthermally on a longer timescale. The best fit parameter of all the excited coherent phonons is reported in Fig. 5.10 (d) and (e) as a function of pump fluence. The lower-frequency modes have a lifetime that ranges from 4 to 8 ps and is independent of the excitation density within experimental accuracy. On the contrary, the lifetime of the LT phonon mode at 4.0 THz is approximately 3 ps at the lowest excitation density and shortens linearly as the pump fluence is increased towards F_C. However, for $F > F_C$, the 4.0 THz phonon lifetime does not go to zero but remains constant at 1.57 ± 0.11 ps. Thus, rather long lifetimes of both the LT phonon modes at 2.1 and 4.0 THz are observed even for the highest

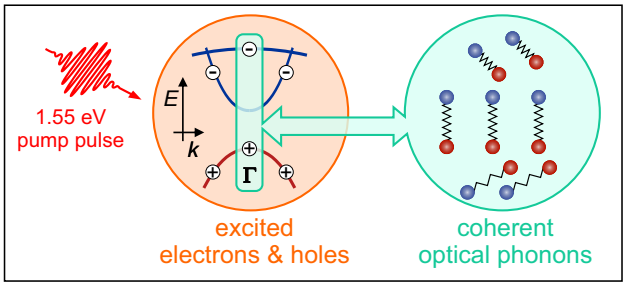

FIGURE 5.11: Activation mechanism of coherent optical phonons in Ta_2NiSe_5 upon photoexcitation with near-infrared (1.55 eV) pulses. Only the excitation of carriers at $k = 0$, which mostly involve charge transfer from Ni to Ta orbitals (cf. Fig. 2.16), couple to the phonon subsystem.

excitation densities, indicative of a long-lived LT crystal symmetry and the **absence of a nonthermally-induced transition to the HT crystallographic phase upon near-infrared photoexcitation**. Furthermore, the unique fluence dependence of the lifetime of the 4.0 THz phonon discloses that this mode decays selectively via scattering with charge carriers excited at the center of the Brillouin zone. This result is quite remarkable given the intrinsic momentum-integration of an optical probe. In fact, the achievement of this information relies on the presented comparison the optical response, being simultaneously sensitive to lattice displacements and carrier density variations, and the photoemission signal, probing the carrier dynamics with momentum resolution.

At this point is worth noting that the coupling between the coherently excited optical phonons and the photoinduced charge carrier distribution at Γ in the vicinity of E_F is also disclosed by time-resolved ARPES, as reported in details in Appendix C. In the tr-ARPES spectra, the coupling to phonons manifests as a periodic modulation of both the spectral position of the upper VB maximum and the transient photoemission intensity around the Fermi level. In particular, both quantities oscillate at the dominant frequency of 2.1 THz, in agreement with the coherent phonon spectrum of the LT phase. Remarkably, the oscillation is clearly resolved upon photoexcitation above F_C, consistent with the persistence of the LT structural phase.

In summary, near-infrared photons cannot perturb the lattice strongly enough to optically induce the structural change to the HT phase. The inhibition of the photoinduced phase transition originates from a twofold effect: (1) at the excitation time, only part of the absorbed energy is transferred to the lattice through the solely transitions (A) at Γ that are coupled to coherent phonons; (2) these transitions saturate due to **optical absorption saturation, thereby limiting the optical perturbation of the LT structure below the threshold for the structural change**. Consequently, the monoclinic symmetry is preserved and the photoinduced lattice dynamics of the LT phase is investigated without the complication of a concurrent structural change. Finally, the activation mechanism of the coherent phonon dynamics is schematically depicted in Fig. 5.11: the activation of coherent optical phonons occurs in Ta_2NiSe_5 via momentum-specific electronic transitions excited at Γ. These involve the buildup of a hole population in the outermost $4p$ Se-$3d$ Ni valence orbitals upon hopping of electrons into empty $5d$ Ta orbitals. The present study reveals that relaxation of the coherent lattice vibrations is independent on the excitation density produced in the system, except for the phonon mode at 4.0 THz, fingerprint of the

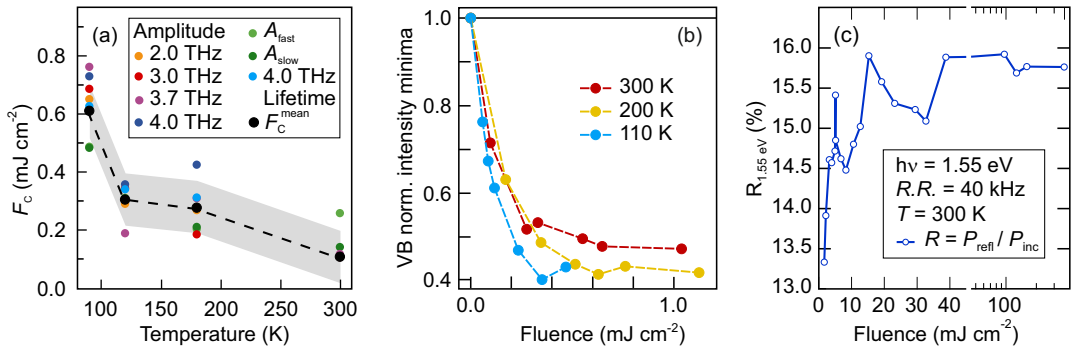

FIGURE 5.12: (a) Temperature dependence of the critical fluence F_C. (b) Temperature dependence of the transient VB population minima at Γ. (c) Fluence-dependent reflectivity at 1.55 eV photon energy and at 300 K.

monoclinic symmetry, whose scattering dynamics directly correlate with the number of holes excited at Γ. Because the latter remains constant above F_C, the LT phonon at 4.0 THz never reaches zero-lifetime. This finding, in combination with the non-vanishing LT phonon amplitude, demonstrate that a nonthermally-induced phase transition is blocked in Ta_2NiSe_5 upon near-infrared photoexcitation.

5.2.5 Robustness of the LT phase against a photoinduced structural change

In many materials [192, 193, 194, 195], the fluence threshold of a photoinduced phase transition depends strongly on the sample temperature and decreases towards T_C, as less energy is necessary to drive the transition in the vicinity of the critical point. Therefore, the question is raised whether by increasing the sample temperature towards T_C, it is possible to observe the photoinduced structural phase transition prior to the occurrence of pump optical absorption saturation. Temperature-dependent coherent optical phonon spectroscopy is thus performed up to 300 K (as reminder, T_C = 328 K). Remarkably, at all temperature, both the reduction of the incoherent optical response, and the saturation of the coherent part manifest above a certain excitation density, indicative of the **lack of photoinduced structural phase transition even close to the instability point.**

The results are summarized in Fig. 5.12 (a) which reports the breaking point of the fluence dependence of all optical observables between 90 and 300 K. At each temperature, similar critical fluence values are observed for all fit parameters, in agreement with the observations at T =120 K. This confirms once more that the dynamics of the lattice and those of the holes at Γ are connected. Therefore, an average F_C is defined which is shown as black circles on the graph (the shaded area is the average error bar). The average F_C reduces by a factor of 6 when the sample is heated from 90 to 300 K. This result reveals a **temperature-dependent absorption saturation threshold for near-infrared pump photons. Consequently, the photoinduced structural change remains inhibited regardless the vicinity to the transition point.**

Notably, the change of saturation threshold between 90 and 120 K is more pronounced than in the higher-temperature range. If this trend would persist for further cooling, at very low temperatures the phase transition may eventually occur as the absorption saturation threshold may be either extraordinarily high or even absent. However, it should be noted that the energy threshold for the phase transition should

also concurrently increase, as the system ground state is moved away from the instability point. This may possibly preserve the system from the photoinduced structural change also at very low temperature. Alltogether, whether the phase transition can be photoinduced close to zero temperature remains for now an open question which may stimulate future investigations.

The temperature dependence of the optical absorption threshold is further verified in the present work in two ways: 1. by means of time-resolved ARPES at different temperatures, and 2. by measuring the fluence-dependent reflectivity at the photon energy of the pump photon (1.55 eV) close to T_C.

1. Fig. 5.12 (d) shows the transient photoemission intensity minimum of the upper VB at Γ as a function of excitation density for three temperature values. Upon heating of the sample towards T_C, the saturation in the VB depopulation continues to manifest and is completed at even lower excitation densities. This indicates that the 'two-level' system behavior of Ta_2NiSe_5 at Γ is very robust upon temperature changes;

2. Fig. 5.12 (d) shows the reflectivity amplitude at 1.55 eV, $R_{1.55\ \mathrm{eV}}$, as a function of the incident laser fluence at 300 K. The signal is given by the power ratio between the reflected and the incident beam. Due to the negligible transmission of Ta_2NiSe_5 at 1.55 eV, the signal can be considered as complementary to the optical absorption intensity. The signal increases slightly with increasing the incident fluence up to a saturation above an incident fluence value of approximately[13] 50 μJ cm^{-2}. This finding ultimately confirms that close to T_C, the optical absorption of Ta_2NiSe_5 at the pump photon energy is very limited.

Therefore, in the low-temperature phase, Ta_2NiSe_5 exhibits a nontrivial temperature dependence of the near-infrared absorption threshold at Γ. Possible origins of this behavior are discussed in the following:

- The continuous shift of the upper VB upon temperature changes [122, 123, 56, 36] may vary the resonant condition for the pump pulse and thus the absorption coefficient at its photon energy. However, this hypothesis is ruled out by temperature-dependent measurements of the dielectric function via optical conductivity [118] and ellipsometry [58]. They show that neither the absorption nor the penetration depth at 1.55 eV depend on the temperature.

- F_C may change due to temperature-dependent variations of rate of free-carrier scattering within the pump pulse duration. At high temperature, more scattering events with, e.g. thermally-activated phonons and hot carriers can depopulate the excited states more rapidly and re-enable the absorption of pump photons within the pulse duration. As a result, the absorption saturation threshold would increases. As this behavior is opposite to the experimental evidences, it cannot be the dominating effect.

- Upon temperature increase towards T_C, the exciton condensate is partially melted. As a result, the number of mobile carriers increases, thus enhancing the Coulombic screening. Consequently, the hole scattering rate at Γ may decrease and lowers the fluence F_C required to reach half-depletion of the upper

[13] It is noted that the reported value is smaller than the one obtained for the transient mid-IR optical response. The discrepancy relies on the uncertainty in the measurements of the laser fluence (the two experiments have been independently performed) and on the effective temperature of the illuminated sample spot which is likely to be higher because no feedback cooling is used in this measurement.

VB at Γ. It is noted that this mechanism leads to a temperature dependence of F_C in agreement with the experimental observation.

In conclusion, the LT monoclinic phase of Ta_2NiSe_5 is proven to be very robust against a photoinduced change and the effect relies on an excitation threshold never exceeding the energy required for the phase transition even if the sample is heated up close to T_C. Further investigation are required to ultimately confirm that the mechanism relies on the hole scattering rate excited at the Γ point. In particular, it is proposed that upon heating the hole scattering slows down because of more efficient screening of the Coulomb interaction. This mechanism would remarkably set a connection between the nonequilibrium properties of the excitonic insulator ground state and the lattice dynamics in Ta_2NiSe_5 launched by near-infrared photons.

5.3 Ultrafast electronic band gap control

In Ta_2NiSe_5, the topmost VB at equilibrium and in the LT phase shifts continuously towards E_F when the temperature is increased towards $T_C = 328$ K (cf. Section 2.7 and Section 5.1.2). It was shown earlier in this chapter that the CB shift oppositely, thus the direct electronic band gap is effectively reduced upon heating (cf. Section 5.1.2). This was the first direct measurement of the electronic band gap narrowing in Ta_2NiSe_5. In the context of this electronic phase transition, theoretical modeling of the LT phase of Ta_2NiSe_5 shows that the electronic band structure in the vicinity of E_F results from a semiconducting ground state superimposed by an excitonic coupling connecting the VB and CB extrema (cf. Subsection 2.6.1 and Subsection 2.7.2). However, at equilibrium it is challenging to disentangle the thermal evolution of the excitonic order parameter from that of the underlying semiconductor band gap. Also, static measurements cannot predict how the dynamics of electronic band gap occur when the system is perturbed by an ultrashort optical excitation and if they show analogy with the thermally induced behavior of the band gap.

The nonequilibrium dynamics of both the occupied and unoccupied electronic band structure of Ta_2NiSe_5 in the LT phase are studied here by means of time-resolved ARPES and 2PPE spectroscopy. This allows to infer the evolution of the electronic band gap following an ultrashort near-infrared photoexcitation (1.55 eV). In particular, two excitation density regimes are identified, whose separation threshold is defined by the absorption saturation of pump photons at Γ (cf. Section 5.2.2). Below F_C, the band gap narrows. This renormalization is explained by the transient enhancement of the screening of the Coulomb interaction by means of the photoexcited carriers, consistent with the behavior of a photoexcited semiconductor. Above F_C, a unique energy downshift of the upper VB at Γ is observed, which is not present elsewhere in the Brillouin zone. This observation indicates a widening of the excitonic insulator band gap which is explained by a nonequilibrium strenghtening of its order parameter. Therefore, the effect of the excitonic condensate on the photoinduced band structure dynamics of Ta_2NiSe_5 is experimentally singled out in the momentum and time domain from the contribution of the semiconducting normal phase. These arguments are supported by Hartree-Fock model calculations of a two-electronic-band system with a momentum-dependent excitonic coupling.

The renormalization of the semiconductor bang gap is presented in Subsection 5.3.1, the enhancement of the excitonic insulator order parameter is discussed in Subsection 5.3.2 and the theoretical calculations are reported in Subsection 5.3.3.

5.3.1 Photoinduced reduction of the electronic band splitting

The LT nonequilibrium electronic band structure of Ta_2NiSe_5 at $T = 110$ K is studied in different energy and momentum regions which are indicated by circled numbers on top of the ARPES (bottom) and 2PPE (top) spectra in Fig. 5.13 (a). These correspond to ① the maximum of the lower VB around the Γ point (i.e. at zero emission angle), ② the dispersive part of the upper VB at -13° emission angle, ③ the flat top of the upper VB around Γ, and ④ the dispersive part of the second lowest CB at -8° emission angle. It is noted that the lowest CB spectrally overlaps with the secondary electron background, preventing robust quantitative analysis of this CB, while the second-lowest CB is well resolved at emission angles close to zero (i.e. close to the Γ point). The red, yellow and orange bars indicate the momentum intervals in which the time-resolved PE data are evaluated.

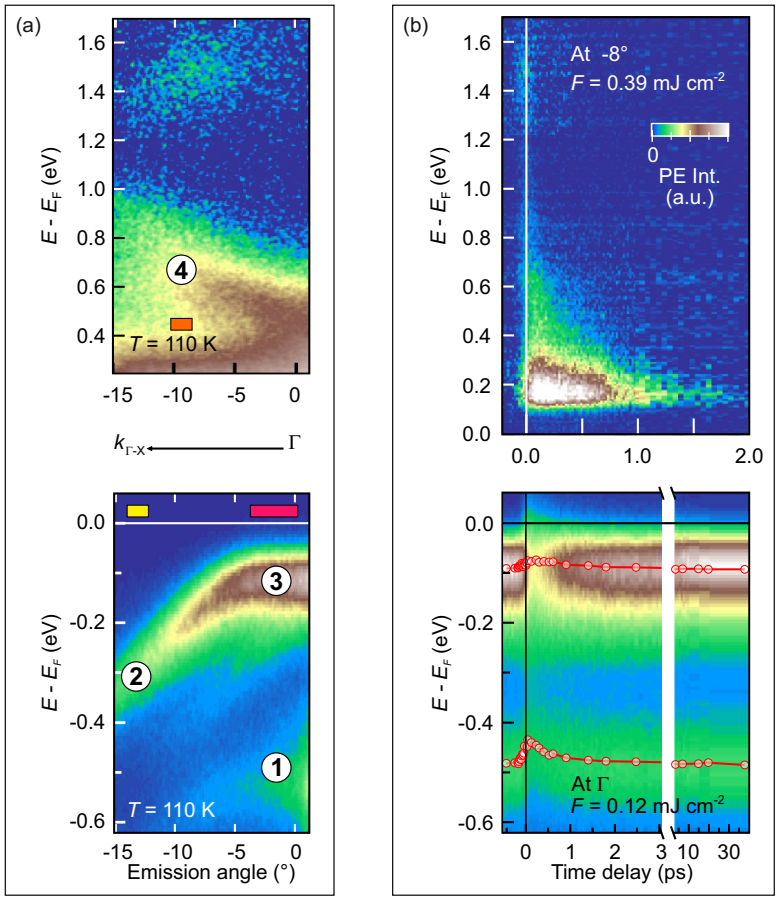

FIGURE 5.13: (a) ARPES (bottom, $h\nu$ = 6.20 eV) and 2PPE (top, $h\nu$ = 5.28 eV) spectra of Ta_2NiSe_5 at 110 K as a function of electron energy and emission angle. (b) Time- and energy-resolved PE intensity in false colors of the occupied (bottom) and unoccupied (top) electronic states at 110 K at normal incidence and at -8° emission angle, respectively. The pump photon energy is 1.55 eV. Both static ARPES spectra are modified from [36].

In the present subsection, the analysis focuses on the ①, ② and ④ parts of the band structure, which are expected to be less affected by the excitonic coupling, and thus should mostly reflect the nonequilibrium behavior of the bare semiconducting Hamiltonian (cf. Subsection 2.7.2). Fig. 5.13 (b) shows the transient photoelectron intensity of the occupied electronic states at Γ (bottom) and the unoccupied ones at -8° (top) as a function of energy with respect to E_F (bottom axis) and pump-probe time delay (left axis) following the photoexcitation with $h\nu$ = 1.55 eV pump photons (cf. experimental scheme in Fig. 5.5 (a) and Fig. 5.8 (a), respectively). Below E_F (bottom) and at negative time delay, the two VBs at equilibrium are measured by 6.20 eV probe photons at $E - E_F \approx$ -0.5 eV and -0.1 eV, respectively (cf. Fig. 5.2). At time zero, when the pump pulse excites the sample, their PE intensity is reduced, and the effect is particularly strong in the upper VB, as discussed in Section 5.2.2. Concurrently, both VBs shift spectrally towards E_F. At later times on the order of hundreds of femtoseconds, both equilibrium energy positions are restored. The shifting behavior is illustrated for both VBs by the red markers and is found to be more pronounced in the lower VB rather than in the topmost one. The analysis resulting in these data points is detailed later (see main text of Fig. 5.14 (a) and Fig. 5.17 (a)). The time- and energy-resolved 2PPE intensity of unoccupied states at

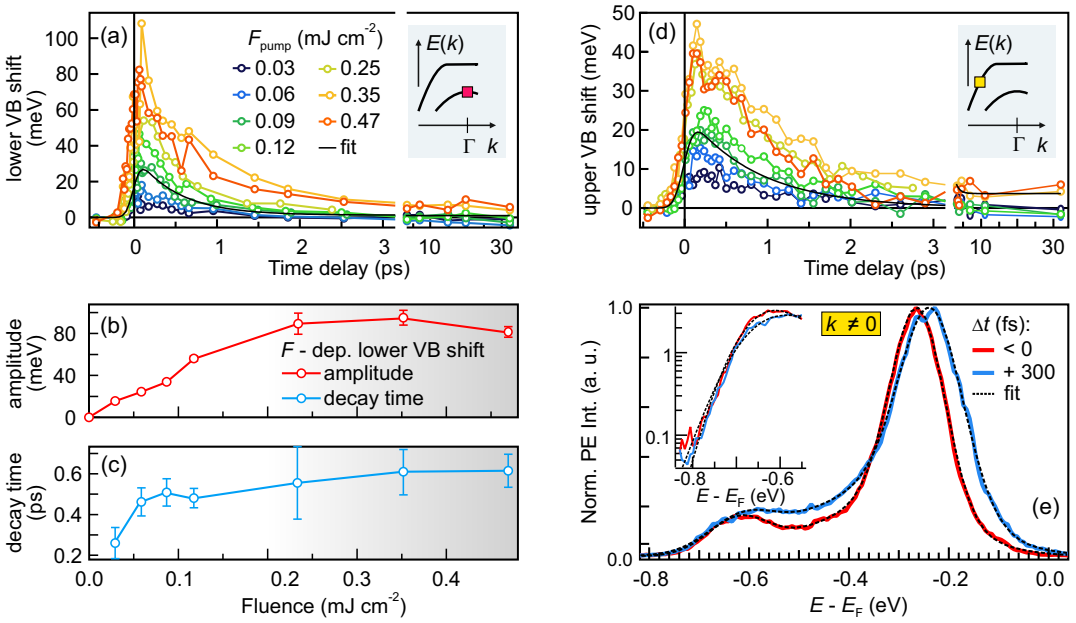

FIGURE 5.14: (a) Transient shift of the lower VB at Γ for different excitation densities. The black line is the single exponential fit to the data convolved with the envelope of the laser pulses. (b) Amplitude and (c) relaxation time of the lower VB shift as a function of pump fluence. (d) Transient shift of the upper VB at -13° for different excitation densities. (e) EDCs at -13° before (blue) and 300 fs (red) after photoexcitation with $F = 0.12$ mJ cm^{-2}. (a) and (d) are taken from [36].

$k \neq 0$ is displayed in Fig. 5.13 (b, top) after subtraction of the noncorrelated intensity at negative time delays. It exhibits three spectral features: at E - $E_F \sim 1.5$ eV, the pulse-duration-limited d band already discussed in Section 5.2.2; at lower energies down to $E - E_F \sim 0.4$, a broad intensity distribution of the dispersive CB, and in the lowest-energy part of the spectrum, the correlated intensity of secondary electrons.

First, the analysis of the occupied states dynamics is discussed. As described earlier in Fig. 5.6 (b), EDCs are extracted at each time delay from the time-resolved PE data at selected momentum intervals and fitted by a superposition of three Gaussian functions multiplied by a FDD function and convolved with the Gaussian instrumental function. These fits provide the transient binding energy of each VB from which the relative transient shifts with respect to the equilibrium energy position are obtained. The transient shift of (1) the lower VB at Γ is reported in Fig. 5.14 (a) for a set of excitation density values. It is evaluated with respect to the equilibrium energy position measured at negative delays. Clearly, the initial shift amplitude increases with increasing pump fluence. However, at the strongest excitations (yellow and red), the amplitude of the abrupt upshift stops to increase. At later times and for all fluences, the upshift reduces again, and eventually, the equilibrium energy position is restored approximately on a one ps timescale. To quantify the abrupt shift and its recovery dynamics, a single exponentially-decaying function convolved with the envelope of the pump and probe pulses (black line) is fit to the data. The best-fit parameters of the initial amplitude and the decay time of the shift are reported in Fig. 5.14 (b) and (c), respectively, as a function of excitation density. The initial VB shift is found to increase proportionally with the excitation density up to the fluence threshold F_C above which pump photon absorption at Γ saturates (gray shade). The time constant for the recovery of the VB equilibrium position shows qualitatively the

same fluence dependence.

The same analysis is repeated at -13° to infer the dynamics of (2) the dispersive part of the upper VB. The results are reported in Fig. 5.14 (d) and show comparable dynamics as that of the lower VB. Indeed, the binding energy with respect to E_F reduces abruptly at the photoexcition time and recovers to the equilibrium value within about 1 ps. Also, the initial energy shift becomes stronger with increasing pump fluence and a saturation is observed for the excitation densities higher than F_C (yellow and red). To confirm that the spectral shift of both the lower VB at Γ and the upper VB at $k \neq 0$ originate from a change of their binding energy and not from a rigid shift of the whole spectrum, two EDCs before (blue) and 300 fs after (red) photoexcitation with 0.12 mJ cm^{-2} are carefully compared in Fig. 5.14 (e). Notably, the comparison applies for all pump fluence values employed. The peak maximum of both VBs is clearly shifted towards E_F at positive delay. Conversely, the low-energy cutoff coincides for the two spectra, indicating that the spectrum does not rigidly shift upon photoexcitation due to, e.g. transient work function changes or a surface photovoltage. Thus, **the binding energy of the occupied electronic states close to E_F reduces upon photoexcitation.** Moreover, the effect is fluence dependent and increases continuously for a larger number of photoexcited holes up to a similar excitation density as the saturation threshold F_C of the pump photon absorption. This strongly suggests that **the observed shifts are connected to the excitation of free carriers at** Γ (i.e. to the mechanism (A) in Fig. 5.5 (a)).

Now, the dynamics of (2) the dispersive CB are investigated. If the CB follows opposite dynamics than the upper VB at comparable momenta, a photoinduced reduction of the electronic band splitting is indeed verified. EDCs of the equilibrium (blue) and excited (red) unoccupied electronic band structure at 8° are displayed in Fig. 5.15 (a). They are extracted from the time-resolved 2PPE data prior to subtraction of the noncorrelated intensity. The spectral intensity of the CB appears in the high-energy part of the spectrum, while the secondary electron distribution dominates the spectrum at much lower energies. As shown by the black dashed curves, the spectra is well fitted by

$$I(E) = \mathrm{erf}\left(\frac{E - E_{\text{cut-off}}}{w_{\text{cut-off}}}\right) \cdot \left[A_{\text{SE}} \cdot e^{-\left(\frac{E-E_{\text{SE}}}{w_{\text{SE}}}\right)} + A_{\text{CB}} \cdot e^{-\left(\frac{E-E_{\text{CB}}}{w_{\text{CB}}}\right)^2}\right], \tag{5.2}$$

where the error function accounts for the low-energy spectrum cutoff, the exponential decay function for the distribution of secondary electrons and the Gaussian for the CB peak. For both spectra, the dashed vertical line of the respective color marks the best-fit energy position of the Gaussian, showing that **the nonequilibrium CB peaks at lower energy relative to E_F than the equilibrium position.** The effect is even clearer when the correlated secondary electron background is subtracted from the spectral intensity, as shown in Fig. 5.15 (b) by the color shaded residual spectra: A spectral weight transfer towards E_F is observed for the peak of the nonequilibrium CB.

This CB spectral weight transfer is studied as a function of time delay and for a set of excitation density by fitting a Gaussian function to the background-subtracted spectra (black solid lines in (b)). The best-fit peak position at each time delay is subtracted from that at equilibrium to obtain the transient shift of the CB. The results for all fluence values are summarized in Fig. 5.15 (c): **upon photoexcitation, the CB spectral intensity is rapidly transferred by few tens of meV towards E_F and recovers its equilibrium energy position on a few hundreds of fs timescale. With increasing pump fluence, the effect is enhanced and the**

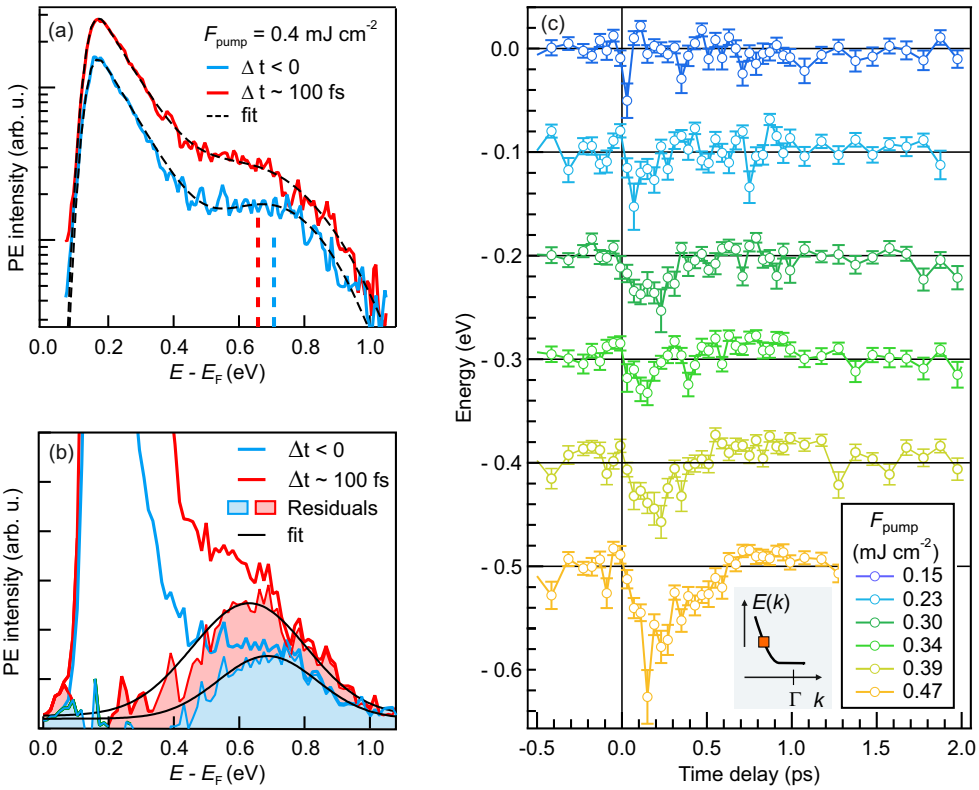

FIGURE 5.15: (a) EDCs before (blue) and after (red) photoexcitation at the 8° emission angle. Dashed line are the fits obtained by Eq. (5.2). (b) Same spectra after subtraction of the secondary electron background. Black solid lines are the Gaussian fits. (c) CB spectral shift as a function of pump-probe time delay for different pump fluences.

recovery delayed. It is pointed out that the same qualitative result is obtained when the non-background-subtracted spectra are analyzed by Eq. (5.2). Moreover, using this fit function it is verified that at time delays following the photoexcitation, a bare change of the transient secondary electron distribution (i.e. keeping constant the energy position of the Gaussian) is not capable to reproduce the nonequilibrium spectrum in the energy region of the CB. Thus, the energy shift of the CB peak is not simply an apparent effect caused by the transient variation of the background intensity but originates from the dynamics photoinduced in the CB.

In this regard, two processes are examined, which are illustrated in Fig. 5.16. Upon photoexcitation, i.e. $\Delta t = 0$, the dispersive CB is populated. The relative PE intensity integrated over the momentum interval Δk results in a Gaussian peak centered at E_0. At positive time delay, both (a) intraband electron thermalization and (b) change of the CB energy can lead to a shift of the peak.

(a) During the intraband thermalization, photoexcited electrons scatter from higher to lower energies, thus emptying gradually the CB from the top. Because the analyzed EDCs are integrated over a finite momentum range Δk, after some time delay the spectral weight transfes downwards and the CB peak appears centered at the lower energy E_1.

(b) The photoenhanced screening of the Coulomb potential can induce a transient renormalization of the electronic band structure and a reduction of the energy splitting between the VB and the CB. If these dynamics occur, the CB would

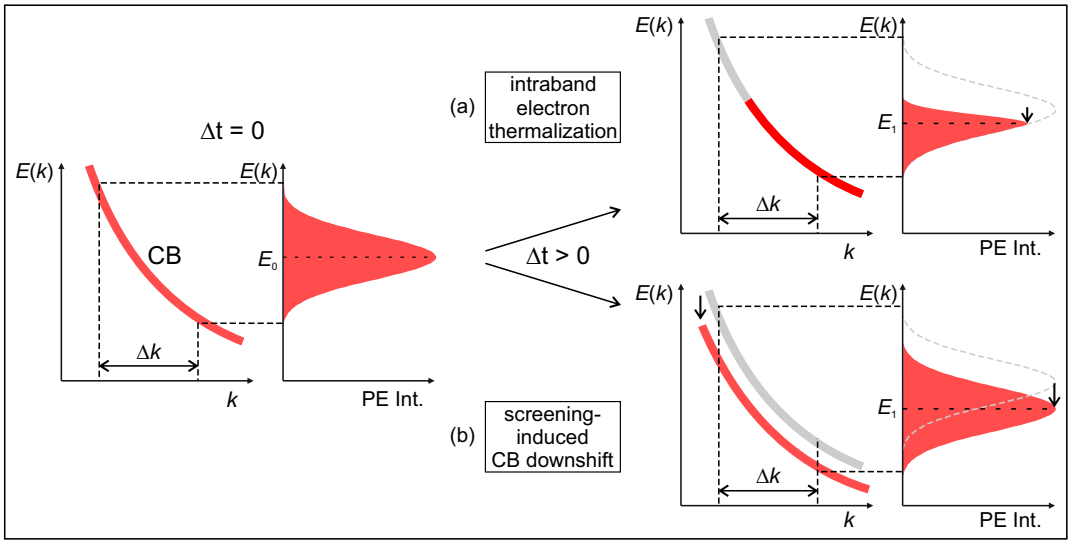

FIGURE 5.16: Dynamical processes that can shift the spectral peak (red shades) of the transiently populated dispersive CB (red curves): (a) the intraband electron thermalization emptying the CB at higher energies (white), and (b) the screening-induced energy downshift of the CB (white to red). Δt is the momentum interval of integration. See main text for detailed description.

shift oppositely to the upper VB at $k \neq 0$ (cf. Fig. 5.14 (d)) and its peak is transiently found at a lower energy. Because the renormalization depends on the number of free carriers, the amplitude of these shifting dynamics is expected to be maximum at early time delays following the photoexcitation and to increase for higher excitation density.

Possibly, both processes take place upon excitation of electrons to the CB and can partecipate to the transient spectral shift of the CB peak. Quantitative disentanglement of the two dynamics is difficult because the spectral shift, which amounts to about 80 meV at the highest pump fluence, occurs within the full width at half maximum of CB peak (of approximately 250 meV at equilibrium). Importantly, even if the CB energy would not change with respect to the equilibrium position, i.e. the spectral shift would be simply caused by intraband electron relaxation, the total band splitting between the VB and the CB would effectively transiently decrease upon photoexcitation by virtue of the upshift of the VB towards E_F.

In conclusion, upon near-infrared photoexcitation the upper VB and the CB at comparable momenta $k \neq 0$ do not shift in energy in the same direction. Instead, their **energy splitting reduces abruptly upon excitation of charge carriers above E_F. The effect increases for larger excitation densities up to F_C, above which absorption saturation of pump photon occurs at Γ and the density of photoholes at the top of the upper VB remains constant. Therefore, these dynamics of the electronic bands at $k \neq 0$ are most likely connected to a screening-induced renormalization of the underlying semiconductor band structure of Ta_2NiSe_5.**

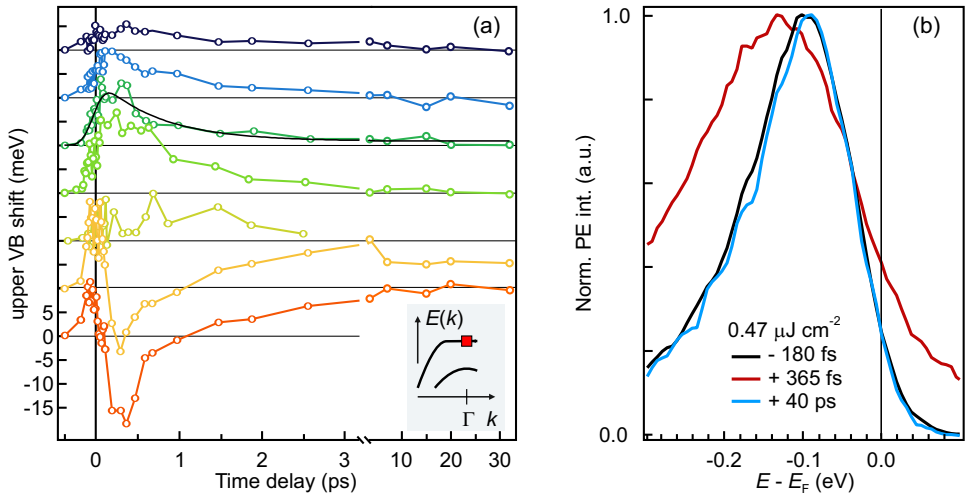

FIGURE 5.17: (a) Transient shift of the upper VB at at Γ. (b) Normalized EDCs at Γ at equilibrium (gray), 190 fs (red) and 40 ps (blue) after photoexcitation with 0.47 mJ cm^{-2} at 110 K. From [36].

5.3.2 Competition of band gap renormalization and exciton condensate enhancement at Γ

The discussion now focuses on the dynamics of ③ the flat top of the upper VB at Γ. Previous equilibrium studies show that this part of the upper VB is characterized by a strong excitonic coupling in the LT phase. Here, it is investigated if this property can have an impact on the dynamics of the band gap on the ultrafat timescale. As already observed in the time-resolved ARPES data in Fig. 5.13 (b), a near-infrared photoexcitation with 0.12 mJ cm^{-2}, i.e. below F_C, induces an abrupt upshift in this part of the electronic band structure, although much less pronouncedly than at the top of the lower VB. Therefore, at this excitation density, the electronic band gap transiently shrinks. In the following section, the dynamics of the upper VB at Γ is investigated as a function of excitation density and compared to that of the other parts of the occupied band structure that were discussed in the previous section. Two competing processes are unveiled which result in either the renormalization or the enhancement of the electronic band gap at Γ. The first is connected to the transient increase of the screening of the Coulomb interaction by means of the photoexcited carriers. The second, nontrivial behavior is proven to rely on the presence of a non-thermal population of strongly interacting electron and holes which contribute to the exciton condensate density. As a result, the order parameter of the excitonic insulator phase is transiently strengthened. These experimental evidences are corroborated by Hartree-Fock calculations which are presented in Section 5.3.3. Eventually, other dynamical processes that could be induced in the electronic band structure by an ultrahort optical pulse are briefly discussed in Section 5.3.4.

Fig. 5.17 (a) shows the photoinduced shift of the flat top VB at Γ relative to the equilibrium position for different pump fluences. These data points are obtained from the energy position of the VB peak maximum at each time delay. The VB intensity function is given by the combination of two Gaussian peaks as described by Eq. (5.1). It is noted that each Gaussian component of the upper VB intensity function exhibits the same qualitative behavior, as reported in detail in Appendix B. As a result, for $F < F_C$ (blue to light green traces), the dynamics resemble the trend observed at $k \neq 0$, although less pronounced at the respective excitation density. Accordingly,

the same fit function (solid black) as in Fig. 5.14 (a) is used to quantify these upshift dynamics and yields to a shift recovery time between 810 and 1150 (each± 110 fs) with increasing the excitation density. Interestingly, this values are comparable to the timescale of the hole relaxation dynamics in the upper VB at Γ at the respective fluence. For $F > F_C$ (orange and red traces), the abrupt upshift is followed by an additional shift in the opposite direction, delayed by ∼200 fs, such that the flat top VB maximum transiently lies at higher binding energies with respect to E_F than its equilibrium position. After approximately 1 ps, this effect is canceled by a slow upward shift of the VB that even "overshoots" its equilibrium position. Such nonmonotonic behavior of the flat top VB at high fluences is indicative of the occurrence of competing phenomena in this part of the electronic band structure, whose investigation is focus of the following discussion.

The delayed downshift and upshift of the flat top VB above F_C are sufficiently pronounced to be directly seen in the raw PE data. To show that, a set of spectra taken before and after photoexcitation with 0.47 mJ cm^{-2} are shown in Fig. 5.17 (b): at 365 fs (red), the upper VB maximum is shifted away from E_F with respect to the equilibrium position (black). At 40 ps (blue), the right-hand side of the upper VB peak coincides with that of the equilibrium spectrum, but the intensity maximum peaks at a slightly lower binding energy with respect to E_F. The latter spectrum suggests that at this late time delay the charge carriers have mostly thermalized within the FDD but the relaxation of the VB is not yet fully complete. The earlier downshift at 365 fs is physically nontrivial and demands more analysis. Notably, the effect amounts up to 18 meV at the highest excitation density. This is a small *relative* shift, but still resolvable due to the high statistics of the time-resolved data (cf. Subsection 3.6.3). Furthermore, these dynamics are still quantitatively significant when compared to the shifts observed in equilibrium as a function of temperature, which reach a maximum value of about 60 meV (cf. Fig. 5.3).

In order to safely assign these downshifting behavior to an actual change of the VB binding energy at Γ, it is now firstly verified that this spectral transfer does not simply originate from a slope change of the Fermi-Dirac distribution (FDD) due to a high electronic temperature. Secondly, it is shown that the effect is robust against the fitting of the spectra with different functions.

As depicted in Fig. 5.18 (a), because the upper VB is energetically close to E_F, its line shape can be affected by a FFD slope change, resulting in an apparent shifting of the peak maximum even in the case the VB does not change its binding energy (compare red to blue shade EDCs for high and low temperature values of the FDD, respectively). In order to test the possible contribution of the FDD to the VB shift, two spectral analysis are performed:

- The nonequilibrium spectrum at 365 fs is fitted in the energy region of the upper VB peak by a fit function consisting of two Gaussians multiplied by the FFD function. The energy position of the two Gaussian peaks is hold at the equilibrium value, while the electronic temperature of the FFD function is a free parameter. Fig. 5.18 (b) shows the obtained fit result (dashed green) on top of the data (red). For comparison, the optimum fit curve (black) described previously is also reported. Clearly, the peak intensity maximum is not captured by the fit when only the electronic temperature is let to vary in the fitting procedure;

- The largest peak shift potentially induced by a change of the FDD slope is estimated by increasing arbitrarily the electronic temperature parameter of the FDD without changing the position of the Gaussian peak. As shown in Fig. 5.18 (c),

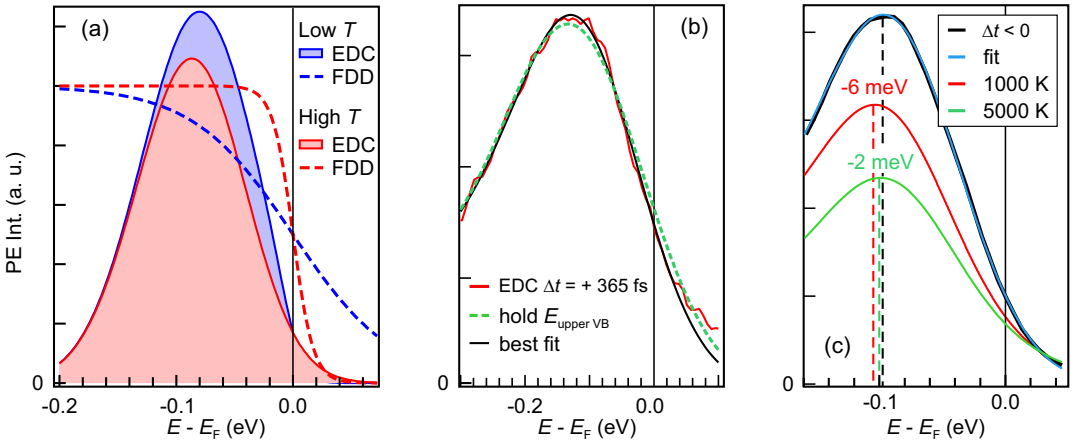

FIGURE 5.18: (a) Impact of a high temperature FDD on the VB line shape. (b) Fitting the VB peak by solely increasing the electronic temperature of the FDD. (c) Simulation of the maximum peak shift achieved by a high temperature FDD. (See main text for details).

this simulated shift amounts up to 6 meV at $T = 1000$ K (red) with respect to the energy position at equilibrium (blue). For even higher temperature values, the FDD function is almost flat, thus it no longer affect the line shape of the VB whose peak maximum is observed to 'shift back' towards E_F(green). The maximum simulated shift of 6 meV is evidently to scarce to reproduce the experimental results (up to 18 meV), indicating that a high temperature FDD function is insufficient to justified the observed energy shift of the VB peak.

These tests verify that an actual change of the Gaussian energy position has to be included in the model, thus the VB effectively shifts towards E_F on the sub-picosecond timescale.

The robustness of the nonmonotonic shifting behavior of the upper VB at Γ and for $F > F_C$ is demonstrated for different fitting procedures applied to the EDCs at $\Delta t = +365$ fs. In the top graph of Fig. 5.19 (a), the fit results are shown by curves of different colors. Clearly, they all successfully describe the EDC (gray empty circles) in the respective energy region, and particularly around the upper VB peak. In the lower graphs of Fig. 5.19 (a), each fit function is explicated. From top to bottom, the tested functions consist of a single Gaussian multiplied by the FDD (blue), two Gaussians (green), and three Gaussians either multiplied or not by the FDD (red). Repeating these spectral analysis on a set of EDCs at various time delays provides the results for the transient VB shift that are summarized in Fig. 5.19 (b). Notably, they all yield qualitatively the same dynamics of the upper VB, namely an abrupt upward and a delayed downward energy shift. These findings prove that the shifting behavior of the VB peak does not depend on the chosen modeling function, thus the relevant dynamics are stable against the performed analysis. In conclusion, a transient nonmonotonic modulation of the VB binding energy isobserved at Γ and upon photoexcitation above F_C.

Fig. 5.20 (a) summarizes the VB energy shifts at each investigated point of the electronic structure of Ta_2NiSe_5 as a function of pump fluence. They have been evaluated at +255 fs time delay following the photoexcitation. Clearly, the upward (positive) shift occurring in the upper VB at $k \neq 0$ (yellow) and in the lower VB at Γ (green) evolves linearly with increasing excitation density and exhibits a slope change at the same critical fluence $F_C = 0.2$ mJ cm^{-2} of the VB depopulation threshold (cf.

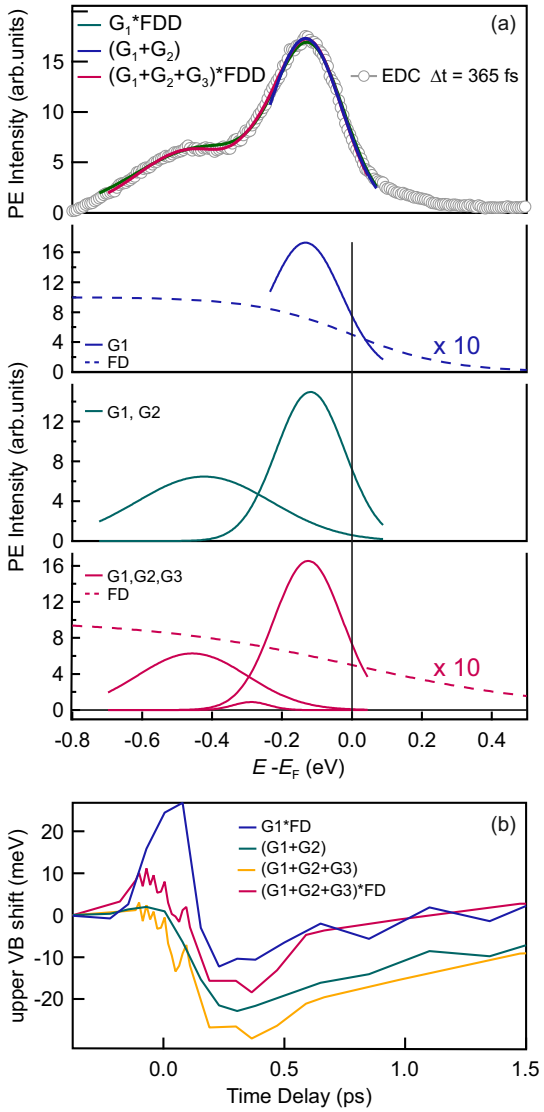

FIGURE 5.19: (a) Comparison of different function fitted to the upper VB at Γ (See main text for details). (b) Resulting transient VB energy shifts with respect to the equilibrium energy position.

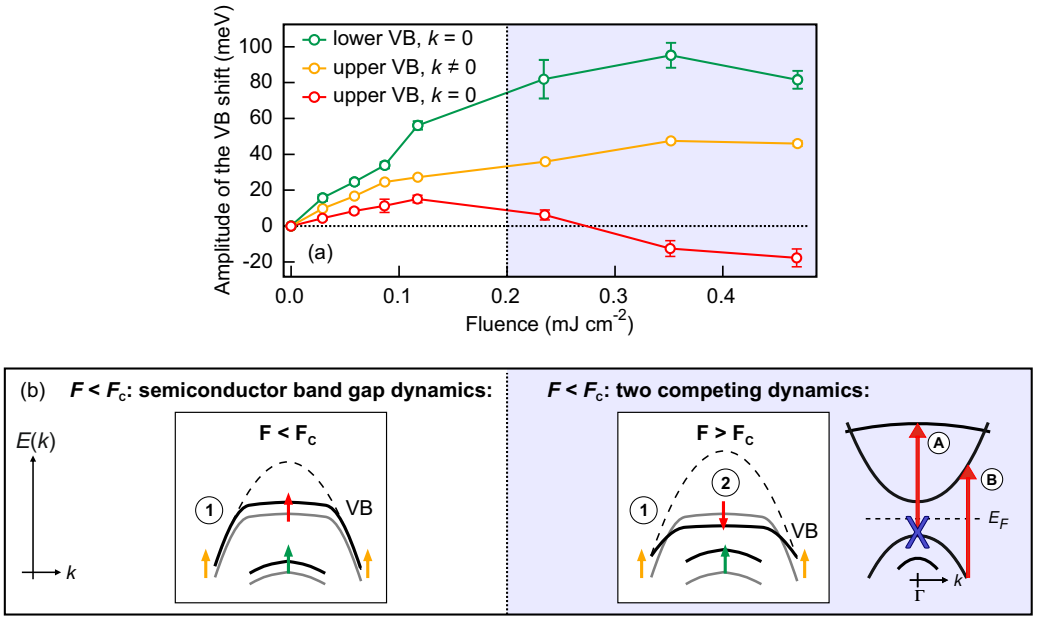

FIGURE 5.20: (a) The fit amplitude of the shift of the lower VB (yellow) and Γ and of the upper VB at $k \neq 0$ (green) and at Γ (red) as evaluated for a delay of 255 fs as a function of the incident pump fluence. (b) The band structure dynamics are schematized for two excitation regimes, below (left) and above (right) F_C, respectively. Adapted from [36].

Fig. 5.7 (b)). The transient shift of the flat top VB at Γ (red) exhibits, on the contrary, a nonmonotonic behavior, revealing that two competing dynamics are at play: While, for $F < F_C$, the flat top VB qualitatively follows the trend of rest of the occupied band structure, an opposite process becomes manifest for $F > F_C$ and causes the flat top VB to undergo a downward (negative) shift: the VB top transiently have a higher binding energy than at equilibrium. The downward shift of the flat top VB seems possibly increases with further increasing the pump fluence above F_C.

These composite VB dynamics are illustrated in Fig. 5.20 (b) and are interpreted as a fingerprint of the dynamics of the electronic band gap. This assumption is justified by the complementary 2PPE spectroscopy study of the photoinduced CB dynamics discussed in Subsection 5.3.1. The equilibrium (photoexcited) VBs are sketched by gray (black) solid lines. For comparison, the black dashed line depicts the photoexcited upper VB in absence of excitonic coupling (cf. Subsection 2.7.2). The left panel shows the global upshift occurring abruptly at excitation densities $F < F_C$: this behavior reflects the shrinking of the electronic band gap immediately after the photoexcitation. To infer the origin of these band gap dynamics it is useful to discuss their fluence dependence. As outlined above, the upshift is enhanced with increasing fluence up to F_C, supporting that the amplitude of the band gap shrinking depends on the number of photoexcited carriers. Moreover, the upshift remains constant above F_C, i.e. in the regime of absorption saturation of pump photons at Γ. Thus, the band gap shrinking must be mainly connected to the density of free carriers that is excited via the transition (A) at the Γ point (cf. schematics of the excitation mechanisms on the right panel of Fig. 5.20 (b)). In optically excited semiconductors, the photoexcited carriers enhance the screening of the Coulomb interaction. Upon a sufficiently large excitation density, this can induce a renormalization of the electronic band gap which transiently narrows [47, 48, 49, 50, 51]. Ta_2NiSe_5 has a low density of states near

E_F, which leads to a very poor screening of the Coulomb interaction at equilibrium. Consequently, even a weak photoexcitation can significantly increase the concentration of free carriers which participate to the screening, thereby inducing a renormalization of the electronic band gap. With increasing pump fluence, the band gap shrinks further. Notably, these dynamics are consistent with the observed reduction of the electronic band gap below F_C. It is then argued that in Ta_2NiSe_5, **the dynamics of the noninteracting, semiconductor band structure governs the modulation of the electronic band gap upon modest photoexcitation densities.**

The ∼200 fs-delayed VB dynamics upon photoexcitation above F_C are depicted in the right panel. While the occupied band structure is globally shifted towards E_F, the top of the upper VB at Γ is pushed away from E_F. Thus, while the renormalization of the semiconducting band structure persists and manifests in the lower VB and in the upper VB at $k \neq 0$ albeit with constant amplitudes, the electronic band gap at Γ is effectively larger than at equilibrium. This behavior is opposite to that at low pump fluences, revealing that two competing dynamics of the upper VB coexist at Γ. To help assigning them, the schematic of the excitation of the electronic band structure is recalled in the following. As shown on the right of Fig. 5.20 (b), above F_C the excitation mechanism at Γ saturates because of optical absorption saturation, while other transitions are further excited at $k \neq 0$. Because the band gap widening appears only above F_C, the excitation (B) are likely to play an important role in this regard. Moreover, as the band gap widening at Γ is in contrast to the dynamics of a photoexcited semiconductor, these dynamics are likely to be connected to the presence of strong excitonic coupling at the flat top of the upper VB. Then, the following explanation is proposed: once the excitation channel (A) saturates, the main contribution to the screening remains constant. Accordingly, the renormalization of the semiconductor band structure does not further change above F_C. However, by means of the non-saturating excitation mechanism (B), the number of electron and holes continue to increase at $k \neq 0$ in the CB and VB, respectively. After intraband thermalization, they collect at the band extrema where the attractive Coulomb interaction is very strong and favors the formation of strongly bound excitons. It is argued that **these excess excitons may be responsible for an enhancement of the condensate density, and thus of the widening the electronic band gap at Γ above F_C.** In the following, this hypothesis is tested theoretically by considering the presence of an excitonic insulator condensate in an out-of-equilibrium two-band semiconductor system.

5.3.3 Hartree Fock modeling of the excitonic insulator band gap enhancement

The experimental results show that in the presence of an exciton condensate, the combination of a nonthermal carrier distributions and a screening-induced electrostatic shift of the underlying semiconductor band structure may lead to an enhancement of the condensate density and a corresponding widening of the band gap at Γ. In order to test this mechanism, Hartree-Fock calculations are performed by D. Golež, Ph. Werner and M. Eckstein. The theoretical model aims at reproducing the nonequilibrium band dispersion of the simplified case of a one-dimensional two-band system with excitonic coupling. The one-dimensionality is justified by the in-plane anisotropy of the electronic band structure of Ta_2NiSe_5, whose dispersion perpendicular to the chain is about 10 times smaller than along the chains [123]. However, the results of the calculation do not depend on the dimensionality which could possibly even enhance the effects observed in 1D [36]. The Hamiltonian is based on the mean-field modeling

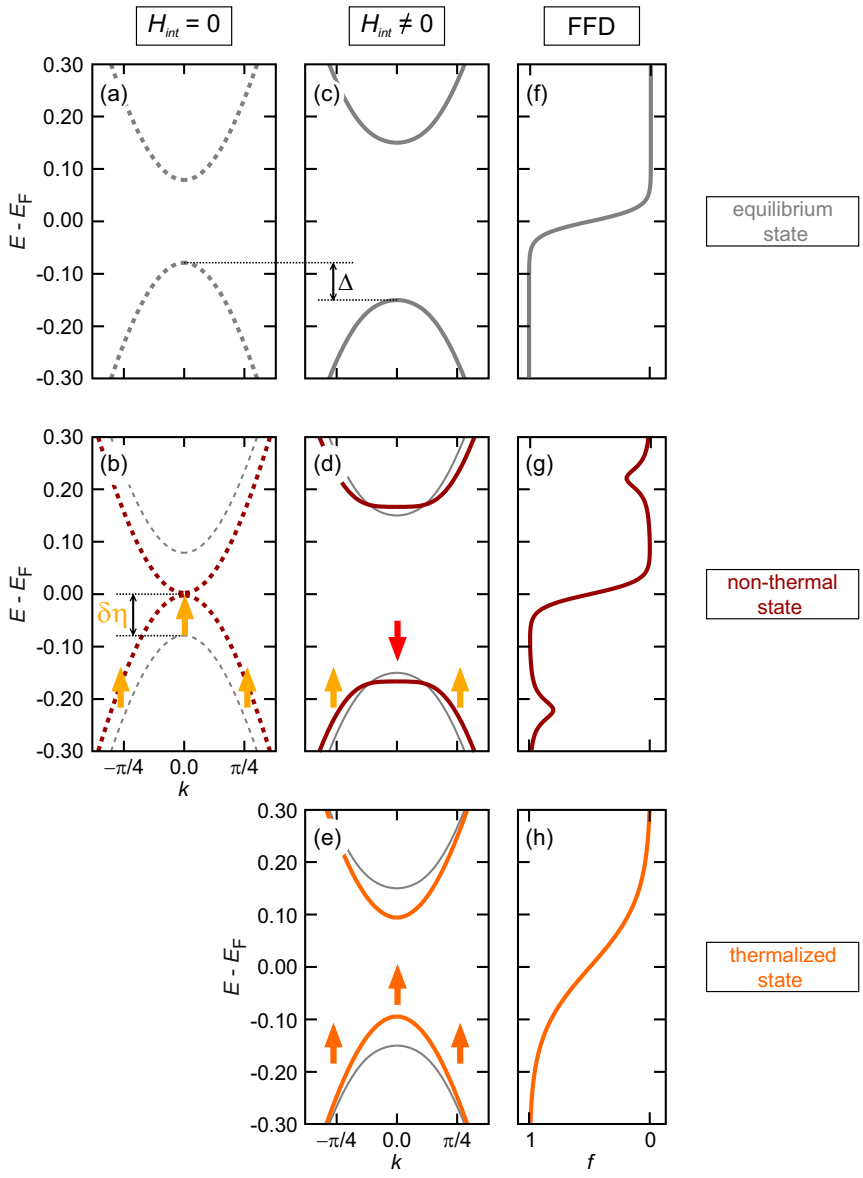

FIGURE 5.21: Hartree-Fock calculations of the band structure of a two-band system without (dashed curves) and with (solid) interband coupling and for different FDDs, i.e. at equilibrium (gray, (c)), before interband relaxation (red, (f)), after interband relaxation (orange, (h)). Adapted from [36].

of the excitonic insulator ground state presented in Subsection 2.6.1, and consists of a noninteracting part, H_0, given by Eq. (2.13) and accounting for the semiconductor band splitting of the HT normal phase, and an interaction term, H_{int}, expressed by Eq. (2.14). The interaction term, H_{int}, introduces a momentum dependent excitonic coupling between the VB and the CB which is strongest at $k = 0$. As a result, a non-vanishing order parameter of the exciton condensate is defined as $\rho_{12} = c^{\dagger}_{k,1} c_{k,2} \neq 0$, such that the density of exciton is non-zero in the ground state. Further details on the model can be found in Appendix D.

The results of the calculations are reported in Fig. 5.21. The band dispersion at equilibrium without excitonic coupling ($H_{\mathrm{int}} = 0$) is shown in (a). It is calculated with the Fermi-Dirac distributions (FDDs) reported in (c). When the interaction between the VB and the CB is 'turned on' in the Hamiltonian ($H_{\mathrm{int}} \neq 0$), the calculation with the same FDD results in the equilibrium band dispersion shown in (b). Clearly, the splitting between the VB and the CB is larger than that of the noninteracting, semiconductor case. Also, the energy difference, Δ, between the interacting and the noninteracting VBs is most prominent at the Γ point. The same holds symmetrically for the CBs. Thus, already at equilibrium, the electronic band gap increases as result of the excitonic coupling and the effect is maximum at Γ where the interaction is the strongest.

Then, the band dispersion of the photoexcited system is calculated. For this case, two effects of the photoexcitation are considered. (i) The presence of a photoexcited carrier population that has not yet thermalized across the band gap. Such nonthermal population is explicitly included in the calculation by taking a nonequilibrium FDD as the one displayed in (f) which consists of a Lorenzian dip (peak) to account for the hole (electron) population in the VB (CB). Various other nonequilibrium FDDs are also applied to corroborate the robustness of the calculated effects. These results can be found in Appendix D. (ii) The excitation of additional free carriers to other electronic bands which are not included in the Hamiltonian but are involved in the experiment. This excitation is considered to enhance the screening and lead to a reduction of the band splitting of the noninteracting band structure, as suggested by the experiment. This effect is mimicked by an opposite shift of the VB and the CB towards each other by an amount $\delta\eta$, as shown in (d). The resulting nonequilibrium band structure is then taken as initial state for the calculation of the nonthermal interacting case where the interaction is simply 'turned on'. The result is displayed in (e). Remarkably, an enhancement of the electronic band gap occurs at Γ while the bands shift towards each other at larger k vectors.

Eventually, the band structure after interband thermalization across the band gap is calculated. Here, the excess energy is expected to be transferred to the condensate whose temperature eventually increases towards the critical point. The thermal electron population is accounted by the high temperature FDD shown in (h). The calculated band dispersion of the interacting system is displayed in (g) and exhibits a band gap reduction at all k vectors.

Notably, the result for the nonthermal population reproduces very well the experimental evidences for $F > F_{\mathrm{C}}$ at time delays around 200 fs (cf. Fig. 5.17 (a), yellow and red data points). Thus, it confirms that the transient band gap widening at Γ is connected to the order parameter of the excitonic insulator phase. More precisely, the calculation indicates that the enhancement of the excitonic insulator gap relies on two conditions: (1) a band splitting reduction that brings the exciton formation into resonance or, equivalently, intensifies the interaction between the VB and the CB, and (2) a delayed interband thermalization that maintains the temperature of the condensate below the melting point. Experiments prove that the first condition is verified

by the screening-induced renormalization of the semiconductor band structure. The second condition reasonably rely on the presence of the band gap which retards the recombination of electrons and holes. As a result, a strongly out-of-equilibrium state manifests in Ta_2NiSe_5, where the electrons and holes in the respective electronic bands bind into coherent excitons, eventually enhancing the condensate density, and thus, the excitonic insulator band gap. Further agreement with the experiment is found in the band gap reduction of the thermalized state (e). This prediction is indeed corroborate by the measured delayed dynamics which set in after ~ 1 ps and manifest in a slow upshift of the VB towards E_F (cf. Fig. 5.17 (a), yellow and red data points).

In conclusion, the combination of time-resolved ARPES with Hartree-Fock modeling demonstrates that **the photoinduced transient widening of the electronic band gap of Ta_2NiSe_5 relies on the existence of an exciton condensate in the LT phase. It manifests upon enhancement of the exciton density by virtue of two effects: the screening-induced electrostatic shift of the underlying semiconductor band structure and the persistence of a nonthermal carrier distribution across the band gap**. The first effect favors a stronger excitonic coupling, while the second retards the heating of the condensate above the melting point. Altogether, these findings prove the possibility to optically manipulate the order parameter of the excitonic insulator on an ultrafast timescale. Also, a transient state of the excitonic insulator ground state is unveiled, which could not be thermally addressed.

5.3.4 Other ultrafast processes influencing the band structure dynamics?

Other effects that can lead to band shifting and, in some cases, to a modulation of the electronic band gap are briefly reviewed in the following. It will be shown that where the effects cannot be ultimately excluded, either they do not conflict with the proposed enhancement of the excitonic insulator order parameter, or they potentially cooperate to prepare the nonequilibrium state necessary to observe such enhancement.

Work function changes by surface photovoltage

In a photoexcited semiconductor, if electrons and holes have different mobility, due to, e.g. different dispersion of the respective bands, an inhomogeneous charge distribution is formed in real space, which is referred to as space charge layer. In case of doping-induced surface band bending, the effect may manifests already at equilibrium. As shown in Fig. 5.22 (a), upon sufficiently intense photoexcitation, a surface photovoltage (SPV) can be produced due to the spatially unbalanced distribution of negative and positive charge carriers[14]. This results in a transient changes of the work function. In time-resolved ARPES, being a surface sensitive technique, the SPV effect manifests with a rigid energy shift of the whole spectrum in the direction of the work function change [197].

Ta_2NiSe_5 is a direct semiconductor and the samples investigated in this work are slightly p-doped. Consequently, a surface band banding may be expected at equilibrium at the interface with the vacuum. The effect should, however, be small because the crystal is cleaved parallel to the atomic planes, thus the charge transport

[14]This is for instance the case in near-infrared photoexcited p-doped GaAs system, for which a surface photovoltage associated with band bending at the interface with vacuum transiently shifts the whole band structure [196].

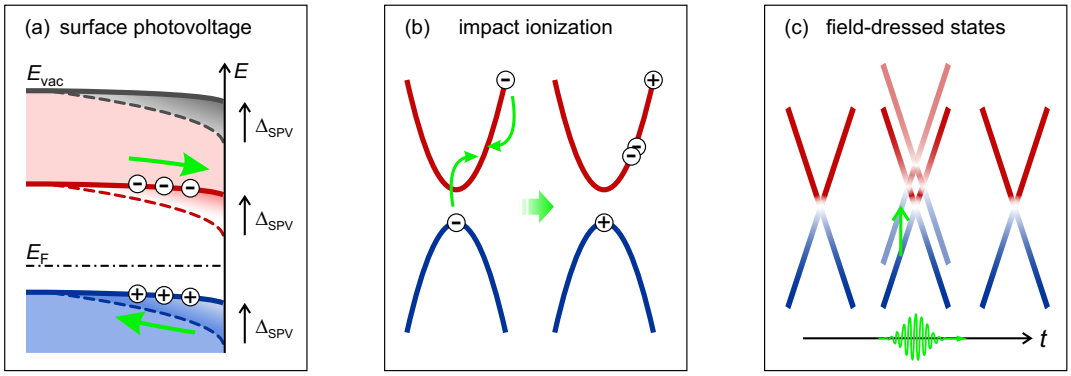

FIGURE 5.22: (a) Surface photovoltage. (b) Impact ionization.(c) Floquet-Bloch and Volkov states. See main text for details.

perpendicular to the surface is strongly reduced by the weak interplane electronic coupling [54, 57]. If, for instance, a downward surface band banding is present at equilibrium and a SPV developed upon photoexcitation, the whole electronic band structure would transiently shift to higher energy at the sample surface due to the electric field generated by the separation of the charges. Notably, in this case the band splitting and thus, the electronic band gap at Γ remain unchanged .

No rigid spectral shift is recorded at any excitation density in the present tr-ARPES study of Ta_2NiSe_5. In fact, (i) the secondary electron cut-off energy does not change at any time delay. (ii) The valence and conduction bands shift oppositely. (iii) At low fluences the amplitude of the shift is different for distinct portions of monitored occupied band structure. (iv) At pump fluences above F_C, the shifts at Γ are even opposite between the upper and the lower VB. Therefore, no evidences of SPV can be found in the transient spectra of Ta_2NiSe_5.

In addition, as discussed earlier, the dynamics of the mid-IR optical response and of the upper VB at Γ show an analogous dependence on the excitation density and are proven to be connected. Consequently, their origin cannot rely on a transient SPV because the optical measurements, being bulk sensitive, would not have been affected.

Impact ionization helping the band gap renormalization

In semiconductors, photoexcited electrons can thermalize via impact ionization [198] on a very short timescale, typically less than few tens of fs. As depicted in Fig. 5.22 (b), the process consists in the scattering of both a valence and a conduction electron towards the bottom of the CB. In this way, the total energy of the system is reduced despite the increase of electrons in the CB. For this reason, the process is also referred to as carrier multiplication. Examples have been reported in common bulk semiconductors like, e.g. silicon [199], SiO_2 and Al_2O_3 [200], as well as in graphene, where the effect is helped by the gap-less band structure at E_F [201], and recently in the 2D parent compound hexagon boron nitride [202].

If impact ionization took place in Ta_2NiSe_5, it would cause at early times after the photoexcitation a further depletion of the top of the VB which adds up up to the depopulation caused by pump photon absorption. As a result, an even larger number of conduction electron would be found in the CB, which could have two effects:

- increasing the efficiency of the screening of the Coulomb interaction, thus favoring the renormalization of the electronic band gap;

- incrementing the electron and hole populations, which can bind into coherent excitons and contribute to the enhancement of the excitonic insulator band gap.

In view of the timescales on which the electronic band gap either narrows or widens in Ta_2NiSe_5, impact ionization can potentially contribute to the screening-induced band gap shrinking as it occurs abruptly after the photoexcitation. However, it cannot directly be responsible for the band gap widening which manifest at later time delays. Potentially, by favoring the band splitting reduction, the impact ionization may help preparing the out-of-equilibrium state for the enhancement of the excitonic insulator order parameter [203, 204].

Gap opening by photon-dressing of electronic states

The interaction of electronic states with an intense periodic electromagnetic potential can produce replicas of the interacting bands. These 'photon-dressed' bands appear in the tr-ARPES spectrum separated by the photon energy and persist only during the illumination time (i.e. effectively up to the duration of the pump pulse) [205]. The effect is illustrated in Fig. 5.22 (c). These band replicas are classified as Floquet-Bloch, if the interacting state is an Bloch electron initial state or Volkov, if the interactin state is the free-electron final state. The first observation was reported on the topological insulator Bi_2Se_3 upon interaction with mid-IR electric field on the order of 1×10^7 V/m and led to the observation of a transient density of states across E_F and band gaps at the crossing of the replicas with the original Dirac cone [206].

It is easy to demonstrate that these field-dressing effects cannot describe the observed dynamics of the excitonic insulator band gap of Ta_2NiSe_5. Firstly, the VB shifts occur on a much longer timescale than the duration of the pump pulse. Particularly, the downshift manifest only about 5 times later, i.e. $\Delta t > +$ 200 fs, than the pump pulse duration (of 40 fs). Additionally, the spectra at the excitation times do not exhibit any transient band replica. Eventually, even if the PE intensity of those replicas would be below the detection limit, it is noted that due to the high photon energy of the employed pump pulses (1.55 eV), it is improbable that these replica would appear on top of the original upper VB. Thus, field-dressing effects are improbable to occur in the present study. In any case, they could have only impact at early times ($<$ 40 fs), thus they are certainly inefficient to explain the observed photoinduced band structure dynamics of Ta_2NiSe_5.

To sum up, different processes are reviewed which are launched by photoexcitation with an ultrashort optical field and can potentially contribute to the ultrafast dynamics of the electronic band structure of Ta_2NiSe_5. Those are the generation of surface photovoltage, the electron relaxation via impact ionization and the photon-dressing of electronic states. The presence of SPV can be excluded in the present work since the measured spectrum do not rigidly shift upon photoexcitation. Conversely, the shifting behavior involves only parts of the spectrum and is even momentum dependent. Impact ionization can be effective only within the first tens of fs. Thereby, it may contribute to the abrupt band gap renormalization by favoring the free-carrier-induced enhancement of the screening. However, it does not explain the delayed band gap widening. Finally, no evidence is found of photon-dressed electronic states whose effect would anyhow not involve either the energy not the timescale of interest for the extraordinary enhancement of the electronic band gap.

5.4 Quasiparticle relaxation dynamics

The optical excitation of a system involves the redistribution of electrons into high-energy unoccupied bands. The following relaxation dynamics is typically regulated by the exchange of energy with other carriers and the phonon bath. The rate of these energy exchanges depends on the strength of the carrier-carrier and carrier-phonon interactions. These interaction strengths may transiently vary with respect to the equilibrium state as a function of the involved energy scales and the density of the excitation. Therefore, the investigation of the photoinduced electron relaxation dynamics in the time, energy and momentum domains can provide information on the effective couplings between degrees of freedom of the systems and the dominant scattering channels during the carrier thermalization.

In this section, the relaxation dynamics of the electron population in the CB near and at the Γ point is studied in the LT phase of Ta_2NiSe_5 by means of time-resolved photoelectron spectroscopy. In particular, two sets of experiments are performed.

(i) After photoexcitation with 1.55 eV photons, the intensity in the high-energy, dispersive part of the CB is monitored by UV photons (5.28 eV) with energy lower than the sample work function (5.40 eV). An exemplary energy- and angle-resolved spectrum is shown in Fig. 5.23 (a) and the red bar indicates the momentum interval of interest for the analysis.

(ii) The bottom of the CB at Γ is probed, after excitation with the same photon energy, by UV photons of higher energy (6.20 eV) exceeding the work function. This allows to avoid spectral overlap between this part of the CB and the secondary electron distribution, as it is the case for the measurements with lower probe photon energy. As displayed in Fig. 5.23 (f), above E_F, a significant photoemission intensity of the CB bottom is recorded (the red bar is again the momentum interval considered in the analysis), while below E_F, direct photoemission occurs from the top of the upper VB. Remarkably, the VB and CB do not cross each other, once more proving the absence of band gap collapse upon photoexcitation, as discussed in the previous section. This observation is even more significant when noting that these measurements are taken at 200 K, i.e. 90 K closer to the critical temperature of the electronic phase transition than for the case of the data set discussed in the previous section. This fact further highlights the robustness of the exciton condensate of Ta_2NiSe_5 against an ultrashort near-infrared excitation.

The discussion of the CB carrier dynamics is organized as follows: first, it is presented how the transient electron population is obtained in the energy and momentum regions of interest. Then, the temporal evolution of the electron population in the CB is qualitatively described to point out nontrivial behaviors that manifest as a function of both energy with respect to E_F and excitation density. Hence, timescale analysis of the relevant transients is presented and different models of the energy and pump fluence dependence are discussed. Finally, the CB electron relaxation dynamics is combined with the build-up of the hole population at the top of the VB, with the aim to comprehensively reconstruct the scattering processes involved in the carrier dynamics across the electronic band gap of the excitonic insulator phase of Ta_2NiSe_5.

5.4.1 Energy and fluence dependent electron relaxation dynamics

The momentum-integrated EDC obtained from the photoemission spectrum in Fig. 5.23 (a) is displayed in (b). It shows that in the chosen momentum interval (red bar), the CB separates in energy from the secondary electron distribution, thus its spectral intensity appears as a distinct peak above approximately 0.5 eV with respect to E_F. The

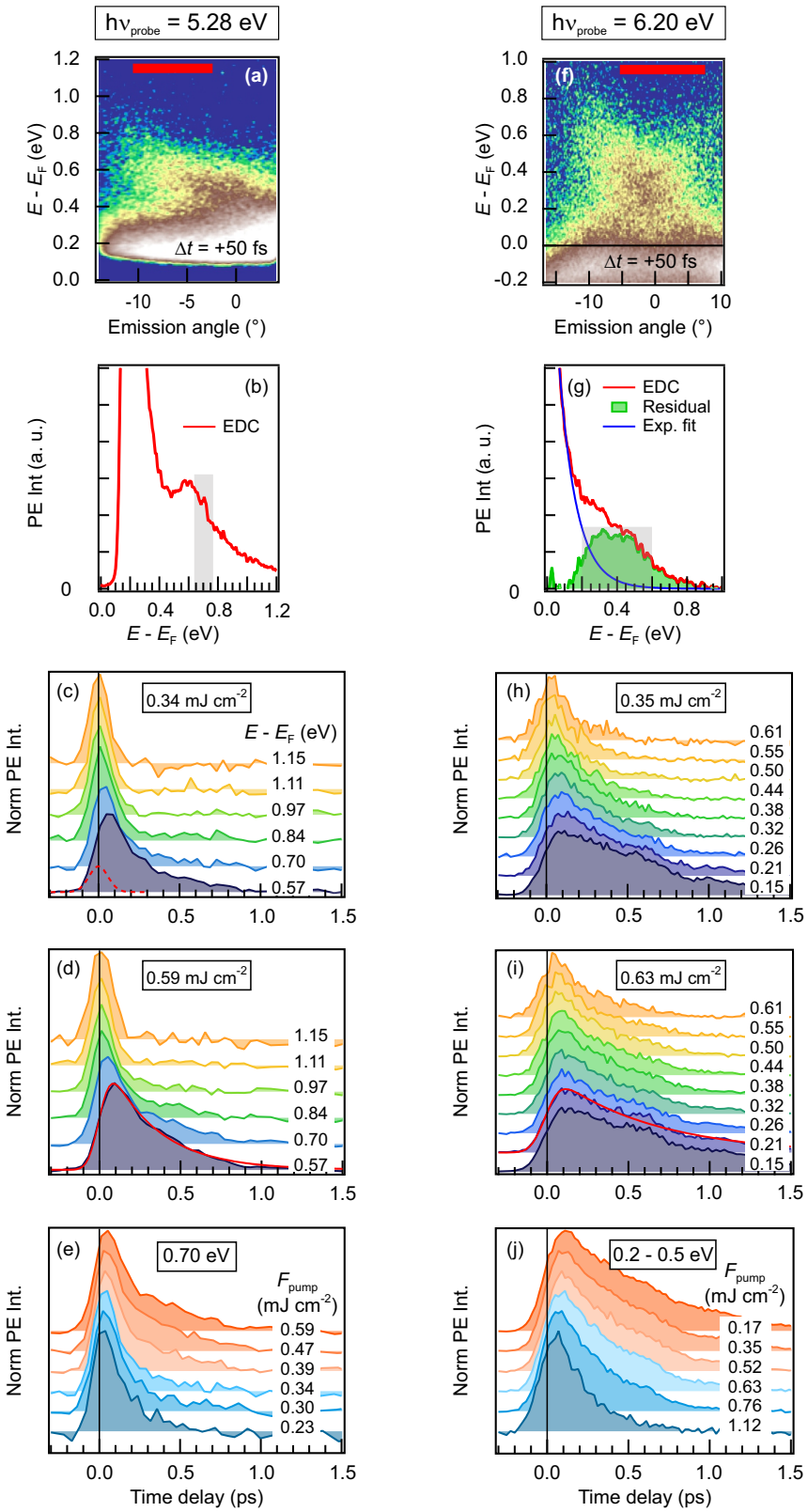

FIGURE 5.23: (a) Energy- and angle-resolved 2PPE spectrum at 110 K with $h\nu_{\text{pump}} = 1.55$ eV and $h\nu_{\text{probe}} = 5.28$ eV. The red bar is the momentum interval of integration of the EDC in (b). (c) and (d) CB population dynamics at various energies relative to E_{F} and at $k \neq 0$ for two pump fluences. (e) Fluence dependence of the CB population dynamics in the energy interval centered at 0.7 eV (gray shade in (b)). (f) Energy- and angle- resolved PE spectrum at 200 K with $h\nu_{\text{pump}} = 1.55$ eV and $h\nu_{\text{probe}} = 6.20$ eV. The red bar is the momentum interval of integration of the EDC in (g). (h) and (i) CB population dynamics at various energies relative to E_{F} and around Γ for two pump fluences. (j) Fluence dependence of the population dynamics at the CB bottom (gray shade in (g)).

energy-resolved transient electron population is therefore evaluated above this intermediate energy by binning the time-resolved data into 130 meV intervals. The obtained transients are reported for two excitation density values in Fig. 5.23 (c) and (d), respectively. The intensities are normalized to their maxima and the curves are displayed in waterfall plot for clarity. The red dashed curve in (c) is the (not normalized) intensity of the pump-probe cross-correlation evaluated on a time-resolution limited flat CB at high energies (not shown, see Fig. 5.8). At both fluences, three effects are immediately observed: upon photoexcitation, the photoemission intensity increases abruptly at high energies; its maximum appears slightly temporally delayed at lower intermediate energies; the intensity decay spans over few hundreds of femtoseconds and slows down at energies towards E_{F}. Remarkably, all these effects become more prominent with increasing the pump fluence, as further exemplified in (e) by a set of transients at the chosen energy of 0.70 eV obtained for various excitation densities. Importantly, it is noted that all those trends are observed also if the spectral intensity of the secondary electrons at each pump-probe delay is subtracted from the data. This indicates that the observed behaviors must predominantly rely on the dynamics of the primary CB electrons.

Fig. 5.23 (g) shows a spectrum (red) in the energy region of the CB minimum around Γ as measured by 6.20 eV probe photons 50 fs after the photoexcitation. At this time delay, a large fraction of excited electrons have not thermalized across the electronic band gap. In the spectrum, its intensity appears on top of the Fermi-Dirac distribution (FDD) of the thermal electrons as additional spectral weight at the expected energy of the CB bottom. To single out the relative spectral feature (green shade), an exponentially decaying function[15] (blue) is fit to the background intensity of the thermal electron population and is subtracted from the original spectrum. The excited electron dynamics at Γ are then retrieved in two ways. First, energy-resolved transients are obtained by binning the non-background-subtracted time-resolved spectra into 50 meV. Two data sets at low and high excitation density are shown in (h) and (i), respectively. Consistently with previous observations at $k \neq 0$, a combined energy and pump fluence dependence of the electron dynamics above E_{F} is observed. In particular, when comparing transients at Γ and $k \neq 0$ for comparable energy and excitation density, they are found to evolve on a similar timescale, which supports the solidity of the results of both experiments. Secondly, the intensity of the background-subtracted peak (green shade in (g)) is integrated between 0.2 and 0.5 eV at various time delays. The obtained transients reflect the evolution of the nonthermal electron population at the CB bottom. A set of these transients is shown in (j) for different pump fluences, confirming that the electron relaxation is delayed for higher excitation densities.

To sum up all the qualitative observations, the transient CB electron occupancy shows a relaxation dynamics that depend on both the excess energy of the electron population and the density of excited carriers. In particular, **the relaxation slightly delays and is slower at energies closer to E_{F}. At all energies, it further slows down with increasing the number of photoexcited electrons in the CB.** In the following, these behaviors are quantified through curve fitting of the transient photoemission intensities.

As described in Chapter 3 by Eq. (3.4), the time-resolved photoemission intensity is rigorously modeled by the response function of the transient population, i.e. the solution of the relative rate equation, convolved with the temporal cross-correlation of the pump and probe pulses. Thus, one would need to know the system response

[15] This function accounts for the first term of the Taylor expansion of the FDD function [207].

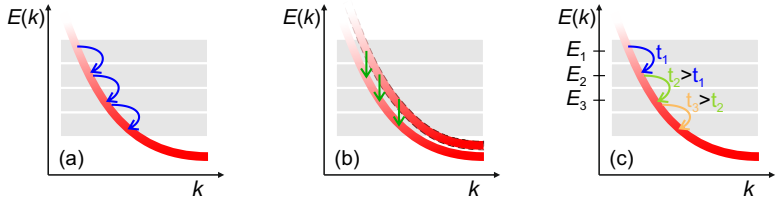

FIGURE 5.24: Effects potentially delaying the transient PE intensity maximum: (a) Electron 'cascade'. (b) CB downshift. (c) Energy-dependent decay time. The gray bars are the energy interval of integration of the PE transients. See main text for details.

function in order to fit the transient curves. In the present study, the decay of the transient electron population is expected to involve mainly two states, i.e. the populated CB and the upper VB. For a simple two-level system, the response function reduces to a single exponentially-decaying component whose convolution with a Gaussian cross-correlation is analytically expressed by[16]

$$I(t) = 0.5 \cdot \left(\mathrm{erf}\left(\frac{t - t_0}{\Delta t} \right) + 1 \right) \cdot \left(A \cdot \exp\left(\frac{t - t0}{\tau} \right) \right). \tag{5.3}$$

Here, the first term models the initial intensity rise with t_0 and Δt determined by the cross-correlation intensity at high-energies (dashed red in (b)). The second term reproduced the population decay at later time delays. For consistency, this fit function is applied to all the energy-resolved transients of both experiments. As visible in (d) and (i) on two exemplary data, the obtained curves (red) fit very well to both transients.

Notably, the model does not explicitly account for the delay of the initial intensity maximum observed before. Nevertheless, this feature can be well reproduced by the fits for all energies and fluences without the need of any ad-hoc component, such as an exponential rise term included in the response function. This is consistent with the fact that the delay of the intensity maximum amounts to only a few tens of fs at most, effectively less than the temporal cross-correlation. Concerning the origin of this retarded intensity maximum, three aspects can be considered which are illustrated in Fig. 5.24. (a) A rapid 'cascade' of high energy electrons into lower energy states. This process occurs during the intraband electron relaxation at large momenta where the CB is dispersive. As consequences, the low-energy part is partially re-filled by electrons scattering from the top part and the population decay is retarded at low energies. Attempts were made to fit the transients to a function that explicitly accounts for this 'build-up' process. However, the fit procedure did not converge. This suggests the process should have little impact on the electron relaxation in the CB. (b) An abrupt energy downshift of the CB at $k \neq 0$, as indeed proven to occur in Ta_2NiSe_5 upon photoexcitation (cf. Fig. 5.15 (c)). As a result of these dynamics, each higher-energy interval of integration would be suddenly 'depleted' in favor of the intensity in the respective lower-energy interval. However, this effect cannot significantly contribute to the delayed intensity maximum of the analyzed transients as the CB downshift amounts to maximum few tens of meV, thus well within the energy intervals of integration used at $k \neq 0$ (130 meV). (c) An actual energy and fluence dependence of the relaxation time constant τ. It can be easily tested that a larger

[16] Fitting with the corresponding convolution function is also performed on a selection of transients and is verified to provide quantitatively comparable results.

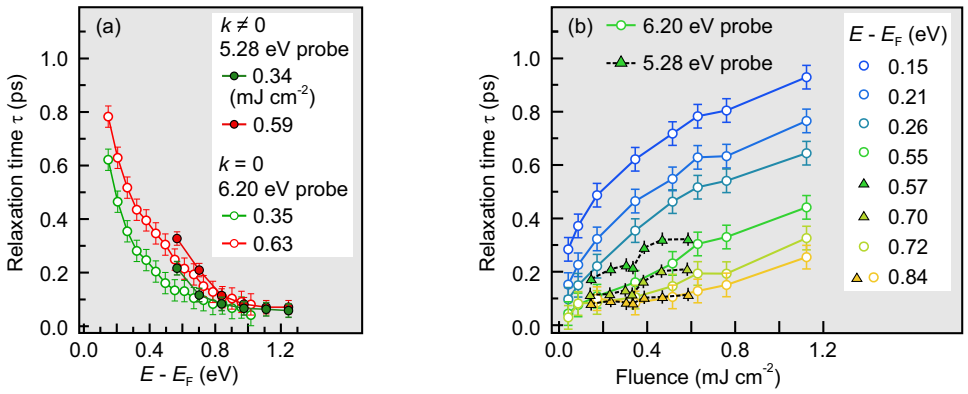

FIGURE 5.25: Relaxation time of CB electrons as a function of (a) energy with respect to E_F and (b) pump fluence. See main text for details.

decay constant τ shifts the maximum of Eq. (5.3) to later time delays. Thus, if the relaxation dynamics slow down at low energies or for high pump fluences, the maximum of the relative transient electron occupancy should appear delayed, in agreement with the experimental observations. In summary, the delayed intensity maximum can be reasonably explained by the combination of two factors: a partial 're-filling' of the CB during the intraband thermalization and, likely more effective, an energy- and fluence-dependent decay dynamics of the CB population.

The best-fit parameters of the relaxation time, τ, are shown in Fig. 5.25. In (a), the results are plotted as a function of the excess energy with respect to E_F, as measured both at $k \neq 0$ by 5.28 eV (full bullets) and around Γ by 6.20 eV (empty bullets) probe photons, respectively. Same line colors corresponds to data taken at similar pump fluences. As already qualitatively observed, data sets recorded by different experiments but at comparable excitation density join rather well within the respective error bars. Altogether, they reveal that **the electron relaxation time increases continuously with decreasing the excess energy relative to E_F.**

In (b), the results of the same analysis are displayed as a function of pump fluence for a series of energy intervals above E_F. Once again, full markers are the data recorded at $k \neq 0$ and empty markers at Γ. The plot shows a weak and rather linear fluence dependence of τ at the highest energies (yellow to green). Towards E_F (dark green to blue), the fluence dependence is stronger at low excitation densities, thus τ increases more rapidly with increasing pump fluence. However, at higher excitation densities a slope reduction is observed and τ increases less. Remarkably, the slope change occurs at a fluence value of approximately 0.2-0.3 mJ cm^{-2}, which well corresponds to the threshold, F_C, for the optical absorption saturation and the excitonic insulator band gap enhancement. Altogether, **at all energies, the electron relaxation time increases continuously with increasing the number of excited carriers. At energies towards E_F, i.e. close to Γ, and for excitation densities above F_C, this fluence-dependent slowing of the electron decay is less pronounced, suggesting a change of the scattering rate and, possibly, the opening of further relaxation channels to the carriers.**

Thus, this quantitative analysis confirms that the timescale for the relaxation of electrons in the CB depends concurrently on the excess energy of the excited electrons with respect to E_F and the excitation density. In the following, both dependencies are interpreted with regard to the dynamics of quasiparticles photoinduced in a low-dimensional system with strong excitonic coupling, as it is the case of Ta_2NiSe_5.

5.4.2 Non-Fermi-liquid quasiparticle behavior

The energy dependence of the quasiparticle relaxation is discussed in the following. The photon energy (1.55 eV) used to excite the electrons results in rather large excess energies, E - E_F. Also, the probed energy region largely exceeds the thermal energy of the system at equilibrium ($k_BT \sim 10$ to 20 meV). Therefore, at these energies, the condition E - $E_F \gg k_BT$ is fulfilled for which electron-electron scattering should play a major role in the quasiparticle decay dynamics (cf. Section 2.2). This observation suggests that the Fermi liquid (FL) model may be applied to reproduce the dependence of τ on the excess energy. The FL model predicts different energy dependencies which connect to the dimensionality of the system. In an ideal 3D FL, τ depends quadratically on the inverse energy. In a 2D FL, a logarithmic correction accounts for the stronger quasiparticle interaction which is due to less efficient screening. As a result of this correction, in the vicinity of E_F, τ is *shorter* in 2D than in 3D at comparable energies. Importantly, in real systems, modifications of the scattering phase space and the Coulombic screening can lead to deviations from the predictions for ideal FLs. Thus, if one of these FL models solidly applies to the data, information on the system dimensionality is retrieved and the electron-electron scattering is proven to dominate the quasiparticle relaxation dynamics. Otherwise, by discussing the origin of apparent deviations from the behavior of ideal FLs, insights on other scattering mechanisms active in the system can be achieved. Furthermore, these deviations may reveal a breakdown of the FL picture which can occur when the electrons are strongly confined in a quasi-1D environment (cf. Section 2.2). As a first indicator of this breakdown, τ should exhibit a linear dependence on the inverse excess energy.

A preliminary consideration is done with regard to the dimensionality of Ta_2NiSe_5. This is based on the character of the orbitals which are involved in the photoexcitation, and thus on the expected dimensionality of the scattering phase space accessed by the photoelectrons. The CB of interest is formed by $5d_{xy}$ Ta orbitals that order in quasi-1D chains within the atomic layers (cf. Ta_2NiSe_5 crystal structure in Fig. 2.14). The upper VB, from which the electrons are photoexcited, originates from quasi-1D chains of $3d_{xz+yz}$ Ni orbitals. These chains run parallel to the Ta chains and hybridize with the $4p$ Se orbitals along the direction perpendicular to the atomic layers. Moreover, the lattice distortion of the LT phase induces interchain hybridization between the Ta and Ni orbitals, i.e. the in-plane anisotropy of the electron transport along and perpendicular to the quasi-1D atomic chains reduces [57]. Therefore, without hybridization, the CB presents a rather defined quasi-1D character. At the same time, its hybridization with the VB points towards a higher-dimensional scattering phase space for the photoexcited electrons. Therefore, it is not straightforward to predict how quasiparticles in the CB will behave with regard to the dimensionality of the phase space in which they are able to scatter. In the first place, both 3D and 2D FL models are tentatively fit to the CB time decay, the electron density being the only fit parameter to be compared with the reference values. It is noted that in metals, the electron density of interest is that of the mobile carriers which contribute to the screening of the electron-electron interaction. For Ta_2NiSe_5, this value is retrieved from Hall resistivity measurements (cf. Fig. 3.22 and [57]). However, in presence of a band gap, the mobile carriers are mostly provided upon excitation of the system, thus the carrier density of interest for the transient screening build-up should be that of the actual photoexcited carriers. Both values will be compared to the fit results.

As reported in Fig. 5.26 (a), the 3D and 2D FL models (red and blue dashed curves) are applied first to the high-energy τ values at $k \neq 0$ (filled circles), only. The best-fit 3D and 2D electron densities results on the order of 10^{23} cm^{-3} and 10^{16} cm^{-2},

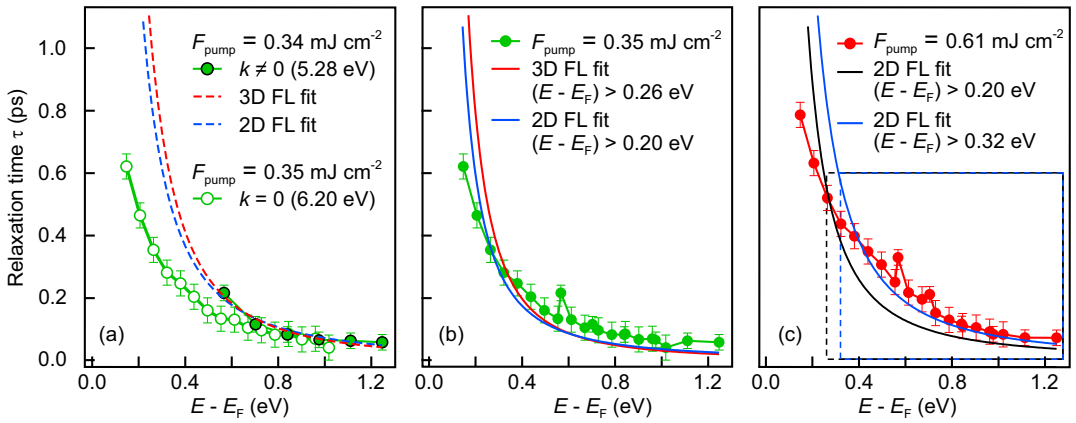

FIGURE 5.26: Electron relaxation time (circles) as a function of energy. (a) The 3D (dashed red) and 2D (dashed blue) FL models are applied to the high-energy τ values at $k \neq 0$. (b) The two models are applied to the combined set of values in the respective energy region of fit convergence. (c) 2D FL model is applied to the high-fluence τ values in two energy intervals (dashed boxes). See main text for details.

respectively. Both values largely exceed the reference carrier densities calculated from Hall resistivity measurements which amount to 10^{17} cm^{-3} and 10^{10} cm^{-2}, respectively[17]. Even when the fit results are compared to the photoelectron density, they again exceed up to three order of magnitudes. The two model curves are projected further at energies towards E_F to be compared to the τ values obtained at Γ (empty circles) for a very comparable fluence. Clearly, both models differ dramatically from the experimental values. All these discrepancies are a first indication that the FL theory does not successfully reproduce the energy-dependent carrier dynamics of the CB.

To confirm this, the two sets of τ values are combined in Fig. 5.26 (b) (filled circles), and the 3D and 2D FL models (red and blue solid curves) are applied again in the full energy range. The agreement is once more poor. First, the 3D and 2D FL models converge within the error bars only at energies above ~ 0.20 eV and ~ 0.26 eV, respectively. Interestingly, these energy thresholds shift to even higher energies for stronger excitation densities. This is exemplified in (c) for a set of τ values obtained for a higher pump fluence: the 2D FL fit converges now only at energies E - $E_F > 0.32$ eV (cf. black with blue curves, the dashed-line boxes of respective colors indicate the energy ranges of fitting). This trend suggests that τ values at energies close to E_F are most probably never captured by the FL models at any fluence. Secondly, the best-fit 3D and 2D carrier densities estimated on the combined data set exceed again the reference values by the same orders of magnitude as the analysis performed only at $k \neq 0$. This confirms that the previous discrepancies were significant and not trivially caused by the small number of fitted points. Evidently, **both 3D and 2D FL models fail to describe the energy dependence of the quasiparticle dynamics of Ta_2NiSe_5 at any energy of the CB with respect to E_F.**

Before discussing the possible origin of these deviations from the FL predictions, a different data analysis is presented, whose results can quantitatively capture the evolution of τ in the whole energy range and for all pump fluences. As reported in Fig. 5.27 (a) to (d) for different excitation densities, a fit function that scales

[17]The 2D carrier density is calculated from the bulk value assuming a homogenous carrier distribution in the volume. See Appendix E.

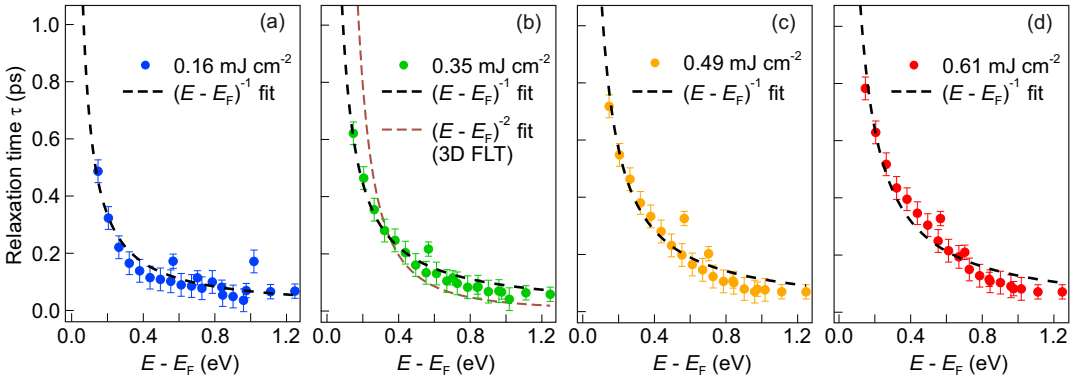

FIGURE 5.27: (a) - (d) Electron relaxation time (circles) as a function of energy for various excitation densities and relative $(E- E_F)^{-1}$ fits (dashed black). In (b), the 3D FL model, i.e. $(\tau \sim (E- E_F)^{-2})$, is reported for comparison.

linearly with the inverse energy describes the evolution of τ impressively well. Remarkably, the τ values at the lowest energies relative to E_F are finally accounted for by the fits at all fluences. Thus, this peculiar energy dependence of τ ultimately attests that electrons photoexcited in the CB of Ta_2NiSe_5 do not relax as ideal quasiparticles in a FL. Consequently, three aspects have to be examined to explain this non-FL behavior. These are: (i) the modification of the electron-electron scattering rate with respect to that of a metallic system; (ii) the activation of decay channels beyond the electron-electron scattering; (iii) the breakdown of the FL model in favor of a 1D-model behavior. The latter will be discussed as first in the following.

A linear scaling of the quasiparticle decay time with the inverse excess energy is predicted for ideal 1D systems in the vicinity of E_F (cf. Section 2.2). It is therefore questionable if the model can explain the energy dependence of the electron relaxation in the CB. The latter, indeed, as discussed before, may offer a quasi-1D scattering environment if the hybridization with other orbitals remains negligible. Three important aspects need then to be considered. First, the 1D model is based on a single electronic band linearly dispersive around E_F. Then, the normal phase is a metallic state with well a defined Fermi level. Second, single quasiparticles in 1D are unstable due to the inevitable interaction with their neighbors. Including the strong electron-electron interaction in the model results in collective excitations of the charge and/or spin density opening a band gap at E_F and typically inducing a periodic lattice distortion. Eventually, because real quasi-1D systems are always integrated in a higher dimensional environment, for the 1D model to be still applicable, their coupling with higher dimensions has to remain negligible.

Comparing with the above, the electronic structure of Ta_2NiSe_5 exhibits two distinct electronic bands separated by a gap around E_F[18], which clearly differs from the case of a metallic 1D chain. Interestingly, one could consider that upon photoexcitation, a transient *quasi-*E_F is defined within the CB at $k \neq 0$. If an instability occurred due to the quasi-1D character of this band, a gap could transiently open at the *quasi-*E_F. During the intraband electron relaxation, the position of this gap may then follow the continuous downshift of the *quasi-*E_F. Effectively, no spectral signature, such as the transient opening of a density wave gap, is observed in the data, although the effects may be experimentally non trivial to resolve. Notably, if

[18]The energy of the Fermi edge is experimentally evaluated on the metallic Au sample holder in electrical contact with the Ta_2NiSe_5 crystal.

these dynamics would take place, the energy dependence of the quasiparticle decay time should be referred to the transient position of the *quasi-*E_F and not to the equilibrium E_F, as it is observed in the present work. Finally, the main achievement of the linear fit model was to account for the relaxation time at energies close to the CB bottom. However, in this energy region the scattering phase space should be majorly affected by the interchain hybridization between the CB and VB orbitals, an effect that likely weakens the quasi-1D character of the band. In conclusion, the electronic band structure of Ta_2NiSe_5 at Γ unlikely accomplish for the constraints set by the 1D model. The photoexcited CB may still undergo a transient instability at $k \neq 0$ in analogy with that of a 1D metallic chain. However, more theoretical support is necessary to test this behavior, which possibly has not been considered so far for any other systems.

Other aspects are now examined with regard to the non-FL behavior of electrons in Ta_2NiSe_5: (i) a modified electron-electron scattering rate and (ii) the concurrence of other decay channels. These will allow to interpret both the energy- and fluence-dependent quasiparticle relaxation dynamics and hopefully open new pathways for theoretical works.

(i) **Reduced scattering phase space and weakly screened electron-electron interaction** The increase of the electron relaxation time for energies closer to E_F is consistent with the reduction of the scattering phase space (cf. Fig. 2.2 (a)), i.e. less final states are available. In low dimensional environments, this behavior competes with the stronger interaction among charges due to the suppression of screening, i.e. electrons scatter more frequently. An example from the literature is now reported, where these aspects lead to an energy dependence of τ comparable to that observed in Ta_2NiSe_5.

Graphite is a layered, narrow-band-gap semiconductor. Around E_F, its band dispersion is nearly linear and the density of states almost vanishes. Interestingly, the measured electron relaxation time scales *linearly* with the inverse excess energy [208]. This non-FL behavior is theoretically reproduced by considering a *bare*, i.e. not screened, Coulomb interaction among electrons in a linearly dispersing conduction band [73]. Clearly, graphite shares significant structural and electronic properties with Ta_2NiSe_5 and it exhibits very comparable energy dependent quasiparticle dynamics. Therefore, it is proposed that in Ta_2NiSe_5, the linear dependence of τ on the inverse energy results from the very weak screening of the Coulomb interaction, which is a characteristic of this material.

The impact of screening on the electron relaxation dynamics is further supported by the observed increase of τ for stronger excitations (cf. Fig. 5.25 (b)): **as more free charge carriers are photoexcited in the system, they can contribute to the screening, thereby reducing the electron-electron scattering rate.** At this point, a remarkable observation is made. At low energies relative to E_F, the fluence dependence of τ shows a slope change at a critical fluence comparable to the saturation threshold of the pump photon absorption, F_C. Fig. 5.28 (a) reports once more the evolution of τ as a function of fluence at the energy comparable to the CB bottom at Γ (blue empty): above F_C, the increase of τ is less pronounced. Notably, this behavior is analogous to the slope change observed in the mid-IR incoherent optical response as a function of pump fluence (black full). The latter effect was correlated with the saturation of the excitation mechanism at Γ keeping constant the number of photoexcited holes at the top of the VB, i.e. the occupancy of the main initial state of the mid-IR transitions. The comparable behavior of the two quantities, τ and A_{fast}, strongly suggests that they both originate from the same mechanism, and specifically from the inhibition of further excitation of free carriers at Γ above F_C.

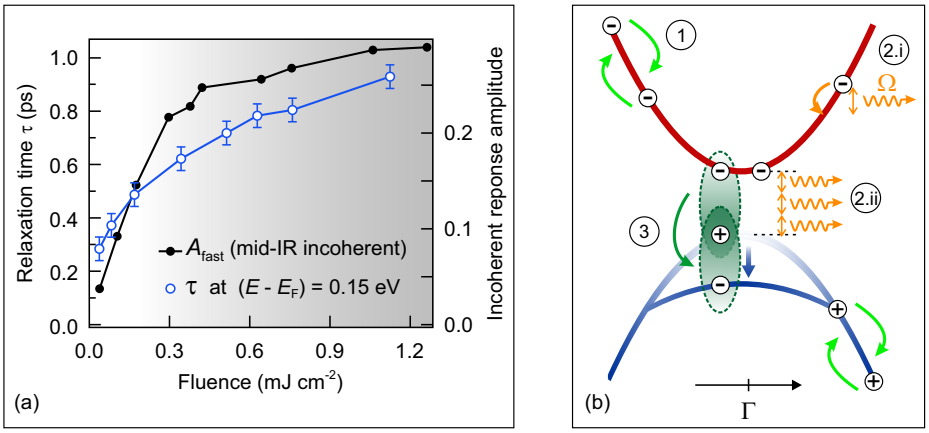

FIGURE 5.28: (a) Comparison of the fluence dependence of τ at the CB bottom (blue empty) and the mid-IR incoherent optical response (black full, the initial amplitude of the fast intensity decay is reported, cf. Fig. 5.9 (d)). (b) Quasiparticle relaxation dynamics in Ta_2NiSe_5: (1) electron-electron scattering; (2) electron-phonon scattering; (3) exciton formation and condensation. See main text.

Therefore, at Γ, τ increases less above F_C as a result of the restricted number of free charges participating to the screening. In other words, **the fluence-dependent evolution of τ at Γ reflects the *effective* transient screening provided by the photoexcited free carriers**, whose number, above F_C, is increased only by further excitations at $k \neq 0$, while it remains constant at the Γ point.

(ii.a) **Decay via electron-phonon scattering** In Ta_2NiSe_5, the maximum optical phonon energy is 40 meV (cf. Section 2.7). At $k \neq 0$, the intraband scattering of quasiparticles can be efficiently assisted by the emission of phonons as there are final states available in the CB at lower energies. At Γ, the energy gap is approximately 330 meV in the LT phase, thus much larger than the maximum phonon energy. Consequently, an electron in the CB bottom does not find any final state for the scattering with a single phonon. In fact, multiphonon emission is required in order to address the first available final state, i.e. the top of the VB. This results in a 'bottleneck' for the quasiparticle decay via scattering with phonons. The relevant rate should be then rather slow at Γ and further reduces with increasing the number of photoelectrons.

(ii.b) **Exciton formation at Γ** At Γ and above F_C, photoelectrons relax within $\sim$ 1 ps. On a very comparable time scale, the electronic band gap at Γ is larger than at equilibrium due to the enhancement of the exciton condensate density (cf. Fig. 5.17 (a)). This concurrence suggests an additional mechanism to explain the change of fluence dependence of the electron relaxation time at the Cb bottom. Moreover, it supports the **contribution of the photoelectrons at the CB bottom to the strengthening of the excitonic insulator order parameter.**

(iii.c) **Electron transport** The VB hole population at Γ fully decays on a slower timescale of few tens of ps (cf. Fig. 5.7 (a)). It is thus asked if a fraction of CB electrons may transfer into the bulk, eventually escaping the detection volume of the probe photons. However, the atomic planes of Ta_2NiSe_5 are only weakly coupled and have a large interlayer distance ($\sim$ 15 Å). All this restricts the electron mobility through the layers [54, 57]. Therefore, electron diffusion into the bulk should only marginally contribute to the CB intensity decay and unlikely can fully account for the retarded recovery of the equilibrium electron occupancy of the VB. Future investigations will aim at clarifying the imbalance between the electrons and the holes dynamics.

To sum up, the combination of all these processes provides a comprehensive description of the relaxation dynamics of conduction electrons in Ta_2NiSe_5. This is depicted in Fig. 5.28. Electrons excited at high energy relative to E_F undergo fast intraband relaxation via electron-electron scattering because their Coulomb interaction is only weakly screened, (1). To conserve the total momentum, hole-hole scattering occurs in the VB (bottom). Additionally, the conduction electrons exchange energy with phonons, (2.i). Upon increase of the excitation density, the Coulomb interaction strength is weakened by the transient increase of screening, and the scattering rate with phonons is reduced as more electrons are excited in the CB. As a result, the relaxation slows down. At energies around the CB bottom, the relaxation dynamics are slower already at low pump fluences due to the limited scattering phase space and the required multiphonon emission, (2.ii). Accordingly, the electron relaxation time increases more rapidly with increasing fluence in this energy range (cf. Fig. 5.25 (d)). This behavior is particularly pronounced at fluences below F_C. However, above F_C, the increase of transient screening is partially impeded by the optical absorption saturation at Γ. This impacts significantly on the electron-electron scattering rate at Γ, whose reduction is accordingly less pronounced above F_C. Furthermore, at Γ and above F_C, (3) electrons are likely favored to leave the CB and bind with the holes at the VB top, thus contributing to the transient increase of the exciton condensate density.

Evidently, these composite dynamics rely on the unique electronic structure of Ta_2NiSe_5, and particularly on the low density of states in the vicinity of E_F and the strong excitonic coupling at the VB and CB extrema. It is argued that both these properties are responsible for the deviation of the photoelectron relaxation dynamics from the FL quasiparticle behavior typical of metallic systems. To corroborate this phenomenological description, an extension of the currently available theory for the quasiparticle dynamics, specifically in an exciton insulator, could be of great help. Hopefully, this work will stimulate theoretical studies in this direction.

In summary, the relaxation dynamics of photoexcited electrons in the CB of Ta_2NiSe_5 are found to depend on both the energy relative to E_F and the excitation density. In particular, the energy dependence of the electron decay time does not follow the predictions for a FL system, consistent with the nonmetallic nature of the ground state of Ta_2NiSe_5 at low temperatures. Interestingly, a linear dependence on the inverse energy is found which most likely results from inefficient screening of the Coulomb interaction. Upon increase of the excitation density, the transient increase of screening slows down the electron relaxation. Remarkable correspondence is found between the fluence dependence of the quasiparticle relaxation dynamics at Γ and of the photoinduced hole population at the top of the VB. This finding reinforces the connection between the quasiparticle relaxation dynamics and the effective transient screening induced by the photoexcited carriers. Moreover, it highlights once more the strong impact of the low density of states in the vicinity of E_F on the photoinduced dynamics of Ta_2NiSe_5. Finally, the formation of coherent excitons above F_C is proposed as additional decay channel for the conduction electrons at Γ. This mechanism would further support that the transient enhancement of the electronic band gap is due to the increase of the exciton condensate density. At the same time, it would ultimately prove that during the occurrence of the band gap widening, the nonequilibrium electron dynamics at Γ does not impact on the stability of the condensate but rather contributes to the strengthening of its order parameter.

5.5 Summary and Conclusion

Ta_2NiSe_5 shows a peculiar electronic band structure and a concomitant electronic and structural phase transition. These aspects make Ta_2NiSe_5 a fascinating and promising material for the study of the role of fundamental interactions on the emergence of new physical properties. At the same time, its complexity presents also a challenge when approaching this study in the equilibrium state of the system because behaviors of different origins manifest in an entangled manner. In this regard, the nonequilibrium approach presented in this thesis work helps to unravel part of this complexity by reconstructing the impact of intrinsic couplings on the ultrafast dynamics of both the electronic structure and the lattice of Ta_2NiSe_5. In particular, experimental and theoretical results achieve to single out the photoinduced behavior of the excitonic insulator band gap of Ta_2NiSe_5, thereby providing the first nonequilibrium fingerprint of this nontrivial phase of matter.

To recap the main findings discussed in this chapter, the photoexcitation of phonons in the low-temperature phase is found to selectively couple to the electronic transitions excited at the Γ point of the Brillouin zone, i.e. at the momentum of the direct band gap. Moreover, the dynamics of one phonon mode specific of the low-temperature monoclinic phase are governed by scattering with the photoexcited carriers at Γ. All this would potentially promise the observation of a photoinduced structural change to the high-temperature orthorhombic phase upon a sufficiently strong photoexcitation. However, the electronic density of states of Ta_2NiSe_5 at Γ is very low and the photon absorption at this k vector rapidly reaches a saturation threshold. Remarkably, this threshold occurs below the energy required for the structural change which consequently remain inhibited.

The electronic band gap exhibits a composite dynamics in the low-temperature phase. These are governed by the screening of the Coulomb interaction provided by the photoexcited carriers and the strong excitonic coupling at the Γ point. The first induces, at any excitation density, an abrupt renormalization, i.e. shrinking, of the band gap. The second is responsible, at excitations above the absorption saturation threshold and at Γ, for a delayed, opposite dynamics of the electronic band gap. Thus, the system evolves transiently into a more insulating state. While the screening-induced dynamics are connected to the nonequilibrium behavior of the underlying semiconducting band structure of Ta_2NiSe_5, the band gap widening is explained by a transient strengthening of the order parameter of the excitonic condensate, in remarkable agreement with Hartree-Fock calculations. These findings thus, identify the impact of the exciton condensate on the nonequilbrium electronic structure of Ta_2NiSe_5. Moreover, they show that the excitonic insulator band gap can be optically modulated on an ultrafast timescale upon tuning of the excitation density.

The relaxation of photoexcited conduction electrons connects to many of the behaviors mentioned above, thereby proving the robustness the presented picture of the ultrafast dynamics of Ta_2NiSe_5. The relaxation time shows an anomalous dependence on the electron excess energy consistent with the weak screening of the Coulomb interaction characteristic of Ta_2NiSe_5. At the conduction band bottom, the excitation-density dependence of the electron relaxation time majorly reflects the build-up of screening by means of the photoexcited hole at the top of the VB. Moreover, indications are found that these photoelectrons may participate to the increase of the exciton condensate density above F_C, thereby contributing to the widening excitonic insulator band gap.

All-in-all, the present study provides a deep understanding of how fundamental interaction, i.e. the electron-hole Coulomb attraction and the electronic coupling to

phonons, regulate the ultrafast dynamics of the electron, exciton and lattice dynamics of Ta_2NiSe_5. Also, it shows the possibility to gain a certain control on the order parameter of the excitonic insulator phase of Ta_2NiSe_5. These results will possibly encourage further nonequilibrium studies of phases of matter which are governed by strong fundamental interactions and whose properties may be dynamically modified by means of light.

6 Conclusions and Perspectives

The presented thesis investigates the role of intrinsic interactions and the impact of the environment on the electronic structure and the ultrafast dynamics of two distinct materials. Both projects, in their diversity, show that the achievement of a profound knowledge of these fundamental interactions and couplings is the first step towards the potential control and modification of the electronic properties of the matter at equilibrium and in the ultrafast time domain.

Quantum electron confinement in ultrathin films of SiO_2 on Ru(0001)

The study of ultrathin films of SiO_2/Ru(0001) provides important insights into the effect of quantum electron confinement in a two-dimensional system and the influence of the image potential at the interface with a metallic substrate. Effectively, an interplay of these two aspects is shown to be essential for the description of the unoccupied electronic structure of the investigated SiO_2/Ru(0001) systems. Remarkably, this finding also holds for a bilayer of SiO_2 on Ru(0001), which previous studies reported being 'quasi-free standing' on the Ru(0001) substrate [37, 15].

The spatial electron confinement inside the oxide film induces a quantization of the SiO_2 conduction band into separated subbands. The energy of these quantum subbands appears altered by the image potential of Ru, indicative of an interaction between the oxide film and the metallic surface. These results indicate that the electronic structure of SiO_2 films is strongly influenced by the electrostatic environment provided by the substrate. Interestingly, oxygen atoms adsorbed on Ru underneath the SiO_2 bilayer further impact on the oxide electronic states by partially reducing their interface electronic coupling and altering their localization inside the oxide. This finding reveals that the electronic structure of SiO_2 bilayers on Ru(0001) is extremely sensitive also to changes of the chemical environment. Therefore, the present work challenges the 'quasi-free standing' character of SiO_2 bilayers on Ru(0001) by disclosing that despite the weak interaction with the substrate, the film is never completely decoupled.

In the future, it will be interesting to further attest how the electron quantum confinement and the coupling to the environment influence the electronic structure of SiO_2/Ru(0001) under different structural parameters and/or external conditions. To give an example, it is nontrivial to predict how the conduction band quantization would result in a single layer of SiO_2 which strongly binds to the Ru(0001) support: while stronger spatial confinement is expected, the influence of the image potential is less predictable. Indeed, due to the closer distance of the oxide to the metal surface, the image potential may either further confine the electrons inside the film or favor the electronic coupling to the bulk Ru, with likely opposite effects on the electronic properties of the system. Furthermore, the presented experimental results will hopefully trigger theoretical works aiming at an extensive description of the electrostatic potential and the electronic structure developing in ultrathin films of SiO_2 on Ru(0001), as well as in other layered systems that interact with their surroundings.

All in all, this study shows that confining electrons in low dimensions leads to the emergence of new electronic states which are spatially localized but can still couple

to the higher-dimensional environment. Consequently, careful characterization of the electrostatic *and* chemical properties of the environment is crucial for the prediction and possibly the modification of the electronic properties of low-dimensional materials.

Interactions governing the nonequilibrium dynamics of the excitonic insulator Ta_2NiSe_5

The nonequilibrium behavior of the quasi-one-dimensional excitonic insulator Ta_2NiSe_5 is studied in this thesis by means of a rich set of time-resolved spectroscopic studies. Intrinsic interactions, more specifically the electron-hole Coulomb attraction and the electron-phonon coupling, are found to govern the ultrafast carrier, exciton and lattice dynamics launched by near-infrared photons. The electron-phonon coupling is partially responsible for the inhibition of the photoinduced structural phase transition. The extraordinarily strong electron-hole interaction promotes, upon intense photoexcitation, the manifestation of a nonequilibrium electronic state which would not be accessible neither thermally nor in absence of strong excitonic coupling. To further appreciate the determinant role of all these fundamental interactions, a more complete overview of the nonequilibrium effects which manifest in Ta_2NiSe_5 is given in the following.

The excitation of coherent optical phonons is coupled to the electronic transitions photoinduced at the Γ point of the Brillouin Zone. However, an optical absorption saturation threshold at Γ limits the perturbation of the phonon subsystem, thereby preventing a photoinduced structural change. As a result, the initial lattice symmetry of Ta_2NiSe_5 is preserved.

Upon photoexcitation, the electronic band gap narrows or even widens on an ultrafast timescale. The narrowing is induced by the transient increase of the screening of the Coulomb interaction by means of the photoexcited carriers. The widening is enabled, at high photoexcitation densities, by the transient enhancement of the exciton condensate density. This is promoted by the intrinsic strong electron-hole attraction, in remarkable agreement with calculations for an excitonic insulator out of the equilibrium. These dynamics highlight the impact of the Coulomb interaction on the nonequilibrum electronic properties of Ta_2NiSe_5. More generally, they prove the possibility to optically manipulate the electronic band gap of this strongly interacting material on an ultrafast timescale.

The relaxation dynamics of the photoexcited electrons are mainly governed by the weakly-screened electron-electron scattering. At Γ, the electron decay rate directly correlates with the effective transient screening provided by the photoexcited charges, and particularly by the photoexcited holes at the top valence band. Upon excitation above the optical saturation threshold, evidences are found that those electrons may leave the conduction band by forming coherent excitons that contribute to the condensate density. This would futher corroborate the mechanism of enhancement of the excitonic insulator band gap. Theoretical support may be helpful to ultimately prove these composite dynamics which appear to strongly rely on the peculiar electronic structure of Ta_2NiSe_5.

In the future, it will be interesting to address the dynamics of the photoexcited states of Ta_2NiSe_5. Experimentally, this requires the preparation of the system out of the equilibrium by means of an ultrashort pulse. Then, at a defined time delay, a pair of pulses are used to perform a pump-probe measurement on the photoexcited, transient state [186, 209]. When applying this approach to time-resolved ARPES, insights on the evolution of the nonequilibrium electronic structure can be achieved. For instance, the dynamics of the transient coherent excitons can be inspected during the

photoinduced widening of the excitonic insulator band gap. Other research directions could focus on the ultrafast dynamics of Ta_2NiSe_5 upon optical perturbation with a lower photon energy in order to exclude the saturating excitation mechanism at the Γ point. In this context, particularly intriguing is the expected nonequilibrium behavior of the excitonic insulator band gap: since no excitation channels should saturate, will the screening-induced band gap narrowing eventually overcome the photoenhancement of the excitonic insulator band gap? Otherwise, will the latter still robustly manifest? Hopefully, these experimental challenges will also offer further perspectives for theorists.

An important message for the study of materials with strong fundamental interactions is delivered by the nonequilibrium dynamics of Ta_2NiSe_5 uncovered in the present thesis work: ultrafast processes can be hindered as well as promoted by the intrinsic couplings of charge carriers with various excitations. Reconstructing the sequence of elementary processes occurring when the system is out of equilibrium and assigning them to the relevant fundamental interaction can provide a powerful tool for the control of the nonequilibirum properties of the matter.

In conclusion, this thesis contributes to the understanding of the electronic structure and the photoinduced ultrafast dynamics of low-dimensional materials in light of their intrinsic interactions and couplings to the environment. A systematic approach is presented for the study of complex systems through the discovery of how each fundamental interaction governs specific physical properties at and out of equilibrium. Eventually, this knowledge can open up pathways for the manipulation of the electronic properties in condensed matter by means of light.

A Near-infrared pump-visible probe reflectivity measurements on Ta_2NiSe_5

Preliminary time-resolved reflectivity measurements are performed with near-infrared pump (1.55 eV) and broadband visible probe [162, 168] to test how the optical response of the system, and particularly its coherent part, changes as a function of sample temperature, photon polarization and laser repetition rate.

In Fig. A.1, the transient reflectivity recorded at $T = 80$ K and at 200 kHz is shown as a function of pump-probe time delay (left) and probe wavelenght (bottom). Upon photoexcitation, the intensity at wavelengths around 620 nm (2.0 eV) and 685 nm (1.8 eV) is strongly suppressed, revealing the presence of two absorption resonances. Their signal evolves towards the initial intensity on a several-ps timescale while it exhibits a periodic modulation due to the activation of coherent phonons (cf. Subsection 3.3.2). Remarkably, at negative delay, a slightly negative intensity indicates that the equilibrium optical response is not completely recovered within the time interval separating two consequent pump pulses (i.e. the inverse of the laser repetition rate which is of 5 μs). In the following, the time-resolved signal at 640 nm is exemplarily characterized in more detail as a function of various experimental parameters.

To achieve this, monochromatic time-resolved reflectivity curves are recorded with lock-in detection upon filtering the broadband visible probe signal with a 10-nm narrow-band filter centered at 640 nm. First, the measurements are performed for different combinations of pump and probe polarization. As indicated by Raman spectroscopy of Ta_2NiSe_5 (cf. Subsection 5.1.1), the direction of the beam polarization relative to the crystallographic axes of Ta_2NiSe_5 impacts on the amplitude of the excited phonon modes. Analogously, by varying the pump and/or probe polarization in the time-resolved optical measurements, different elements of the Raman tensor are addressed. As shown in Fig. A.2 (a), the geometry of the pump-probe optical experiment is such that the two beams propagate almost collinear towards the sample with an angle of incidence of approximately 45°. Thus, when a beam is polarized perpendicularly to the optical table ('s'), the electric field oscillates along the c crystallographic axis and in the plane of the sample surface. When the beam polarization is parallel to the optical table ('p'), the electric field splits into one component normal to the sample surface and one parallel to the a axis, which is the direction of the Ta and Ni atomic chains.

Fig. A.2 (b) shows two transients (dashed curves) recorded with 'p'-polarized probe photons after photoexcitation with 'p'- (blue) and 's' (red) pump photons, respectively. After subtraction of the single exponential decay function fitted to the incoherent optical signal, the bare coherent optical response (solid curves) is obtained for both measurements. The relevant fast Fourier transforms (FFT) are shown in Fig. A.2 (c): clearly, the excitation of coherent phonon is more efficient when the polarization of the pump photons is of 'p'-type, i.e. it has a component along the atomic chain. As displayed in Fig. A.2 (d), the same holds for the polarization of the probe beam. Thus, the optimal combination for the generation and the detection of an intense coherent phonon response is given when both beams are 'p'-polarized. Notably, this is also the

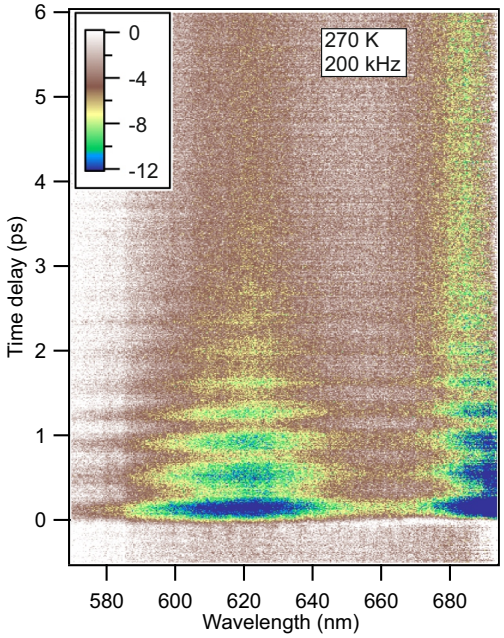

FIGURE A.1: Broadband transient reflectivity in the LT phase with pulse repetition rate of 200 kHz and 'p'-polarized 1.55 eV pump and white light probe photons.

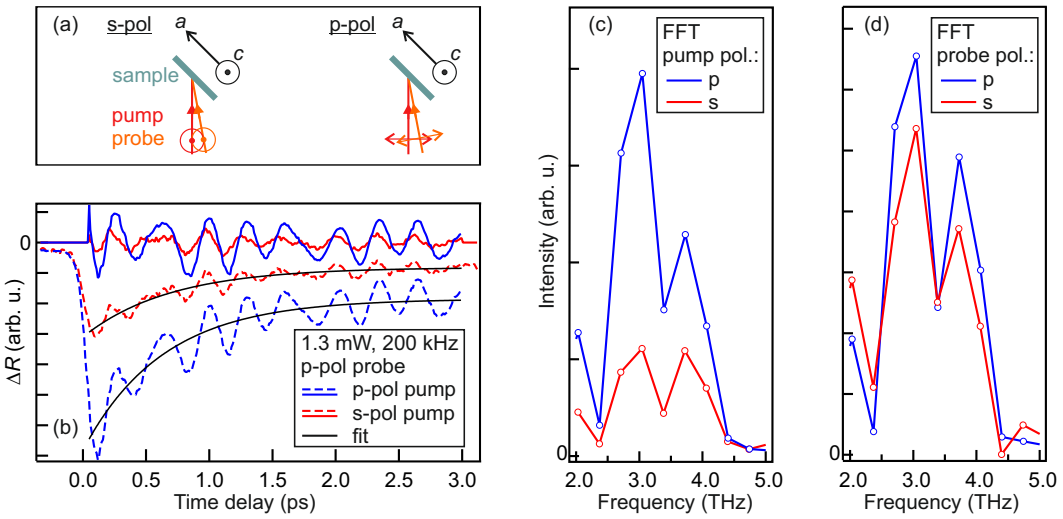

FIGURE A.2: (a) The two polarization schemes used in the optical pump-probe experiment. (b) 'p'-polarized transient reflectivity at 640 nm (dashed blue and red curves) with different pump polarization. The bare coherent optical response (solid blue and red curves) is obtained upon subtraction of the respective fits of the incoherent optical response (black curve). (c)-(d) FFT of the bare coherent response for different combination of pump and probe polarization.

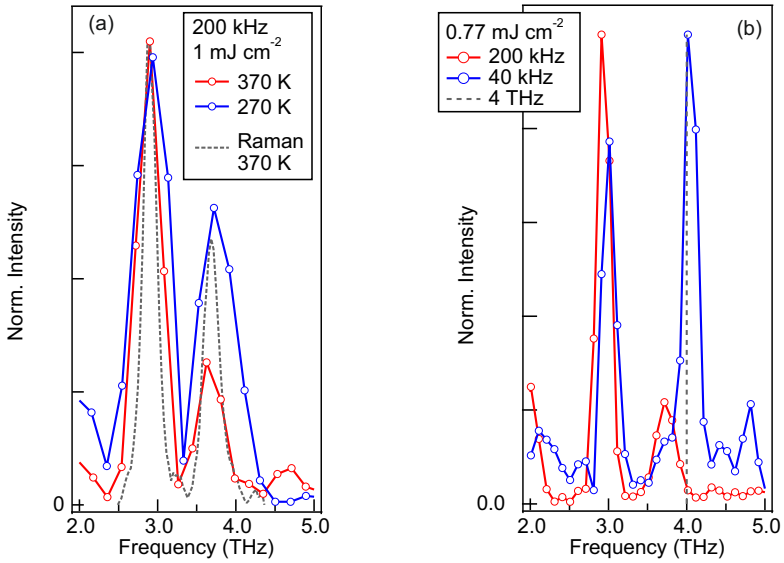

FIGURE A.3: Comparison of the FFT of the coherent optical response (a) below (blue) and above (red) T_C when measured with pulse repetition rate of 200 kHz, and (b) below T_C when measured with pulse repetition rate of 40 (blue) and 200 kHz (red).

direction along which the deformation of the lattice occurs during the phase transition (cf. Subsection 5.1.1).

The influence of the repetition rate on the coherent optical response of Ta_2NiSe_5 is tested in order to ensure that the lattice dynamics of the LT phase is detected and avoid effect of pump-induced heating of the system. Indeed, as already mention above, at 200 kHz the optical signal clearly reveals an incomplete relaxation dynamics within the time interval between two pump pulses. To test the effect on the coherent phonon response, Fig. A.3 (a) shows the FFT of the periodic signal at 640 nm taken both below (T = 270 K, blue curve) and above (T = 370 K, red curve) the critical temperature for the phase transition, T_C. For comparison, the Raman spectrum above T_C is also displayed (gray dashed curve). The two FFT spectra are comparable and exhibit two peaks at 3.0 and 3.7 THz in agreement with the Raman spectrum of the HT phase. Then, the pulse repetition rate is decreased to 40 kHz and the FFT spectrum below T_C is measured again and compared to that recorded at 200 kHz for comparable excitation density. The results are shown in Fig. A.3 (b): The spectrum at 40 kHz (blue curve) exhibits an additional peak at 4.0 THz which is not observed in the measurements at 200 kHz (red curve). From the Raman spectrum, it is known that this phonon mode is specific of the LT structural phase of Ta_2NiSe_5 and disappears in the HT phase. Since this mode is never observed at 200 kHz, it is concluded that, at this high repetition rate, the lattice dynamics is not launched from the LT ground state but rather from a 'pre-excited' state whose energy is not fully dissipated prior to the arrival of the next pulse. Possibly, local heating builds up over real time which can explain both the residual signal intensity at negative time delays and the absence of the LT phonon mode at 4.0 kHz due to a thermally driven structural change. For these reasons, all time-resolved measurements of Ta_2NiSe_5 presented in this thesis are performed at the lower repetition rate of 40 kHz.

The coherent mid-IR optical response discussed in Section 5.2.4 is fitted by a superposition of exponentially damped cosine functions. The amplitude decay parameter

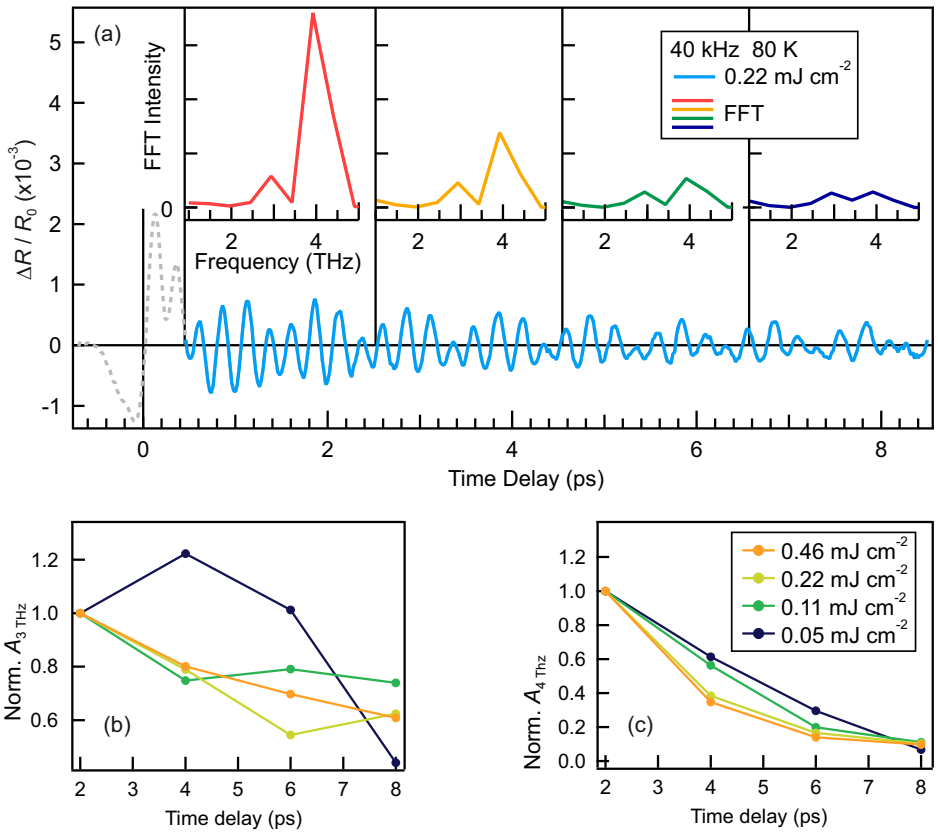

FIGURE A.4: (a) Time-resolved coherent optical response at 640 nm and in the insets, the relative FFTs on a sliding window of 2 ps. (b) and (c) Time-resolved FFT peak intensity normalized to the first data point for the 3.0 and 4.0 THz coherent phonon, respectively, and for different pump fluences.

of each cosine component is assigned to the lifetime of the respective phonon mode. This analysis reveals that the lifetime of the LT phonon mode at 4.0 THz depends on fluence. Particularly, it decreases with increasing the excitation density. Here, a complementary study is presented which provide comparable information on the phonon lifetime as a function of pump fluence. The time-resolved coherent response at 640 nm is shown in Fig. A.4 (a). Because the measurement is performed at 40 kHz with both 'p' polarized beams, the FFT results in an intense peak at 4.0 THz and a weaker one at 3.0 THz. This is visible in all the FFTs of Fig. A.4 (a, insets) that are applied on a sliding window of 2 ps time delay between $\sim$ 0.4 and 8.4 ps. The amplitude of the 3.0 THz mode remains rather constant, indicative of a lifetime on the order of, or even longer than, the time window explored. The amplitude of the 4.0 THz mode dominates at early time decays and rapidly decreases over time, revealing a much shorter litefime. These findings are complementary to the results shown for the mid-IR (cf. Fig. 5.10 (d) and (e)).

Fig. A.4 (b) and (c) show the amplitude of each FFT peak as a function of time delay and for various pump fluence values. All curves are normalized to the amplitude in the earlies time window. Clearly, while the temporal evolution of the 3.0 THz mode amplitude is almost unaffected by the pump fluence, the amplitude of the 4.0 THz mode decreases rapidly for stronger photoexcitations, once more consistent with the expected fluence dependence of its lifetime (cf. Fig. 5.10 (e)).

B Analysis of the time-resolved ARPES spectra of Ta_2NiSe_5

Here, the spectral analysis of the nonequilibrium occupied electronic band structure of Ta_2NiSe_5 in the LT phase is explained. EDCs are extracted at specific electron momenta and pump-probe time delays from the tr-resolved ARPES data set. The spectra exhibit two peaks corresponding to the two VBs that are the closest to E_F around Γ (i.e. $k = 0$). Thus, EDCs are modeled by a sum of Gaussian peaks multiplied by the Fermi-Dirac occupation distribution (FDD) and convolved with another Gaussian to account for the experimental energy resolution. This reads

$$\left(\sum_{i=1}^{3} \mathrm{A} \cdot e^{\frac{-(E-E_i)^2}{w_i^2}} \cdot \frac{1}{e^{\frac{E-E_F}{k_B T}} + 1}\right) * e^{-\left(\frac{E}{\Delta E}\right)^2} \tag{B.1}$$

An example of the model and each component is shown in Fig. B.1. The Gaussian peak (1) at higher binding energy relative to E_F fits to the lower VB, while the sum of the other two Gaussians, (2) and (3), is used to reproduce the asymmetric shape of the upper VB. The green curve shows the Gaussian instrumental resolution function and the dashed line is the normalized FDD.

The results obtained at Γ are summarized in Fig. B.1 (b) - (g) for two exemplary excitation densities, below (blue) and above (red) F_C[1], respectively. All amplitudes (Fig. B.1 (b) - (d)) decrease rapidly at time zero and recover their equilibrium value on a ~ 1 ps timescale. When the system is excited below F_C, the amplitude reduction is more pronounced at the higher fluence. The energy position of the three Gaussian peaks (Fig. B.1 (e) - (g)) changes promptly towards E_F and recovers monotonically to the equilibrium position. When the excitation exceeds F_C, the peak (1), i.e. the lower VB, shows qualitatively the same dynamics with a more intense initial shift amplitude. On the contrary, both peaks (2) and (3) modeling the upper VB exhibit a non-monotonic shifting behavior. In particular, within approximately 200 fs, they both shift downward to higher binding energies than their initial values. Subsequently, their shift is reversed and the their binding energy reduces, eventually, to lower values than at equilibrium. The best-fit parameters of the Gaussians (2) and (3) are used to reconstruct the transient spectral function of the upper VB and to evaluate its energy position at each time which is defined from the energy of the maximum intensity of the combined peak (see discussion in Chapter 5).

[1] F_C is the critical fluence for the absorption saturation of near-infrared pump photons at Γ.

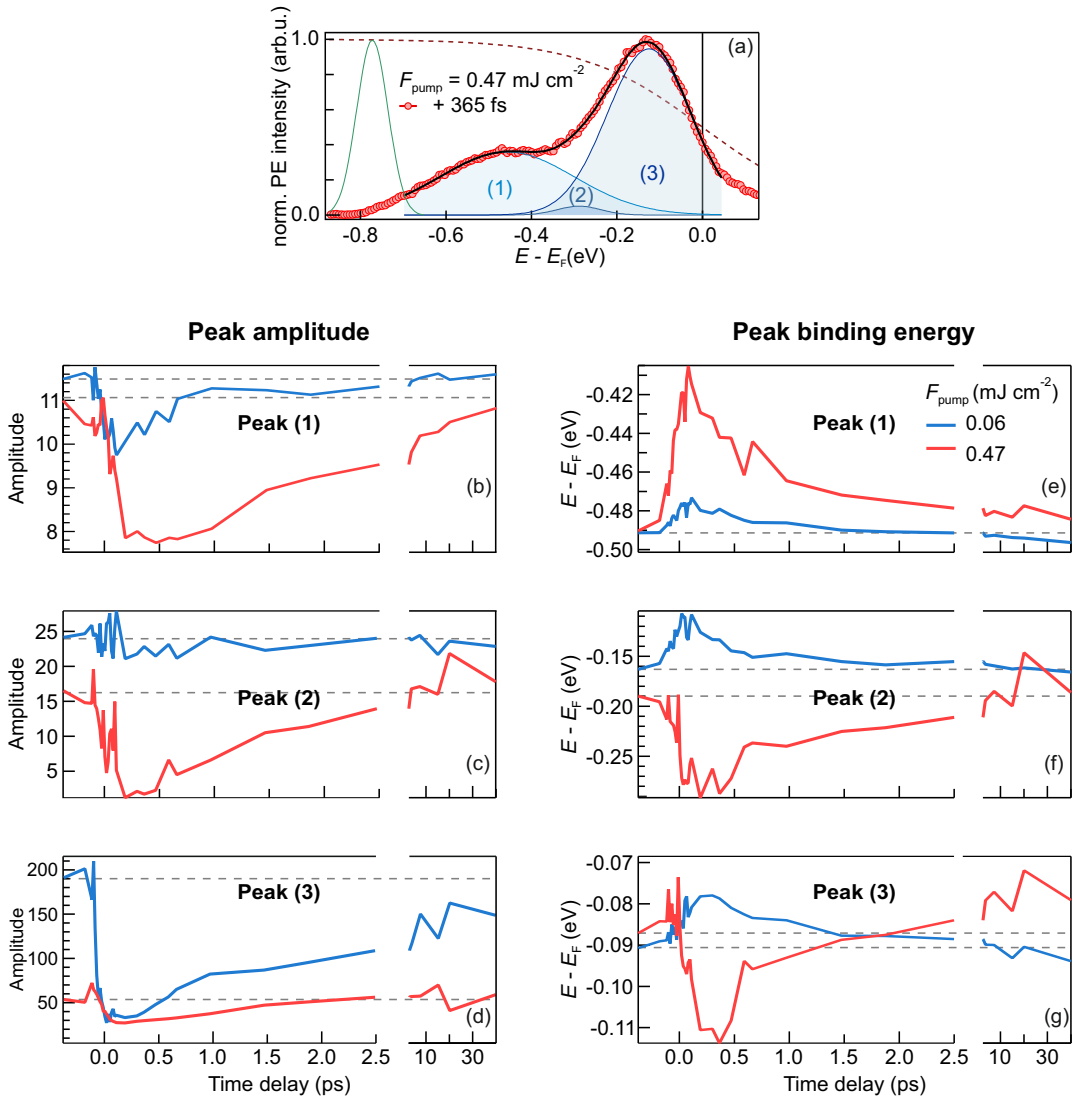

FIGURE B.1: (a) EDC at Γ, 365 fs after photoexcitation with 0.47 mJ cm^{-2} and at 110 K (solid red). The fit curve (black line) is composed of three Gaussian peaks (blue shades) multiplied by a FDD distribution (red dashed curve), and convolved with a Gaussian accounting for the energy resolution (green curve). (b) - (g) Best-fit parameters of the peak amplitude and binding energy relative to E_F for two data set at low (blue) and high (red) fluence, respectively. See text for details.

C Coherent optical phonons in Ta_2NiSe_5 probed by tr-ARPES

As discussed in Chapter 5, the activation of coherent optical phonons in Ta_2NiSe_5 occurs via coupling with the charge carriers excited at the Γ point of the Brillouin zone (cf. Section 5.2.4). Also, the saturation of absorption of pump photons at Γ above a critical excitation density F_C limits the optical perturbation of the lattice which, indeed, continues to exhibit the phonon spectrum of the LT phase. Consistent with these results, it is shown here that after photoexcitation with pump fluence exceeding F_C, both the energy position of the upper VB at Γ and the transient photoemission (PE) intensity around E_F are modulated at a dominant frequency corresponding to the LT optical coherent phonon at 2.1 THz. This is a further confirmation of the momentum-specific electron-phonon coupling and the persistence of the LT structural phase against a photoinduced phase transition in Ta_2NiSe_5.

Fig. C.1 (a) shows the transient PE intensity as a function of energy with respect to E_F (left) and pump-probe time delay (bottom). The measurement is performed in the LT phase at 110 K and with a pump fluence of 0.47 mJ cm^{-2}, i.e. more than twice the F_C value at this temperature. A time-periodic modulation of the PE intensity of both the upper VB and the spectral weight above E_F is visible already by eye. Additionally, the transient energy position of the upper VB with respect to E_F is plotted as a function of time delay (dashed blue curve) after spectral fitting at each delay step: clearly, it exhibits an oscillatory behavior persisting for several picoseconds.

In order to resolve this modulation of the upper VB binding energy, the spectral intensity around the peak maximum at each time delay is fitted by one Gaussian function multiplied by the FFD and convolved with the instrumental resolution. The best-fit energy position of the Gaussian function provides the data points reported on top of the 2D spectrum in (a). The same data points are shown as blue markers in Fig. C.1 (d) after subtraction of the binding energy at equilibrium in order to quantify the absolute transient modulation of the peak energy position. For comparison, these data points are superimposed by the transient shift of the upper VB already presented in Fig. 5.17 (a) (yellow curve) where spectra at various time delays were averaged for better statistics. Clearly, the results of the two analysis are well consistent with each other, verifying the solidity of the observed effects. At the excitation time, an abrupt positive shift (i.e. towards E_F) occurs, followed by a $\sim$ 200 fs-delayed negative shift which brings the VB maximum to lower binding energies than at equilibrium. Then, on a several-picoseconds timescale, a positive shift occurs again. On top of these dynamics, the data set evaluated with finer time delay steps resolves a fast oscillation. The slower, non-monotonic dynamics are discussed in detail in Subsection 5.3.2 with regard to the optical modulation of the excitonic insulator band gap. The oscillatory dynamics is analyzed via FFT which reveals a component at 2.1 THz, in excellent agreement with the frequency of the lower-frequency optical phonon of the LT phase.

Fig. C.1 (b) shows the PE intensity as a function of time delay between 0.5 and 4.0 ps after integration over energies below and above E_F, as indicated by the red box in Fig. C.1 (a). The signal is subtracted from the non-correlated intensity at

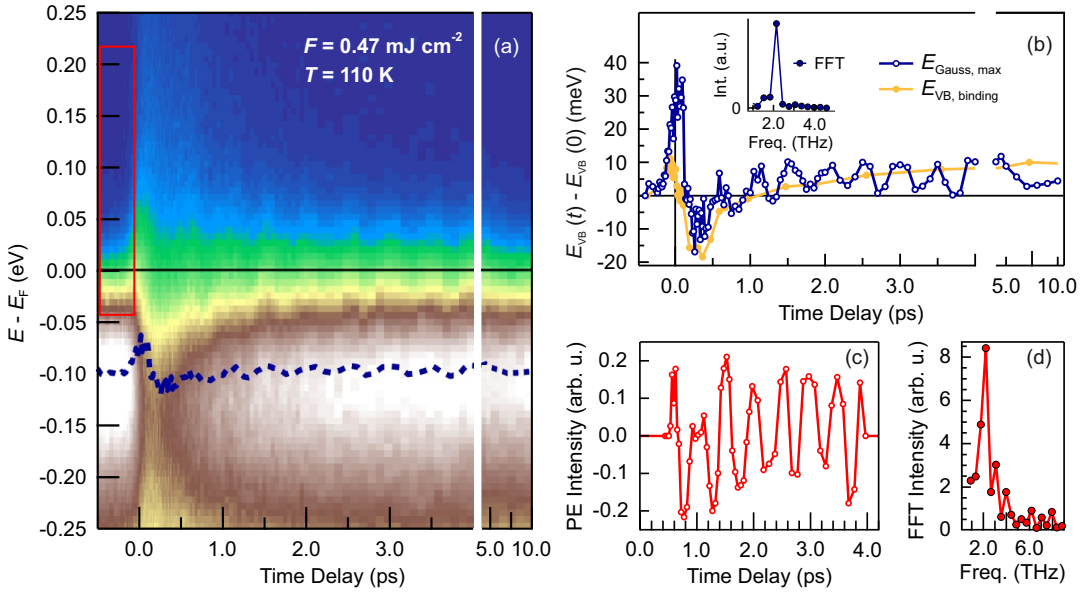

FIGURE C.1: (a) Time-resolved ARPES of Ta_2NiSe_5 at 110 K and 0.47 mJ cm^{-2} pump fluence. The blue dashed curve tracks the binding energy relative to E_F of the upper VB. (b) The same curve as in (a), shifted by the equilibrium VB binding energy with respect to E_F and superimposed by the transient VB shift evaluated for larger time delay steps (yellow curve). In inset, the relative FFT. (c) PE intensity integrated over the energy region marked the red box in (a). (d) FFT spectrum of PE intensity in (b).

negative time delays. Upon fast-Fourier transformation (FFT), a dominant component at 2.1 THz is obtained, as shown in Fig. C.1 (d). Possibly, other two modes at approximately 3 and 4 THz were resolved, but their intensities are almost at the signal-to-noise limit. The FFT spectrum is very comparable with that of the LT phononic response retrieved by coherent optical phonon spectroscopy, thus supporting the coupling of phonons with the carrier density at Γ.

Since it was demonstrated that the LT phase persists for excitation densities largely exceeding F_C, the observed periodic modulation of the PE intensity near the Γ point is also expected to persists. This is tested on a set ot tr-ARPES data recorded at 200 K, i.e. even closer to T_C. Fig. C.2 (a) shows the transient PE intensity at Γ integrated between -0.06 eV and +0.09 eV with respect to E_F, for a set of excitation densities well above F_C. The curves are shifted on the left axis for clarity: an oscillation with period of approximately half-ps is visible at all fluences, as indicated by the two gray dashed lines marking two consecutive oscillation peaks. As shown in Fig. C.2 (b), the FFT of two data sets shows again an intense component at 2.1 THz and a weaker one at 3.0 THz, consistent with the FFT spectrum obtained at 110 K. The mode at 4.0 THz is not observed at any fluence. Effectively, it should be noted that the sample temperature is rather close to that at which the Raman mode at 4.0 THz thermally disappears (T = 275 K). Thus, the 4.0 THz mode amplitude might be too small to be resolved in this data set. Because the FFT intensity of the 3.0 THz peak is very weak, it is neglected in the fit function. Therefore, the transients are fitted by a single exponentially-damped cosine function (blue curve)[1].

[1]A double-cosine function is also tested but the fit cannot solidly converge for all fluences due to the negligible intensity of the higher-frequency mode and the rather narrow time-window of data points available.

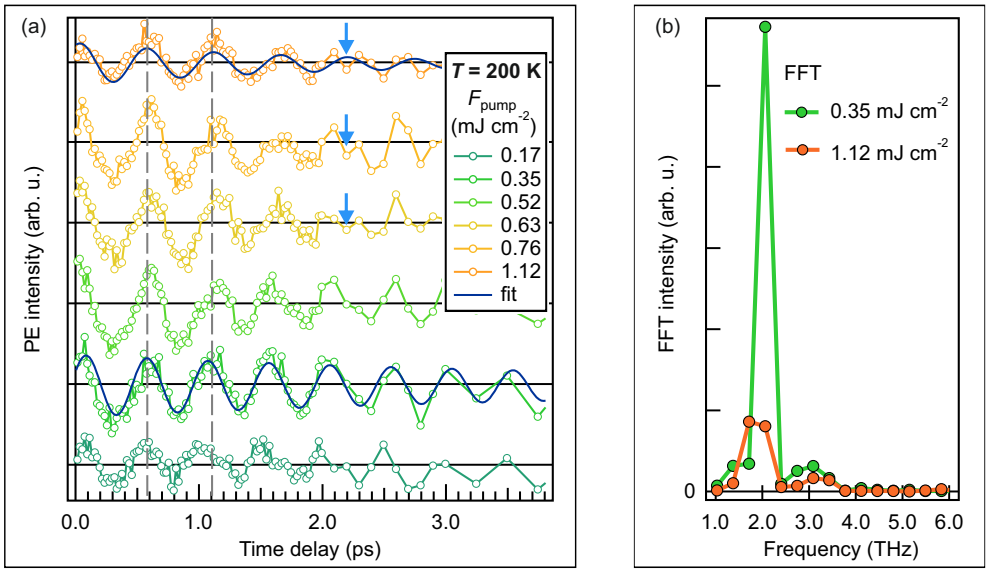

FIGURE C.2: Transient PE Intensity at 200 K integrated over a 15 meV-narrow energy interval around E_F for various pump fluences. The blue curves are the exponentially damped cosine fits. The dashes lines indicate two consecutive maxima of the phonon oscillation at $\sim$ 2.1 THz. The light blue arrows indicate a higher-frequency modulation of the PE intensity. (b) FFT of the transient PE intensity at 0.35 and 1.12 mJ cm^{-2} pump fluence.

The best-fit frequency parameter is 2.1 THz, with no significant change with increasing fluence, in agreement with the previous results obtained with optical probe. Notably, the fit curve reproduces well the data at the lower fluences (green circles). For stronger excitation, the fit converges up to $\sim$ 2 ps, while deviates from the experimental data points at later delays (yellow circles). Indeed, when qualitatively comparing the data before and after 1 ps at the highest fluence values, an additional modulation at higher frequency is observed at later time delays, as indicated by the black arrows. This may confirm the presence of other phonon components, however the signal is weak to allow for a more complex fit. Importantly, the LT phonon component at 2.1 THz is clearly resolved at any fluence well above F_C.

In conclusion, the electron-phonon coupling at Γ manifests in the nonequilibrium electronic structure with a modulation of both the binding energy of the upper VB and the PE intensity at Γ and close to E_F at the frequency of the LT phonon mode at 2.1 THz. Since the photoinduced structural phase transition is inhibited by optical absorption saturation at Γ in Ta_2NiSe_5, these modulations consistently persist for a wide range of fluences above F_C. This finding ultimately corroborates the entanglement between the electron and lattice nonequilibrium dynamics in Ta_2NiSe_5.

D Hartree-Fock calculations on a 1D two-band system

The nonthermal state of a system with excitonic coupling is calculated by D. Golež and co-workers in the mean-field Hartree-Fock approximation. The discussion of the results is given in Subsection 5.3.3. Here, the model and its application is described.

The model is based on a one-dimensional two-band system of spin-less fermions with a direct electronic band gap at $k = 0$. The total Hamiltonian reads $\mathrm{H}_0 + \mathrm{H}_{\mathrm{int}}$, where the noninteracting part H_0 is

$$\mathrm{H}_0 = \sum_{k,\alpha} (\epsilon_{k,\alpha} + \eta_\alpha)\, c^\dagger_{k,\alpha} c_{k,\alpha}, \tag{D.1}$$

with the band dispersion given by $\epsilon_{k,1,(2)} = -(+)2t_0\cos(k)$. The $c_{k,\alpha}$ are the annihilation operators for an electron with momentum k in the orbital $\alpha = 1, 2$. The bare band splittings η =1,2 are chosen such that band 1(2) is totally occupied (unoccupied). The hopping parameter t_0 is chosen such that the ground state dispersion in the noninteracting case matches the experimental one. This term alone describes the bare semiconductor band structure whose VB at equilibrium is shown in Fig. D.1 (a) as dashed gray curve.

The coupling between the bands is described by a local density-density Coulomb interaction term of the form

$$\mathrm{H}_{\mathrm{int}} = \frac{1}{2} \sum_i U n_{i,1} n_{1,2}. \tag{D.2}$$

The interaction value U is obtained by the comparison of the calculated and the equilibrium ARPES spectra in both the interacting and noninteracting state. For the ground state calculations, the parameter values are $t_0 = 0.26$ eV, $U/t_0 = 3.0$ and the

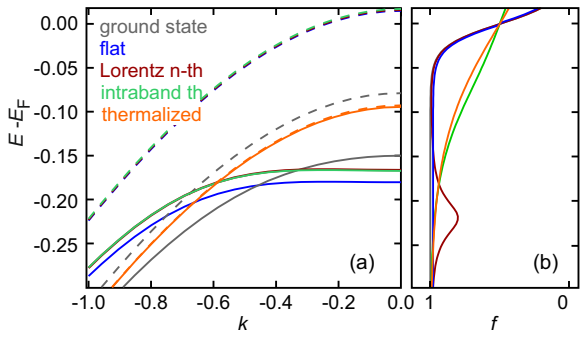

FIGURE D.1: Comparison of the ground state dispersion to those obtained from various FDD functions both in the noninteracting (dashed) and interacting (solid) case. In (a), the calculated VB dispersions, in (b) the corresponding FFD functions in the energy region below E_{F}. From [36].

relative bare band splitting $(\eta_2 - \eta_1)/t_0 = 2.1$. The excitonic instability arises from the attractive Coulomb interaction between the electrons in the upper (cunduction) band and the holes in the lower (valence) band, leading to a condensation of the excitons which are formed across the direct electronic band gap. The order parameter of the condensate is then defined as $\rho_{12} = c^{\dagger}_{k,1} c_{k,2} \neq 0$. Adding this term to the Hamiltonian leads to a VB with higher binding energy relative to E_{F}, as displayed by the solid gray curve on Fig. D.1 (a).

The experimentally observed abrupt band gap narrowing is mimicked by a reduction of the bare band splitting $\delta\eta = \eta_2 - \eta_1$ between the VB and CB, while the effect of the nonthermal distribution on the band gap size is determined from self-consistent Hartree-Fock calculations. In order to show that the results do not depend on the particular choice of the distribution function, several parametrizations of the nonthermal FDD function are tested. They are displayed on Fig. D.1 in the energy range below E_{F} (b): (blue) an additional constant population of holes (electrons); (red) a Lorentzian peak (dip) in the Fermi-Dirac distribution function below (above) E_{F}, namely $f_{nth}(\epsilon, A, E_{textc}) = f_{FD}(\epsilon, 0) + A\gamma^2/((\epsilon - E_{textc})^2 + \gamma^2)$, where $f_{FD}(\epsilon, \mu)$ is the FFD centered at $\mu = E_{\mathrm{F}} = 0$, A is the amplitude, γ the width and E_{textc} the center position of the Lorentzian peak (dip); (green) intraband thermalized distributions at elevated temperatures.

As shown in Fig. D.1 (a), for all these nonthermal distributions and for the same excitation density n_{ex}, the band gap at Γ is enhanced in the interacting case (solid VBs) while it always narrows when the coupling term $\mathrm{H_{int}}$ is switched off (dashed VBs). On the contrary, for the thermalized FFD (solid orange in Fig. D.1 (b)), both the bare and the coupled VBs shift towards E_{F}, thus the band gap narrows. Finally, it is noted that for all the employed nonequilibrium FFD, the VB at large k exhibits an upward shift also in the presence of the excitonic instability.

E Calculated surface carrier density of Ta_2NiSe_5

The 3D carrier density of Ta_2NiSe_5 obtained from measurements of the Hall resistivity at different temperatures is used to estimate the corresponding 2D carrier density. Two assumptions are made: 1. the carrier density is uniform within the unit cell; 2. a single three-atoms-thick layer of the crystal structure of Ta_2NiSe_5 is taken as the 2D unit.

The unit cell of Ta_2NiSe_5 consists of two of such 2D units, as shown in Fig. E.1. The lattice constants are labeled by a, b, and c, and their values are taken from [117]. Then, by knowing the 3D carrier density $n_{3D,T}$ at a temperature T, the number of electrons, $N_{2D,T}$, in one layer, i.e. one 2D unit, is simply given by:

$$N_{2D,T} = 1/2 \cdot n_{3D,T} \cdot a \cdot b \cdot c \tag{E.1}$$

where the pre-factor $1/2$ accounts for the number of layers in the unit cell.

The surface density of carrier $n_{2D,T}$ is then obtained as

$$n_{2D,T} = \frac{N_{2D,T}}{a \cdot c} \tag{E.2}$$

This value is used in Subsection 5.4.2 as a reference to be compared with the best-fit parameter of the 2D FL model of the energy dependent electron decay time.

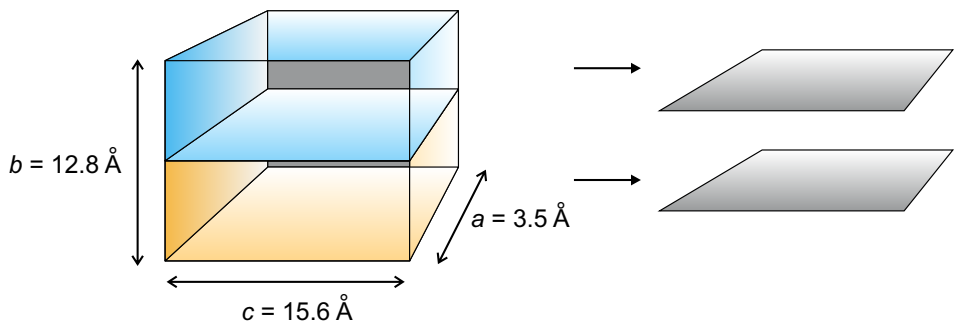

FIGURE E.1: Schematic of the layered unit cell and the 2D crystal units of Ta_2NiSe_5.

Bibliography

[1] M. Bauer, A. Marienfeld, and M. Aeschlimann. "Hot electron lifetimes in metals probed by time-resolved two-photon photoemission". In: *Progress in Surface Science* 90.3 (2015), pp. 319 –376. ISSN: 0079-6816. DOI: https://doi.org/10.1016/j.progsurf.2015.05.001. URL: http://www.sciencedirect.com/science/article/pii/S0079681615000192.

[2] N. F. Mott. "The Electrical Resistance of Dilute Solid Solutions". In: *Mathematical Proceedings of the Cambridge Philosophical Society* 32.2 (1936). DOI: doi:10.1017/S0305004100001845.

[3] D. Baeriswyl and L. Degiorgi. *Strong interactions in low dimensions*. Ed. by D. Baeriswyl and L. Degiorgi. Lluwer Academic Publisher, 2004.

[4] F. J. Morin. "Oxides Which Show a Metal-to-Insulator Transition at the Neel Temperature". In: *Phys. Rev. Lett.* 3 (1 July 1959), pp. 34–36. DOI: 10.1103/PhysRevLett.3.34. URL: https://link.aps.org/doi/10.1103/PhysRevLett.3.34.

[5] M. DiDomenico et al. "Raman Spectrum of Single-Domain $BaTiO_3$". In: *Phys. Rev.* 174 (2 Oct. 1968), pp. 522–530. DOI: 10.1103/PhysRev.174.522. URL: https://link.aps.org/doi/10.1103/PhysRev.174.522.

[6] A Jayaraman. "Influence of Pressure on Phase Transitions". In: *Annual Review of Materials Science* 2.1 (1972), pp. 121–142. DOI: 10.1146/annurev.ms.02.080172.001005. eprint: https://doi.org/10.1146/annurev.ms.02.080172.001005. URL: https://doi.org/10.1146/annurev.ms.02.080172.001005.

[7] S. Frank et al. "Carbon Nanotube Quantum Resistors". In: *Science* 280.5370 (1998), pp. 1744–1746. ISSN: 0036-8075. DOI: 10.1126/science.280.5370.1744. eprint: http://science.sciencemag.org/content/280/5370/1744.full.pdf. URL: http://science.sciencemag.org/content/280/5370/1744.

[8] J. J. Paggel, T. Miller, and T.-C. Chiang. "Quantum-Well States as Fabry-Pérot Modes in a Thin-Film Electron Interferometer". In: *Science* 283.5408 (1999), pp. 1709–1711. ISSN: 0036-8075. DOI: 10.1126/science.283.5408.1709. eprint: http://science.sciencemag.org/content/283/5408/1709.full.pdf. URL: http://science.sciencemag.org/content/283/5408/1709.

[9] S. Ogawa, H. Nagano, and H. Petek. "Optical Intersubband Transitions and Femtosecond Dynamics in Ag /Fe(100) Quantum Wells". In: *Phys. Rev. Lett.* 88 (11 Feb. 2002), p. 116801. DOI: 10.1103/PhysRevLett.88.116801. URL: https://link.aps.org/doi/10.1103/PhysRevLett.88.116801.

[10] D. Wegner, A. Bauer, and G. Kaindl. "Electronic Structure and Dynamics of Quantum-Well States in Thin Yb Metal Films". In: *Phys. Rev. Lett.* 94 (12 Apr. 2005), p. 126804. DOI: 10.1103/PhysRevLett.94.126804. URL: https://link.aps.org/doi/10.1103/PhysRevLett.94.126804.

[11] M. Velick and Peter S. Toth. "From two-dimensional materials to their heterostructures: An electrochemist's perspective". In: *Applied Materials Today* 8 (2017). 2D Materials in Electrochemistry, pp. 68 –103. ISSN: 2352-9407. DOI: https://doi.org/10.1016/j.apmt.2017.05.003. URL: http://www.sciencedirect.com/science/article/pii/S235294071730080X.

[12] R. E. Peierls. *Quantum theory of Solids*. Oxford University Press Inc., 1955. DOI: 10.1093/acprof:oso/9780198507819.001.0001.

[13] G. Grüner. *Density Waves in Solids*. Ed. by D. Pines. Perseus Publishing, 2000.

[14] T. Giamarchi. "Theoretical Framework for Quasi-One Dimensional Systems". In: *Chemical Reviews* 104.11 (2004). PMID: 15535641, pp. 5037–5056. DOI: 10.1021/cr030647c. eprint: https://doi.org/10.1021/cr030647c. URL: https://doi.org/10.1021/cr030647c.

[15] H.-J. Freund and G. Pacchioni. "Oxide ultra-thin films on metals: new materials for the design of supported metal catalysts". In: *Chem. Soc. Rev.* 37 (10 2008), pp. 2224–2242. DOI: 10.1039/B718768H. URL: http://dx.doi.org/10.1039/B718768H.

[16] S. Z. Butler et al. "Progress, Challenges, and Opportunities in Two-Dimensional Materials Beyond Graphene". In: *ACS Nano* 7.4 (2013). PMID: 23464873, pp. 2898–2926. DOI: 10.1021/nn400280c. eprint: https://doi.org/10.1021/nn400280c. URL: https://doi.org/10.1021/nn400280c.

[17] K. F. Mak and J. Shan. "Photonics and optoelectronics of 2D semiconductor transition metal dichalcogenides". In: *Nature Photonics* 10 (Mar. 2016), pp. 216–. URL: http://dx.doi.org/10.1038/nphoton.2015.282.

[18] P. Avouris, T. F. Heinz, and T. Low. *2D Materials: Properties and Devices*. Ed. by P. Avouris, T. F. Heinz, and T. Low. Cambridge University Press, 2017.

[19] C. Gong et al. "Electronic and Optoelectronic Applications Based on 2D Novel Anisotropic Transition Metal Dichalcogenides". In: *Advanced Science* 4.12 (2017), p. 1700231. DOI: 10.1002/advs.201700231. eprint: https://onlinelibrary.wiley.com/doi/pdf/10.1002/advs.201700231. URL: https://onlinelibrary.wiley.com/doi/abs/10.1002/advs.201700231.

[20] M. Zeng et al. "Exploring Two-Dimensional Materials toward the Next-Generation Circuits: From Monomer Design to Assembly Control". In: *Chemical Reviews* 118.13 (2018). PMID: 29381058, pp. 6236–6296. DOI: 10.1021/acs.chemrev.7b00633. eprint: https://doi.org/10.1021/acs.chemrev.7b00633. URL: https://doi.org/10.1021/acs.chemrev.7b00633.

[21] H. Petek and S. Ogawa. "Femtosecond time-resolved two-photon photoemission studies of electron dynamics in metals". In: *Progress in Surface Science* 56.4 (1997), pp. 239 –310. ISSN: 0079-6816. DOI: https://doi.org/10.1016/S0079-6816(98)00002-1. URL: http://www.sciencedirect.com/science/article/pii/S0079681698000021.

[22] S. Hellmann et al. "Time-domain classification of charge-density-wave insulators". In: *Nature Communication* 3 (2012). DOI: https://www.nature.com/articles/ncomms2078.

[23] C. Giannetti et al. "Ultrafast optical spectroscopy of strongly correlated materials and high-temperature superconductors: a non-equilibrium approach". In: *Advances in Physics* 65.2 (2016), pp. 58–238. DOI: 10.1080/00018732.2016.1194044. eprint: https://doi.org/10.1080/00018732.2016.1194044. URL: https://doi.org/10.1080/00018732.2016.1194044.

[24] S. Hüfner. *Photoelectron spectroscopy*. Springer, 1996.

[25] B. Straughan. *Spectroscopy*. Ed. by B. P. Straughan and S. Walker. Chapmann and Hall Ltd., 1976.

[26] M. Dantus, Mark J. Rosker, and Ahmed H. Zewail. "Real-time femtosecond probing of "transition states" in chemical reactions". In: *The Journal of Chemical Physics* 87.4 (Aug. 1987), pp. 2395 –2397. DOI: 10.1063/1.453122. eprint: https://doi.org/10.1063/1.453122. URL: https://doi.org/10.1063/1.453122.

[27] M. J. Rosker, Marcos Dantus, and Ahmed H. Zewail. "Femtosecond real-time probing of reactions. I. The technique". In: *The Journal of Chemical Physics* 89.10 (Nov. 1988), pp. 6113–6127. DOI: 10.1063/1.455427. eprint: https://doi.org/10.1063/1.455427. URL: https://doi.org/10.1063/1.455427.

[28] R. Haight et al. "Picosecond Time-Resolved Photoemission Study of the InP(110) Surface". In: *Phys. Rev. Lett.* 54 (12 Mar. 1985), pp. 1302–1305. DOI: 10.1103/PhysRevLett.54.1302. URL: https://link.aps.org/doi/10.1103/PhysRevLett.54.1302.

[29] Ahmed H. Zewail. "4D Ultrafast electron diffraction, crystallography, and microscopy". In: *Annual Review of Physical Chemistry* 57.1 (2006). PMID: 16599805, pp. 65–103. DOI: 10.1146/annurev.physchem.57.032905.104748. eprint: https://doi.org/10.1146/annurev.physchem.57.032905.104748. URL: https://doi.org/10.1146/annurev.physchem.57.032905.104748.

[30] U. Bovensiepen, H. Petek, and M. Wolf. *Dynamics at Solid state surfaces and interfaces*. Ed. by U. Bovensiepen, H. Petek, and M. Wolf. Vol. 1. Wiley-VCH, 2012.

[31] D. Wegkamp and Julia Stähler. "Ultrafast dynamics during the photoinduced phase transition in VO_2". In: *Progress in Surface Science* 90.4 (2015), pp. 464 –502. ISSN: 0079-6816. DOI: https://doi.org/10.1016/j.progsurf.2015.10.001. URL: http://www.sciencedirect.com/science/article/pii/S0079681615000301.

[32] Daniel Wegkamp et al. "Instantaneous Band Gap Collapse in Photoexcited Monoclinic VO_2 due to Photocarrier Doping". In: *Phys. Rev. Lett.* 113 (21 Nov. 2014), p. 216401. DOI: 10.1103/PhysRevLett.113.216401. URL: https://link.aps.org/doi/10.1103/PhysRevLett.113.216401.

[33] L. Sojchevska et al. "Ultrafast switching to a Stable Hidden Quantum State in an Electronic Crystal". In: *Science* 344.6180 (2014), pp. 177–180.

[34] Ed. J. Sie et al. "Valley-selective optical Stark effect in monolayerWS_2". In: *Nat. Mater.* 14.290 (2014). DOI: 10.1038/nmat4156. URL: https://doi.org/10.1038/nmat4156.

[35] M. Mitrano et al. "Possible light-induced superconductivityin K_3C_{60} at high temperature". In: *Nature* 530 (2016), pp. 461–464.

[36] S. Mor et al. "Ultrafast Electronic Band Gap Control in an Excitonic Insulator". In: *Phys. Rev. Lett.* 119 (8 Aug. 2017), p. 086401. DOI: 10.1103/PhysRevLett.119.086401. URL: https://link.aps.org/doi/10.1103/PhysRevLett.119.086401.

[37] S. C. Street, C. Xu, and D. W. Goodman. "The physical and chemical properties of ultrafast oxide films". In: *Annual Review of Physical Chemistry* 48.1 (1997). PMID: 15012439, pp. 43–68. DOI: 10.1146/annurev.physchem.48.1.43. eprint: https://doi.org/10.1146/annurev.physchem.48.1.43. URL: https://doi.org/10.1146/annurev.physchem.48.1.43.

[38] Mengen Wang et al. "Energy Level Shifts at the Silica/Ru(0001) Heterojunction Driven by Surface and Interface Dipoles". In: *Topics in Catalysis* 60.6 (May 2016), pp. 481–491. ISSN: 1572-9028. DOI: 10.1007/s11244-016-0704-x. URL: https://doi.org/10.1007/s11244-016-0704-x.

[39] T. Fauster and W. Steinmann. "Two-photon photoemission spectroscopy of image states". In: 2 (1995). Ed. by P. Halevi, p. 347. DOI: 10.1016/B978-0-444-82198-0.50015-1.

[40] R. P. Gupta. "Electronic structure of crystalline and amorphous silicon dioxide". In: *Phys. Rev. B* 32 (12 Dec. 1985), pp. 8278–8292. DOI: 10.1103/PhysRevB.32.8278. URL: https://link.aps.org/doi/10.1103/PhysRevB.32.8278.

[41] L. Lichtenstein et al. "Probing the properties of metal-oxide interfaces: silica films on Mo and Ru supports". In: *Journal of Physics: Condensed Matter* 24.35 (2012), p. 354010. URL: http://stacks.iop.org/0953-8984/24/i=35/a=354010.

[42] D. Löffler et al. "Growth and Structure of Crystalline Silica Sheet on Ru(0001)". In: *Phys. Rev. Lett.* 105 (14 Sept. 2010), p. 146104. DOI: 10.1103/PhysRevLett.105.146104. URL: https://link.aps.org/doi/10.1103/PhysRevLett.105.146104.

[43] R. Włodarczyk et al. "Tuning the electronic structure of ultrathin crystalline silica films on Ru(0001)". In: *Phys. Rev. B* 85 (8 Feb. 2012), p. 085403. DOI: 10.1103/PhysRevB.85.085403. URL: https://link.aps.org/doi/10.1103/PhysRevB.85.085403.

[44] A. Chernikov et al. "Exciton Binding Energy and Nonhydrogenic Rydberg Series in Monolayer WS_2". In: *Phys. Rev. Lett.* 113 (7 Aug. 2014), p. 076802. DOI: 10.1103/PhysRevLett.113.076802. URL: https://link.aps.org/doi/10.1103/PhysRevLett.113.076802.

[45] N. F. Mott. "The transition to the metallic state". In: *The Philosophical Magazine: A Journal of Theoretical Experimental and Applied Physics* 6.62 (1961), pp. 287–309. DOI: 10.1080/14786436108243318. eprint: https://doi.org/10.1080/14786436108243318. URL: https://doi.org/10.1080/14786436108243318.

[46] D. Jérome, T. M. Rice, and W. Kohn. "Excitonic Insulator". In: *Phys. Rev.* 158 (2 June 1967), pp. 462–475. DOI: 10.1103/PhysRev.158.462. URL: https://link.aps.org/doi/10.1103/PhysRev.158.462.

[47] K. F. Berggren and B. E. Sernelius. "Band-gap narrowing in heavily doped many-valley semiconductors". In: *Phys. Rev. B* 24 (4 Aug. 1981), pp. 1971–1986. DOI: 10.1103/PhysRevB.24.1971. URL: https://link.aps.org/doi/10.1103/PhysRevB.24.1971.

[48] A. Oschlies, R. W. Godby, and R. J. Needs. "First-principles self-energy calculations of carrier-induced band-gap narrowing in silicon". In: *Phys. Rev. B* 45 (23 June 1992), pp. 13741–13744. DOI: 10.1103/PhysRevB.45.13741. URL: https://link.aps.org/doi/10.1103/PhysRevB.45.13741.

[49] S. Pagliara et al. "Photoinduced π-π^* Band Gap Renormalization in graphite". In: *J. Am. Chem. Soc.* 133.16 (Mar. 2011), pp. 6318–6322. DOI: doi:10.1021/ja1110738.

[50] A. Chernikov et al. "Population inversion and giant bandgap renormalization in atomically thin WS_2 layers". In: *Nature Photonics* 9 (June 2015), pp. 466–. URL: https://doi.org/10.1038/nphoton.2015.104.

[51] E. A. A. Pogna et al. "Photo-Induced Bandgap Renormalization Governs the Ultrafast Response of Single-Layer MoS_2". In: *ACS Nano* 10.1 (2016). PMID: 26691058, pp. 1182–1188. DOI: 10.1021/acsnano.5b06488. eprint: https://doi.org/10.1021/acsnano.5b06488. URL: https://doi.org/10.1021/acsnano.5b06488.

[52] Y. Dou et al. "Band-gap shrinkage in n-type-doped CdO probed by photoemission spectroscopy". In: *Phys. Rev. B* 55 (20 May 1997), R13381–R13384. DOI: 10.1103/PhysRevB.55.R13381. URL: https://link.aps.org/doi/10.1103/PhysRevB.55.R13381.

[53] J. Wagner. "Band-gap narrowing in heavily doped silicon at 20 and 300 K studied by photoluminescence". In: *Phys. Rev. B* 32 (1985), pp. 1323–1325. URL: https://doi.org/10.1063/1.340257.

[54] F. J. Di Salvo et al. "Physical and structural properties of the new layered compounds Ta_2NiS_5 and Ta_2NiSe_5". In: *Jour. of the Less-Comm. Met.* 116.1 (1986), p. 51. DOI: https://doi.org/10.1016/0022-5088(86)90216-X. URL: http://www.sciencedirect.com/science/article/pii/002250888690216X.

[55] T. Kaneko et al. "Orthorhombic-to-monoclinic phase transition of Ta_2NiSe_5 induced by the Bose-Einstein condensation of excitons". In: *Phys. Rev. B* 87 (3 Jan. 2013), p. 035121. DOI: 10.1103/PhysRevB.87.035121. URL: https://link.aps.org/doi/10.1103/PhysRevB.87.035121.

[56] K. Seki et al. "Excitonic Bose-Einstein condensation in Ta_2NiSe_5 above room temperature". In: *Phys. Rev. B* 90 (15 Oct. 2014), p. 155116. DOI: 10.1103/PhysRevB.90.155116. URL: https://link.aps.org/doi/10.1103/PhysRevB.90.155116.

[57] Y. F. Lu et al. "Zero-gap semiconductor to excitonic insulator transition in Ta_2NiSe_5". In: *Nature Communications* 8 (Feb. 2017), pp. 14408–. URL: http://dx.doi.org/10.1038/ncomms14408.

[58] T. I. Larkin et al. "Giant exciton Fano resonance in quasi-one-dimensional Ta_2NiSe_5". In: *Phys. Rev. B* 95 (19 May 2017), p. 195144. DOI: 10.1103/PhysRevB.95.195144. URL: https://link.aps.org/doi/10.1103/PhysRevB.95.195144.

[59] M Bradler, C. Homann, and E. Riedle. "Mid-IR femtosecond pulse generation on the microjoule level up to 5μm at high repetition rates". In: *Opt. Lett.* 36.21 (Nov. 2011), pp. 4212–4214. DOI: 10.1364/OL.36.004212. URL: https://doi.org/10.1364/OL.36.004212.

[60] S. Mor et al. "Inhibition of the photoinduced structural phase transition in the excitonic insulator Ta_2NiSe_5". In: *Phys. Rev. B* 97 (11 Mar. 2018), p. 115154. DOI: 10.1103/PhysRevB.97.115154. URL: https://link.aps.org/doi/10.1103/PhysRevB.97.115154.

[61] C. Kittel. *Introduction to Solid State Physics*. 8th. Wiley, 2005.

[62] P. Hofmann. *Solid State Physics - An introduction*. WILEY-VCH, 2008.

[63] R. Fischer and T. Fauster. "Coupling of image states to quantum-well states for Au on Pd(111)". In: *Phys. Rev. B* 51 (11 Mar. 1995), pp. 7112–7115. DOI: 10.1103/PhysRevB.51.7112. URL: https://link.aps.org/doi/10.1103/PhysRevB.51.7112.

[64] X.-Y. Zhu et al. "Photo-induced electron transfer to molecular quantum structures on a metal surface". In: *Surf. Sci.* 451 (2000), pp. 244–249. URL: https://doi.org/10.1016/S0039-6028(00)00038-8.

[65] J. Zhao et al. "Molecular Electronic Level Alignment at Weakly Coupled Organic Film/Metal Interfaces". In: *ACS Nano* 8.10 (Oct. 2014), pp. 10988–10997. DOI: DOI:10.1021/nn5049969.

[66] L. D. Landau. "The Theory of Fermi Liquid". In: *JETP* 3.6 (Jan. 1957), p. 920. DOI: https://doi.org/10.1016/B978-0-08-010586-4.50095-X.

[67] J. J. Quinn and R. A. Ferrell. "Electron Self-Energy Approach to Correlation in a Degenerate Electron Gas". In: *Phys. Rev.* 112 (3 Nov. 1958), pp. 812–827. DOI: 10.1103/PhysRev.112.812. URL: https://link.aps.org/doi/10.1103/PhysRev.112.812.

[68] G. F. Giuliani and J. J. Quinn. "Lifetime of a quasiparticle in a two-dimensional electron gas". In: *Phys. Rev. B* 26 (8 Oct. 1982), pp. 4421–4428. DOI: 10.1103/PhysRevB.26.4421. URL: https://link.aps.org/doi/10.1103/PhysRevB.26.4421.

[69] P. S. Kirchmann. "Ultrafast Electron Dynamics in Low-Dimensional Materials". PhD thesis. 2008. URL: https://refubium.fu-berlin.de/handle/fub188/8954.

[70] J. M. Luttinger. "Analytic Properties of Single-Particle Propagators for Many-Fermion Systems". In: *Phys. Rev.* 121 (4 Feb. 1961), pp. 942–949. DOI: 10.1103/PhysRev.121.942. URL: https://link.aps.org/doi/10.1103/PhysRev.121.942.

[71] C. W. Nicholson. "Electronic Structure and Dynamics of Quasi-one Dimensional Materials". PhD thesis. 2017. URL: https://refubium.fu-berlin.de/handle/fub188/22174.

[72] G. Grimvall. *The Electron-Phonon Interaction in Metals*. North-Holland, 1981.

[73] J. González, F. Guinea, and M. A. H. Vozmediano. "Unconventional Quasiparticle Lifetime in Graphite". In: *Phys. Rev. Lett.* 77 (17 Oct. 1996), pp. 3589–3592. DOI: 10.1103/PhysRevLett.77.3589. URL: https://link.aps.org/doi/10.1103/PhysRevLett.77.3589.

[74] J. J. Sakurai. *Modern Quantum Mechanics*. Ed. by S. W. Johnson. Addison Wesley, 1993.

[75] A. Zangwill. *Physics at Surface*. 1996. DOI: http://dx.doi.org/10.1017/CBQ9780511622564.

[76] H. Lüth. *Solid Surfaces, Interfaces and thin films*. Ed. by Springer. 2010.

[77] J.-C. Deinert. "Zinc Oxide Surfaces and Interfaces: Electronic Structure and Dynamics of Excited States". PhD thesis. 2016. URL: https://depositonce.tu-berlin.de/handle/11303/5786.

[78] J. H. Davies. *The phyics of low-dimensional semiconductors*. Ed. by J. H. Davies. Cambridge University Press, 1998.

[79] U. Höfer et al. "Time resolved Coherent Photoelectron Spectroscopy of Quantized Electronic States on Metals Surfaces". In: *Science* 277.5331 (Sept. 1997), pp. 1480–. URL: http://science.sciencemag.org/content/277/5331/1480.abstract.

[80] E. V. Chulkov et al. "Lifetimes of Image-Potential States on Copper Surfaces". In: *Phys. Rev. Lett.* 80 (22 June 1998), pp. 4947–4950. DOI: 10.1103/PhysRevLett.80.4947. URL: https://link.aps.org/doi/10.1103/PhysRevLett.80.4947.

[81] J. Güdde and U. Höfer. "Femtosecond time-resolved studies of image-potential states at surfaces and interfaces of rare-gas adlayers". In: *Progress in Surface Science* 80.3 (2005), pp. 49 –91. ISSN: 0079-6816. DOI: https://doi.org/10.1016/j.progsurf.2005.10.003. URL: http://www.sciencedirect.com/science/article/pii/S0079681605000560.

[82] C. B. Harris et al. "Femtosecond dynamics of electrons on surfaces and at interfaces". In: *Annual Review of Physical Chemistry* 48.1 (1997). PMID: 15012454, pp. 711–744. DOI: 10.1146/annurev.physchem.48.1.711. eprint: https://doi.org/10.1146/annurev.physchem.48.1.711. URL: https://doi.org/10.1146/annurev.physchem.48.1.711.

[83] J. D. McNeill et al. "Interfacial quantum well states of Xe and Kr adsorbated on Ag(111)". In: *The Journal of Chemical Physics* 105.9 (1996), pp. 3883–3891. DOI: 10.1063/1.472209. eprint: https://doi.org/10.1063/1.472209. URL: https://doi.org/10.1063/1.472209.

[84] J. D. McNeill et al. "Dynamics and Spatial Distribution of Electrons in Quantum Wells at Interfaces Determined by Femtosecond Photoemission Spectroscopy". In: *Phys. Rev. Lett.* 79 (23 Dec. 1997), pp. 4645–4648. DOI: 10.1103/PhysRevLett.79.4645. URL: https://link.aps.org/doi/10.1103/PhysRevLett.79.4645.

[85] W. Berthold et al. "Influence of Ar, Kr, and Xe layers on the energies and lifetimes of image-potential states on Cu(100)". In: *Applied Physics A* 78.2 (Jan. 2004), pp. 131–140. ISSN: 1432-0630. DOI: 10.1007/s00339-003-2310-6. URL: https://doi.org/10.1007/s00339-003-2310-6.

[86] Ar. Hotzel. "Electron dynamics of image potential states in weakly bound adsorbate layers: A short review". In: *Progress in Surface Science* 82.4 (2007). Dynamics of Electron Transfer Processes at Surfaces, pp. 336 –354. ISSN: 0079-6816. DOI: https://doi.org/10.1016/j.progsurf.2007.03.009. URL: http://www.sciencedirect.com/science/article/pii/S0079681607000196.

[87] J. R. Chelikowsky and M. Schlüter. "Electron states in α-quartz: A self-consistent pseudopotential calculation". In: *Phys. Rev. B* 15 (8 Apr. 1977), pp. 4020–4029. DOI: 10.1103/PhysRevB.15.4020. URL: https://link.aps.org/doi/10.1103/PhysRevB.15.4020.

[88] X. D. Fan, J. L. Peng, and L. A. Bursill. "Joint Density of States of Wide-Band-Gap Materials by Electron Energy Loss Spectroscopy". In: *Modern Physics Letters B* 12.13 (1998), pp. 541–554. DOI: 10.1142/S0217984998000640. eprint: http://www.worldscientific.com/doi/pdf/10.1142/S0217984998000640. URL: http://www.worldscientific.com/doi/abs/10.1142/S0217984998000640.

[89] I. Sohrab Beigi and Steven G. Louie. "Self-Trapped Excitons in Silicon Dioxide: Mechanism and Properties". In: *Phys. Rev. Lett.* 95 (15 Oct. 2005), p. 156401. DOI: 10.1103/PhysRevLett.95.156401. URL: https://link.aps.org/doi/10.1103/PhysRevLett.95.156401.

[90] R. Salh. "Crystalline Silicon - Properties and Uses". In: ed. by Sukumar Basu. IntechOpen, 2011. Chap. Defect related luminescence in silicon dioxide network: a review, pp. 137–138.

[91] H. W. Klemm et al. "Preparation of silica films on Ru(0001): A LEEM/PEEM study". In: *Surface Science* 643 (2016). Present challenges in surface science, a special issue in honour of Dietrich Menzel, pp. 45 –51. ISSN: 0039-6028. DOI: https://doi.org/10.1016/j.susc.2015.05.017. URL: http://www.sciencedirect.com/science/article/pii/S0039602815001429.

[92] E. Gao, B. Xie, and Z. Xu. "Two-dimensional silica: Structural, mechanical properties, and strain-induced band gap tuning". In: *Journal of Applied Physics* 119.1 (2016), p. 014301. DOI: 10.1063/1.4939279. eprint: https://doi.org/10.1063/1.4939279. URL: https://doi.org/10.1063/1.4939279.

[93] B. Yang et al. "Thin silica films on Ru(0001): monolayer, bilayer and three-dimensional networks of [SiO4] tetrahedra". In: *Phys. Chem. Chem. Phys.* 14 (32 2012), pp. 11344–11351. DOI: 10.1039/C2CP41355H. URL: http://dx.doi.org/10.1039/C2CP41355H.

[94] H. Klemm. "Formation and properties of Ultrathin silicon dioxide films on Ru(0001): an in-situ spectro-microstopy study". PhD thesis. 2017.

[95] C. Büchner et al. "Adsorption of Au and Pd on Ruthenium-Supported Bilayer Silica". In: *The Journal of Physical Chemistry C* 118.36 (2014), pp. 20959–20969. DOI: 10.1021/jp5055342. eprint: https://doi.org/10.1021/jp5055342. URL: https://doi.org/10.1021/jp5055342.

[96] M. Lisowski et al. "Ultra-fast dynamics of electron thermalization, cooling and transport effects in Ru(001)". In: *Applied Physics A* 78.2 (Jan. 2004), pp. 165–176. ISSN: 1432-0630. DOI: 10.1007/s00339-003-2301-7. URL: https://doi.org/10.1007/s00339-003-2301-7.

[97] A. P. Seitsonen. "Theoretical investigations into adsorption and co-adsorption on transition-metal surfaces as mmodel to heterogeneous catalysis". PhD thesis. 2002. URL: https://depositonce.tu-berlin.de/handle/11303/547.

[98] C. Gahl. "Electron transfer and solvation dynamics in ice adsorbed on metal surfaces". PhD thesis. 2004. URL: https://refubium.fu-berlin.de/handle/fub188/12124.

[99] P. Phillips. *Advanced Solid State Phyics*. Ed. by Cambridge University Press. 2nd ed. Cambridge University Press, 2012.

[100] R. S. Knox. "Solid State Physics". In: ed. by F. Seitz and D. Turnbull. Academic Press N. Z., 1963. Chap. Theory of Exciton.

[101] W. Kohn. "Excitonic Phases". In: *Phys. Rev. Lett.* 19 (8 Aug. 1967), pp. 439–442. DOI: 10.1103/PhysRevLett.19.439. URL: https://link.aps.org/doi/10.1103/PhysRevLett.19.439.

[102] C. Monney et al. "Probing the exciton condensate phase in $1T$-$TiSe_2$2 with photoemission". In: *New Journal of Physics* 12.12 (2010), p. 125019. URL: http://stacks.iop.org/1367-2630/12/i=12/a=125019.

[103] K. Rossnagel, L. Kipp, and M. Skibowski. "Charge-density-wave phase transition in $1T - TiSe_2$: Excitonic insulator versus band-type Jahn-Teller mechanism". In: *Phys. Rev. B* 65 (23 May 2002), p. 235101. DOI: 10.1103/PhysRevB.65.235101. URL: https://link.aps.org/doi/10.1103/PhysRevB.65.235101.

[104] H. Cercellier et al. "Evidence for an Excitonic Insulator Phase in $1T-TiSe_2$". In: *Phys. Rev. Lett.* 99 (14 Oct. 2007), p. 146403. DOI: 10.1103/PhysRevLett.99.146403. URL: https://link.aps.org/doi/10.1103/PhysRevLett.99.146403.

[105] C. Monney et al. "Revealing the role of electrons and phonons in the ultrafast recovery of charge density wave correlations in $\mathbf{1}T-\mathbf{TiSe_2}$". In: *Phys. Rev. B* 94 (16 Oct. 2016), p. 165165. DOI: 10.1103/PhysRevB.94.165165. URL: https://link.aps.org/doi/10.1103/PhysRevB.94.165165.

[106] W Ketterle et al. "Bose-Einstein condensation of ultracold atomic gases". In: *Physica Scripta* 1996.T66 (1996), p. 31. URL: http://stacks.iop.org/1402-4896/1996/i=T66/a=004.

[107] L. V. Butov et al. "Towards Bose-Einstein condensation of excitons in potential traps". In: *Nature* 417 (May 2002), pp. 47–. URL: https://doi.org/10.1038/417047a.

[108] L.V. Butov. "Exciton condensation in coupled quantum wells". In: *Solid State Communications* 127.2 (July 2003). Quantum Phases at the Nanoscale, pp. 89 –98. ISSN: 0038-1098. DOI: https://doi.org/10.1016/S0038-1098(03)00312-0. URL: http://www.sciencedirect.com/science/article/pii/S0038109803003120.

[109] B. I. Halperin and T. M. Rice. "Possible Anomalies at a Semimetal-Semiconductor Transition". In: *Rev. Mod. Phys.* 40 (1968), p. 755. URL: http://journals.aps.org/rmp/abstract/10.1103/RevModPhys.40.755.

[110] R. H. Friend et al. "Semimetallic character of $TiSe_2$ and semiconductor character of TiS_2 under pressure". In: *Journal of Physics C: Solid State Physics* 10.24 (1977), p. L705. URL: http://stacks.iop.org/0022-3719/10/i=24/a=006.

[111] J. A. Wilson and John A. Wilson. "Concerning the semimetallic character of TiS_2 and $TiSe_2$". In: *Solid State Communications* 22.9 (1977), pp. 551 – 553. ISSN: 0038-1098. DOI: https://doi.org/10.1016/0038-1098(77)90133-8. URL: http://www.sciencedirect.com/science/article/pii/0038109877901338.

[112] R. H. Friend, D. Jerome, and A. D. Yoffe. "High-pressure transport properties of TiS_2 and $TiSe_2$". In: *Journal of Physics C: Solid State Physics* 15.10 (1982), p. 2183. URL: http://stacks.iop.org/0022-3719/15/i=10/a=019.

[113] F. J. Di Salvo, D. E. Moncton, and J. V. Waszczak. "Electronic properties and superlattice formation in the semimetal $TiSe_2$". In: *Phys. Rev. B* 14 (10 Nov. 1976), pp. 4321–4328. DOI: 10.1103/PhysRevB.14.4321. URL: https://link.aps.org/doi/10.1103/PhysRevB.14.4321.

[114] T. Pillo et al. "Photoemission of bands above the Fermi level: The excitonic insulator phase transition in $1T-TiSe_2$". In: *Phys. Rev. B* 61 (23 June 2000), pp. 16213–16222. DOI: 10.1103/PhysRevB.61.16213. URL: https://link.aps.org/doi/10.1103/PhysRevB.61.16213.

[115] E. Möhr-Vorobeva et al. "Nonthermal Melting of a Charge Density Wave in $TiSe_2$". In: *Phys. Rev. Lett.* 107 (3 July 2011), p. 036403. DOI: 10.1103/PhysRevLett.107.036403. URL: https://link.aps.org/doi/10.1103/PhysRevLett.107.036403.

[116] A. Kogar et al. "Signatures of exciton condensation in a transition metal dichalcogenide". In: *Science* 358.6368 (2017), pp. 1314–1317. ISSN: 0036-8075. DOI: 10.1126/science.aam6432. eprint: http://science.sciencemag.org/content/358/6368/1314.full.pdf. URL: http://science.sciencemag.org/content/358/6368/1314.

[117] S. A. Sunshine and J. A. Ibers. "Structure and physical properties of the new layered ternary chalcogenides tantalum nickel sulfide (Ta_2NiS_5) and tantalum nickel selenide (Ta_2NiSe_5)". In: *Inorg. Chem.* 24 (1985), p. 3611. DOI: DOI:10.1021/ic00216a027.

[118] Y. Okamura. Private communication. 2014.

[119] P. Debye. "Zur Theorie der spezifischen Wärmen". In: *Annalen der Physik* 344.14 (1912), pp. 789–839. DOI: 10.1002/andp.19123441404. eprint: https://onlinelibrary.wiley.com/doi/pdf/10.1002/andp.19123441404. URL: https://onlinelibrary.wiley.com/doi/abs/10.1002/andp.19123441404.

[120] J. F. Annett. *Superconductivity, Superfluids and Condensates*. Oxford University Press Inc., 2004.

[121] T. Kaneko et al. "Electronic structure of Ta_2NiSe_5 as a candidate for excitonic insulators". In: *Journal of Physics: Conference Series* 400.3 (2012), p. 032035. URL: http://stacks.iop.org/1742-6596/400/i=3/a=032035.

[122] Y. Wakisaka et al. "Excitonic insulator state in Ta_2NiSe_5 probed by photoemission spectroscopy." In: *Phys. Rev. Lett.* 103 (2 July 2009), p. 026402. DOI: 10.1103/PhysRevLett.103.026402. URL: https://link.aps.org/doi/10.1103/PhysRevLett.103.026402.

[123] Y. Wakisaka et al. "Photoemission Spectroscopy of Ta_2NiSe_5". In: *J. Supercond. Nov. Magn.* 25 (2012), p. 1231. DOI: doi:10.1007/s10948-012-1526-0.

[124] D. Ihle et al. "Bound state formation and the nature of the excitonic insulator phase in the extended Falicov-Kimball model". In: *Phys. Rev. B* 78 (19 Nov. 2008), p. 193103. DOI: 10.1103/PhysRevB.78.193103. URL: https://link.aps.org/doi/10.1103/PhysRevB.78.193103.

[125] V.-N. Phan, K. W. Becker, and H. Fehske. "Spectral signatures of the BCS-BEC crossover in the excitonic insulator phase of the extended Falicov-Kimball model". In: *Phys. Rev. B* 81 (20 May 2010), p. 205117. DOI: 10.1103/PhysRevB.81.205117. URL: https://link.aps.org/doi/10.1103/PhysRevB.81.205117.

[126] J. Hubbard. "Electron correlations in narrow energy bands". In: *Proceedings of the Royal Society A* 276 (Nov. 1963), pp. 237–257. DOI: DOI:10.1098/rspa.1963.0204.

[127] T. Hertel et al. "Femtosecond time-resolved photoemission of electron dynamics in surface Rydberg states". In: *Journal of Vacuum Science & Technology A: Vacuum, Surfaces, and Films* 15.3 (1997), pp. 1503–1509. DOI: 10.1116/1.580570. eprint: http://dx.doi.org/10.1116/1.580570. URL: http://dx.doi.org/10.1116/1.580570.

[128] A Damascelli. "Probing the Electronic Structure of Complex Systems by ARPES". In: *Physica Scripta* 2004.T109 (June 2004), p. 61. URL: http://stacks.iop.org/1402-4896/2004/i=T109/a=005.

[129] H. Hertz. "Üeber einen Einfluss des ultravioletten Lichtes auf die electrische Entladung (On the influence of ultraviolet light on the electric discharge)". In: *Annalen der Physik* 267 (1887), pp. 983–1000. DOI: 10.1002/andp.18872670827.

[130] A. Einstein. "Über einen die Erzeugung und Verwandlung des Lichts betreffenden heuristischen Gesichtspunkt (Concerning an Heuristic Point of View Toward the Emission and Transformation of Light.)" In: *Annalen der Physik* 17 (1905), pp. 132–148. DOI: 10.1002/andp.19053220607. URL: https://doi.org/10.1002/andp.19053220607.

[131] H. B. Michaelson. "The work function of the elements and its periodicity". In: *Journal of Applied Physics* 48.11 (1977), pp. 4729–4733. DOI: 10.1063/1.323539. eprint: https://doi.org/10.1063/1.323539. URL: https://doi.org/10.1063/1.323539.

[132] J. D. Koralek et al. "Experimental setup for low-energy laser-based angle resolved photoemission spectroscopy". In: *Rev. Sci. Instrum.* 78 (2007). DOI: http://dx.doi.org/10.1063/1.2722413.

[133] P. J. Feibelman and D. E. Eastman. "Photoemission spectroscopy—Correspondence between quantum theory and experimental phenomenology". In: *Phys. Rev. B* 10 (12 Dec. 1974), pp. 4932–4947. DOI: 10.1103/PhysRevB.10.4932. URL: https://link.aps.org/doi/10.1103/PhysRevB.10.4932.

[134] A. Damascelli, Z. Hussain, and Z.-X. Shen. "Angle-resolved photoemission studies of the cuprate superconductors". In: *Rev. Mod. Phys.* 75 (2 Apr. 2003), pp. 473–541. DOI: 10.1103/RevModPhys.75.473. URL: https://link.aps.org/doi/10.1103/RevModPhys.75.473.

[135] J. B. Pendry. "Theory of Photoemission". In: *Surf. Sci.* 57 (Mar. 1976), pp. 679–705. DOI: https://doi.org/10.1016/0039-6028(76)90355-1.

[136] J. Osterwalder. "Surface and Interface Science - Volume 1 - Concepts and Methods". In: John Wiley & Sons, Inc., 2013. Chap. Electron Based Methods: 3.2.2 Photoelectron Spectroscopy and Diffraction. ISBN: 978-3-527-40488-9. URL: http://tinyurl.sfx.mpg.de/utqn.

[137] J. D. Koralek et al. "Laser Based Angle-Resolved Photoemission, the Sudden Approximation, and Quasiparticle-Like Spectral Peaks in $Bi_2Sr_2CaCu_2O_{8+\delta}$". In: *Phys. Rev. Lett.* 96 (1 Jan. 2006), p. 017005. DOI: 10.1103/PhysRevLett.96.017005. URL: https://link.aps.org/doi/10.1103/PhysRevLett.96.017005.

[138] M. Calandra and F. Mauri. "Electron-phonon coupling and electron self-energy in electron-doped graphene: Calculation of angular-resolved photoemission spectra". In: *Phys. Rev. B* 76 (20 Nov. 2007), p. 205411. DOI: 10.1103/PhysRevB.76.205411. URL: https://link.aps.org/doi/10.1103/PhysRevB.76.205411.

[139] F. Schmitt et al. "Transient Electronic Structure and Melting of a Charge Density Wave in $TbTe_3$". In: *Science* (2008). DOI: DOI:10.1126/science.1160778.

[140] J. Schäfer et al. "Electronic Quasiparticle Renormalization on the Spin Wave Energy Scale". In: *Phys. Rev. Lett.* 92 (9 Mar. 2004), p. 097205. DOI: 10.1103/PhysRevLett.92.097205. URL: https://link.aps.org/doi/10.1103/PhysRevLett.92.097205.

[141] T. Yoshida et al. "Correlated electronic states of $SrVO_3$ revealed by angle-resolved photoemission spectroscopy". In: *Journal of Electron Spectroscopy and Related Phenomena* 208.Supplement C (2016). Special Issue: Electronic structure and function from state-of-the-art spectroscopy and theory, pp. 11 – 16. ISSN: 0368-2048. DOI: https://doi.org/10.1016/j.elspec.2015.11.012. URL: http://www.sciencedirect.com/science/article/pii/S0368204815002868.

[142] J. A. Sobota et al. "Distinguishing Bulk and Surface Electron-Phonon Coupling in the Topological Insulator Bi_2Se_3 Using Time-Resolved Photoemission Spectroscopy". In: *Phys. Rev. Lett.* 113 (15 Oct. 2014), p. 157401. DOI: 10.1103/PhysRevLett.113.157401. URL: https://link.aps.org/doi/10.1103/PhysRevLett.113.157401.

[143] S. Gerber et al. "Femtosecond electron-phonon lock-in by photoemission and x-ray free-electron laser". In: *Science* 357.6346 (2017), pp. 71–75. ISSN: 0036-8075. DOI: 10.1126/science.aak9946. eprint: http://science.sciencemag.org/content/357/6346/71.full.pdf. URL: http://science.sciencemag.org/content/357/6346/71.

[144] R. Loudon. *The quantum Theory of light*. 2001.

[145] M. Weinelt. "Time-resolved two-photon photoemission from metal surfaces". In: *J. Phys.: Condens. Matter* 14 (2002), R1099. URL: http://stacks.iop.org/0953-8984/14/i=43/a=202.

[146] J. Stähler. "Freezing hot electrons- Electron Transfer and Solvation Dynamics at D_2O and NH_3- Metal Interfaces". PhD thesis. 2007. URL: https://refubium.fu-berlin.de/handle/fub188/3655.

[147] L. Bogner. "Ultrafast Relaxation Dynamics after Optical Excitation of Hybrid Inorganic/Organic Systems". In: *PhD Thesis* (2015). URL: https://refubium.fu-berlin.de/handle/fub188/10953.

[148] J. Stähler et al. "Real-Time Measurement of the Vertical Binding Energy during the Birth of a Solvated Electron". In: *Journal of the American Chemical Society* 137.10 (2015). PMID: 25611976, pp. 3520–3524. DOI: 10.1021/ja511571y. eprint: https://doi.org/10.1021/ja511571y. URL: https://doi.org/10.1021/ja511571y.

[149] F. Wooten. *Optical properties of solics*. Academic Press, 1972.

[150] C. V. Raman. "A new radiation". In: *Indian Journal of Physics* 2 (1928), pp. 387–398. URL: http://www.jstor.org/stable/24101519.

[151] G. Landsberg. "Molekulare Lichtzerstreuung in festen Körpern. I - Lichtzerstreuung im kristallinischen Quarz und ihre Temperaturabhängigkeit (Molecular light scattering in solid bodies. I - Light scattering in crystalline quartz and its temperature dependence)". In: *Zeitschrift für Physik* 43.9 (Sept. 1927), pp. 773–778. ISSN: 0044-3328. DOI: 10.1007/BF01397337. URL: https://doi.org/10.1007/BF01397337.

[152] D. A. Long. *The Raman effect*. 2002.

[153] T. Dekorsy, G. C. Cho, and H. Kurz. *Coherent phonons in condensed media*. Ed. by M. Cardona and G. Güntherodt. Berlin, Heidelberg: Springer Berlin Heidelberg, 2000, pp. 169–209. ISBN: 978-3-540-48755-5. DOI: 10.1007/BFb0084242. URL: https://doi.org/10.1007/BFb0084242.

[154] R. Rosei and D. W. Lynch. "Thermomodulation specta of Al, Au, and Cu". In: *Phys. Rev. B.* 5.10 (May 1972). DOI: https://doi.org/10.1103/PhysRevB.5.3883.

[155] J. Demsar, J. L. Sarrao, and A. J. Taylor. "Dynamics of photoexcited quasiparticles in heavy electron compounds". In: *Journal of Physics: Condensed Matter* 18.16 (Apr. 2006), R281. URL: http://stacks.iop.org/0953-8984/18/i=16/a=R01.

[156] S. I. Anisimov, B. L. Kapeliovich, and T. L. Perel'Man. "Electron emission from metal surfaces exposed to ultrashort laser pulses". In: *Soviet Journal of Experimental and Theoretical Physics* 39 (Aug. 1974), pp. 776–781. URL: http://adsabs.harvard.edu/abs/1974JETP...39..375A.

[157] P. B. Allen. "Theory of thermal relaxation of electrons in metals". In: *Phys. Rev. Lett.* 59 (13 Sept. 1987), pp. 1460–1463. DOI: 10.1103/PhysRevLett.59.1460. URL: https://link.aps.org/doi/10.1103/PhysRevLett.59.1460.

[158] K. Ishioka and O. V. Misochko. "Coherent lattice oscillations in solids and their optical control". In: *Progress in Ultrafast Intense Laser Science* (2009). DOI: https://doi.org/10.1007/978-3-642-03825-9_2.

[159] H. J. Zeiger et al. "Theory for displacive excitation of coherent phonons". In: *Phys. Rev. B* 45 (2 Jan. 1992), pp. 768–778. DOI: 10.1103/PhysRevB.45.768. URL: https://link.aps.org/doi/10.1103/PhysRevB.45.768.

[160] K. Ishioka, M. Kitajima, and O. V. Misochko. "Temperature dependence of coherent A1g and Eg phonons of bismuth". In: *Journal of Applied Physics* 100.9 (2006), p. 093501. DOI: 10.1063/1.2363746. eprint: https://doi.org/10.1063/1.2363746. URL: https://doi.org/10.1063/1.2363746.

[161] Stanford Research Systems. *About Lock-in amplifiers*. Tech. rep.

[162] D. Wegkamp. "Ultrafast electron dynamics and the role of screening". PhD thesis. 2015. URL: https://refubium.fu-berlin.de/handle/fub188/3387.

[163] L. Foglia. "Ultrafast dynamics and energy loss channels at a hybrid organic inorganic interface". PhD thesis. 2015. URL: https://depositonce.tu-berlin.de/handle/11303/5210.

[164] C. Rulliére. *Femtosecond Laser Pulses*. Ed. by C. Rulliére. Springer, 2005.

[165] D. E. Spence, P. N. Kean, and W. Sibbett. "60-fsec pulse generation from a self-mode-locked Ti:sapphire laser". In: *Opt. Lett.* 16.1 (Jan. 1991), pp. 42–44. DOI: 10.1364/OL.16.000042. URL: https://doi.org/10.1364/OL.16.000042.

[166] R. L. Fork, O. E. Martinez, and J. P. Gordon. "Negative dispersion using pairs of prisms". In: *Opt. Lett.* 9.5 (May 1984), pp. 150–152. DOI: 10.1364/OL.9.000150. URL: https://doi.org/10.1364/OL.9.000150.

[167] D. Wegkamp et al. "Phase retrieval and compression of low-power white-light pulses". In: *Appl. Phys. Lett.* 99.101101 (2011). URL: http://dx.doi.org/10.1063/1.3635396.

[168] L. Foglia, M. Wolf, and J. Stähler. "Ultrafast dynamics in solids probed by femtosecond time-resolved broadband electronic sum frequency generation". In: *Applied Physics Letters* 109.20 (Nov. 2016), p. 202106. DOI: 10.1063/1.4967838. eprint: https://doi.org/10.1063/1.4967838. URL: https://doi.org/10.1063/1.4967838.

[169] M. K. Reed, M. K. Steiner-Shepard, and Negus D. K. "Widely tunable femtosecond optical parametric amplifier at 250 kHz with a Ti:sapphire regenerative amplifier". In: *Opt. Lett.* 19.22 (Nov. 1994), pp. 1855–1857. DOI: 10.1364/OL.19.001855. URL: https://doi.org/10.1364/OL.19.001855.

[170] Oxford Instrument. *Windows for cryogenic environments*. URL: https://www.oxford-instruments.com/OxfordInstruments/media/nanoscience/PDFs/OptistatDry/Optistat-Windows-Brochure_Medium_Single-pages_web.pdf.

[171] N. Demirdöven et al. "Dispersion compensation with optical materials for compression of intense sub-100-fs mid-infrared pulses". In: *Opt. Lett.* 27.6 (Mar. 2002), pp. 433–435. DOI: 10.1364/OL.27.000433. URL: https://doi.org/10.1364/OL.27.000433.

[172] J.-C. Deinert. "Zeit- und winkelaufgelöste Zweiphotonen-Photoemissionsspektroskopie: Aufbau und Charakterisierung des Experiments anhand der Cu(111)- und D_2O/Cu(111)-Oberfäche". MA thesis. 2011. URL: http://w0.rz-berlin.mpg.de/pc/electrondynamix/wp-content/uploads/2018/04/deinert_diplom2011.pdf.

[173] T. Pelzer et al. "Electronic structure of the Ru(0001) surface". In: *Journal of Physics: Condensed Matter* 12.10 (2000), p. 2193. URL: http://stacks.iop.org/0953-8984/12/i=10/a=305.

[174] W. Moritz et al. "Structure Determination of the Coincidence Phase of Graphene on Ru(0001)". In: *Phys. Rev. Lett.* 104 (13 Apr. 2010), p. 136102. DOI: 10.1103/PhysRevLett.104.136102. URL: https://link.aps.org/doi/10.1103/PhysRevLett.104.136102.

[175] L. Lichtenstein et al. "The Atomic Structure of a Metal-Supported Vitreous Thin Silica Film". In: *Angewandte Chemie International Edition* 51.2 (2011), pp. 404–407. DOI: 10.1002/anie.201107097. eprint: https://onlinelibrary.wiley.com/doi/pdf/10.1002/anie.201107097. URL: https://onlinelibrary.wiley.com/doi/abs/10.1002/anie.201107097.

[176] J. Güdde, W. Berthold, and U. Höfer. "Dynamics of Electronic Transfer Processes at Metal/Insulator Interfaces". In: *Chemical Reviews* 106.10 (2006). PMID: 17031986, pp. 4261–4280. DOI: 10.1021/cr050171s. eprint: https://doi.org/10.1021/cr050171s. URL: https://doi.org/10.1021/cr050171s.

[177] K. Gillmeister, M. Kiel, and W. Widdra. "Image potential states at transition metal oxide surfaces: A time-resolved two-photon photoemission study on ultrathin NiO films". In: *Phys. Rev. B* 97 (8 Feb. 2018), p. 085424. DOI: 10.1103/PhysRevB.97.085424. URL: https://link.aps.org/doi/10.1103/PhysRevB.97.085424.

[178] K. Giesen et al. "Two-photon photoemission via image-potential states". In: *Phys. Rev. Lett.* 55 (3 July 1985), pp. 300–303. DOI: 10.1103/PhysRevLett.55.300. URL: https://link.aps.org/doi/10.1103/PhysRevLett.55.300.

[179] R. W. Schoenlein et al. "Femtosecond Studies of Image-Potential Dynamics in Metals". In: *Phys. Rev. Lett.* 61 (22 Nov. 1988), pp. 2596–2599. DOI: 10.1103/PhysRevLett.61.2596. URL: https://link.aps.org/doi/10.1103/PhysRevLett.61.2596.

[180] M. Wolf et al. "Direct and indirect excitation mechanism in two-photon photoemission spesctroscopy of Cu(111) and CO/Cu(111)". In: *Phys. Rev. B* 59 (8 Feb. 1999), pp. 5926–5935. DOI: 10.1103/PhysRevB.59.5926. URL: https://link.aps.org/doi/10.1103/PhysRevB.59.5926.

[181] M. Winter, E. V. Chulkov, and U. Höfer. "Trapping of Image-Potential Resonances on a Free-Electron-like Surface". In: *Phys. Rev. Lett.* 107 (23 Nov. 2011), p. 236801. DOI: 10.1103/PhysRevLett.107.236801. URL: https://link.aps.org/doi/10.1103/PhysRevLett.107.236801.

[182] P. B. Littlewood et al. "Models of coherent exciton condensation". In: *Journal of Physics: Condensed Matter* 16.35 (2004), S3597. URL: http://stacks.iop.org/0953-8984/16/i=35/a=003.

[183] A. Nakano et al. "Antiferroelectric distortion with anomalous phonon softening in the excitonic insulator Ta_2NiSe_5". In: *Phys. Rev. B* 98 (4 June 2018), p. 045139. DOI: 10.1103/PhysRevB.98.045139. URL: https://link.aps.org/doi/10.1103/PhysRevB.98.045139.

[184] T. I. Larkin et al. "Infrared phonon spectra of quasi-one-dimensional Ta_2NiSe_5 and Ta_2NiS_5". In: *Phys. Rev. B* 98 (12 Sept. 2018), p. 125113. DOI: 10.1103/PhysRevB.98.125113. URL: https://link.aps.org/doi/10.1103/PhysRevB.98.125113.

[185] S. Y. Kim et al. "Layer-Confined Excitonic Insulating Phase in Ultrathin Ta_2NiSe_5 Crystals". In: *ACS Nano* 10.9 (2016). PMID: 27526274, pp. 8888–8894. DOI: 10.1021/acsnano.6b04796. eprint: https://doi.org/10.1021/acsnano.6b04796. URL: https://doi.org/10.1021/acsnano.6b04796.

[186] S. Wall et al. "Ultrafast changes in lattice symmetry probed by coherent phonons". In: *Nature Communication* 3 (Mar. 2012). DOI: doi:10.1038/ncomms1719. URL: https://www.nature.com/articles/ncomms1719.

[187] G. Lucazeau. "Effect of pressure and temperature on Raman spectra of solids: anharmonicity". In: *Journal of Raman Spectroscopy* 34.7-8 (2003), pp. 478–496. ISSN: 1097-4555. DOI: 10.1002/jrs.1027. URL: http://dx.doi.org/10.1002/jrs.1027.

[188] D. Werdehausen et al. "Coherent order parameter oscillations in the ground state of the excitonic insulator Ta_2NiSe_5". In: *Science Advances* 4.3 (2018). DOI: 10.1126/sciadv.aap8652. eprint: http://advances.sciencemag.org/content/4/3/eaap8652.full.pdf. URL: http://advances.sciencemag.org/content/4/3/eaap8652.

[189] R. V. Yusupov et al. "Single-Particle and Collective Mode Couplings Associated with 1- and 2-Directional Electronic Ordering in Metallic $R\mathrm{Te}_3$ (R = Ho, Dy, Tb)". In: *Phys. Rev. Lett.* 101 (24 Dec. 2008), p. 246402. DOI: 10.1103/PhysRevLett.101.246402. URL: https://link.aps.org/doi/10.1103/PhysRevLett.101.246402.

[190] H. Schäfer, V. V. Kabanov, and J. Demsar. "Collective modes in quasi-one-dimensional charge-density wave systems probed by femtosecond time-resolved optical studies". In: *Phys. Rev. B* 89 (4 Jan. 2014), p. 045106. DOI: 10.1103/PhysRevB.89.045106. URL: https://link.aps.org/doi/10.1103/PhysRevB.89.045106.

[191] V. R. Morrison et al. "A photoinduced metal-like phase of monoclinic VO_2 revealed by ultrafast electron diffraction". In: *Science* 346.6208 (2014), pp. 445–448. ISSN: 0036-8075. DOI: 10.1126/science.1253779. eprint: http://science.sciencemag.org/content/346/6208/445.full.pdf. URL: http://science.sciencemag.org/content/346/6208/445.

[192] M. K. Liu et al. "Photoinduced Phase Transitions by Time-Resolved Far-Infrared Spectroscopy in V_2O_3". In: *Phys. Rev. Lett.* 107 (6 Aug. 2011), p. 066403. DOI: 10.1103/PhysRevLett.107.066403. URL: https://link.aps.org/doi/10.1103/PhysRevLett.107.066403.

[193] M. Porer et al. "Non-thermal separation of electronic and structural orders in a persisting charge density wave". In: *Nature Mater.* 13 (2014), p. 857. URL: https://doi.org/10.1038/nmat4042.

[194] J. Lourembam et al. "Evidence for Photoinduced Insulator-to-Metal transition in B-phase vanadium dioxide". In: *Sci. Rep.* 6 (2016), p. 25538. DOI: doi:10.1038/srep25538.

[195] Zhensheng Tao et al. "The nature of photoinduced phase transition and metastable states in vanadium dioxide". In: *Sci. Rep.* 6 (Dec. 2016), p. 38514. DOI: doi:10.1038/srep38514. URL: https://doi.org/10.1038/srep38514.

[196] S.-L. Yang et al. "Electron propagation from a photo-excited surface: implications for time-resolved photoemission". In: *Applied Physics A* 116.1 (July 2014), pp. 85–90. ISSN: 1432-0630. DOI: 10.1007/s00339-013-8154-9. URL: https://doi.org/10.1007/s00339-013-8154-9.

[197] M. Alonso, R. Cimino, and K. Horn. "Surface Photovoltage Effects in Photoemission from Metal-GaP(110) Interfaces: Importance for Band-Bending Evaluation". In: *Phys. Rev. Lett.* 65 (7 Aug. 1990), pp. 939–939. DOI: 10.1103/PhysRevLett.65.939. URL: https://link.aps.org/doi/10.1103/PhysRevLett.65.939.

[198] W. Shockley. "Problems related top-n junctions in silicon". In: *Czechoslovak Journal of Physics* 11.2 (Feb. 1961), pp. 81–121. ISSN: 1572-9486. DOI: 10.1007/BF01688613. URL: https://doi.org/10.1007/BF01688613.

[199] A. T. Tarekegne et al. "Impact ionization dynamics in silicon by MV/cm THz fields". In: *New Journal of Physics* 19.12 (2017), p. 123018. URL: http://stacks.iop.org/1367-2630/19/i=12/a=123018.

[200] C. Karras et al. "The impact ionization coefficient in dielectric materials revisited". In: *Proc.SPIE* 8190 (2011), pp. 8190 –8190 –9. DOI: 10.1117/12.899267. URL: https://doi.org/10.1117/12.899267.

[201] I. Gierz et al. "Tracking Primary Thermalization Events in Graphene with Photoemission at Extreme Time Scales". In: *Phys. Rev. Lett.* 115 (8 Aug. 2015), p. 086803. DOI: 10.1103/PhysRevLett.115.086803. URL: https://link.aps.org/doi/10.1103/PhysRevLett.115.086803.

[202] Y. Hattori et al. "Impact ionization and transport properties of hexagonal boron nitride in a constant-voltage measurement". In: *Phys. Rev. B* 97 (4 Jan. 2018), p. 045425. DOI: 10.1103/PhysRevB.97.045425. URL: https://link.aps.org/doi/10.1103/PhysRevB.97.045425.

[203] P. Werner, K. Held, and M. Eckstein. "Role of impact ionization in the thermalization of photoexcited Mott insulators". In: *Phys. Rev. B* 90 (23 Dec. 2014), p. 235102. DOI: 10.1103/PhysRevB.90.235102. URL: https://link.aps.org/doi/10.1103/PhysRevB.90.235102.

[204] D. Golež, P. Werner, and M. Eckstein. "Photoinduced gap closure in an excitonic insulator". In: *Phys. Rev. B* 94 (3 July 2016), p. 035121. DOI: 10.1103/PhysRevB.94.035121. URL: https://link.aps.org/doi/10.1103/PhysRevB.94.035121.

[205] F. Mahmood et al. "Selective scattering between Floquet-Bloch and Volkov states in a topological insulator". In: *Nature Physics* 12 (Jan. 2016), pp. 306–. URL: http://dx.doi.org/10.1038/nphys3609.

[206] Y. H. Wang et al. "Observation of Floquet-Bloch States on the Surface of a Topological Insulator". In: *Science* 342.6157 (2013), pp. 453–457. ISSN: 0036-8075. DOI: 10.1126/science.1239834. eprint: http://science.sciencemag.org/content/342/6157/453.full.pdf. URL: http://science.sciencemag.org/content/342/6157/453.

[207] M. Goano. "Series expansion of the Fermi-Dirac integral Fj(x) over the entire domain of real j and x". In: *Solid-State Electronics* 36.2 (1993), pp. 217 – 221. ISSN: 0038-1101. DOI: https://doi.org/10.1016/0038-1101(93)90143-E. URL: http://www.sciencedirect.com/science/article/pii/003811019390143E.

[208] S. Xu et al. "Energy Dependence of Electron Lifetime in Graphite Observed with Femtosecond Photoemission Spectroscopy". In: *Phys. Rev. Lett.* 76 (3 Jan. 1996), pp. 483–486. DOI: 10.1103/PhysRevLett.76.483. URL: https://link.aps.org/doi/10.1103/PhysRevLett.76.483.

[209] S. Wall et al. "Tracking the evolution of electronic and structural properties of VO_2 during the ultrafast photoinduced insulator-metal transition". In: *Phys. Rev. B* 87 (11 Mar. 2013), p. 115126. DOI: 10.1103/PhysRevB.87.115126. URL: https://link.aps.org/doi/10.1103/PhysRevB.87.115126.

Publication list

Publications in the Framework of this Thesis

Selene Mor, Marc Herzog, Denis Golež, Philipp Werner, Martin Eckstein, Naoyuki Katayama, Minoru Nohara, Hide Takagi, Takashi Mizokawa, Claude Monney, Julia Stähler. *Ultrafast Electronic Band Gap Control in an Excitonic Insulator.* Phys. Rev. Lett. **119**, 086401 (2017)

Selene Mor, Marc Herzog, Johannes Noack, Naoyuki Katayama, Minoru Nohara, Hide Takagi, Annette Trunschke, Takashi Mizokawa, Claude Monney, Julia Stähler. *Inhibition of the photoinduced structural phase transition in the excitonic insulator* Ta_2NiSe_5. Phys. Rev. B **97**, 115154 (2018)

Publications on other Topics

Stefania Pagliara, Gianluca Galimberti, **Selene Mor**, Matteo Montagnese, Gabriele Ferrini, M. S. Grandi, Pietro Galinetto, and Fulvio Parmigiani *Photoinduced* π-$\pi*$ *Band Gap Renormalization in Graphite.* J. Am. Chem. Soc., 133 (16), pp 6318-6322 (2011)

Federico Cilento, Stefano Dal Conte, Giacomo Coslovich, Simone Peli, Nicola Nembrini, **Selene Mor**, Francesco Banfi, Gabriele Ferrini, Hiroshi Eisaki, Mun K Chan, Chelsey J. Dorow, Michael J. Veit, Martin Greven, Dirk van der Marel, Riccardo Comin, Andrea Damascelli, Laurenz Rettig, Uwe Bovensiepen, Massimo Capone, Claudio Giannetti, Fulvio Parmigiani *Photo-enhanced antinodal conductivity in the pseudogap state of high-*T_C *cuprates* Nat. Comm. volume 5, 4353 (2014)

Academic curriculum vitae

For reasons of data protection, the curriculum vitae is not published in the electronic version.

Acknowledgements

So many are the people that walked (with) me during these years and made my PhD way this unforgettable experience...

First of all I would like to thank Martin Wolf for giving me the opportunity to work in his department. I really enjoyed the stimulating environment and the open atmosphere from which I have learned a lot for the past years. Thanks to both Martin Wolf and Martin Weinelt for being my doctoral supervisors.

A very special thank to Julia, for letting me join her group and supervising my project with great care and constant encouragement. Thanks for the possibility to develop my ideas while always finding in you the needed adjustment and support on my route. I feel very lucky for the rich experience you offered me.

Multiple thanks to Marc for guiding my first steps in the lab as a PhD student and later joining many experiments and lab adventures. I am thankful to you for your support in my thesis and being always open for scientific discussion.

Thanks, Claude, for bringing up the exciting project that turned into my main PhD work. Even more for your knowledge I had the opportunity to access through our collaboration. It has been very stimulating working with you.

A big big big thank to my amazing group: Angelika, Boubacar, Clemens, Daniel, Jan, Katharina, Laura, Lea, Lukas, Marc (see above!), Sam, Sarah, Sesha, Stefano. My PhD life would not have been as continuously (!) exciting, almost always (!!) smooth, certainly never (!!!) hopeless without even a single one of you!

Un ringraziamento extra a Laura, co-founder della tradizione del buon caffè in ufficio, sempre pronta per una buona chiecchierata scientifica e non! A Ste von Ponkaral, complice nelle più imprevedibili imprese laseristiche, con un occhio sempre vigile e premuroso al di là del suo monitor.

Thanks to the many colleagues and friends for the enjoyable time I had with you at and outside FHI. Specially, Chris, Michele, Will, Natalia, Vasilis, Julius, Alex, you've been great supporters.

A sincere thank to Marcel, Sven, Albrecht and Daniel, your precious help and support these years has been much more than 'technical'.

A 'sparkling' thank to Manuel and Ines for making my life at work easier in many aspects and being such faithful fans whenever I was stepping on a stage (more to come)!

Danke Sandra, Sophie, Xixi und Anne, dass ihr immer da wart...troz unserer ständigen unerfolgreichen Doodles!

Grazie Monica, perché in qualunque paese fossi, eri sempre un po' anche a Berlino, anzi in Jonasstrasse 31!

Thanks Bjørt, for all the great exchange we had while talking, listening, laughing, crying ... always in such an open and natural way.

Danke Hendrikje, für die ganze Unterstützung meiner intensiven Schreibphase durch deine Wörter, dein Zuhören und unseres unschätzbar tolles Musikmitmachen!

Grazie cuginetta Gaia, se sono arrivata qui é anche perché non vedo l'ora di riraccontarci i nostri PhD in un mare di risate!

Grazie Ste, perché anche senza le puntuali telefonate del sabato alle 11:30 (sigh), c'eri e c'era anche il tuo Buddha!

Grazie Chiara, per avermi incoraggiata in ogni momento di questo percorso, con affetto unico e efficacia ineguagliabile. (Si direbbe che mi conosci un gran bene :*)

Grazie alla mia famiglia e particolarmente ai miei nonni per essermi stati vicini sempre, telefonicamente e...culinariamente!

Grazie Gio ed Eli, perché con un fratello e una sorella così, che conoscono le tue debolezze, i tuoi punti di forza e i tuoi sogni talvolta ancor prima e meglio di te, è come avere un paio d'ali per atterrare sempre al sicuro o per volare ancora più in alto!

Grazie di cuore a voi, mamma e papà, di avermi sempre seguita e lasciata andare in ogni mio passo. Sentire sempre che c'eravate e che ero libera sono state una carica inesauribile per questi anni.

A te, Gian, un grazie che non si può misurare per aver creduto ogni istante in me. Con te è (stato) tutto un altro giro di blues.

Selbstständigkeitserklärung

Sämtliche verwendeten Hilfsmittel, Hilfen und Quellen sind an der entsprechenden Stelle angegeben. Ich versichere, dass ich auf dieser Grundlage diese Arbeit selbstständig verfasst habe. Diese Arbeit wurde bisher weder in gleicher noch ähnlicher Form einer anderen Prüfungskomission vorgelegt oder veröventlicht.

Berlin, Thursday 16th May, 2019
Selene Mor